Digital Heterodyne Holography for Plasmonic Nanostructures

Sarah Yasmine Suck

THÈSE DE DOCTORAT
DE L'UNIVERSITÉ PIERRE ET MARIE CURIE

Spécialité

Physique

(ED 397 - Physique et Chimie des Matériaux)

Préparée à l'Institut Langevin - Ondes et Images

Présentée par

Sarah Yasmine Suck

Pour obtenir le grade de

DOCTEUR de l'UNIVERSITÉ PIERRE ET MARIE CURIE

Sujet de la thèse :

Digital Heterodyne Holography for Plasmonic Nanostructures

Soutenue le 02 novembre 2011

devant le jury composé de :

M.	**BOUHELIER**	**Alexandre**	**Rapporteur**
M.	**COLLIN**	**Stéphane**	**Examinateur**
Mme	**DEL FATTI**	**Natalia**	**Rapporteur**
M.	**DE WILDE**	**Yannick**	**Membre invité**
Mme	**MAÎTRE**	**Agnès**	**Président**
M.	**TESSIER**	**Gilles**	**Directeur de thèse**
M.	**VOGELGESANG**	**Ralf**	**Examinateur**

Université Pierre & Marie Curie - Paris VI
Bureau d'accueil
Inscription des doctorants et base de données
Esc G, 2e étage
15 rue de l'École de Médecine
75270 PARIS Cedex 06

Tél Secrétariat : 01 42 34 68 35
Fax : 01 42 34 68 40
Tél pour les étudiants de A à EL : 01 42 34 69 54
Tél pour les étudiants de EM à MON : 01 42 34 68 41
Tél pour les étudiants de MOO à Z : 01 42 34 68 51
E-mail : scolarite.doctorat@upmc.fr

Remerciements

De faire une thèse n'est pas un travail solitaire, mais un travail en équipe, dans un groupe avec des échanges réguliers, dans un laboratoire avec des contributions de plusieurs personnes. Ici je voudrais m'en servir de quelques pages de mon manuscrit pour remercier à toutes les personnes qui ont contribué à un très bon déroulement de ma thèse.

Tout d'abord je tiens à remercier Natalia Del Fatti et Alexandre Bouhelier pour avoir accepté de rapporter sur mon travail. Je remercie aussi Agnès Maître, Stéphane Collin et Ralf Vogelgesang pour avoir accepté d'être membres du jury de thèse comme examinateurs. Grâce à un jury très intéressé et curieux j'ai pu profiter d'un échange très fructueux et animé pendant la discussion de ma soutenance.

Un remerciement particulier va à la Fondation Pierre-Gilles de Gennes qui m'a permis de faire ma thèse en premier lieu grâce à son financement pendant ces 3 ans. Je remercie aussi son directeur, M. Gilles Rubinstenn, qui a poursuivi ma thèse un peu de loin mais toujours avec beaucoup d'intérêt.

Les deux personnes à qui je dois le plus sont mes deux directeurs de thèse: Gilles et Yannick. En premier lieu ils m'ont accepté comme doctorante bien que j'étais sans aucun background optique. Néanmoins ils m'ont aidé beaucoup à obtenir le financement pour faire une thèse chez eux et m'ont soutenu dès le début de ma thèse.

Gilles a su partager avec moi sa solide expertise dans la domaine d'optique expérimentale et théorique. Gilles était toujours disponible quand j'avais des questions ou des problèmes de manips. Son encadrement et son soutient ont été indispensables à la réussite de mon travail. Gilles était toujours ouvert à des nouveaux idées ou des projets. Un exemple est le projet de simulation: quand je voulais commencer des simulations des propriétés optiques - malgré notre ignorance mutuelle - Gilles s'est montré toute de suite très intéressé et a acheté sans un cillement le matériel nécessaire (le logiciel coûteux et un ordinateur puissant). Grâce à sa patience, son calme et sa sérénité il était très agréable de travailler ensemble avec Gilles ce que j'ai beaucoup apprécié durant ma thèse!

Le jour de ma soutenance Yannick s'est défini comme "assistant" (et pas comme encadrant) dont je ne suis pas d'accord. La raison pour sa définition venait probablement du fait que Yannick et moi n'avions jamais eu d'occasion de vraiment travailler ensemble bien que il a été prévu. Malheureusement le temps limité de la thèse ne le permettait plus.

Mais au contraire j'ai vu Yannick toujours comme mon (deuxième) directeur de thèse. Il était toujours intéressé à mes avancements pendant ma thèse. J'ai partagé avec Yannick mes approches, mes problèmes, mes avancés et mes résultats. Et quand je rencontrais des problèmes, Yannick a souvent su donner des conseils très appréciés pour les résoudre et surmonter. Yannick est toujours de bonne humeur et souriant, non seulement très tôt le matin quand il fait son tour de dire bonjour au monde, mais aussi très tard le soir, et toujours dispo pour discuter de ci et ça, même dans des moments de stress.

Nous n'avons pas eu une vie de groupe "classique"; dans le sens que nous avons travaillé tous dans le même thématique de la plasmonique mais sur des sujets très différents. Au début de ma thèse nous avons eu entre des membres de groupe peu d'échanges sur nos différents projets. Vers le dernier tiers de ma thèse Yannick et Gilles ont initié des réunions de groupe hebdomadaires que j'ai apprécié beaucoup! Pendant nos discussions (plus au moins animés dépendant de la réactivité des personnes à l'heure matinale) autour du café et souvent trop de croissants et de viennoiseries, j'ai appris beaucoup, à la fois des travaux au sein de notre groupe et des travaux des autres laboratoires partout dans le monde. Merci à Nok, Arthur et Léo pour leurs présences et leurs contributions!

Je dois remercier beaucoup "l'équipe" de LPN: Nathalie Bardou qui à participé énormément à la fabrication difficile des échantillons précieuse, Christophe Dupuis qui a mené avec son expertise l'observation et la caractérisation des nanostructures et avec qui j'ai passé des heures rigolos devant le MEB. Bien-sûr je n'oublie pas à remercier Stéphane Collin. Sans son collaboration et son expertise ma thèse n'aurait pas pu être réalisé! C'était une collaboration très agréable et très fructueuse.

Je voudrais remercier Sébastien qui m'a fait découvrir les "dark modes". Son expertise dans la plasmonique et sa connaissance immense de tout ont apporté beaucoup des idées intéressants, des aperçus fascinants sur mon sujet et ont attribué à l'analyse des résultats. Finalement, grâce à Seb et à ses commentaires toujours constructives nous avons publié ensemble un très beaux article!

Je tiens à remercier Rémi Carminati. Son expertise dans la théorie est incontestée, sa connaissance de l'optique est infiniment vaste et son éloquence impressionnante. Pendant ma thèse il a évoqué son intérêt à la technique de l'holographie hétérodyne (Rémi a aussi fourni une partie de l'analyse pour ma thèse) et m'a assurée de l'intérêt et de l'avantage de cette technique dans le monde de la plasmonique.

Je voudrais remercier Srdjan Acimovic qui a fait sa thèse à l'ICFO. Je l'ai connu sur internet à travers des forums de physique qui discutaient des simulations dans la plasmonique en utilisant Comsol. Srdjan m'a donné beaucoup des conseils qui m'ont fait avancé quand j'avais des problèmes avec Comsol.

Je remercie Gilles (encore!), Sylvain, François et Jean-Paul pour leur aide et disponi-

bilité pendant les TP que j'ai eu d'occasion d'avoir encadré avec eux.

Many thanks au meilleur bureau du monde: Étienne, Virginie, Valentina, Rémi et Hugues. On a rigolé beaucoup pendant ces derniers 3 ans. L'atmosphère dans notre bureau a contribué beaucoup à la joie de venir au travail et a adouci chaque jour du travail, en outre des bonbons qui ne manquaient jamais!

Bien-sûr, je n'oublie pas dans mes remerciements mes voisines du bureau à côté: Salma, Karla, Ioana, Nok et Emilie! Les "filles" avaient des bons conseils pour des problèmes et tenaient toujours un sourire toutes prêtes ce qui a soulevé mon esprit immédiatement quand quelque chose allait mal.

La Montagne a aussi contribué à avoir passé beaucoup des bons moments avec des collègues et des amis du labo autour d'un verre de T-Punch ou d'une pinte de bière, absorbés dans des discussions scientifiques ou plus souvent non-scientifiques.

Un grand merci va aussi à Daniel qui nous (nous = venant de l'ESPCI) a permis de participer à son cours de "renforcement musculaire" à l'ENS. Bien-sûr sans Max je n'aurais jamais découvert ce cours. Merci, Max, aussi pour ta bonne humeur imperturbable. Merci aussi aux autres co-sportifs Étienne et Anne! C'était toujours un plaisir de m'activer d'une manière sportive. Le sport du jeudi midi me manquera beaucoup.

Voici une liste (pas exhaustive) de tous ceux qui se sont pas encore trouvé dans la liste de remerciement, mais à qui je voudrais remercier. Sans eux cette expérience aurait été différemment:

Sonia (!), Elika, Sandrine, Arik, Dominika, Jochen, Benedikt, Matthias, Stéphanie, Christelle, Delphine, Corinne, Matthias et TV5 dans ma salle de manips, Patricia, Emmanuel, Jean-Marie, Claude, SSOP1, Cargèse, Porquerolles, Mario et ses cafards, Taekwondo, Jonas, Heldmuth, Alexandre, Michaël, Mickaël, Michael (ceci n'est pas une faute de frappe), Cédric, Natalia, Caroline, Charles, Sylvie, Lara, Charles et son rhum délicieux, Alexandre, Emanuele, Nazim, Romain, Farin Urlaub, Tom, Matthias, Micha, Thomas und Judith, Daniel, PC Café, Die Ärzte, Beatsteaks, des pique-niques aux champs de mars, Montsouris, Lucie, Fadi, Georges, Steve, Anis, 2× Julien, Pierre, Cyril, Maxime, Mattia et Delphine, Vélib, Dexter, Game of Thrones, Big Bang Theory, Quartier Latin, financiers aux thé vert, Golosino, Sorin, Yasmina, Michaela, Roberta, Gym Combat, Marcoussis, grèves, Vendé, Saint Gildas, Honfleur, Mme Denis, Bordeaux, Thaïlande, San Francisco, Dresden, DPG, CLEO, Matlab, Google, Danielle Fournier, M. Bok, la salle stagiaires, LaTeX, la Sardaigne, le Champagne à et de Troyes, l'Internationale, Julie, Take it Easy, les fêtes, Picard, Hoa, la bière à Leuven, linie 21, Radium, Marie Curie, Paula, Sylvain et Alice, Elena, Christoph und Bertille, Giorgio, Kevin, Michele et Marie, Alessandro, Enrico, footings, les catacombes (I'm still waiting, Sylvain), parc floral, Roberto, Sergio e Maria, Time Warp, Thriller, cupcakes, Lavazza, spiegel.de, et ... Paris.

Natürlich möchte ich auch meiner Familie danken, die mich immer in allen meinen

Entscheidungen unterstützt haben (und sogar bis nach Paris mit dem Auto gefahren sind, um mir bei meiner Verteidigung beizustehen und Bier und Plätzchen aus Deutschland mitzubringen...). Ohne sie und deren Sichtweise auf die Dinge von aussen (beim wahrsten Sinne des Wortes) wäre alles viel schwieriger gewesen. Danke!

Finalmente, un grande ringrazio va a Romano: mio amore, mio amico, mio compagno senza di liu gli ultimi tre anni sarebberonno stati molto piu difficile. Romano mi ha sempre incoraggiato et risollevato quando avevo i dubbi delle mie decisione e non ha mai smesso di sostenermi. Grazie!

Abstract

In this thesis we study the scattering characteristics of plasmonic nanostructures by improving and adapting digital heterodyne holography, which is a powerful tool delivering a three-dimensional cartography of scattered light, and which has the advantage of allowing fast full-field imaging.

Spectroscopic measurements were carried out to record the scattering spectra of single nanoobjects and complement holographic measurements. In order to get a deeper insight into the measured far-field scattering characteristics, we developed a numerical model based on the finite element method. This model allowed us to simulate the scattered fields of nanostructures both in the near- and far-field either in a reflection or transmission configuration for the illumination. The model yielded a good agreement with experimental results.

We studied numerous gold nanostructures prepared by electron beam lithography on glass substrates, ranging from simple, elementary nanoobjects to novel nanostructures. While the former allowed us to validate the technique, more sophisticated structures allowed us to observe that their scattering pattern is extremely sensitive to external and internal factors, such as the polarization and the wavelength of the incident light or the structure's geometry and its resonance wavelength. We recognize so called "hot spots" in the far-field, which are zones on the chain that scatter light more intensely than others. In addition, we show that the technique of photothermal heterodyne holography is a novel method to study the temperature increase and heat distribution in heated plasmonic nanostructures due to its ability to directly probe a temperature increase.

Keywords

digital holography; nanoantennas; radiation patterns; photothermics; numerical simulation; heterodyne detection

Résumé

Dans cette thèse, nous étudions les caractéristiques de diffusion de nanostructures plasmoniques tout en adaptant et améliorant l'holographie hétérodyne numérique, qui est une technique d'imagerie plein champ pour mesurer en trois dimensions le diagramme de rayonnement. En outre, nous avons effectué de nombreuses mesures spectroscopiques pour enregistrer les spectres de diffusion de nanoobjets uniques. Afin d'obtenir une compréhension plus profonde des caractéristiques du champ diffusé que nous mesurons, nous avons développé un modèle numérique basé sur la méthode des éléments finis. Ce modèle nous a permis de simuler le champ proche et le champ lointain d'une nanostructure avec une onde incidente en réflexion ou en transmission. Nous obtenons un excellent accord entre nos résultats expérimentaux et calculés.

Dans cette thèse, nous avons étudié de nombreux nanostructures d'or fabriquées sur du verre par lithographie électronique. Des structures simples nous ont permis de valider la technique. Des objets plus sophistiques nous ont ensuite permis de constater que leur diagramme de diffusion est extrêmement sensible aux facteurs externes et internes, tels que la polarisation et la longueur d'onde de la lumière incidente ou la géométrie de la structure et sa longueur d'onde de résonance. En outre, nous montrons que la technique de l'holographie hétérodyne photothermique mesure directement l'augmentation de la température, et ainsi, se présente comme une nouvelle méthode pour étudier la distribution de la chaleur dans des nanostructures plasmoniques.

Mots-clefs

holographie numérique; nanoantennes; diagramme de diffusion; photothermique; simulation numérique; détection hétérodyne

Titre de la thèse

Holographie hétérodyne numérique pour l'étude des nanostructures plasmoniques

Contents

Introduction

Plasmonics is an upcoming discipline that is primarily concerned with the manipulation of light at the nanoscale. Plasmonics explores the interaction processes between light and metal nanofilms or metal nanostructures. One of the most fascinating features of plasmonic structures is their ability to squeeze light into volumes less than one hundredth of a wavelength in size which is quite spectacular if one thinks about it.

Interesting effects such as this make plasmonics a very attractive research field which is rapidly developing in physics, biophotonics, chemistry and medicine, numerous potential and promising applications. These range from enhanced sensing and spectroscopy for chemical identification and detection of biomolecules or biological agents, drug design, high-resolution microscopy, to signal propagation with metal-based waveguides and solar cells.

The characteristic near- and far-field of a plasmonic nanostructure can be regarded as its fingerprint. The far-field of a plasmonic nanostructure delivers information about its plasmon resonance, whereas the near-field gives access to its capability to enhance and confine fields. The angular emission or scattering of nanostructures is particularly interesting when dealing with nanoantennas, since one of their most interesting functions is their ability of controlling the direction of emission. Techniques that allow to gain insight into the angular scattering information are important for the study of nanoantennas. Therefore, it is fundamental to obtain the full knowledge of the three-dimensional (3D) electromagnetic field around a nanoobject interacting with a light source, in order to exploit and tune the plasmon properties of nanostructures.

Today, however, few experimental tools exist to obtain a complete three-dimensional knowledge of the electromagnetic field. In order to record the electromagnetic field in three dimensions either scanning techniques have to be used or techniques that allow the measurement of the field's amplitude and phase. Scanning near-field optical microscopy achieves exceptional resolutions and has also proven its ability to detect both amplitude and phase of electromagnetic fields in plasmonic structures (Hillenbrand and Keilmann 2000; Vogelgesang *et al.* 2008; Esteban *et al.* 2008). However, this technique remains of heavy use, is time consuming and restricted to the near-field.

A technique that gives access to the angular information of the electromagnetic field is back focal plane imaging. The back focal plane of a bright-field reflection microscope or of a confocal microscope contains information about the sample, as positions in the back

focal plane map to diffraction angles from the sample. This kind of imaging has been applied recently to nanoantennas in order to map their emission patterns (Curto *et al.* 2010).

A couple of years ago, our laboratory developed the technique of (off-axis) digital heterodyne holography and showed that this technique is very well adapted to the detection of weakly scattering objects, like nanoobjects, due to its excellent sensitivity (Gross and Atlan 2007). It has been successfully applied to image and localize metal nanoparticles of 50 nm diameter in three-dimensions, either for fixed particles spin coated on a glass substrate or in free motion within a water suspension (Atlan *et al.* 2008; Absil *et al.* 2010). More recently, it has been shown that gold nanobeads, functionalized and fixed on the membrane of live cells, can be detected in order to obtain a three-dimensional image of the cell surface (Warnasooriya *et al.* 2010; Joud *et al.* 2011).

One of the main advantages of holography, a technique that relies on interferometry, is its ability to measure the amplitude and phase. Therefore, one hologram, which can be measured in less than 1 second, contains the whole 3D information of the recorded scattered light. Furthermore, holography allows also the access to the angular scattering pattern of a nanostructure since the angular spectrum of the hologram can be obtained by computing the scattered field in the Fourier space. Hence, digital heterodyne holography proves to be a powerful tool to deliver a three-dimensional cartography of the light scattered by nanoparticles, by combining a fast imaging technique with the ability to access the angular scattering information of a nanostructure.

In this thesis work, we apply the technique of digital heterodyne holography to plasmonic nanoobjects. To our knowledge, we are the first who characterized in three dimensions the light scattered by plasmonic nanostructures using holography. This study analyses extensively the plasmonic properties of a large variety of lithographically fabricated gold nanostructures, ranging from elementary objects like single disks and rods, structures of two coupled disks and rods, to a large variety of more complex structures, e.g. chains of nanodisks and pairs of long, tapered triangles.

This work is organized as follows: We will start with a short introduction to plasmonics and will give an overview of various geometries and applications of nanoantennas.

The second chapter will deal entirely with the principle and the technique of holography. We will present different holographic setups that we have developed for the use of diverse applications, i.e. photothermal heterodyne holography and scanning heterodyne holography. In this context, we will show that photothermal holography delivers direct access to the temperature increase of a heated sample, whereas the latter imaging technique allows to gain insight into the frequency domain of a system by systematically detuning the heterodyne beating frequency..

In addition, in the course of this thesis work, we developed a simulation model based

on the finite element method (FEM), for the numerical analysis of the far- and near-field scattering of plasmonic nanostructures. This model which will be presented in the third chapter, has been applied to model various nanostructures in order to get a deeper insight into their scattering behaviour.

The fourth chapter will extensively discuss the results obtained on elementary nanostructures which include single disks and two coupled disks and rods. We will show that both our experimental and numerical techniques used for the characterization of the far- and near-field scattering of plasmonic nanostructures obtain results that are in excellent agreement with theoretical predictions. We will present the first three-dimensional cartographies of light scattered by nanoobjects.

The fifth and last chapter finally addresses the study of more sophisticated nanoobjects. We will present an extensive study of the scattering characteristics of various chains of nanodisks with different disk numbers and disk spacings. In this context, we will demonstrate that depending on the illumination configuration, different modes can be excited, resulting into different characteristics of the scattered (far) field which can be imaged via holography. Furthermore, we will demonstrate that a nanodisk chain can be seen as a nanoantenna structure due to its ability to strongly scatter light in one direction. In the second part of this chapter we will apply the technique of photothermal holography to study the heating and the coupling of these chains. Lastly, a preliminary study on pairs of gold triangles will reveal the appearance of resonant modes dependent on the width of the triangles.

Chapter 1

Plasmonics and Optical Antennas

Table of contents

"· · · by chance I was keeping one of the metal plates at a very high distance from the ground while the other one was in the ground. Using this arrangement the signals became so strong that I was able to transmit up to one kilometer away. From that moment on the progress increased enormously. The plate at the top - the antenna - was raised more and more and the other one - the terra - was buried in the ground."

Guglielmo Marconi (1895)

"· · · is it possible, for example to emit light from a whole set of antennas, like we emit radio waves from an organized set of antennas to beam the radio programs to Europe? The same thing would be to beam the light out in a definite direction with very high intensity."

Richard Feynman (1959)

1.1 A Short Introduction to Plasmonics

In the last decade, the trend towards nanoscience and nanotechnology increased rapidly. This trend is motivated by the fact that as we move to smaller scales the underlying physical laws change from macroscopic to microscopic and new physical effects become prominent that may be exploited in future technological applications (Novotny and Hecht 2006). The expanding demand for smaller and faster optical and electronic devices has considerably increased the interest in **nano-optics**, a research field that covers all types of studies that include optical interactions with matter on a subwavelength scale.

One of the major emerging fields from nano-optics is **plasmonics** which is based on the interaction processes between electromagnetic radiation and conduction electrons at conducting interfaces or in conductive nanostructures, called *surface plasmon polaritons* and *localized surface plasmons*. Whereas the former are created at a dielectric-conductive interface, the latter are excited in conductive nanostructures. Although all conductive materials support plasmons, the noble metals silver and gold are mostly associated with the field of optical plasmonics since their plasmon resonances lie close to the visible region of the spectrum, and they enable relatively low losses in this range, which allows plasmon excitation by standard optical sources and methods. One of their most interesting properties is their ability to enhance and confine the electric field in 1, 2 or 3 dimensions of sub-lambda size. The field of plasmonics is based on exploiting plasmons for a variety of tasks, by designing and manipulating the geometry of metallic structures, and consequently their plasmon-resonant properties.

The strongly increasing research in the field of plasmonics in the last decade can be attributed to several factors. The increasing development of state of the art lithographic and chemical methods allow the fabrication of a wide variety of well defined nanoparticles and complex nanostructures. This has opened the possibility to engineer the plasmon response on a nanoscale. This control opens completely new possibilities in materials science, communications, biochemistry and medicine (Pelton, Aizpurua, and Bryant 2008). Furthermore, the modelling and simulation techniques of the optical response of complex nanostructures have been greatly expanded. Hence, experimental observations can be verified by comparing to theoretical predictions. This interplay enables an optimization of the studied nanostructures and their properties.

Another factor that has supported the rise of research in plasmonics is the significant progress accomplished in developing experimental techniques for the study of plasmonic structures. Nowadays, measurements of optical absorption and scattering spectra of single nanoparticles are feasible, scanning near-field optical microscopy enables the spatial characterization of the near-field of a large variety of plasmonic nanostructures, and ultrafast time-scales can be accessed to probe the dynamics of plasmonics.

The history of localized surface plasmons in metal nanostructures dates further back

to Roman times, when metallic nanoparticles were used for the staining of glass. The most famous and most ancient example is the fourth-century Lycurgus cup from the British museum, whose glass looks green in reflected light, but ruby red in transmitted light. Those colours are complementary evidence that there is little optical loss inside the glass. Such colloidal suspensions of gold, silver and other metals have been widely used in stained glass since the Middle Ages. Depending on the particle sizes, transmission through a silver colloid can yield yellow light and transmission through gold ruby red. Metallic nanoparticles transmit light with an intensity that strongly depends on the incident and viewing angles. The magnificent coloured light from stained glass of the Sainte Chapelle in Paris is assumed to be largely due to the plasmonic resonances (Stockman 2011).
The mathematical foundation of these particle plasmons was established by Mie in 1908.

Historically, the mathematical description of the surface plasmon modes was established in the early 20th century when Sommerfeld and Zenneck studied the propagation of radio waves along a surface of a conductor of finite conductivity in the context of wireless telegraphy (Sommerfeld 1899; Sommerfeld 1909; Zenneck 1907). These early investigations focused on frequencies much lower than that of visible light. The phenomenological difference of plasmonic surface waves and plane electromagnetic waves in free-space is however very small. Around the same period, Wood studied the reflection of visible light at metallic gratings and noted the observation of "anomalous" intensity drops in spectra (Wood 1902). This phenomenon was later theoretical described by Fano (Fano 1941). Finally in the 70s, Kretschmann and Raether realized the excitation of Sommerfeld's surface waves with visible light using prism coupling (Kretschmann and Raether 1968; Kretschmann 1971). With this a unified description of surface plasmon polaritons was established (Maier 2007).

In the following, we will elucidate the basic physics of plasmonics by describing surface plasmon polaritons and the localized surface plasmons. For a better understanding of the physics and its consequences of the latter we will introduce the quasi-static approximation and discuss briefly the impact of retardation effects.

1.1.1 Surface Plasmon Polaritons

Surface plasmon polaritons (SPP) are electromagnetic excitations propagating as a longitudinal wave at the interface between a dielectric and a conductor. Their field intensities fall off exponentially in the direction normal to the surface, the wave is therefore evanescent. Those surface waves arise via the coupling of the electromagnetic fields to oscillations of the conductor's electron plasma. The waves are transverse-magnetic (TM), i.e. their magnetic field is perpendicular to their wave vector $\vec{k}_{SPP}$ and in the plane of interface.

The *dispersion relation* of SPPs propagating at the interface between a metal of dielectric function $\varepsilon(\omega)$ and a dielectric half space, described via the dielectric function ε_{medium},

is given by (Maier 2007):

$$k_{SPP} = \frac{\omega}{c}\sqrt{\frac{\varepsilon \cdot \varepsilon_{medium}}{\varepsilon + \varepsilon_{medium}}} \tag{1.1}$$

where ω denotes the angular frequency and c the velocity of light. Equation 1.1 reveals that the wave vector of a SPP is always higher than that of an electromagnetic wave of the same frequency propagating in the adjacent dielectric alone. Because the wave vector in the plane must be conserved - a condition equivalent to conservation of the in-plane component of linear momentum - it is impossible to excite a SPP and fulfil the phase matching condition at an interface by an electromagnetic wave propagating in the dielectric. A SPP cannot radiate into the dielectric, therefore, the SPPs are also called "dark waves" (Stockman 2011). SPPs, however, can be excited using the so-called Otto or Kretschmann geometry in which a prism made of a dielectric material with higher optical index increases the k-vector to allow the excitation of SPPs. In the Kretschmann configuration, for example, the excitation light passes through a prism and is incident on the lower interface of a thin metal film. The medium above the metal is dielectric and typically air. The evanescent field of the light wave at the upper interface of the metal is then able to excite a SPP wave under total internal reflection condition.

1.1.2 Localized Surface Plasmons

Localized surface plasmons, or surface plasmons (SP), are non-propagating excitations of the conduction electrons of metallic nanostructures coupled to the electromagnetic field. These modes arise from the scattering of a small, sub-wavelength metal nanoparticle in an oscillating electromagnetic field. The curved surface of the particle exerts an effective restoring force on the driven electrons, so that a resonance can arise, leading to field amplification both inside and in the near-field zone outside the particle. This resonance is called the localized surface plasmon resonance. The sub-wavelength size of the particle has also the consequence that plasmon resonances can be excited by direct light illumination without having to fulfil the phase-matching condition, in contrast to propagating surface plasmons.

To first approximation, the electrons of the metal nanoparticle move freely and, driven by an external light's electric field, are periodically displaced with respect to the lattice ions. This displacement creates charges with opposite signs at opposite surfaces. Because these charges attract each other, they create also restoring forces. The result is an electron oscillator, whose quantum is called surface plasmon and whose frequency is determined by the restoring force and effective mass of the electron. The frequency of the SPs depends on many factors, notably the physical properties of the metal and of the surrounding dielectric material, the size and shape of the nanoparticle.

1.1.3 Single Particle Plasmon Resonances - The Quasi-Static Approximation

The oscillations of localized surface plasmons originate from the characteristic dielectric response of metals at optical frequencies. At resonance the polarizability is resonantly increased resulting in enhanced scattering, absorption and near-field intensities.

A full theoretical treatment of the interaction of a nanoparticle with an electromagnetic wave is beyond our scope. For a better understanding of the underlying physics let us introduce the *quasi-static approximation*, which is a simple model describing well the main results from such an interaction in first approximation.

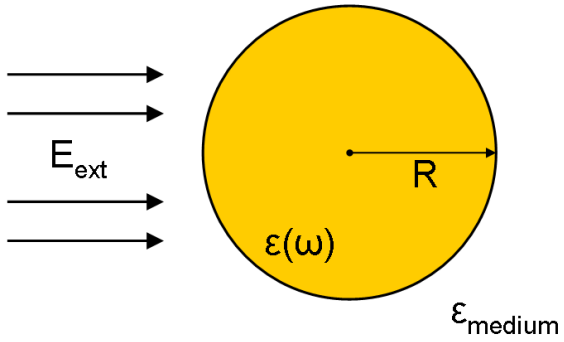

Figure 1.1 – Sketch of the model of the quasi-static approximation. A homogeneous sphere is placed into an external electrostatic field E_{ext}.

The response of sub-wavelength sized particles to a plane-wave illumination can be analysed using the quasi-static approximation which is illustrated in Fig. 1.1. This model neglects retardation, i.e. effects due to self-induction of electromagnetic fields, by considering only a region in space which is much smaller than the wavelength of light, so that the electromagnetic phase is constant throughout the region of interest. Consequently, the quasi-static approximation is only valid for particles that are smaller in size than the skin depth d_s of the metal. [1] For small spherical particles with a radius much smaller than the wavelength, this condition is fulfilled. We consider now a sphere of polarizable material with a radius R and a dielectric constant ε, embedded in a medium with dielectric constant ε_{medium}, under the influence of a static electric field E_{ext}. The external field induces a dipole moment in the sphere. The polarizability is written as (Bohren and Huffman 1983):

$$\alpha = 4\pi R^3 \varepsilon_0 \frac{\varepsilon - \varepsilon_{medium}}{\varepsilon + 2\varepsilon_{medium}} \tag{1.2}$$

It is evident from Eq. (1.2) that in vacuum (i.e. $\varepsilon_{medium} = 1$) this expression exhibits a resonance when the real part of ε approaches -2. Replacing the static dielectric constant

[1] The skin depth is the extent to which a field penetrates the metal surface and is given by $d_s = \lambda/(4\pi\sqrt{\varepsilon})$.

ε with the wavelength dependent form $\varepsilon(\omega) = \varepsilon_1(\omega) + i\varepsilon_2(\omega)$, the dielectric function of a noble metal, for example gold and silver, fulfils the resonance condition $\varepsilon_1(\omega) \to -2$ at visible frequencies. Hence, at resonance the real part of the denominator in Eq. (1.2) almost vanishes and causes a strongly increased induced dipole moment $\mu_P = \alpha \cdot E_{ext}$. This in turn leads to enhanced scattering and local fields.

For nanoparticles with an elongated shape, the electron oscillation is non-isotropic and localized either along the principle axes or at the edges and corners of the nanoparticle, leading to an additional shape-dependent depolarization and splitting of the surface plasmon resonance into several modes (such as longitudinal or transverse modes for nanorods) (Lal *et al.* 2007).

The electrostatic theory for light scattering by sub-wavelength sized spherical particles has a relatively simple extension to ellipsoidal particles. In particular, we are interested in the scattering by disks and rods which can be described as spheroidal particles in a first approximation. A rod can de described by a prolate (cigar-shaped) particle, whereas a disk is approximately an oblate (pancake-shaped) particle. The polarizability α_i of such an ellipsoidal particle along the axis i is given by (Bohren and Huffman 1983):

$$\alpha_i = V\varepsilon_0 \, \frac{\varepsilon(\omega) - \varepsilon_{medium}}{3\,\varepsilon_{medium} + 3\,L_i[\varepsilon(\omega) - \varepsilon_{medium}]} \tag{1.3}$$

V is the particle's volume and L_i is a geometrical factor related to the shape of the particle and given by

$$L_i = \frac{a_1 a_2 a_3}{2} \int_0^\infty \frac{dq}{(a_i^2 + q)\; f(q)} \tag{1.4}$$

where $f(q) = \sqrt{(q + a_1^2)(q + a_2^2)(q + a_3^2)}$. The ellipsoid is described by its semiaxis $a_1 \leq a_2 \leq a_3$, specified by $\frac{x^2}{a_1^2} + \frac{y^2}{a_2^2} + \frac{z^2}{a_3^2} = 1$. The geometrical factors satisfy $\sum_{i=1}^{3} L_i = 1$, and for a sphere $L_1 = L_2 = L_3 = \frac{1}{3}$.

A detailed analysis of the resonance position as a function of the aspect ratio (i.e. the ratio of the long axis radius to the short axis radius of the particle) using Eq. (1.3) shows that the resonance position depends approximately linearly on the aspect ratio: an increased aspect ratio leads to a red shifted resonance. Furthermore, the influence of the refractive index of the surrounding medium has to be considered as well. Increasing the refractive index leads to a red-shift of the resonance and a narrowing of its linewidth (Sönnichsen 2001). This red-shift is due to the shielding of surface charges by the polarization of the embedding medium.

We have seen that the theory of scattering and absorption of radiation by a small sphere predicts a resonant field enhancement due to a resonance of the polarizability α in expression (1.2) if $Re\{\varepsilon(\omega)\} \to -2\,\varepsilon_{medium}$. The nanoparticle acts like an electric dipole which resonantly absorbs and scatters electromagnetic fields. This theory, though valid

only for very small particles, provides a good approximation for particles of sizes below 100 nm in the visible or near-infrared frequency range.

For larger particles, where the quasi-static approximation is no longer valid due to significant phase changes of the driving field over the particle volume, an electrodynamic approach is required. Mie developed a complete theory of the scattering of electromagnetic radiation by spherical particles (Mie 1908). The approach of the *Mie theory* is to expand the internal fields and the scattered fields into a set of normal modes described by vector harmonics (Bohren and Huffman 1983; Kreibig and Vollmer 1995). The physical consequences of the first-order corrections to the quasi-static approximation will be shortly examined in the following section.

1.1.4 Theoretical Considerations beyond the Quasi-Static Limit: Retardation Effects

For large particles with sizes not negligible compared to the wavelength, the quasi-static approximation breaks down due to retardation effects. The effect of retardation of the exciting field over the volume in the particle leads to a shift in the plasmon resonance. Further, the retardation of the depolarization field inside the particle also leads to a shift in resonance (Meier and Wokaun 1983). For noble metals, the overall shift is towards lower energies, i.e. the dipole resonance position red-shifts with increasing particle size. Intuitively, this effect can be understood by considering that the distance between the charges at opposite interfaces of the particle increases with the particle size. This leads to a smaller restoring force and therefore a lowering of the resonance frequency (Maier 2007).

Another retardation effect that has to be taken into account is the reduction of absorption (which is directly related to the imaginary part of $\varepsilon(\omega)$, i.e. $Im\{\varepsilon(\omega)\}$), due to the increase of polarization. In order to account qualitatively for this effect, we have to consider the influence of radiation damping which leads to an attenuation in polarization. Radiation damping is caused by a direct radiative decay of the coherent electron oscillations into photons (Kokkinakis and Alexopoulos 1972), and it is the main cause of the weakening of the strength of the dipole plasmon resonance as the particle volume increases (Wokaun *et al.* 1982). As a result, the influence of radiation damping countervails the increase of polarization in strength due to the reduction of absorption.

In summary, the plasmon resonance of particles beyond the quasistatic regime is damped by two competing processes: a radiative decay process into photons, dominating for larger particles, and a non-radiative process due to absorption.

1.2 Optical Antennas

The concept of optical antennas has its origin in near-field optics (Novotny 2007a; Bharadwaj *et al.* 2009; Biagioni *et al.* 2011) when, in 1928, Edward Synge proposed the use of a tiny gold particle for localizing optical radiation on a sample surface and thereby surpassing the diffraction limit in optical imaging (Synge 1928). This particle can be viewed as an optical antenna, a structure that converts the energy of incident optical radiation into localized energy or vice versa, depending on whether the antenna occupies the role of a receiver or a transmitter.

Nanoantennas are the optical analogue of radio and microwave antennas. Since the wavelength is considerably lower, the size of the antenna must be reduced accordingly, which has only recently become feasible. They can be used to resonantly enhance light scattering (Greffet 2005; Mühlschlegel *et al.* 2005). Strictly speaking, antennas incorporate a transducer or a source of energy, but in a broader sense, entirely passive structures are here also called nanoantennas.

Nanoantennas are of great interest since they allow unique control of absorption and emission at the nanometer scale: confinement of the electromagnetic field to sub-wavelength dimensions (Farahani *et al.* 2005), field enhancement (Zhang *et al.* 2010; Kühn *et al.* 2006) and directivity of the emitted light (Taminiau *et al.* 2007; Curto *et al.* 2010).

Optical antennas fulfil the same function as their radio analogues, but with properties that differ in important ways. At radio-frequencies, metals behave like perfect conductors, with a skin depth that is negligible compared to the size of the antenna. But at optical frequencies, the skin depth is on the scale of tens of nanometers, i.e. on the scale of the nanoantenna size, and the metal behaves like a plasma strongly coupled to incident light. As a result, the antenna geometry scales with an effective wavelength that differs from the wavelength of the incident light (Novotny 2007b) in contrast to the size dependence of analogue antennas. Moreover, optical antennas can take various unusual forms and their properties may be strongly shape and material dependent due to their surface plasmon resonances.

1.2.1 Properties of Optical Antennas

Nanoantennas can be characterized using the same terminology as used for radio-frequency (RF) antennas. In the following, we briefly introduce the principle properties describing an antenna.

The function of an antenna is to enhance the transmission efficiency from the transmitter to the receiver. This enhancement can be achieved by increasing the total amount of the radiation released by the transmitter. This property is described by the *antenna*

efficiency:

$$\varepsilon_{rad} = \frac{P_{rad}}{P} = \frac{P_{rad}}{P_{rad} + P_{loss}} \tag{1.5}$$

where P is the total power dissipated by the antenna, P_{rad} is the radiated power and P_{loss} is the power dissipated into heat.

The *directivity* D is a measure of an antenna's ability to concentrate radiated power into a certain direction. It corresponds to the angular power density $p(\theta, \phi)$ relative to an isotropic radiator and is expressed by:

$$D(\theta, \phi) = \frac{4\pi}{P_{rad}}\, p(\theta, \phi) \tag{1.6}$$

When the direction (θ, ϕ) is not explicitly stated, one usually refers to the direction of maximum directivity, i.e. $D_{max} = (4\pi/P_{rad})\ max\{p(\theta, \phi)\}$. The combination of antenna efficiency and directivity results into the *antenna gain*:

$$G = \frac{4\pi}{P}\, p(\theta, \phi) = \varepsilon_{rad}\, D \tag{1.7}$$

Since perfectly isotropic radiators do not exist in reality, it is more convenient to use the *relative gain* by referring to an antenna of a known directional pattern. For this description a dipole antenna is normally used as a reference because of its relative simple radiation pattern. Recently, Huang *et al.* characterized the relative gain of coupled gold antenna pairs using the dipole-like scattering from a single particle as reference (Huang *et al.* 2008).

Radio wave antennas have strict design rules that relate to the wavelength of incident radiation. However, at optical frequencies these rules are no longer valid, the antenna responds to an effective wavelength which is reduced compared to the incident wavelength. The effective wavelength λ_{eff} is related to the incident wavelength λ by the *wavelength scaling* relation derived by Novotny (Novotny 2007b):

$$\lambda_{eff} = n_1 + n_2\, (\frac{\lambda}{\lambda_P}) \tag{1.8}$$

where λ_P is the plasma wavelength of the metal and n_1 and n_2 are constants depending on the geometry and dielectric parameters of the antenna.

1.2.2 Nanoantenna Geometries

During the last years many different types of nanoantennas have been proposed. Here, we would like to present some geometries that have been fabricated and investigated experimentally.

Single Nanoparticles One of the simplest structures are single nanospheres and nanorods. In fact, the use of a single nanoparticle as an antenna has already been proposed by Synge as we have noted earlier. Synge's nanoparticle takes freely propagating radiation and localizes it on a sample which has the role of the receiver. Since then, single nanoparticles have been successfully applied to enhance the sensitivity of fluorescence and Raman spectroscopy at a single molecular level (Biagioni *et al.* 2011; Anger *et al.* 2006; Kühn *et al.* 2006; Rogobete *et al.* 2007; Mohammadi *et al.* 2008).

Coupled Nanoparticles Coupled nanoparticles can act as optical antennas: they couple efficiently in the near-field to photon emitters to enhance their interaction with the far-field. Nanostructures composed of two coupled nanospheres have been proposed as the analogue of RF Hertzian dipole antennas (Alu and Engheta 2008) and are expected to have a high radiation efficiency due to the reduced density inside the spheres. For such structures it is important to tune efficiently the gap size. Recently, it has been demonstrated that the programmed assembly of DNA functionalized gold nanoparticles is a technique that allows to tune particle sizes and spacings (Bidault *et al.* 2008; Bonod *et al.* 2010) with a high accuracy. Furthermore, it has been shown that a pair of coupled metallic nanoparticles coupled to a dielectric microsphere builds a highly efficient optical antenna (Devilez *et al.* 2010a).

The coupling of two nanorods represent the analogue to half-wave RF antennas (Mühlschlegel *et al.* 2005; Ghenuche *et al.* 2008; Pramod and Thomas 2008). Very recently Greffet et al. have introduced the concept of impedance for a nanoantenna (Greffet *et al.* 2010) which provides a practical tool for the design of nanoantennas.

Bowtie Nanoantennas Bowtie antennas are constituted of two triangles facing each other tip-to-tip (Fromm *et al.* 2004; Schuck *et al.* 2005; Fischer and Martin 2008). The advantage of the bowtie antenna compared to a pair of nanorods, is that it efficiently suppresses the field enhancement at the outer ends of the structure. Furthermore, they are considered to have higher field enhancements in the gap because of a larger lightning-rod effect at the apex. In reality, however, this effect is limited by the radius of curvature at the apex. Bowtie antennas are applied to enhance molecular fluorescence (Farahani *et al.* 2005; Kinkhabwala *et al.* 2009), Raman scattering (Fromm *et al.* 2006) and for the light confinement beyond the diffraction limit when fabricated on the facet of a quantum-cascade laser (Yu *et al.* 2007).

Yagi-Uda Nanoantennas The optical analogue of a RF Yagi-Uda antenna has been theoretical proposed (Li *et al.* 2007; Taminiau *et al.* 2008) and since then experimentally verified (Kosako *et al.* 2010; Curto *et al.* 2010). The main advantage of an optical Yagi-Uda antenna is its very good directivity. Its unidirectional response is appealing in terms of enhanced sensitivity for detection. Similarly to their RF counterparts, nanometer-sized

Yagi-Uda antennas consist of a resonant single-wire antenna ($\pi/2$ phase shift between the driving field and the induced charge oscillations) arranged between a reflector (phase shift $> \pi/2$) and a set of directors (phase shift $< \pi/2$). To this purpose, the inter-element distance is important to achieve the desired interference between direct and reflected radiation (Biagioni *et al.* 2011).

Periodic Grooves Surrounding a Nanoaperture An antenna design that caught the attention of the nanoantenna community a couple of years ago (Lezec *et al.* 2002) is composed of a single nanoaperture surrounded by periodic grooves. The central nanoaperture reduces the sampling volume and enables single molecule analysis at high concentrations with enhanced excitation and emission rates. The periodic grooves act like an antenna to further concentrate the electromagnetic energy at the central aperture and to control the directivity of the radiated light. This design merges the light localization from the nanoaperture with the extended near- to far-field conversion capabilities from the concentric grooves. Recently, full directional control of the fluorescence emission from molecules in water solution has been demonstrated by using an optical antenna made of a nanoaperture surrounded by a periodic set of shallow grooves in a gold film (Aouani *et al.* 2011).

1.2.3 Applications of Optical Antennas - State of the Art

When Mühlschlegel *et al.* demonstrated that a thin metallic rod resonantly enhances light emission (Mühlschlegel *et al.* 2005; Greffet 2005), their important discovery bridged the fields of electrical engineering and nano-optics and led to a rapid and exponential growth of the research in the domain of nanoantennas. Since then, manifold applications of nanoantennas have been reported, and the number of publications is still increasing. To give a short overview of the state of the art of nanoantennas, we would like to highlight some noteworthy and interesting applications of nanoantennas and the latest advances in research.

Wavelength Tuning We have seen that the characteristics of a nanoparticle are generally determined by its shape and material. In the case of an optical antenna composed of two or more particles, its characteristics are related to near-field interactions between the individual elements. Essentially such a structure remains a passive device. However, in order to enable a controlled optical exchange between two nanoscale objects, an external control of an antenna is highly desirable. In order to tune the near-field coupling externally, it was shown that the length and the gap of an antenna can be tuned mechanically by precise nanomanipulation with the tip of an atomic force microscope (Merlein *et al.* 2008). However, this technique has the drawback of an inflexible tuning, that cannot be controlled over short time-scales.

In this context, Bouhelier and co-workers demonstrated an active control over antenna performances by an external electrical trigger. The authors used an anisotropic load medium to control the electromagnetic interaction between the individual elements of an optical antenna, resulting in a strong polarization and tuning response (Berthelot *et al.* 2009). Furthermore, they demonstrated by using this kind of external control, that the scattering diagram of an antenna can be externally adjusted (Huang *et al.* 2010).

Nano-Trapping Usually, for the trapping of nanoparticles high laser powers are needed to create trapping forces large enough to overcome the Brownian motion. The advantage of the trapping of plasmonic structures is their capability to localize and enhance light in their near-field E_n. For a particle much smaller than the trapping light wavelength, the trapping force is proportional to the gradient of $|E_n|^2$. In the case of plasmonic structures the electric field can be enhanced and spatially localized in an area much smaller than the diffraction limit. As a consequence, for similar illumination intensities, these structures generate much larger gradient forces than in the case of far-field trapping. Plasmonic trapping has been demonstrated experimentally by showing that cells and dielectric beads have been successfully trapped using a patterned surface with an illumination intensity much lower than that for far-field trapping (Righini *et al.* 2008). In another study the authors used a metallic nanoantenna to trap living bacteria for several hours with their orientation fixed by the asymmetry of the antennas (Righini *et al.* 2009).

Recently, Zhang *et al.* demonstrated the trapping of gold nanoparticles with diameters of 10 nm which correspond to the gap size of the used plasmonic antennas (Zhang *et al.* 2010). The analysis of the scattering spectra allowed the observation of trapping events due to a modification of the surface plasmon resonance. These studies draw the path towards a new generation of integrated devices to manipulate small specimen and observe nanoscopic processes.

Nano-Sensing The group around Giessen and Alivisatos demonstrated recently an antenna-enhanced hydrogen sensing at the single-particle level (Liu *et al.* 2011). By placing a single palladium nanoparticle near the tip region of a gold nanoantenna, they detected the changing optical properties of the system on hydrogen exposure by dark-field microscopy. Their concept paves the road towards the observation of single catalytic processes in nanoreactors and biosensing on the single-molecule level.

Antennas in Near-Field Imaging In near-field optics the probe that is used to scan the surface of a sample can be seen as an optical antenna. One of the first studies exploiting this concept involved attaching spherical gold nanoparticles, tuned to resonate at the wavelength of the incident light, to glass probes. It was found that scanning these resonant spheres close to single fluorescent molecules leads to an enhanced fluorescence and a reduction of lifetime (Anger *et al.* 2006; Kühn *et al.* 2006). It has been shown

that such a nanoprobe results into a spatial resolution of 50 nm. In order to achieve higher resolutions, antennas with strongly localized fields, smaller nanoparticles, sharper antenna ends or narrower gaps are required.

In this context, Taminiau et al. positioned a resonant nanoantenna, in form of a nanorod, at the end of a metal-coated near-field probe leading to an enhanced localized field near the antenna apex. This field was mapped with single fluorescent molecules which revealed a spatial localization of 25 nm (Taminiau *et al.* 2007).

Furthermore, the fabrication of bowtie antennas on the apex of silicon atomic-force microscope tips has been reported (Weber-Bargioni *et al.* 2010). When excited at resonance these antennas enhance the local silicon Raman scattering intensity.

Antennas for Photodetection The application of optical antennas in photodetectors is interesting since a nanoantenna increases the absorption cross-section. In the case of a photodetector it means that the light flux that impinges on the detector is increased. Thus, by using nanoantennas the size of a photodetector can be drastically reduced. Tang et al. experimentally demonstrated that the active volume of a germanium photodetector can be reduced to sub-lambda size using a Hertz dipole antenna, resonating in the near-infrared wavelength range, resulting into an enhanced detection sensitivity (Tang *et al.* 2008).

Recently, Knight et al. developed a structure composed of a metallic nanoantenna on a semiconductor surface which can be used as a polarization-specific light detector being highly compact and wavelength resonant (Knight *et al.* 2011). In this device, photons couple into the nanoantenna and excite resonant plasmons, which decay into energetic, so called "hot" electrons injected over a potential barrier at the nanoantenna-semiconductor interface, resulting in a photocurrent.

Directional Emission In the radio-frequency regime a typical antenna design for high directivity is the Yagi-Uda antenna which consists of an array of antenna elements driven by a single feed element. It has been shown that by fabricating a corresponding array of nanoparticles, similar radiation patterns can be obtained in the optical regime (Li *et al.* 2007; Pellegrini *et al.* 2009; Dorfmüller *et al.* 2011). In this context, Kosako *et al.* presented the experimental demonstration of directional control of radiation from a nano-optical Yagi-Uda antenna composed of tuned gold nanorods (Kosako *et al.* 2010). Their results show clearly that the basic principles of RF antenna design can be applied to the optical regime.

Shortly after, the unidirectional emission of a single emitter, a quantum dot, has been successfully demonstrated by coupling the emitter to a nanofabricated Yagi-Uda antenna (Curto *et al.* 2010). The emitter is placed in the near-field of the antenna so that the emitter drives the resonant feed element of the antenna. The resulting lumines-

cence of the quantum dot is highly directed into a narrow angular cone. Furthermore, the directionality can be controlled by tuning the dimensions of the antenna. These results demonstrate the potential of optical antennas to communicate light to, from and between nano-emitters to be used for quantum optical technologies, planar biochemical sensors, and light-harvesting and emission devices.

1.3 Conclusion

The rapidly growing research field plasmonics has yielded unique phenomena based on light-metal interactions that may give rise to new, useful applications and technologies, ranging from 'light-on-a-chip' to 'lab-on-a-chip' (Lal *et al.* 2007). Here, we gave a brief introduction into the physics of surface plasmons polaritons and particle plasmons.

Optical antennas emerged recently from near-field optics and since then have been widely studied as a tool to manipulate and control light at the nano-scale. We have presented the main parameters that are used to describe a nanoantenna, in analogy to 'classical' antennas working in the radio-frequency range. Several possible geometries of a nanoantenna have been discussed, and we gave an overview of recent advances in the research field of nanoantennas.

One of the most interesting parameters of an antenna is its directivity. In this context, we have presented two recent studies that measured the angular radiation pattern of nanoantennas of the Yagi-Uda type. The two groups used two approaches: One method consists of recording the antenna emission in the plane perpendicular to the antenna with a photodiode (Kosako *et al.* 2010). Another method is based on confocal microscopy in which the emission intensity distribution is imaged on the back focal plane of a high-NA objective (Curto *et al.* 2010). In the course of this work, we will show that holography as well has the capability of measuring angular scattering patterns. This is due to the simultaneous recording of both amplitude and phase in holography which therefore gives access to the three-dimensional information of the scattered field and thus, to the angular scattering spectrum of the hologram simply by calculating the scattered field's Fourier transform.

Chapter 2

Digital Heterodyne Holography

Table of contents

"The future cannot be predicted, but futures can be invented."

Dennis Gabor (1964)

In 1948 Dennis Gabor invented holography (Gabor 1948; Gabor 1949), a work for which he received the Nobel prize in Physics 23 years later. Holography is a method to record and reconstruct the amplitude and phase of a wavefield. A hologram is an interference pattern that is photographically or otherwise recorded, between the wavefield scattered from the object and the so called reference wave. A hologram is usually recorded on a flat surface, but contains information about the entire three-dimensional wavefield. This information is coded in form of interference patterns, usually not visible to the human eye due to the high spatial frequencies it contains. In "classical holography" the object wave is reconstructed by illuminating the hologram with the reference wave again. This wave reconstructed by passive means is indistinguishable from the original object wave. An observer recognizes a three-dimensional image with all effects of perspective and depth of focus (Schnars and Jüptner 2002; Schnars and Jüptner 2005).

2.1 Historical Overview

In Gabor's original setup, the axes of both the object wave and the reference wave are parallel. This *in-line* configuration leads to a reconstructed image, the real image, superimposed by the bright reconstruction wave and a second image, the so called "twin image", or virtual image. In 1964 Leith and Upatnieks (Leith and Upatnieks 1962; Leith and Upatnieks 1964) improved this in-line holography by introducing an *off-axis* reference wave. By doing so, the two images and the reconstruction wave are spatially separated. In the late 1960s and early 70s the first steps towards digital holography were made by Goodman and Lawrence and the Yaroslavski group (Goodman and Lawrence 1967; Kronrod *et al.* 1972). They sampled optically enlarged parts of in-line and Fourier holograms recorded on a photographic plate. The digitized "conventional" holograms were reconstructed numerically.

In 1994 Schnars and Jüptner made a big step forward by developing the direct recording of Fresnel holograms with charged coupled device (CCD) cameras (Schnars and Jüptner 1994). The numerical recording allows the direct calculation of phase and amplitude. Schnars and Jüptner used the off-axis configuration which, however, has the drawback of a low spatial resolution of the CCD camera due to the off-axis angle which must be limited to few degrees. From then on, digital holography enabled full digital recording and processing of holograms, without any photographic recording as an intermediate step, and has nowadays many applications in a widespread range.

In 1997, Yamaguchi introduced phase-shifting digital holography, a method to circumvent the restriction in the reconstructed image area caused by the off-axis setup (Yamaguchi and Zhang 1997). In their proposed in-line configuration, the reference beam is phase shifted with respect to the object beam. Thus, the twin image is suppressed in computer reconstruction. In the year 2000, the Depeursinge group (Cuche *et al.* 2000)

developed a method to filter spatially the zero-order and eliminate the twin-image in digital off-axis holography. In the same year, Le Clerc et al. presented a holography method based on heterodyne detection of the amplitude and phase (Le Clerc *et al.* 2000). In this technique the phase shift is achieved by frequency shifting the reference beam. They show that a frequency shift created by combining two acousto-optic modulators, results into a very accurate phase shift.

A couple of years ago a variant of the heterodyne holography scheme was proposed combining the properties of off-axis and phase-shifting holography (Gross and Atlan 2007). This technique enables to filter numerically the zero-order image alias and the technical noise of the reference. The authors demonstrated that the obtained sensitivity and signal-to-noise ratio (SNR) are excellent.

Outline

This chapter is structured as follows: Firstly, the basic principles of holography are discussed. The process of hologram recording and hologram reconstruction is described, and the technique of off-axis holography is presented, a technique to separate the different diffraction orders. Then, digital holography is introduced, and we discuss the impact on the reconstruction process which is performed numerically. We present the method of digital heterodyne off-axis holography which achieves an excellent detection sensitivity for weak signals making it an ideal technique for the imaging of nanoobjects. In this context, we introduce the photothermal heterodyne holography, which proved recently its application to detect gold nanobeads under a photothermal modulation (Absil *et al.* 2010). Lastly, we show that the heterodyne technique gives access to the frequency domain by varying the heterodyne beating frequency. We present two applications. As a validation we measured the frequency components of the temperature variations in an integrated circuit. Furthermore, we applied this method to the detection of the frequency domain of gold rods in a Brownian regime.

2.2 Principles of Holography

Holography consists of two processes: the recording of the hologram and the hologram reconstruction. Since holography is based on the interference of two light waves, the light source must have a sufficient coherence length.

The general setup of holography is shown in Fig. 2.1. The coherent light source is split into two partial waves by a beam splitter. To record a hologram the object is illuminated by the first wave. The object scatters light that is reflected to the recording medium, e.g. a photographic plate, that is placed at a distance d from the object. The second wave, the so called reference wave, illuminates the light sensitive medium directly where it interferes

with the scattered light from the object. The interference pattern is recorded, e.g. by chemical development of the photographic plate. The recorded interference pattern is called hologram.

Then, the original object wave is reconstructed by illuminating the hologram with the reference wave, see right image in Fig. 2.1. The observer sees the three-dimensional reconstructed object at a distance d, which is the position where the object had been before. This image is named virtual image.

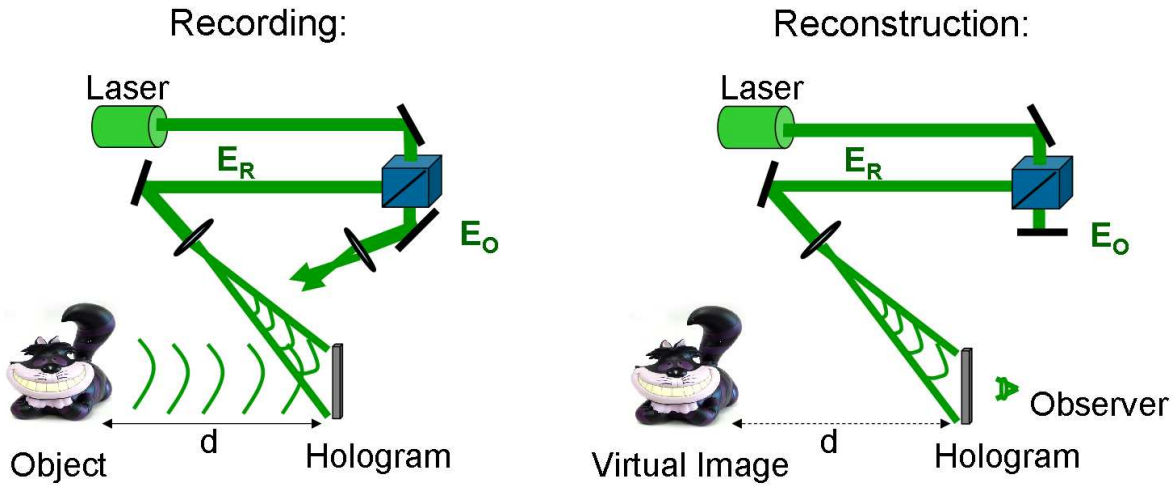

Figure 2.1 – Illustration of the hologram recording (left) and reconstruction (right).

Mathematical Description of the Hologram Recording The holographic process is described mathematically using the simplified formalism where the light wave is modelled by a complex number E which represents the electric field of the light wave. The amplitude and phase of the light are represented by the absolute value A and the angle ϕ of the complex number. Using this formalism, the complex amplitudes of the object wave E_O and the reference wave E_R are described as

$$E_O(x,y,z) = A_O(x,y,z)exp(i\phi_O(x,y,z)) \tag{2.1}$$
$$E_R(x,y,z) = A_R(x,y,z)exp(i\phi_R(x,y,z)) \tag{2.2}$$

where $A_O(x,y,z)$, $A_R(x,y,z)$ are the real amplitudes and $\phi_O(x,y,z)$, $\phi_R(x,y,z)$ are the phases. When both waves interfere at the surface of the recording medium, the intensity is calculated as follows ($*$ denotes the complex conjugate):

$$\begin{aligned} I(x,y,0) &= |E_O(x,y,0) + E_R(x,y,0)|^2 \\ &= (E_O(x,y,0) + E_R(x,y,0)) \cdot (E_O(x,y,0) + E_R(x,y,0))^* \\ &= E_O(x,y,0)E_O^*(x,y,0) + E_R(x,y,0)E_R^*(x,y,0) \\ &\quad + E_O(x,y,0)E_R^*(x,y,0) + E_R(x,y,0)E_O^*(x,y,0) \end{aligned} \tag{2.3}$$

The first two terms can be written as $I_O(x,y,0) = E_O(x,y,0)E_O^*(x,y,0)$ and $I_R(x,y,0) = E_R(x,y,0)E_R^*(x,y,0)$, and correspond to the intensity of scattered light by the object and by the reference wave, respectively. $I_O(x,y,0)$ and $I_R(x,y,0)$ do not contain any phase information, hence they do not contribute to the object reconstruction in contrast to the other two terms.

Considering that we have a photographic plate which is exposed to these two beams and then developed, its transmittance T is given by [1]:

$$\begin{aligned} T(x,y,z) &= T_0 + C \cdot I(x,y,0) \\ &\propto I(x,y,0) \end{aligned} \tag{2.4}$$

Hence, in the following we neglect both T_0 and C, and we write that T is proportional to $I(x,y,0)$.

Reconstruction of a Hologram The reconstruction of the object is done by illuminating the hologram with the reference wave. Then, the resulting wave E_H is the product of the transmittance and the reference wave, and the observer sees a three dimensional virtual image:

$$E_H(x,y,z) \propto E_R(x,y,z) \cdot I(x,y,0)$$

$$\begin{aligned} E_H(x,y,z) \propto\ & E_R(x,y,z) \cdot (I_R(x,y,0) + I_O(x,y,0)) && (2.5) \\ & + E_R(x,y,z) \cdot (E_O(x,y,0)E_R^*(x,y,0)) && (2.6) \\ & + E_R(x,y,z) \cdot (E_R(x,y,0)E_O^*(x,y,0)) && (2.7) \end{aligned}$$

Each of the four terms in Eq. 2.5 represents a wave emerging from the hologram, resulting from the scattering at the primarily recorded interference pattern.

1. The first term (2.5) corresponds to the zero order of diffraction and restores basically the reference wave.

2. The second term (2.6) corresponds to the $+1$ diffraction order. It is proportional to the diffracted wave by the object during the recording procedure. This term gives the *virtual image* that is perceived by the observer at the distance d from the recording medium which corresponds to the position that was initially the object's position.

3. The third term (2.7) corresponds to the -1 diffraction order and results into the *real image* of the object. The real image is positioned symmetrically with respect to the virtual image, i.e. at a distance $-d$ from the recording medium.

[1] T_0 is the amplitude transmission of the unexposed plate. $T_0 \simeq 0$ since an unexposed plate is opaque. C is a constant and given by $C = \tau \cdot \beta$. The two constants, τ and β denote the exposure time and the slope of the amplitude transmittance versus exposure characteristic of the light sensitive material, respectively. In digital holography, using CCD cameras as recording medium, T_0 is not relevant.

Since we are interested only in the virtual image, the other two diffraction orders have to be differentiated from the virtual image. In a conventional *in-line* configuration, i.e. when the propagation of the reference wave and the object wave are along the same direction, all beams are parallel, and the three diffraction orders are overlapping. Using *off-axis* holography, the virtual image, the real image and the zero-order image are spatially separated (Leith and Upatnieks 1962). In this configuration, the reference beam builds an angle θ_R to the direction of propagation of the object wave, as shown in Fig. 2.2. Since the experimental setup that we used is based on off-axis holography, its principle and consequences for the reconstruction are explained in the following.

2.2.1 Off-Axis Holography

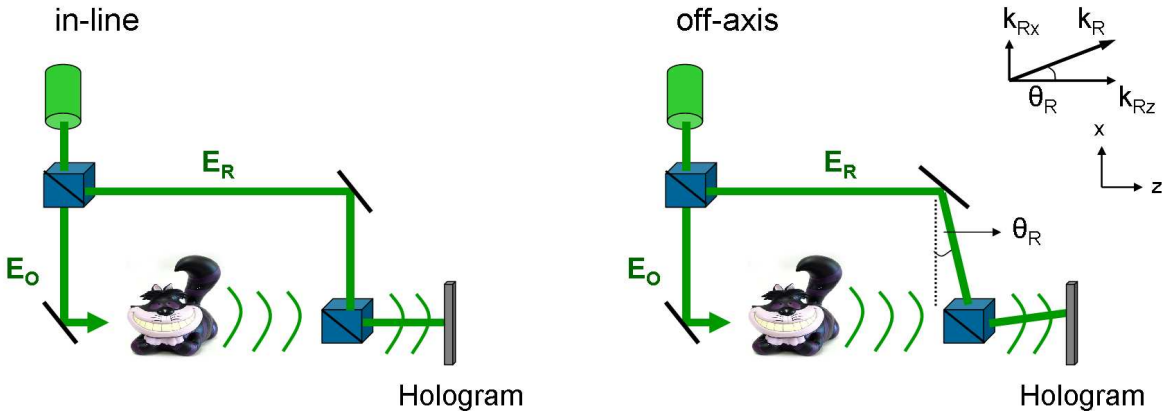

Figure 2.2 – In-line holography (left) vs. off-axis holographic setup (right). The reference beam in the off-axis scheme is tilted by an angle θ_R with respect to the object beam.

The idea of off-axis holography is that if E_O and E_R arrive in the hologram plane with separated directions, the different terms will vary at different spatial frequencies and, as a consequence, will propagate along separated directions during the reconstruction. Comparing both the left and right images in Fig. 2.2, one can see that, in contrast to the in-line configuration, the reference beam is tilted at an angle θ_R with respect to the object beam in off-axis holography. Hence, this tilt has to be taken into account when describing the complex amplitude of the reference beam.

$$\begin{aligned} E_R(x,y,0) &= A_R exp(ik_R r) \\ E_R(x,y,0) &= A_R exp(i(k_{Rx}x + k_{Rz}z)) \end{aligned} \tag{2.8}$$

As can be seen from the inset in the right image in Fig. 2.2, the reference wave propagates with a tilted reference wave vector k_R where $k_{Rx} = \sin\theta_R k$ and $k_{Rz} = \cos\theta_R k$ with k as the wave vector of the object field. Note that the z-component of the reference wave

vector produces a constant phase shift $k_{Rz}z$ which can be ignored. Thus, the resultant intensity at the hologram plane is:

$$\begin{aligned} I(x,y,0) &= |E_R(x,y)|^2 + |E_O(x,y)|^2 \\ &\quad + E_O(x,y,0)A_R exp(-ik\sin\theta_R x) \\ &\quad + E_O^*(x,y,0)A_R exp(ik\sin\theta_R x) \end{aligned} \tag{2.9}$$

The phase factor $exp(-ik\sin\theta_R x)$ in the third term indicates that the wave producing the virtual image is deflected with an angle $-\theta_R$ with respect to the direction of the illumination wave. The same factor appears in the fourth term but with the opposite sign, meaning that the wave producing the real image is deflected with an angle θ_R.

If we now consider the Fourier transform of the hologram intensity, the influence of the two phase factors $exp(\pm ik\sin\theta_R x)$ can be interpreted as a translation of the spatial frequencies associated with the real and the virtual images. Assuming that the illumination wave for reconstruction is in normal incidence, the spatial frequencies of the zero order of diffraction are located in the center of the Fourier plane, and the spatial frequencies of the interference terms vary at different carrier frequencies which are located symmetrically with respect to the center of the Fourier plane (Cuche *et al.* 2000): $-k\sin\theta_R/(2\pi)$ for the virtual image and $k\sin\theta_R/(2\pi)$ for the real image. Therefore, the different terms of the reconstructed wave front can be spatially filtered, if it is assured that the offset angle θ_R is large enough, so that the three images do not overlap. In this context, Cuche *et al.* developed a digital method to eliminate the zero order of diffraction and the twin image in off-axis holography. The authors showed that the spatial filtering can be performed digitally by multiplication of the computed Fourier transform of the hologram with a numerically defined mask (Cuche *et al.* 2000). From the point of view of signal processing, it is interesting to realize that the off-axis geometry introduces a spatial modulation of the interference terms. The method of spatial filtering can be considered to be equivalent to the application of a bandpass filter, which results in an enhancement of the SNR.

2.3 Digital Holography

Digital holography [2] differs from "classical" holography in the reconstruction process which is not performed optically but numerically. The hologram is electronically recorded, e.g. by using a CCD camera. [3] In digital holography the recorded intensity distribution

[2] Digital holography can refer to either digitally written or digitally read holograms. The former approach led to *Computer Generated Holography* which generates artificial holograms by numerical methods. Afterwards these digitally generated holograms are reconstructed optically. However, this technique is not considered here, and in the scope of this work we will always refer to digital holography as a technique that digital reads and processes optically generated holograms.

[3] It is also possible to digitize a hologram which was recorded beforehand on a photographic plate, as was done in the earliest digital holograms.

of the hologram is multiplied by the reference wavefield in the hologram plane, and the diffracted field in the image plane is determined by numerical processing which is based on the fast Fourier transform algorithm proposed by Cooley and Tukey (Cooley and Tukey 1965).

The advantages of digital holography are numerous. Since the hologram is coded numerically, it is not necessary to process the photographic plate to reconstruct a real image. Moreover, in digital holography the reconstructed wave field is a complex function, therefore both the intensity and the phase can be calculated. This is in contrast to the case of optical hologram reconstruction where only the intensity is made visible. It has been shown that digital holography can be efficiently employed to compensate for aberrations (Stadelmaier and Massig 2000; Nicola *et al.* 2002) and for correcting image reconstruction in the presence of severe anamorphism (Nicola *et al.* 2001). Further interesting applications of digital holography rely on the possibility of carrying out whole reconstruction of the recorded wave front, i.e. the determination of intensity and of the phase distribution of the wavefield at any arbitrary plane located between the object and the recording plane. The last application is one of our particular interest since we are interested in reconstructing the scattered light of objects in all three dimensions, i.e. at any plane z of interest.

The Fresnel-Kirchhoff Integral The diffraction of a light wave at an aperture (in this case a hologram) which is mounted perpendicular to the incoming beam is described by the Fresnel-Kirchhoff integral:

$$\Gamma(\xi,\eta) = \frac{i}{\lambda}\int_{-\infty}^{+\infty}\int_{-\infty}^{+\infty} dxdy\; E_H(x,y)E_R(x,y)\frac{exp(-i\frac{2\pi}{\lambda}\rho)}{\rho} \tag{2.10}$$

with

$$\rho = \sqrt{(x-\xi)^2 + (y-\eta)^2 + d^2} \tag{2.11}$$

where $E_H(x,y)$ is the hologram function and ρ is the distance between a point in the hologram plane and a point in the reconstruction plane. Figure 2.3 clarifies the coordinate system for the numerical hologram reconstruction. The diffraction pattern is calculated at a distance d behind the CCD plane which means it reconstructs the complex amplitude in the plane of the real image (Schnars and Jüptner 2002). Equation 2.10 is the basis for the numerical hologram reconstruction. Because the reconstructed wavefield $\Gamma(\xi,\eta)$ is a complex function, both intensity and phase can be calculated.

2.3.1 Numerical Holographic Reconstruction

There are a number of numerical methods available to calculate the holographic diffraction (Cuche *et al.* 1999; Yamaguchi *et al.* 2001; Zhang and Yamaguchi 1998; Marquet

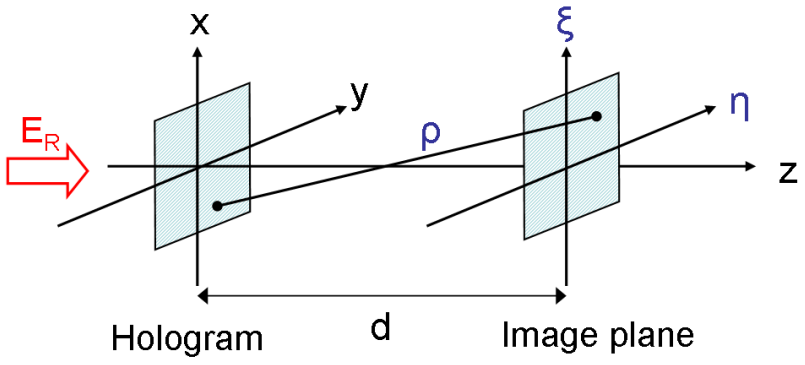

Figure 2.3 – Coordinate system for numerical hologram reconstruction.

et al. 2005; Yu and Kim 2005; Kreis *et al.* 1997; Mann *et al.* 2005). The most common method uses the *Fresnel approximation*.

Fresnel Approximation The approximation of spherical Huygens wavelets by parabolic surfaces allows the calculation of the diffraction integral using a single Fourier transform, called the Fresnel transformation (Cuche *et al.* 1999).

$$\begin{aligned}\Gamma(\xi,\eta) &= \frac{i}{\lambda d} exp(-id\frac{2\pi}{\lambda}) exp[-i\frac{\pi}{\lambda d}(\xi^2+\eta^2)] \\ &\cdot \int_{-\infty}^{+\infty}\int_{-\infty}^{+\infty} dxdy\ E_H(x,y)E_R(x,y) exp[-i\frac{\pi}{\lambda d}(x^2+y^2)] \\ &\cdot exp[i\frac{2\pi}{\lambda d}(x\xi+y\eta)]\end{aligned} \tag{2.12}$$

Equation 2.12 enables the reconstruction of the wavefield in a plane behind the hologram, in the plane of the real image. In the case of discretized sensors like CCDs, the same formalism can also be used to describe the *discrete Fresnel transformation* where the variables (ξ,η) describing the position in the reconstruction plane are substituted by the discrete variables $\nu = \xi/(\lambda d)$ and $\mu = \eta/(\lambda d)$ (Schnars and Jüptner 2002).

The function $\Gamma(\xi,\eta)$ can be digitized if the hologram function $E_H(x,y)$ is sampled on a rectangular raster of $N \times N$ points, with steps Δx and Δy along the coordinates. Δx and Δy are the distances between neighbouring pixels on the CCD in the horizontal and vertical directions. With these discrete values we obtain the following relation between the real pixel size and the reconstructed pixel size:

$$\Delta\xi = \frac{\lambda d}{N\Delta x} \text{ and } \Delta\eta = \frac{\lambda d}{N\Delta y} \tag{2.13}$$

And Eq. 2.12 converts to:

$$\begin{aligned}\Gamma(m,n) &= \frac{i}{\lambda d}\, exp[-i\pi\lambda d(\frac{m^2}{N^2\Delta x^2}+\frac{n^2}{N^2\Delta y^2})] \\ &\cdot \sum_{k=0}^{N-1}\sum_{l=0}^{N-1} E_H(k,l)E_R(k,l)exp[-i\pi/(\lambda d)(k^2\Delta x^2+l^2\Delta y^2)] \\ &\cdot exp[i2\pi(\frac{km}{N}+\frac{ln}{N})]\end{aligned} \tag{2.14}$$

This is the discrete Fresnel transform for $m = 0, 1, \cdots, N-1$ and $n = 0, 1, \cdots, N-1$, denoting the sum over all pixels.

From Eq. 2.13 it is evident that the pixel distances in the reconstructed image, $\Delta\xi$ and $\Delta\eta$, are different from those of the hologram matrix. At first sight there seems to be a reduction in resolution by applying the numerical Fresnel transform. On closer examination one recognizes that Eq. 2.13 corresponds to the diffraction-limited resolution of optical systems: the hologram is the aperture of the optical system with a side length $N\Delta x$. According to the theory of diffraction at a distance d behind the hologram a diffraction pattern develops. $\Delta\xi = \lambda d/(N\Delta x)$ is therefore the size of the diffraction pattern (or speckle diameter) in the plane of the reconstructed image, which limits the resolution. This can be regarded as the "automatic scaling" algorithm, always setting the resolution of the image reconstructed by a discrete Fresnel transform to the physical limit (Schnars and Jüptner 2002).

Since the direct numerical processing of the Fresnel-Kirchhoff integral is time consuming, an equivalent formalism is more suitable. This formulation makes use of the convolution theorem and is called the *convolution method*.

The Convolution Method Demetrakopoulos and Mittra first applied this processing method to the numerical reconstruction of sub-optical [4] holograms (Demetrakopoulos and Mittra 1974; Schnars and Jüptner 2002). Later this approach was applied to optical holography (Kreis *et al.* 1997). Following this work, the diffraction formula of Eq. 2.10 can be written as:

$$\Gamma(\xi,\eta) = \int_{-\infty}^{+\infty}\int_{-\infty}^{+\infty} dxdy\; E_H(x,y)E_R(x,y)g(\xi,\eta,x,y) \tag{2.15}$$

where the impulse response $g(\xi,\eta,x,y)$ is given by

$$g(\xi,\eta,x,y) = \frac{i}{\lambda}\sqrt{(x-\xi)^2+(y-\eta)^2+d^2} \tag{2.16}$$

Eq. 2.16 shows that the linear system characterized by $g(\xi,\eta,x,y) = g(\xi-x,\eta-y)$ is space invariant: the superposition integral is a convolution. This allows the application of

[4] In sub-optical holography an object is typically illuminated using acoustic or microwave sources.

the convolution theorem which states that the Fourier transform (FT) of the convolution of (E_H E_R) with g is the product of the individual transforms FT$\{E_H\ E_R\}$ and FT$\{g\}$:

$$FT\{(E_H\ E_R) \otimes g\} = FT\{E_H\ E_R\} \cdot FT\{g\} \tag{2.17}$$

So $\Gamma(\xi, \eta)$ can be calculated by first Fourier transforming ($E_H\, E_R$), then multiplying with the Fourier transform of g, and taking an inverse Fourier transform of this product. The whole process requires all three Fourier transforms, which are effectively carried out using the FFT algorithm. Because FT$\{g\}$ can be calculated analytically, the reconstruction procedure is reduced to the calculation of two Fourier transforms. The pixel sizes of the images reconstructed by the convolution method are equal to those of the hologram, i.e. $\Delta\xi = \Delta x$ and $\Delta\eta = \Delta y$, in contrast to those of the Fresnel approximation (see Eq. 2.13).

Another reconstruction method is the *angular spectrum method* (Yu and Kim 2005) which involves two Fourier transforms, plus simple filtering of the angular spectrum.

2.3.2 Phase Shifting Holography

In 1997 Yamaguchi and Zhang proposed the phase-shifting holography technique (Yamaguchi and Zhang 1997). This methods allows the suppression of the zero-order and twin-images in an in-line holographic setup by recording several images with a different phase for the object beam. In their experiment the phase shift was created by a modulation of the optical path length. Therefore, a mirror is introduced in the reference arm and moved by a piezoelectric transducer actuator. Le Clerc *et al.* presented a heterodyne holographic scheme in which the reference beam is dynamically phase shifted by frequency shifting (Δf) the reference field (Le Clerc *et al.* 2000). This can be done with acousto-optic modulators (AOM). However, the use of AOMs requires typical working frequencies in the range of MHz. Such a high frequency modulation is nowadays not detectable even with a fast digital camera. Therefore, two AOMs, working at 80 MHz and 80 MHz+Δf, respectively, are used. The offset in frequency has the advantage that the resulting phase shift is highly accurate. This technique is called *heterodyne holography* because it is based on heterodyne techniques which are classical in interferometry, where high frequency signals are converted to lower frequencies by combining two frequencies.

When the reference beam, phase shifted either by a modulation in the optical path or by a frequency modulation, interferes with the object wave, the CCD camera records the following intensity:

$$\begin{aligned} I_H &= (E_O + E_R) \cdot (E_O + E_R)^* \\ &= I_O + I_R \\ &\quad + A_O A_R^* \cdot exp(-i\omega_{mod} t) \\ &\quad + A_O^* A_R \cdot exp(i\omega_{mod} t) \end{aligned} \tag{2.18}$$

As can be seen from Eq. 2.18 the phase shift allows a differentiation of the diffraction orders. In order to suppress the -1 and 0 diffraction orders of the hologram, we will now show that an even number of phase shifted images can be recorded, using methods such as the fours-phase detection.

Four-Phase Demodulation Method The four-phase demodulation method consists in recording a sequence of images with a relative phase shift $\Delta\phi = \pi/2$ between two consecutive frames.

If the reference wave is frequency-shifted by tuning two acousto-optic modulators, AOM1 and AOM2, an accurate phase shift $\Delta\phi$ is obtained with a heterodyne beating frequency:

$$\Delta\omega = \omega_{AOM1} - \omega_{AOM2} \tag{2.19}$$

This modulation will be recorded using a frame rate frequency of the CCD camera at $\omega_{CCD} = 4\Delta\omega$. The camera records a sequence of m frames I_k starting at instants t_k:

$$t_k = k \cdot \frac{2\pi}{\omega_{CCD}} \tag{2.20}$$

Under these conditions, images are identical for indices m which are congruent modulo 4, i.e. images are repeated every 4 images. We can therefore obtain a series of 4 images by varying the index m from 1 to 4 in the case of four-phase detection:

$$\begin{aligned} I_m &= I_O + I_R \\ &\quad + A_O A_R^* \cdot exp(-i\omega_{CCD} t_m/4) \\ &\quad + A_O^* A_R \cdot exp(i\omega_{CCD} t_m/4) \end{aligned} \tag{2.21}$$

where each of the 4 images I_m is the result of the sum: $I_m = \sum_{k=0}^{n} I_{4k+m}$ (n is the number of the total amount of images taken). This summation has the advantage of increasing the SNR of each I_m images compared to a single image I_k. Hence, regarding only the $+1$ order, which we are interested in, the phase factor becomes:

$$exp(i\omega_{CCD} t_m/4) = exp(im\pi/2) = i^m \tag{2.22}$$

By summing the images I_m, affected with a pre-factor i^m, we obtain the complex hologram E_H:

$$\begin{aligned} E_H(x,y,0) &= \sum_{m=0}^{3} i^m I_m(x,y) = (I_0 - I_2) + i(I_1 - I_3) \\ &= \sum_{m=0}^{3} i^m (I_O + I_R) && (2.23) \\ &\quad + \sum_{m=0}^{3} (+1)^m A_O A_R^* && (2.24) \\ &\quad + \sum_{m=0}^{3} (-1)^m A_O^* A_R && (2.25) \end{aligned}$$

where the term Eq. 2.23 denotes the zero order, term Eq. 2.24 the +1, and term Eq. 2.25 the −1 order, respectively. Since the number of the recorded images is even, the first and the third term are eliminated, and the second term is maximized. Hence, the demodulated hologram contains only the information of the "true" image.

2.3.3 Digital Heterodyne Off-Axis Holography

We have seen that off-axis holography is a useful configuration to separate the diffraction orders in digital holography. However, the object field of view is reduced since one must avoid the overlapping of the image with the conjugate image alias.

The phase-shifting method based on in-line digital holography records several images with a different phase for the object beam. It is then possible to reconstruct only the complex object field because aliases can be removed by taking image differences. It was shown that using heterodyne holography, the phase shift is rendered highly accurate by frequency shifting the illumination beams.

Gross and Atlan proposed a digital holography technique that combines off-axis geometry and heterodyne holography (Gross and Atlan 2007). Figure 2.4 illustrates the proposed setup arrangement. Note that a lens is introduced into the reference arm to expand the size of the reference beam in order to ensure that the whole CCD camera is illuminated. This technique uses additionally the spatial filtering method (Cuche *et al.* 2000) to filter out numerically the zero-order image and the noise attached to it. Hence, this technique enables the recording and reconstruction of holographic images at very low signal levels with a very good SNR.

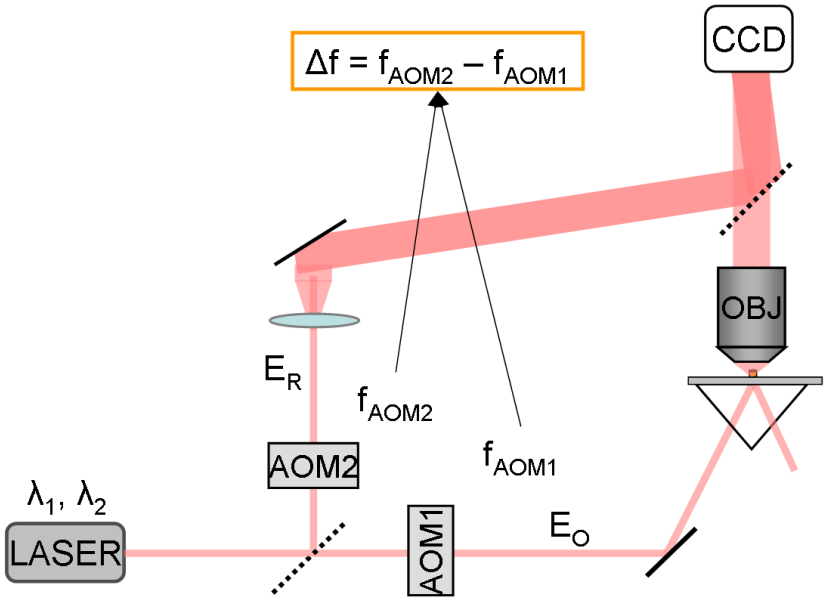

Figure 2.4 – Description of the heterodyne off-axis holography.

The elimination of the noise can be understood if we consider that the off-axis heterodyne holography has the function of a double filtering process in both the spatial and temporal frequency domains. In the case of a very weak object signal, the majority of the technical noise is within the reference beam, because the majority of the technical noise is within the intense reference signal. First, most of this noise is removed due to the phase-shifting filtering process by taking the difference of successive images. This filtering occurs in the temporal frequency domain. The second filtering process is due to the off-axis configuration. Since the reference beam extends within a few spatial modes (i.e. a few pixels of the k-space), its noise is located near the center of the k-space. Hence, the spatial filtering removes all the technical noises that lie out of the relevant region, and mostly those which are located at the center of the k-space. This spatial filtering process is clarified in Fig. 2.5 which illustrates the numerical filtering procedure to separate the $+1$ diffraction order from the other two.

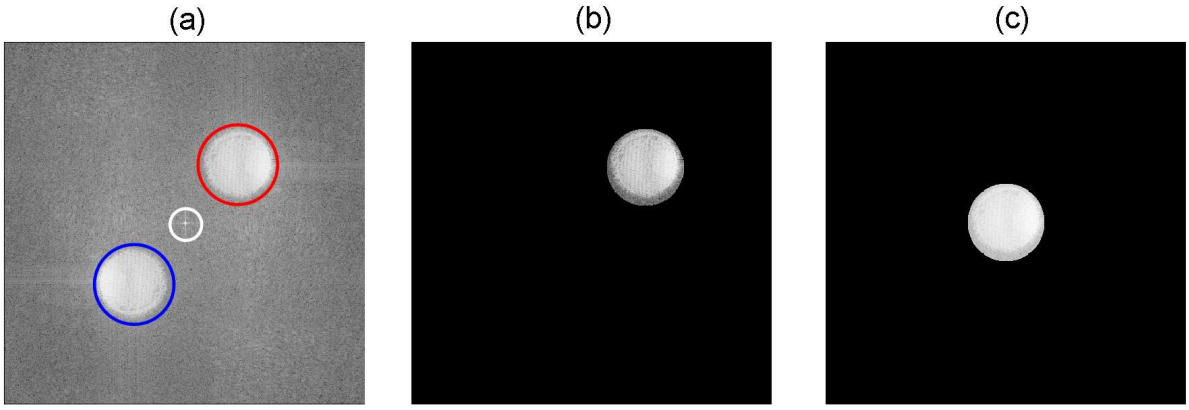

Figure 2.5 – k-space filtering in off-axis holography: (a) k-space of the recorded hologram showing the three diffraction order: zero order (white circle), -1 order (blue circle) and $+1$ order (red circle). (b) spatial filtering by sectioning the $+1$ order. (c) centering of the selected order in the k-space for further numerical processing.

This efficient noise filtering makes it an appropriate technique for performing holography with an extremely low signal level, as in the case of imaging of nanoobjects. Recently, it has proven its extreme sensitivity and its ability to detect the scattering pattern of simple nanoobjects such as gold nanoparticles (Absil *et al.* 2010; Warnasooriya *et al.* 2010). Furthermore, it has been shown that heterodyne holography can deliver an accurate 3D picture of the light scattered by complex objects, as nanodisk chains (Suck *et al.* 2011).

The scope of this work is the imaging of nanoobjects, and in particular, the study of three-dimensional images of the scattered light by nanoobjects. Thus, digital heterodyne holography (DHH) in off-axis configuration is a perfect tool for this kind of studies. Since almost all holographic measurements are based on the heterodyne off-axis holography scheme, we describe in the following the details of the used experimental setup.

2.3.4 Experimental Setup of DHH

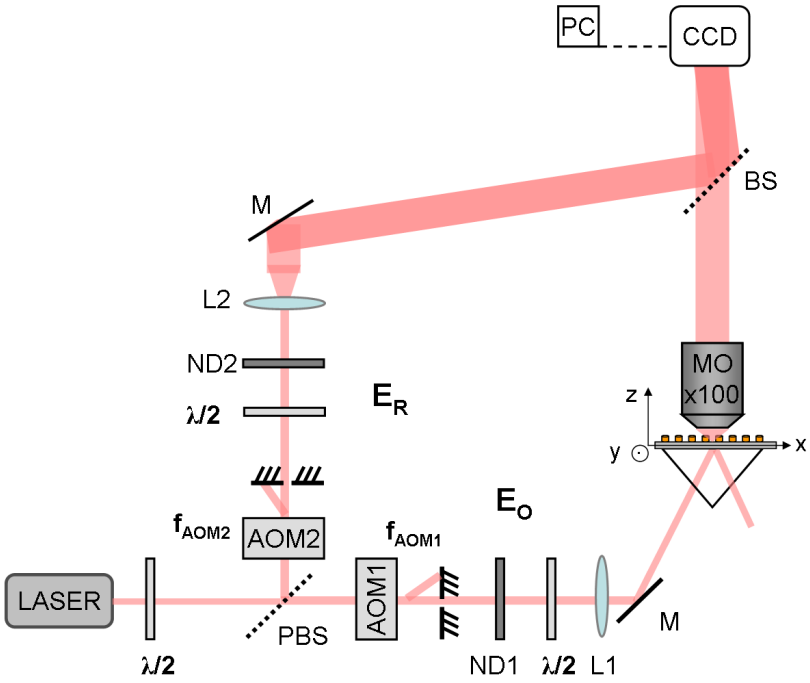

Figure 2.6 – Experimental setup based on heterodyne off-axis holography: $\lambda/2$, half-wave plate; (P)BS (polarizing) beam splitter; AOM1, AOM2, acousto-optic modulators; ND1, ND2, neutral density filters; M, mirror; MO, microscope objective; L1, L2, lenses.

The experimental setup we used is schematically depicted in Fig. 2.6. The laser beam is separated in reference (E_R) and object arms (E_O). In order to avoid a tedious setting of the arm lengths, long coherence length single mode laser diodes were used. Two single mode laser diodes were at disposition, one supplying a wavelength of $\lambda_1 = 658$ nm (P= 50 mW) and the other a wavelength of $\lambda_2 = 785$ nm (P= 80 mW). [5] Another setup, operating at $\lambda_1 = 532$ nm (P= 80 mW) was also developed (see Ch. 2.5.1).

Both arms, E_R and E_O, are frequency-shifted by two acousto-optical modulators (AOM1, AOM2) at frequencies f_{AOM1} and f_{AOM2} creating an accurate phase shift. Half-wave plates ($\lambda/2$) associated to polarizing beam splitters (PBS) are used to distribute the intensity between the reference E_R and illumination E_O beams, in addition to neutral density filters (ND1, ND2), so that most of the available light (typically 90%) illuminates the object. Two lens systems are introduced in both arms. L1 results into a focused object beam and L2 into a slightly expanded reference beam in order to fully illuminate the CCD camera.

To align the polarization of both beams and allow interference, both beams pass through half-wave plates. The glass substrate of the sample is coupled to a prism using an index matching liquid and illuminated in total internal reflection (TIR) configuration to achieve

[5] Note that most of the measurements were performed at the wavelength $\lambda_2 = 785$ nm.

dark field illumination. The scattered field is collected by a microscope objective (OBJ) which has a magnification of 100× and a numerical aperture of NA= 0.95 in air and reaches the camera where it interferes with an expanded reference beam forming an angle $\theta_R \approx 1°$ with respect to the optical axis. The CCD camera ("Roper Cascade 512F EMCCD", 512×512 pixels, with a pixel size of 16×16 μm^2) is triggered at a frame rate of $f_{CCD} = 16$ Hz, and typically uses an integration time of $t_{int} = 50$ ms. The reference signal interferes in an off-axis manner with the scattered object signal in the plane of the CCD camera. Due to the heterodyne detection, the resulting interference pattern is modulated at a beat frequency $\Delta f = f_{AOM1} - f_{AOM2}$, and the hologram is recorded by the camera at a rate $f_{CCD} = 4\Delta f$, using the four-phase detection method. In general, the holograms were obtained by recording 36 image frames, i.e. 9 series of 4 images, thus a total acquisition time of 2 seconds is needed for a single hologram.

Numerical Reconstruction Procedure The numerical reconstruction is achieved after k-space filtering and involves two Fourier transformations (FT). We use the standard convolution method which yields a calculation grid equal to the pixel size. To calculate the convolution product, we have used the Fourier method as in (Le Clerc *et al.* 2000). The CCD camera records a real space hologram $E_H(x, y, z = 0)$ in the CCD plane ($z = 0$). The hologram $\hat{E}_H$ in the CCD reciprocal plane (i.e. in the $z = 0$ k-space) is obtained by the Fourier transformation. The complete procedure to reconstruct a hologram at any given plane consists of 4 steps:

1. First Fourier Transform: $\hat{E}_H(k_x, k_y, 0) = FT\{E_H(x, y, 0)\}$
2. Spatial filtering: $\hat{E}_H^{SF}(k_x, k_y, 0) = SF\{\hat{E}_H(k_x, k_y, 0)\}$
3. Propagation: $\hat{E}_H^{SF}(k_x, k_y, z) = \hat{E}_H^{SF}(k_x, k_y, 0) \cdot G(k_x, k_y, z)$
4. Second Fourier Transform: $E_O(x, y, z) = FT^{-1}\{\hat{E}_H^{SF}(k_x, k_y, z)\}$

with $G(k_x, k_y, z)$ as the kernel function that describes the propagation from 0 to z in the k-space:

$$G(k_x, k_y, z) = exp(iz\frac{k_x^2 + k_y^2}{k}) \tag{2.26}$$

This function corresponds to the numerical counterpart of the reference wave.

In the first step, by performing a Fourier transformation on the recorded hologram $E_H(x, y, 0)$ we move to the frequency space. This allows us to perform as a second step the spatial filtering (SF) in the k-space in order to eliminate the unwanted diffraction orders and thus, reduce the technical noise. To select the relevant first-order image information and to suppress the zero-order and twin-image aliases, we use the k-space filtering (also spatial filtering) method developed by Cuche et al. (Cuche *et al.* 2000). In this method we select in the k-space of the recorded hologram a bright zone that contains only the

spatial frequencies of the true image. Note that this selection is made possible by the off-axis geometry that has translated the true image away from the center in the k-space matrix. The location of the true image can be precisely adjusted by tuning the angle between the reference and object beam.

The selected area is then copied in the center of a 512×512 zero matrix. This procedure is called *zero padding*. The calculation of the holograms in the k-space and in the real space at a chosen plane z is thus done on this calculation grid.

In the third step, the resulting complex field $\hat{E}_H^{SF}(k_x, k_y, 0)$ is multiplied with the z-propagation function $G(k_x, k_y, z)$, defined in Eq. 2.26, which describes the propagation in the k-space from 0 to any z-plane, and we obtain $\hat{E}_H^{SF}(k_x, k_y, z)$. This step can be repeated for different z-planes in view of obtaining a three-dimensional object field information. As a last step, we perform the inverse Fourier transformation to move again to the spatial domain. A three-dimensional complex matrix $E_O(x, y, z)$ is obtained which contains the amplitude and phase information of the scattered field of the object under study.

Impact of Frequency Modulation Beyond this, an interferometry setup based on the heterodyne technique has the unique possibility to enable the frequency investigation of phenomena modulated at any frequency F_{Var} by detuning the frequency shift, $\Delta f = f_{AOM2} - f_{AOM1}$, due to the acousto-optic modulators, appropriately. Supposing a variable frequency F_{Var}, then in heterodyne holography the frequency modulation of the object beam is given by:

$$f_{AOM1} = f_{AOM2} - \frac{1}{4} \cdot f_{CCD} - F_{Var} \tag{2.27}$$

Now, we have three possibilities to adjust F_{Var}:

1. $F_{Var} = 0$ (static case)
2. $F_{Var} =$ constant (dynamic case)
3. $F_{Var} =$ variable (scanning case)

The *static case* corresponds to the "classic" heterodyne holography setup presented above. The total frequency modulation is one quarter of the camera frame rate which is used for the four-phase detection.

In the second case, so called *dynamic case*, a constant frequency is added to the modulation. This case allows the investigation of phenomena modulated at any frequency F_{Var}. An application of the *dynamic case* has recently been demonstrated by Absil *et al.* when reporting photothermal heterodyne holography of gold nanoparticles. Using this technique, a heating laser, modulated at a constant frequency $F_{Var} = F_{Heat}$, created a modulation of the local refraction index in a region of the sample. This modulation was then detected by heterodyne imaging. The authors showed that tens of particles, down to

diameters of 10 nm, could be localised simultaneously and selectively in three dimensions with near-diffraction resolution. This technique will be explained in detail in Ch. 2.4.

The third case describes the *scanning case*, when the modulation frequency is dynamically shifted. This kind of technique with a variable detection frequency enables the detection of the entire frequency domain of a system. This detection technique has been successfully validated in a basic system when mapping the frequency domain of the temperature in an integrated circuit (Suck *et al.* 2010). Furthermore, the method was applied to detect the frequency domain of nanorods in a Brownian regime. Both applications of the scanning case will be presented and discussed in Ch. 2.5.

2.4 Photothermal Heterodyne Holography

In the precedent section we have shown that digital holography is a powerful 3D imaging tool, based on interferences between a signal of the optical field of interest and a reference beam. Combined with the heterodyne technique it offers the frequency investigation of phenomena modulated at any frequency by correctly detuning the heterodyne beating frequency.

Here, we present the technique of photothermal heterodyne holography which is able to achieve three dimensional imaging of absorbing nanoobjects submitted to a modulated photothermal excitation. Heated nanoobjects induce a temperature modulation and a small refractive index variation (typically 10^{-3} to 10^{-5} K^{-1}) in the surrounding medium. This relatively large heated region scatters light towards the camera where it interferes with the phase-shifted reference beam. The beating frequency of the setup is tuned at the frequency of the photothermal excitation which permits to detect principally the heated objects.

Photothermal excitation is a well established technique for the sensitive detection of absorbing objects. A modulated optical beam is sent on the sample, creating a localised heating, which in turn induces a variety of phenomena including e.g. infrared emission, thermal expansion, or refractive index changes (Rosencwaig *et al.* 1985). When detected with good sensitivity, these phenomena can deliver information on the optical absorption of the sample. Recently, these techniques have been adapted to the detection of metal nanoparticles (Boyer *et al.* 2002) or nanotubes (Berciaud *et al.* 2007), specially in the context of biological studies (Lasne *et al.* 2006). Relying on absorption, which scales as the volume of the particle, is clearly an advantage for the detection of very small particles in comparison to scattering, which varies as the square of the particle volume.

This section presents the experimental setup of photothermal heterodyne holography. The principle of the detection of exclusively the photothermal signal is explained. Furthermore we analyse qualitatively the origin of the detected photothermal signal and prove that the photothermal signal is indeed proportional to the induced temperature in the

nanoobject. This makes our method a novel technique to probe the temperature in metal nanoobjects.

2.4.1 Experimental Setup of Photothermal DHH

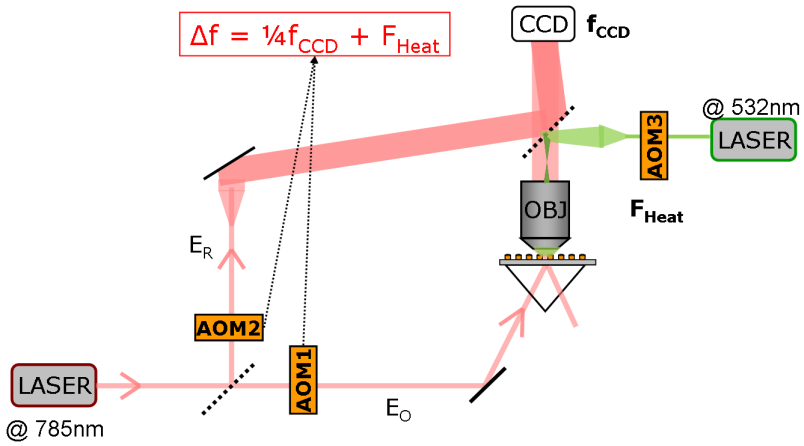

Figure 2.7 – Setup of Photothermal Heterodyne Holography.

Figure 2.7 depicts the setup of photothermal holography. It is based on the off-axis setup of heterodyne holography as shown in Fig. 2.4. The holographic arms use a single mode laser emitting at $\lambda_2 = 785$ nm.

The photothermal excitation is delivered by a 2 W, continuous multimode solid state laser at $\lambda = 532$ nm, which is sine-modulated in amplitude by a third acousto-optical modulator, AOM3. Unlike AOMs 1 and 2, it serves as a heating power modulator by using a 80 MHz carrier, modulated in amplitude at F_{Heat}. This beam is directed into the objective by a dichroïc beamsplitter (at 532 nm). The polarization of the heating beam can be adjusted by a combination of a half wave plate and a polarizing beam splitter. Thus, a polarization along each axis of the sample plane can be achieved.

An adjustable beam expander slightly uncollimates the beam to illuminate a $2-200$ μm diameter region of the sample. At high laser power, an additional notch filter ensures that no heating light reaches the camera. This excitation, when hitting a point-like object in a homogeneous medium, creates a spherical region in which the temperature is modulated. A local modulation of the refractive index appears in this heated region due to photothermal effects, and is investigated by synchronizing the setup to $F_{Var} = F_{Heat}$, resulting into a beating frequency of $\Delta f = 1/4 f_{CCD} + F_{Heat}$. The reconstruction procedure of the hologram follows the 4-step method explained in Ch. 2.3.3.

Applications Recently, the imaging method of photothermal heterodyne holography was applied in our laboratory to the imaging of gold nanoparticles with a diameter of down to 10 nm (Absil *et al.* 2010). Photothermal heterodyne holography provides an

enhancement of the SNR by several orders of magnitude compared to direct holography, even for moderate heating densities. This technique is extremely selective with respect to dust, since metallic nanoparticles display a much stronger absorption. The heated particles can be localised in three dimensions with near-diffraction resolution by a numerical reconstruction.

The 3D study of the diffusion pattern of individual particles or heated particles is of great interest since it allows an effective discrimination using the shape of diffusion diagrams. Details of the results are found in (Absil *et al.* 2010).

Whereas the former study concentrated on the detection and localisation of very small nanoparticles, we were interested in applying the photothermal heterodyne holography to detect the induced temperature in a plasmonic nanoobject. This study will be extensively discussed in Ch. 5.3. We will show results on nanochains and present an analytical approach to analyse the detected photothermal signal.

2.5 Frequency Domain Detection by Heterodyne Holography

We have seen that heterodyne holography allows a dynamically shifted beating frequency which enables the imaging of the entire frequency domain of the system under study.

Here, we will describe a method based on heterodyne holography that scans the frequency sidebands by systematically detuning one of the beams. This technique has been successfully applied to the frequency resolved temperature imaging of an integrated circuit. Furthermore, we used this detection method to study the frequency domain of Brownian movement of gold nanorods in an aqueous solution.

Joud *et al.* demonstrated recently that sideband digital holography can be used to quantitative measure the oscillation amplitude of vibrating objects (Joud *et al.* 2009). The authors used heterodyne holography to selectively detect the frequency sidebands of the light scattered by the object, shifted by n times the vibration frequency.

First, we present our results of the temperature mapping of an integrated circuit. This study was chosen as a primary validation of the detection concept on an uncomplicated micro-system. In view of this work, we are interested mainly in the study of metal nanoobjects. Regarding our main scope, i.e. the application to plasmonics, we performed some measurements of the frequency domain of nanorods moving in an aqueous solution in the Brownian regime. The result of the heterodyne detection in this case reflects well the expected behaviour of the signal as a function of frequency.

2.5.1 Application 1: Frequency-Resolved Temperature Imaging of Integrated Circuits

The scanning heterodyne imaging method is applied to image the temperature of an integrated circuit and to map its frequency domain content. An integrated circuit is supplied with a modulated current resulting into a temperature modulation. The frequency content for this modulation is detected using an object beam and a reference beam, frequency-shifted to create a beating of the interference pattern. The experimental setup will be characterized in the frequency domain. We will present and discuss the obtained frequency domain spectra of the temperature.

High frequencies and integration densities make temperature and thermal management a crucial aspect of integrated circuit design. Methods able to acquire temperature maps at submicron scales are well explored, since they are essential in order to validate thermal models and improve microelectronic devices. Infra-red imaging is a powerful tool, but its optical resolution is limited to a few micrometers. Thermoreflectance (Farzaneh *et al.* 2009) offers the advantage of being a non-invasive optical technique capable of determining temperature variations with good spatial resolutions in the visible or near UV range.

It is well known that a change in temperature ΔT induces a variation in the optical reflectivity ΔR of the material described in first approximation by:

$$\frac{\Delta R}{R} = \frac{1}{R}\frac{\partial R}{\partial T}\Delta T = \kappa \Delta T \tag{2.28}$$

where κ is the thermoreflectance coefficient depending on the material and on the light wavelength (De Freitas *et al.* 2005).

The knowledge of the time or frequency dependence of the temperature is also essential, as it can allow the localization of transient overheating or of areas working at different multiples of the clock frequency, but has received much less attention. Time domain experiments (Farzaneh *et al.* 2009; Ezzahri *et al.* 2009; Huxtable *et al.* 2004) require potentially disruptive short pulses with high peak powers and large repetition frequencies to obtain sufficient average light intensities. So far, few techniques exist permitting the spectral analysis of the temperature, and none allow full field images. Due to the limited bandwidth of detectors or lock-in amplifiers, most time or frequency domain techniques use some form of heterodyning to lower the apparent frequency of the thermal phenomenon. Dilhaire *et al.* use a beating between the repetition frequency of pulsed lasers (Dilhaire *et al.* 2008), Altet *et al.* power up the device by two excitations (Altet *et al.* 2009), and Tessier *et al.* created a beating between the excitation and the illumination beams (Tessier *et al.* 2001). In this context, we present a purely optical heterodyne interferometry for the purpose of frequency resolved full field temperature imaging.

The Experimental Setup The experimental setup is schematically shown in Fig. 2.8. It uses a single-mode doubled Nd-YAG laser operating at 532 nm. Since this wavelength is

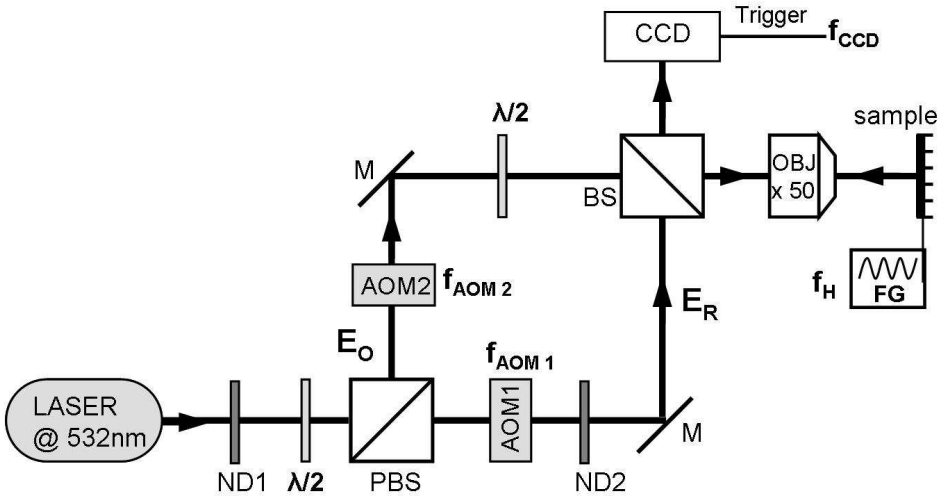

Figure 2.8 – Experimental setup of frequency resolved thermoreflectance measurements.

very different from the ones previously used (in the red wavelength range), we developed an entirely new setup for this experiment.

The laser beam (80 mW, $\lambda = 532$ nm) is separated with a polarizing beam splitter (PBS) in reference (E_R) and object arms (E_O). Half wave plates ($\lambda/2$) and neutral densities (ND1, ND2) allow control of the optical power in each arm. The object beam is focused on the sample by a microscope objective (OBJ, 50×magnification, $NA = 0.6$, air) and illuminates a 100×100 μm^2 region of the sample which consists of a series of five polysilicon resistive stripes ($R \approx 500\ \Omega$) in an integrated circuit. A function generator (FG) supplies a modulated heating voltage V_H at a frequency f_H.
The non-polarizing beam splitter (BS) serves for optical mixing of the reflected object beam with the reference beam which results into a fringe pattern recorded with a CCD camera (DALSA 1M30, 1024×1024 square pixel matrix, triggered at a frame rate $f_{CCD} = 28$ Hz). Since both beams are frequency shifted by acousto-optical modulators (AOM1, AOM2) at f_{AOM1} and f_{AOM2} around 80 MHz, the interference pattern is modulated at a beating frequency $\Delta f = f_{AOM2} - f_{AOM1}$ allowing accurate and sensitive phase shifting interferometry. By using the four-phase method the complex signal amplitude is obtained from a sequence of 4 consecutive CCD intensity images (Le Clerc *et al.* 2000), and the frequency shift between both beams is $\Delta f = \frac{1}{4} f_{CCD} + F_{Var}$ where F_{Var} is the supplementary frequency which can be chosen according to requirements.

As stated before, this setup enables the frequency investigation of phenomena modulated at any frequency F_{Var} by detuning Δf appropriately. We use a tunable analysis frequency F_{Var}, to detect frequency modulated photothermal phenomena.

The Integrated Circuit and its Temperature The integrated circuit is supplied with a frequency modulated electrical current resulting into a variation in temperature

which is also modulated but may contain different spectral components induced by the thermal or electrical response of the device. According to Eq. 2.28 a modulation of the optical reflectance at the surface of the circuit appears which affects the amplitude and phase of the object beam reflected from the device surface. A CCD camera detects the interference between the object beam and the phase-shifted reference beam; the reconstruction of the image is achieved numerically. For the temperatures and frequencies used here, the surface displacements are of the order of a few 100 nm which is accurately measured in phase images. The quantitative interpretation of these thermoelastic signals, however, is considerably more difficult than that of the amplitude signal ΔR (see Eq. 2.28) which can be quantitatively converted to temperature information. For this reason, the presented results are based on amplitude measurements.

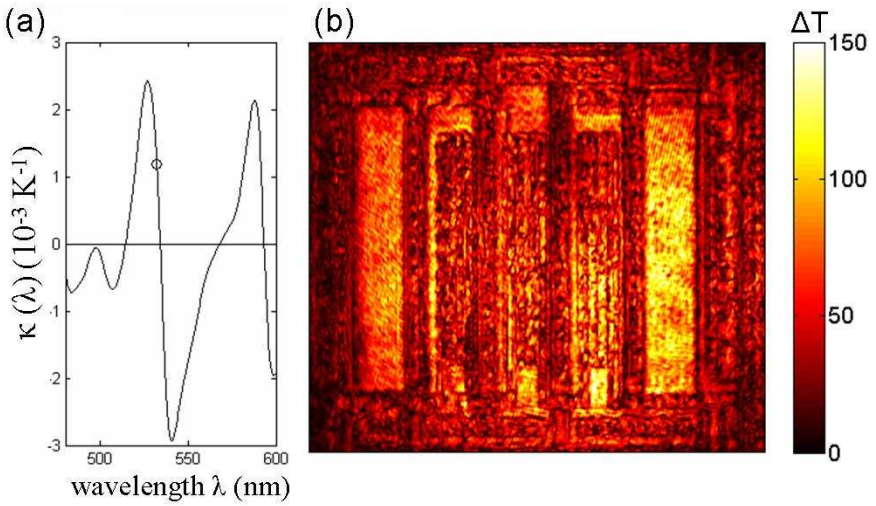

Figure 2.9 – (a) Thermoreflectance spectrum $\kappa(\lambda)$ measured on the heater resistors. The circle indicates the value of the conversion factor belonging to the chosen wavelength. (b) Reconstructed thermal image ($90 \times 90\mu m^2$) obtained under a sine modulation with $f_H = 66$ Hz and $V_H = 14.2$ V. Note that the colour bar gives ΔT in the resistors. This image results from an accumulation over 50 heating periods.

Our purpose is to obtain temperature maps of the integrated circuit, therefore knowing the exact value of the conversion factor κ in Eq. 2.28 is essential. Because κ is wavelength dependent, it is also important to choose the wavelength which maximizes its value in order to optimize the quality of the signals. A spectral sensitivity study of κ (extensively described in (Tessier *et al.* 2003)) of the device under investigation is conducted with a non-coherent white light source (see Fig. 2.9(a)). For a wavelength of 532 nm the value of κ is $1.2 \cdot 10^{-3}\mathrm{K}^{-1}$ which is near the optimal value of $2.4 \cdot 10^{-3}\mathrm{K}^{-1}$ at 527 nm. Any thermoreflectance image obtained on the polysilicon with $\lambda = 532$ nm can be converted into a temperature map using this coefficient (Fig. 2.9(b)) and $\Delta T = \frac{1}{\kappa}\frac{\Delta R}{R}$ following Eq. 2.28.

Phase Analysis The analysis of the phase was not the central purpose of this study. However, we considered the quality of the information that the phase could contribute to the signal. For the temperatures and frequencies used for the measurements with the integrated circuit, the surface displacements are of the order of a few 100 nm, i.e. a fraction of the wavelength. The phase of the interferometric signal can therefore provide an accurate measurement of this displacement. In Fig. 2.10 we show the phase image of the resistors obtained under square modulated heating with $f_H = 2$ kHz and a heating voltage of $V_H = 14,2$ V at the beating frequency $F_{Var} = 2$ kHz. The image demonstrates several circular phase maxima around the heater resistors which can be interpreted as surface displacements. Since thermoelastic displacements result from thermal expansion, all heated materials contribute to this signal. In a microelectronic structure such as this one, tens of layers of different materials are present, and therefore, a quantitative analysis is extremely difficult to achieve.

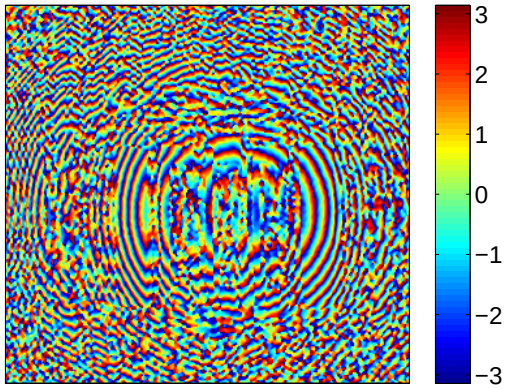

Figure 2.10 – Phase image of the resistors obtained at the beating frequency $F_{Var} = 2$ kHz under square modulated heating with $f_H = 2$ kHz and a heating voltage of $V_H = 14,2$ V.

Characterization of the Setup In order to identify the sensitivity of our measuring technique the setup needs to be characterized. The lowest temperature variation that we are able to resolve is limited by the setup noise. Additionally, the acquisition time influences the quality of the final image. We performed a series of measurements under static conditions ($V_H = 14$ V, $F_{Var} = f_H = 60$ Hz, sine-modulation) and then deduced the relative change of reflectivity $\Delta R/R$ for all final images. An accumulation of 10 heating periods, i.e. 5 sec of acquisition time in practice, results into $\Delta T_{noise} = 0.72$ K and a SNR of 14.6.

With an image accumulation over 50 heating periods, i.e. an acquisition time of 15 sec in practice, we achieve a temperature noise $\Delta T_{noise} = 0.35$ K and a SNR of 20. The latter

acquisition time is a good compromise between measurement duration and image quality, and was used in all following measurements.

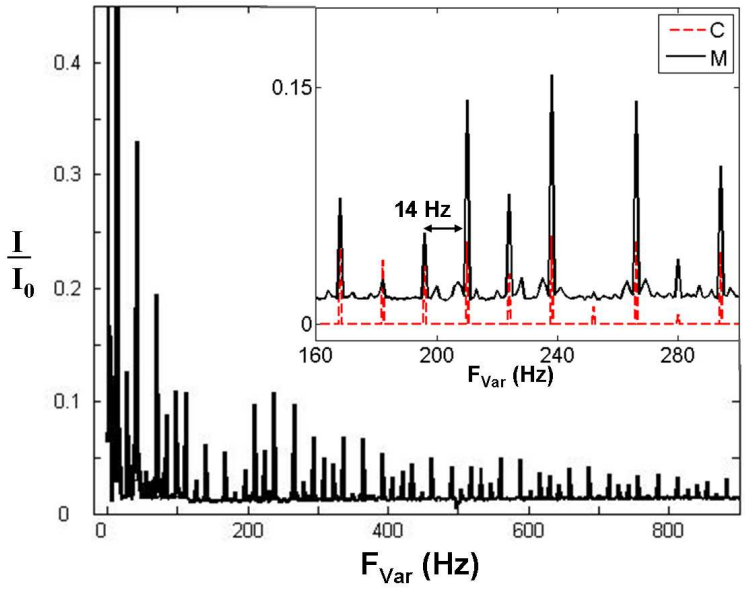

Figure 2.11 – Frequency spectrum of the setup at $V_H = 0$ V. A $sin(f)/f$ oscillation is observed with 14 Hz period. The normalized reflectivity is plotted against the frequency F_{Var}. The inset graph compares measured (straight line) and calculated (dashed line) frequency spectra (both normalized) in a frequency range of 140 Hz. The offset in the measured spectrum compared to the calculated one is caused by background noise.

In order to identify possible background signals, measurements were performed without heating the device ($V_H = 0$, $f_H = 0$) by detuning F_V from 0 up to 1000 Hz with steps of 80 Hz and determining the reflectivity of the resistors as a function of F_{Var}. We measured a frequency spectrum that is independent from the sample: an oscillation of type $sin(f)/f$ with continuously decreasing amplitude (Fig. 2.11).
This phenomenon is attributed to the frequency background caused by the image acquisition by the CCD camera. In fact, the camera exposition combines a trigger and a square frequency modulation at 28 Hz with an integration time of $t_{int} = 32$ ms, which is in the time-domain mathematically described as a convolution between a Dirac comb $y_D(t)$ and a rectangular function $y_\Pi(t)$:

$$y_{CCD}(t) = y_D(t) \otimes y_\Pi(t) \tag{2.29}$$

The Fourier transform of Eq. 2.29 results into the product of a Dirac comb and a $sin(f)/f$ function in the frequency domain:

$$\begin{aligned} \tilde{y}_{CCD}(f) &= y_D(t) \cdot y_\Pi(t) \\ &= \sum_{n=0}^{\infty} \delta(f - n\, f_{CCD}) \frac{2t_{int}\, sin(2\pi f \cdot t_{int})}{2\pi f \cdot t_{int}} \end{aligned} \tag{2.30}$$

Figure 2.12 illustrates the frequency domain of the camera exposure.

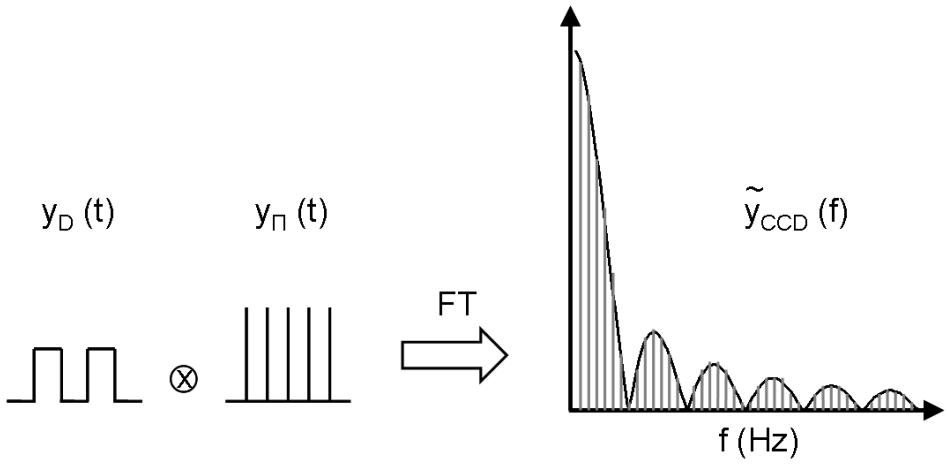

Figure 2.12 – Scheme illustrating the frequency domain of the camera exposure.

In experiments (inset in Fig. 2.11), we observed a period of $\frac{1}{2}f_{CCD} = 14$ Hz. This period is caused by the effect of the signal demodulation. In 4−phase shifting interferometry the demodulated complex field amplitude E is obtained from a sequence of 4 consecutive phase shifted CCD intensity images by $E = (I_0 - I_2) + j(I_1 - I_3)$ where the relative phase shift between two consecutive images is $\Delta\varphi = \frac{\pi}{2}$ (Le Clerc *et al.* 2000). Hence, the demodulated signal E is proportional to the difference between even, $(I_0 - I_2)$, and odd images, $(I_1 - I_3)$, respectively. These are recorded with an effective period of $\frac{1}{2}f_{CCD}$ which explains the observed 14 Hz-frequency oscillation.

Using this characterization of the signals intrinsic to the measuring method, we are able to extract the contribution of demodulation from the measured frequency spectra.

Temperature Imaging of an Integrated Circuit under Modulated Excitation
After having completely characterized the setup, we performed a more complex frequency study by heating the integrated circuit under a square excitation at $f_H = 2$ kHz and detuning continuously F_{Var} from 0 to 14 kHz. The spectral analysis of ΔT is plotted in Fig. 2.13. The scheme on the top illustrates the temperature modulation and the expected frequency contents of ΔT. Various peaks at $F_{Var} = (2n-1)f_H$ are observed corresponding to the odd harmonics which are the characteristics of a quasi-square thermal response. Note that for $F_{Var} < 2$ kHz the parasitic demodulation signal has been extracted; for high frequencies, i.e. $F_{Var} \geq 2$ kHz, the background signal is negligible compared to the thermal effect.

In the inset of Fig. 2.13 we plotted the measured frequency spectrum (continuous line) and the corresponding Fourier transform of a calculated square-wave signal modulated at 2 kHz (dotted line) in the frequency domain. The simple matlab program describing the square-wave function is presented in Appx. B. Due to normalization, the ratio of

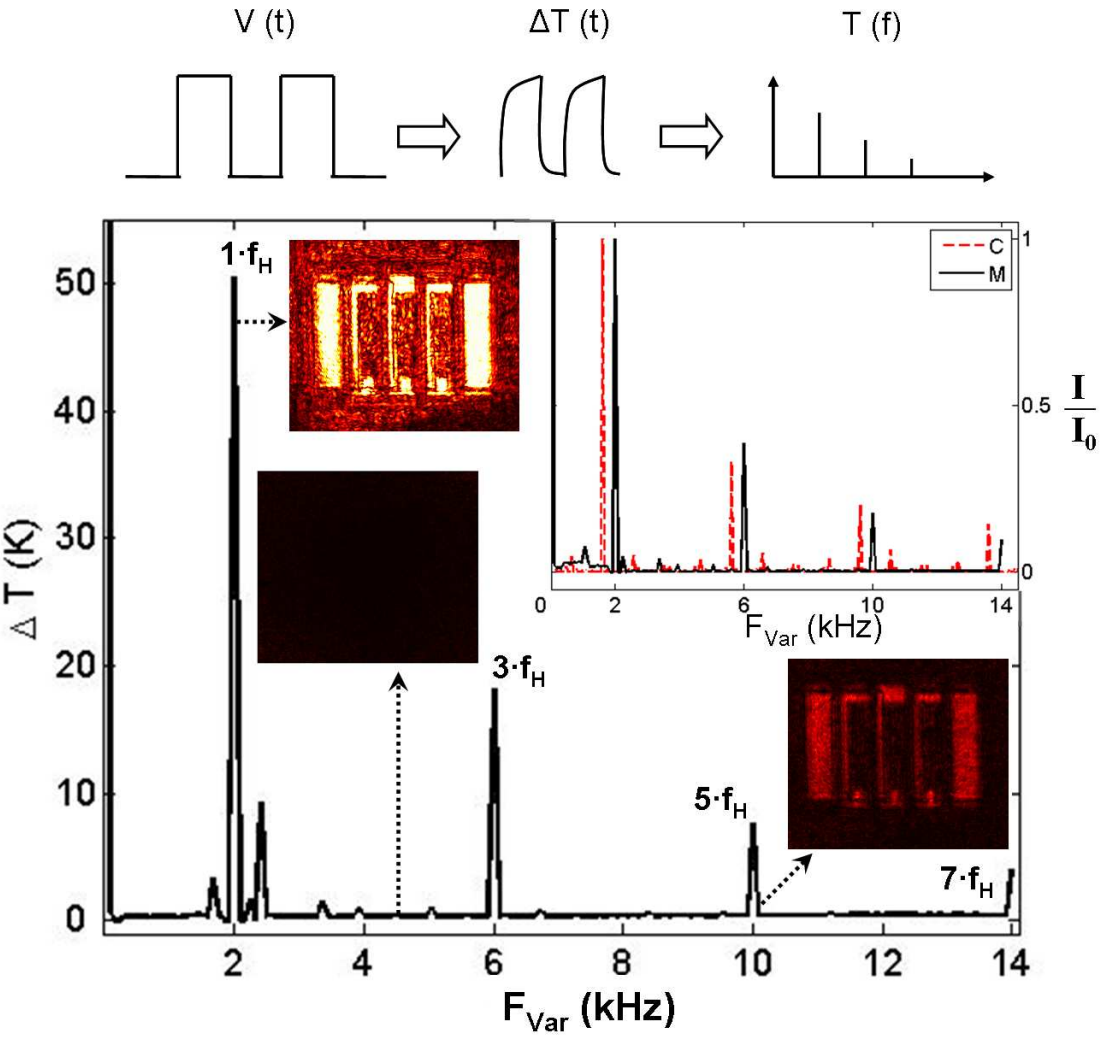

Figure 2.13 – Thermal frequency spectrum under square modulation with $f_H = 2$kHz. The scheme on the top illustrates the temperature modulation and the resulting expected frequency content of ΔT. The 3 inset images show temperature maps (within equal temperature range: $0-50$ K) obtained at 3 frequencies F_{Var} (2kHz, 4.56kHz, 10kHz). The inset graph compares measured (straight line) and calculated frequency spectrum (dashed line). Both spectra are normalized. For better visibility, the calculated spectrum is 400Hz frequency-shifted to the left.

both principal peaks (at 2 kHz) is 1, the amplitudes of the subsequent peaks differ about ±13%. This difference is probably due to the nonlinear thermal behaviour of the sample. Further, to highlight the power of our imaging technique, thermal images taken at 3 different excitation frequencies F_{Var} are shown in Fig. 2.13. These insets clarify very well the difference between imaging in resonant ($F_{Var} = 2$ kHz $= f_H$: SNR= 130, very high contrast image; $F_{Var} = 10$ kHz $= 5f_H$: SNR= 24, lower but still well visible contrast image) and in non-resonant beating frequencies ($F_{Var} = 4.56$ kHz $\neq (2n-1)f_H$: SNR= 4, no contrast at all) and points out the excellent frequency sensitivity of our technique.

Conclusion on Frequency Resolved Temperature Imaging We have presented a sensitive fast-imaging technique based on heterodyne interferometry dedicated to the measurement of photothermal phenomena with rich harmonic contents. The technique enables to detect and resolve temperature-frequency maps with high sensitivity. The temperature resolution is estimated as 0.35 K for 15 sec of accumulation. An acquisition time of less than 5 sec results in temperature resolution of 0.72 K. In terms of sensitivity or speed (both parameters are strongly correlated), this method offers performances very similar to these of classical CCD thermoreflectance (Tessier *et al.* 2001). Increasing the sensitivity with long accumulations is difficult with this technique, however, since fringes tend to drift for long acquisition times. The main strengths of this technique are to be found in its unique possibilities to access frequency-resolution while keeping the strong advantages of full field imaging.

The detection of unknown modulations of a photothermal signal is conceivable, and frequency dependent properties of samples can be analysed which opens interesting applications notably for the thermal management in integrated circuits. E.g. in numerical integrated circuits, regions operating at frequencies unequal to multiples of the clock frequency could be imaged using this method.

2.5.2 Application 2: Frequency Detection in the Brownian Regime of Gold Nanorods

We apply the technique of frequency shifting holography to the study of the dynamics of nanoparticles by scanning its frequency domain. Small particles suspended in a fluid undergo continuous random displacements. The so called *Brownian motion* is described primarily by a relation between the diffusion coefficient and the friction coefficient of the particle, but its description includes rotational as well as other degrees of freedom. A couple of years ago, Han *et al.* observed for the first time, coupling effects of rotational and translational motions in anisotropic macromolecules (Han *et al.* 2006).

In the last years, several studies of the dynamics of nanoparticles have been reported. The first measurement of ballistic Brownian motion of particles in a liquid was recently

demonstrated (Huang *et al.* 2011). Investigations of the coupling effects of rotational and translational dynamics were extended to carbon nanofibers (Bhaduri *et al.* 2008). Holographic video microscopy was applied to track the three-dimensional translation and rotational diffusion of copper oxide nanorods (Cheong and Grier 2010). The execution of an optical torque on nanorods was used to investigate the nonlinear motion of glass nanorods (Shelton *et al.* 2005), and recently Ruijgrok *et al.* applied an optical trap to measure the dynamics of rotational Brownian fluctuations and the heating of gold nanorods (Ruijgrok *et al.* 2011). In the context of plasmonic sensors, Sönnichsen and Alivisatos utilized the polarized light scattering from individual gold nanorods in a dark-field microscope to determine their orientation as a function of time (Sönnichsen and Alivisatos 2005).

Most of those studies performed time dependent measurement methods. Especially in the case of nanoparticles in water which exhibit quite fast rotational and translational dynamics, time dependent measurements need a fast camera and high sensitive camera for the detection. Here, we approach the investigation of Brownian motion of nanoparticles by detecting the frequency domain. In our study we use gold nanorods in an aqueous solution, and using the digital heterodyne holographic setup the scattered light of nanorods is measured. Due to their anisotropy the rods exhibit translational and rotational motions. Hence, the intensity of the detected light scattering changes depending on the orientation of the rod, and one observes a blinking. Using a variable beating frequency we can exploit the frequency domain of the rods' dynamics.

Furthermore, applying an external heating on the nanorods, we demonstrate that this technique allows the determination of the temperature increase of the nanorods.

Brownian Motion of Nanorods Brownian motion (Brown 1828) refers to the random motion of a particle suspended in a medium due to the random collisions of other particles with the object. The origin of this motion was largely unexplained until Einstein's famous paper (Einstein 1905) that established a relation between the diffusion coefficient of a Brownian particle and its friction coefficient. One year later, Einstein extended the concept of Brownian dynamics to rotational and other degrees of freedom (Einstein 1906a; Einstein 1906b).

When studying the Brownian motion of an elliptical particle, additionally to the translational motion one has to consider rotational dynamics. Whereas the translational motion is characterized by the mean square displacement, $\langle \Delta x^2 \rangle = 2D_t t$, the rotational motion is given by the mean square angle of rotation, $\langle \Delta \theta^2 \rangle = 2D_r t$, where D_t and D_r are the translational and rotational coefficients, respectively, and t is the time.

First, Perrin explored the coupling of translational to rotational motion of anisotropic particles (Perrin 1934; Perrin 1936). An uniaxial anisotropic particle is characterized by two translational hydrodynamical friction coefficients, $\gamma_{\parallel}$ and $\gamma_{\perp}$, respectively, for motion

parallel and perpendicular to its long axis.

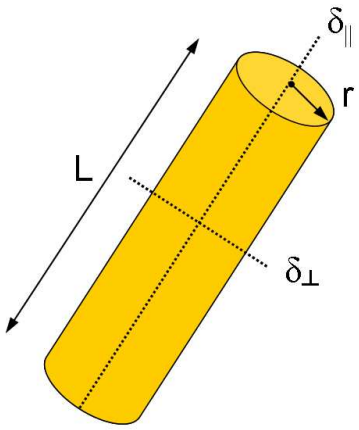

Figure 2.14 – Sketch showing the geometry of the rod and the corresponding rotational coefficients $\delta_{\parallel}$ and $\delta_{\perp}$.

The rotational motion coefficient is characterized by the constant δ which takes into account the differentiation between the rotation around the symmetric axis, $\delta_{\parallel}$, and around a perpendicular axis, $\delta_{\perp}$, see Fig. 2.14 for clarification. Both coefficients, γ and δ, depend on the detailed shape of the Brownian particle and have been analytically calculated for the case of a cylinder (Tirado and Garcia de la Torre 1979; Tirado and Garcia de la Torre 1980).

Experimental Setup In our experiments we used commercially available gold nanorods in an aqueous solution. The rods have a length $L = 60 \pm 10\%$ nm and a diameter $d = 25 \pm 10\%$ nm. The manufacturer specifies the longitudinal plasmon resonance of the rod as $\lambda_{res,long} = 650$ nm and the axial resonance as $\lambda_{res,axial} = 530$ nm.

The measurements were performed using a thin, flat glass chamber made of a glass substrate, paraffin tape in which we cut a cell of 4 mm diameter and a coverslip (see inset in Fig. 2.15 for clarification). With a paraffin tape thickness of 200 μm, we obtained a chamber volume of 2.5 μL. The rod solution was diluted with pure water with a ratio 1 : 9.

Gold nanoparticles show strong light scattering at the plasmon resonance wavelength which is orders of magnitude greater than that of a non-metallic object of the same size. Additionally, it has been shown that gold nanorods are extremely strong light scatterers due to the combination of the lightning rod effect and the suppression of interband damping (Sönnichsen *et al.* 2002). Hence, in a configuration of total internal reflection this property enables almost background free imaging of the scattered light of nanorods.

The experimental setup which is based on off-axis heterodyne holography is presented in Fig. 2.15. In order to maximize the detected scattering signal we use a laser with a

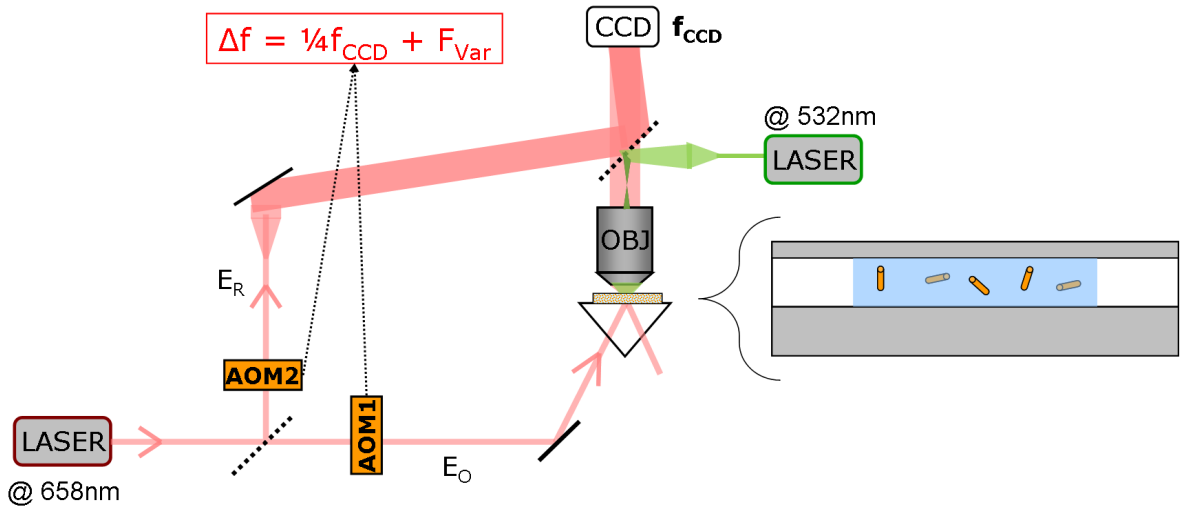

Figure 2.15 – Setup used for the detection of the rod's rotational motion. The heterodyne beating frequency is steadily varied. A second laser at $\lambda_{Heat} = 532$ nm can be applied for heating. The objective has a magnification of $\times 50$ with $N.A. = 0.6$ in air. The inset depicts the fluid glass chamber, made of a glass substrate, paraffin tape and a coverslip (from bottom to top).

wavelength of $\lambda = 658$ nm which is close to the rod's longitudinal resonance wavelength. The reference and the object arms in the setup are frequency shifted by two acousto-optical modulators, resulting into a beating frequency of $\Delta f = \frac{1}{4} f_{CCD} + F_{Var}$ where F_{Var} is a variable scanning frequency that is steadily changed from 0 to 1000 Hz with a frequency step of 10 Hz. At each frequency we obtain by the four-phase method an image which is an average of 7 holograms. By taking the Fourier transform of the measured hologram, after spatial filtering, we simply extract the mean signal in the k-space which is then plotted as a function of F_{Var}. Since we use a slow frame rate of $f_{CCD} = 16$ Hz compared to the average displacement of a nanorod, we are not sensitive to the exact position of a nanorod. However, by varying the beating frequency, we scan the frequency domain of the detected signal.

Furthermore, the setup has the possibility to heat the nanorods by applying a photothermal excitation delivered by a continuous multimode solid state laser at $\lambda_{Heat} = 532$ nm with an average power of about 20 mW.

Results and Discussion The graph in Fig. 2.16 shows a plot of the mean value $\langle I_k \rangle$ as a function of F_{Var} with $I_k(k_x, k_y, 0) = \hat{E}_H^{SF}(kx, ky, 0)$ where $E_H(x, y, 0)$ is the measured hologram, thus the detected signal (see Ch. 2.3.3).

The plot reveals that the signal $\langle I_k \rangle$ decreases with increasing frequency. In order to understand this behaviour better, let us analyse the origin of the detected signal.

Generally, the detected signal is composed of the light scattered by the nanorods, back-

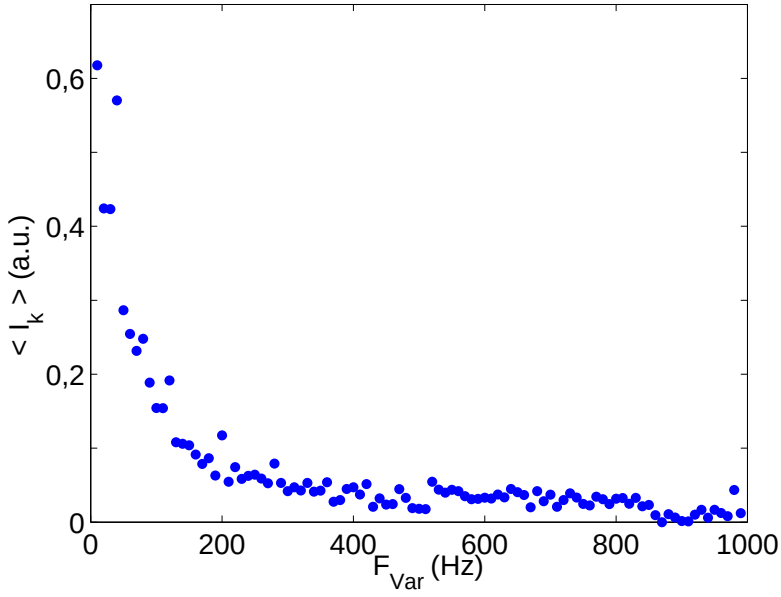

Figure 2.16 – Signal $\langle I_k \rangle$ as a function of frequency F_{Var}

ground signal and technical noise. We have seen that the technique of heterodyne off-axis holography in total internal reflection configuration is a background free detection that eliminates almost all technical noise, and we can assume that the detected signal results entirely from the nanorods.

The intensity of the scattered light underlies fluctuations which are due to the Brownian fluctuations of the positions and orientations of the rods. In the experiment one observes a random blinking on the CCD camera. In the context of Brownian dynamics, the fluctuating positions and orientations are described by the translational and rotational motion. Both mean-square displacement and mean-square angle of rotation are linear in time, thus inverse proportional to frequency:

$$\langle \Delta x^2 \rangle = 2D_{t,\parallel/\perp} \frac{1}{f} \tag{2.31}$$

$$\langle \Delta \theta^2 \rangle = 2D_{r,\parallel/\perp} \frac{1}{f} \tag{2.32}$$

Since it can be assumed that a rotational motion of a rod around its small axis, i.e. perpendicular to its long axis, does not cause a strong change of the scattered intensity, we can neglect this component. The translational, $D_{t,\parallel}$ and $D_{t,\perp}$, and rotational diffusion coefficients, $D_{r,\parallel}$, are given for a cylinder by (Tirado and Garcia de la Torre 1979; Tirado

and Garcia de la Torre 1980):

$$D_{t,\parallel} = \frac{k_B T}{2\pi\eta L}[ln(\frac{L}{2r} - \gamma_\parallel)] \quad (2.33)$$

$$D_{t,\perp} = \frac{k_B T}{4\pi\eta L}[ln(\frac{L}{2r} - \gamma_\perp)] \quad (2.34)$$

$$D_{r,\parallel} = \frac{3k_B T}{\pi\eta L^3}[ln(\frac{L}{2r} - \delta_\parallel)] \quad (2.35)$$

where η denotes the viscosity of the fluid which is in our case water, i.e. $\eta_{H_2O} = 1.002$ mPa·s at 20°C. k_B denotes the Boltzmann constant, T is the temperature, L and r the length and the radius of the rod, respectively. For our rod geometry we obtain: $\gamma_\parallel = 0.18$, $\gamma_\perp = 0.96$ and $\delta_\parallel = 0.2525$. We calculate the translational diffusion coefficients of $D_{t,\parallel} = 11.30\ \mu\text{m}^2\text{s}^{-1}$ and $D_{t,\perp} = 9.83\ \mu\text{m}^2\text{s}^{-1}$, and a rotational diffusion coefficient of $D_{r,\parallel} = 2.01 \cdot 10^4\ \text{rad}^2\text{s}^{-1}$.

This means that during the time it takes to record one image (the integration time of a frame is 50 ms), the rod has in average a rms displacement of $\sqrt{\langle\Delta x^2\rangle} \cong 1\ \mu$m and a rms rotation of $\sqrt{\langle\Delta\theta^2\rangle} = 44.9$ rad. This has no effect however, when a heterodyne modulation of the beam is used to investigate this phenomenon at high frequencies.

It was shown that light scattered off gold nanorods is strongly polarized along the long axis (Sönnichsen *et al.* 2002; Sönnichsen 2001). In our setup, both beams pass through a half wave plate in order to align their polarization and allow interference. Since we have only interference, i.e. a detectable signal, when the scattered light by the nanorods has the same polarization as the reference beam, we have a polarization sensitive detection. This leads us to the assumption that our setup is more sensitive to the rotational dynamics of nanorods than to their translational motions, and we can assume that the detected blinking results primarily from the rotational motion. The translational motion dynamics is neglected, and we can assume that the detected signal is decoupled from the translational coefficient and thus, carries mostly the frequency domain information of the rotational dynamics.

Taking these considerations into account, the measured frequency dependency can be described entirely by the frequency behaviour of Eq. 2.32 using relation Eq. 2.35. However, it must be noted that the signal that we detect is proportional to the mean-square angle, i.e. $\langle I_k\rangle \propto \sqrt{(\langle\Delta\theta^2\rangle)}$, meaning that we do not have an absolute measurement but a relative measurement.

Determination of the Temperature Increase of Heated Nanorods Equation 2.35 demonstrates that the diffusion coefficient is temperature-dependent. Rising the temperature of the nanorod leads to an increase in D_r which results in an increase of the rotational dynamics, $\langle\Delta\theta^2(T)\rangle$: the rod rotates faster. Hence, when increasing the temperature we can expect a change in the behaviour of the detected signal in the frequency domain.

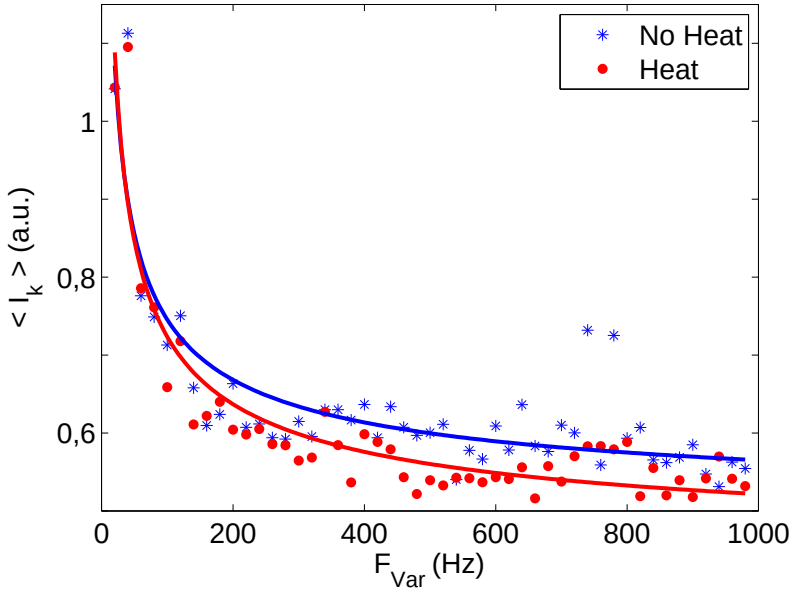

Figure 2.17 – Signal $\langle I_k \rangle$ as a function of frequency F_{Var} at heating for two different measurements: for unheated (blue symbols) and heated (red symbols, $P_{Heat} = 20$ mW) particles. The continuous lines are the corresponding fits of type $y(x) = a \cdot x^{\frac{1}{2}} + b$.

Figure 2.17 plots two series of measurements. Whereas the blue symbols correspond to a measurement without heating, the red symbols results from a measurement where the nanorods were heated (the heating was achieved at $\lambda_{Heat} = 532$ nm at a power of about 20 mW for a surface of 180 μm^{-2}). We applied a fit of type $\langle I_k \rangle (F_{Var}) = a \cdot {F_{Var}}^{-\frac{1}{2}} + b$ to the measurements which are plotted as continuous lines in Fig. 2.17. We obtain different values for the factor a, i.e. $a_{noheat} = 2.6379 \pm 0.2148$ (no heat, blue line) and $a_{heat} = 2.9526 \pm 0.1681$ (heat, red line).

Assuming that the signal carries the information of the frequency domain of the mean-square angle of rotation $\langle \Delta\theta^2 \rangle$, the decay factor a is proportional to the square root of temperature $\sqrt{T}$. Hence, by calculating the ratio of a_{heat} to a_{noheat}, we can estimate the increase in temperature, i.e. $\frac{T_2}{T_1} = (a_{heat}/a_{noheat})^2 = 1.25 \pm 0.35$, where T_1 corresponds to room temperature and T_2 to the raised temperature. Due to the uncertainties in the a factors of the fits, $\frac{T_2}{T_1}$ results into a relative high uncertainty of 27.7%. Assuming an initial temperature of 20°C, we calculate an increase in temperature of $\Delta T = 5 \pm 7$°C with an uncertainty larger than the temperature increase itself. However, studies of heating in similar gold nanorods and nanospheres (Seol *et al.* 2006; Bendix *et al.* 2010; Ruijgrok *et al.* 2011) have shown similar temperature increases.

Calculation of Temperature Increase A quantitative description of the temperature increase around a sphere placed in an infinite medium can be derived using the following

equations:

$$\Delta T = \frac{P_{abs}}{4\pi r C} \tag{2.36}$$

$$P_{abs} = \frac{\sigma_{abs} P_{laser}}{A} \tag{2.37}$$

σ_{abs} is the absorption cross section, P_{laser} is the power of the laser and P_{abs} is the power that is absorbed by the surface A which corresponds to the surface that is illuminated, (i.e. heated), by the heating beam, i.e. here 78 μm. C is the conductivity of water (0.6W/K m), and r is the radial distance from the particle centre. Ruijgrok *et al.* examined analytically the difference between temperature profiles around a sphere and an ellipsoid with a moderate aspect ratio (see supplementary material). The authors did the approximation that the heat conductivity is infinite, and that therefore, the temperature in the nanorod is uniform. They compared the temperature change of an ellipsoid to that of a sphere of the same volume, and they showed that for a rod having an aspect ratio of 2, the temperature change is less than 5%. As a result, the nanorod can be replaced by a sphere of the same volume. To evaluate the absorption cross section of a nanorod,

$$\sigma_{abs} = \frac{\omega n}{c} \cdot Im\{\alpha/\varepsilon_0\} \tag{2.38}$$

we calculate the polarizability α of a prolate spheroid in dipole approximation. With an average laser power of 20 mW at a wavelength of 532 nm, reaching a surface of about 180 μm^2, we estimate a temperature increase of $\Delta T = 0.04$ K at the surface of the rod.

This large discrepancy is difficult to explain, since on the one hand, we used a very simplified model to calculate the temperature increase in one single nanorod, and on the other hand we measured a temperature increase with a relative large uncertainty. Furthermore, trapping effects due to the heating beam could result into the creation of clusters of nanorods, which have different dynamics than a single rod. Another aspect that could play a role is the near-field interaction of closely spaced nanorods which may lead - on short time scales - to an increased interaction with the heating beam, and therefore an increase in temperature which is not considered in the simplified model.

Trapping effects on a polarization dependent orientation of the nanorods can also play a role in the observed signals. Rotational trapping would tend to reduce the observed signal in the presence of heating. Trapping of nanorods cannot be eliminated, however. For this reason, other sets of measurements, using a hot wire instead of an optical heating have to be carried out.

Conclusion We have demonstrated that the technique of frequency shifting heterodyne holography enables the frequency detection of Brownian nanorods. The technique is in particular sensitive to the rotational dynamics of gold nanorods. Hence, we can in a first approximation assume that the detected signal is proportional to the mean-square

angle of rotation, and the measured results reflect very well the expected frequency behaviour of $\langle I_k \rangle \propto {F_{Var}}^{-\frac{1}{2}}$. This makes an excellent technique to study qualitatively and quantitatively the Brownian dynamics of gold nanoparticles.

In addition, it was shown that a heating of the nanorods results into a variation of the rotational coefficient D_r which causes a change in the slope of the measured signal dependency $\langle I_k \rangle (F_{Var})$. By comparing two measurements, one without heating, one with heating, we evaluated the temperature increase as $\Delta T = 5$ K with however a large uncertainty of 27.7%. In order to fully describe the dynamics of the gold nanorods additional measurements and simulations are necessary.

2.5.3 Conclusion on Frequency Detection

In conclusion, we have shown that the method of the tunable frequency modulation in the heterodyne holography technique allows various novel applications in very different domains of research. In order to validate the technique on a known system with a small degree of complexity we investigated the thermal frequency domain of an integrated circuit. The sample was supplied with a modulated current resulting into a temperature modulation. The full-field imaging technique based on heterodyne holography enabled the high sensitive detection of temperature-frequency maps, resulting into frequency domain spectra of the temperature with excellent precision.

After the validation of frequency shifting heterodyne holography to detect the frequency domain of a known modulation, we applied our frequency sensitive technique to an unknown frequency content. Since this thesis work is primarily concentrated on the study of nanoobjects, we were interested in investigating the Brownian dynamics of gold nanorods. We have shown that our setup is almost entirely sensitive to the rotational dynamics of nanorods. The detected signal is proportional to the mean-square angle of rotation, and the measurements resulted into a frequency behaviour reflecting well the frequency spectra of the nanorods which is characterized by an inverse square root decrease of the signal with frequency. In addition, by heating the nanorods we have shown that a small temperature increase resulted into a detectable change in the frequency spectrum.

Hence, we can summarize that the frequency shifting technique of heterodyne holography proved to be a powerful tool to detect the frequency domain of a system.

2.6 Conclusion on Digital Heterodyne Holography

In conclusion, we have shown that the technique of digital heterodyne holography in off-axis configuration results into an excellent sensitivity for the detection of weak signals which makes it an appropriate technique for the imaging of nanoobjects.

We have demonstrated that the heterodyne technique enables the detection of a pho-

tothermal signal by correctly detuning the beating frequency. It will be shown that this technique can be applied to investigate the heating of nanostructures; the details and the results of this study will be discussed in Ch. 5.

Furthermore, based on the heterodyne detection principle, we have developed a new imaging technique that scans the frequency domain of a system, by varying systematically the heterodyne beating frequency. This method is called frequency scanning heterodyne imaging. In order to test and apply this technique, we chose to measure the thermal frequency content in an integrated circuit. Therefore, we developed an entirely new setup for the experiments. Another application of the frequency domain detection used heated nanorods in a liquid in view of studying their rotational Brownian dynamics.

Chapter 3

The Nanostructures under Study

Table of contents

"Nanoart"

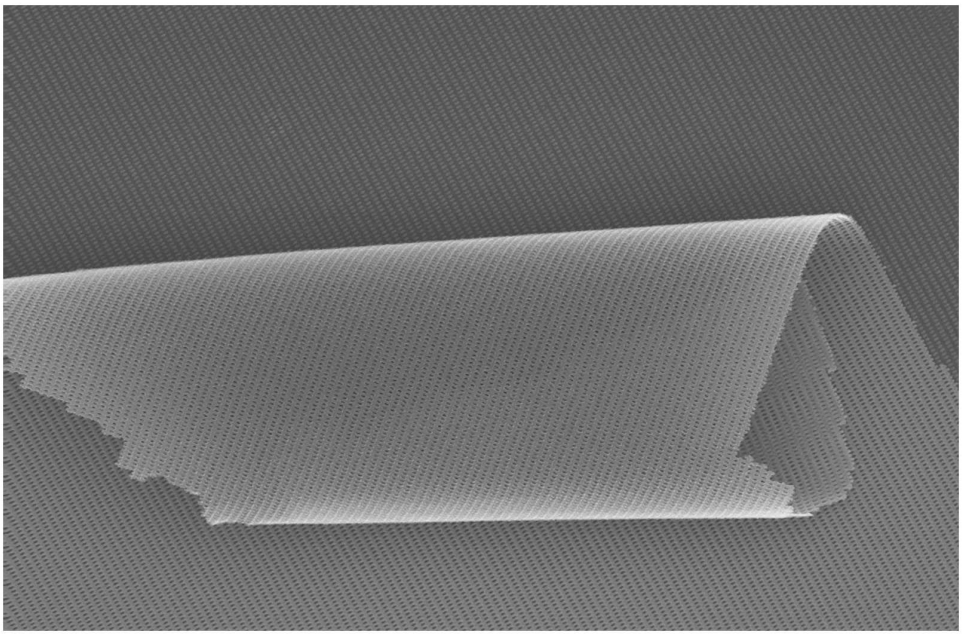

Although this thesis work is mainly based upon the analysis and study of holographic images, we availed ourselves of other investigation methods for the purpose of adding supplementary physical insights and thus, completing the study on plasmonic nanostructures. In addition to holography, on the one hand we performed extensive measurements of the scattering spectra of single nanoobjects, and on the other hand we developed a simulation model based on the finite element method. Both investigation methods will be introduced and explained in this chapter.

Furthermore, we will present the different types of nanostructures that we have investigated during the course of this work. We will comment the geometry of the samples, the nanofabrication process, and some images of the fabricated nanostructures will be presented.

3.1 Design of the Nanostructures

In this work we designed various nanostructures with the purpose to have a large variety of nanoobjects ranging from simple objects to more sophisticated geometries. The different geometries of the nanostructures that we took interest in are illustrated in Fig. 3.1 (a-c), and can be sorted in three types:

* chains of nanodisks
* single and coupled nanorectangles
* pairs of tapered, coupled triangles

Chain of nanodisks have been mainly studied in the context of plasmonic waveguiding and energy transport. In the present case we are rather interested into its spectral and spatial scattering properties. Different chains are fabricated by varying the number of disks, the disk diameter and the disk spacing (see Fig. 3.1 (a)).
The coupled nanorectangles - or nanorods - build a classical structure. In the last years these structures have attracted a widespread interest in the domain of nanooptics and plasmonics. Two coupled nanorectangles are considered as a realization of a simple nanoantenna. Here, we introduced two main variables, the arm length and the width of the feed gap (see Fig. 3.1 (b)).
The triangular geometry is a novel structure. As can be seen from Fig. 3.1 (c) the triangular structures are composed of two closely-spaced right-angled tapered triangles. The ratio between the legs is 500, which gives a very narrow angle of $\alpha = 0.11°$ and thus, a very slowly changing width of the leg. This structure has been designed in view of studying resonant modes as a function of the size of the short leg and the gap width. Illuminated under light polarized along the short leg direction, this design may be considered as coupled rods or coupled line pairs.

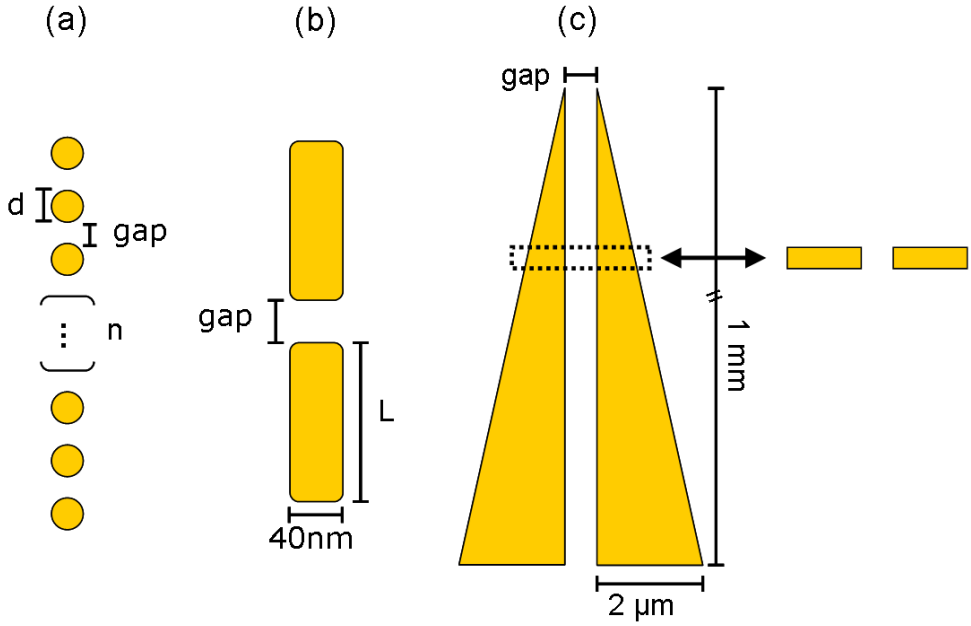

Figure 3.1 – Schemes of the top view of the different nanostructure types: (a) nanodisk chain, (b) two rectangles and (c) a pair of triangles.

To fabricate a large diversity of plasmonic structures, we introduced different variables such as the gap width or the nanostructure size. Their respective size ranges are listed in the following:

gap width: $0\ \text{nm} \leq \text{gap} \leq 100\ \text{nm}$

disk diameter d: $d_1 = 100\ \text{nm}$, $d_2 = 150\ \text{nm}$

disk number n**:** $1 \leq n \leq 20$

rectangle length L**:** $50\ \text{nm} \leq L \leq 350\ \text{nm}$ (the rod width is fixed at 40 nm)

As Fig. 3.2 illustrates, the sample contains several periodic arrays of the different nanostructure geometries. Along the vertical direction of the array, the length of the nanostructure is varied, i.e. n for the chains or L for the rods, while the gap width increases along the horizontal direction. The first columns in each array contain single nanostructures, i.e. single nanodisks or single nanorectangles. The separation distance between two adjacent nanoobjects is between 30 μm and 50 μm to exclude near- or far-field interaction between neighbouring nanoobjects. Far-field scattering takes place with a distance dependence of d^{-1}, whereas near-field interactions of adjacent structures show a d^{-3} dependence and dominate at small distances. To facilitate polarization dependent measurements, each structure is fabricated two times: oriented along the horizontal and the vertical direction of the sample (see Fig. 3.2).

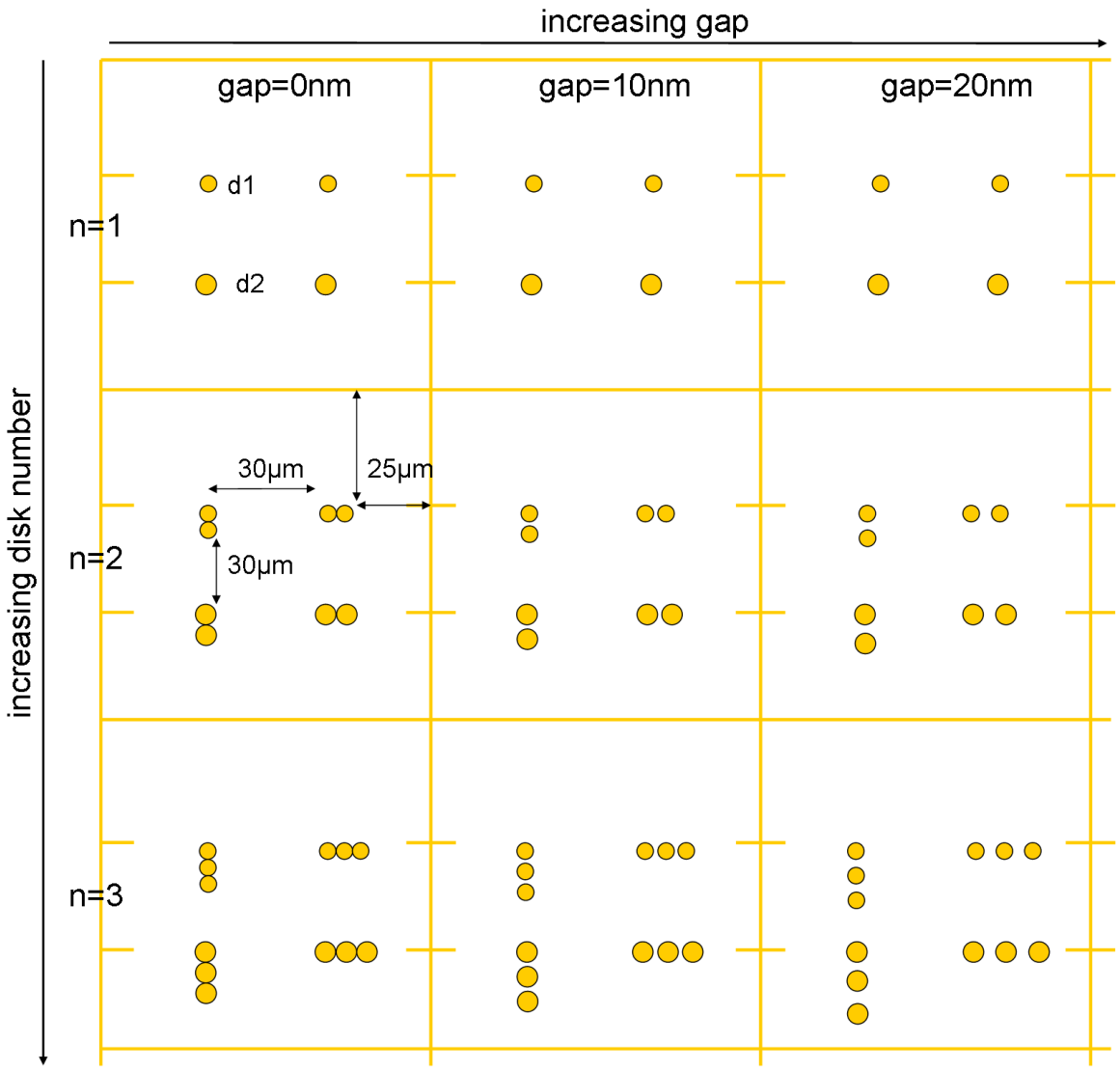

Figure 3.2 – Sketch illustrating the arrangement of the nanoobjects in the array. Note that the illustration is not to scale.

Furthermore, for a better identification of the single nanostructures on the glass substrate, a gold lattice has been introduced in the fabrication process of later samples. Each window has a surface of $80 \times 80\ \mu m^2$ in which four nanoobjects of the same type, but with different orientations (and disk diameters in the case of the disk chains), are arranged. The frame has a width of 2 μm, and the distance to the nearest nanostructure is 25 μm. Figure 3.2 illustrates the gold lattice. Additionally, at each side of the nanostructures markers have been included for a better identification of the position of the individual nanoobjects.

3.1.1 Nanostructure Fabrication

A study and characterization of single nanoobjects implies that the geometries are well defined, in particular the width of the gap, and that the nanostructures are correctly fabricated. This request is achieved by using a high resolution electron beam lithography process that has been very well established in the clean room facilities of the LPN (Laboratoire de Photonique et de Nanostructures, CNRS) with the indispensable help of Stéphane Collin, Nathalie Bardou and Christophe Dupuis.

For the fabrication of the gold nanostructures, a glass substrate is used, on which a thin film of lithography resist (polymethyl methacrylate, PMMA) is coated. The choice of the glass substrate is indispensable if we want to perform transmission measurements. After electron beam lithography, a 2 nm thick Cr adhesion layer is deposited which has little (and mostly negligible) influence on the optical properties. And then on top of it, a 30 nm thick gold film is deposited using thermal evaporation of the metal. The last step of the fabrication process is the lift-off procedure which removes all the material on the remaining resist. 30 nm thick nanostructures of gold are obtained.

Scanning electron microscope (SEM) images of examples of some of the successfully fabricated nanostructures are shown in Fig. 3.3 and 3.4. The SEM images in Fig. 3.3 show different chains composed of 4 (a), 11 (b) and 20 (c) nanodisks. It is seen that the dimensions of the disks are well defined, and that the disks are well spaced. We measure maximal deviations in disk size of 10% and maximal deviations in gap width of 25%. It is remarked that deviations in gap width are perforce connected to deviations of the spaced nanostructures since the lithography process defines the gap width via the centre-to-centre distance between the structures. That is why the gap width can underlie stronger size variations. Figure 3.3 (d) showing a detail of a high resolution SEM image with a tilted sample of a chain, displays the excellent imaging quality of the SEM. The height of the disks is very well revealed, and the grain size of the deposited Au can be identified. Note that even the grains of the silica substrate are distinguishable.

Images of different coupled rectangular structures are presented in Fig. 3.4 (a) and (b). It is seen that the edges of the rectangles are rounded, thus we call them rods. Analysing the geometry, it is seen that the width of the rods is slightly larger than expected. The

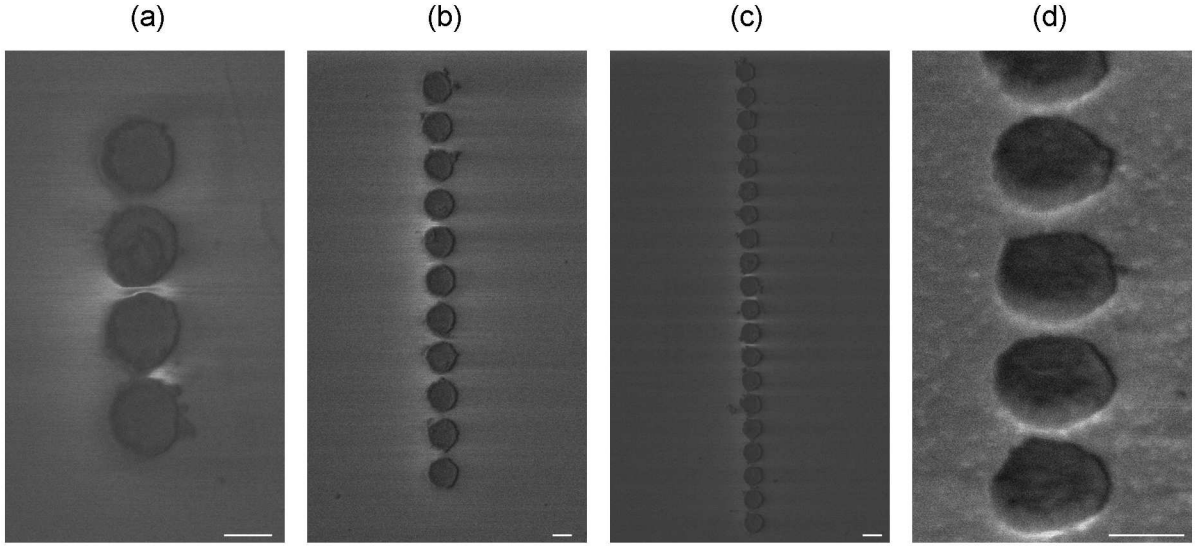

Figure 3.3 – SEM images of nanodisk chains: (a) n=4, d=150 nm, gap=20 nm, (b) n=11, d=150 nm, gap=40 nm, (c) n=20, d=150 nm, gap=30 nm. (d) SEM image with a tilted sample ($45°$) of a detail of a chain (n=16, d=150 nm, gap=30 nm). The length of the scale bar is 100 nm.

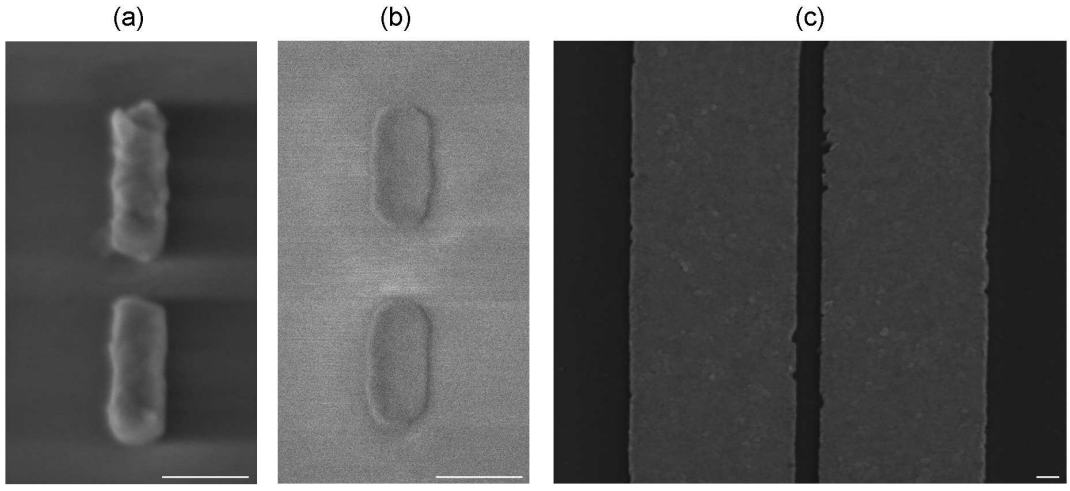

Figure 3.4 – SEM images of nanorods and triangles: (a) two coupled nanorods with L=140 nm, gap=75 nm and (b) L=170 nm, gap=50 nm. (c) Detail of two triangles separated by a gap of 100 nm. The length of the scale bar is 100 nm.

measured width is up to 60 nm wide compared to an expected width of 40 nm. In contrast, the rod length displays an incertitude of only up to 2.5%, thus it can be assumed that the fabricated rod structures are well in the expected length range.

Lastly, the SEM image in Fig. 3.4 (c) shows a detail of two 100 nm separated triangles. In this part of the structure, the triangles have a width of about 730 nm. As the SEM image proves, this width is constant over a length of 1.9 μm. The gap is well realized apart from tiny imperfections.

During the course of our work, many samples containing these nanostructures have been fabricated. The fabrication process, which is very delicate for such structures, and the sample design have been consistently ameliorated. Several factors had to be assured:

- The lift-off process which should remove all residual material that could pollute the nanostructures and, hence, perturb the measurements.
- The correctness of the nanofabrication, i.e. the realization of the gaps between the individual elements in the nanostructures and of the proper sizes.
- It had to be assured that the nanostructures could be easily retrieved using an optical system.

In conclusion, an overall high quality of gold nanostructures fabricated on a glass substrate has been achieved which is confirmed by the here presented SEM images.

3.2 Spectroscopy of Single Nanoobjects

In the following we will describe the technique with which the spectrally resolved scattering intensities were measured. The experimental setup for the spectral investigation of individual nanoobjects is sketched in Fig. 3.5. The setup is composed of three devices: a dark field objective, an imaging spectrometer and a CCD camera. The objective (Olympus, magnification: 50×, numerical aperture: 0.75) is used in dark-field mode in order to illuminate the sample at highly oblique angles using a white light source. The scattered light of surface features of the sample (in our case the surface features correspond to the nanostructures under investigation) re-enters the objective, while the scattered light of the flat glass substrate falls outside the acceptance angle. Hence, the background signal is almost omitted resulting into an enormous increase in contrast.
An imaging spectrometer (ImSpector V8E, Specim) is placed between the microscope and the high sensitive CCD camera (Roper Cascade 512 F EMCCD, frame transfer 512×512, $16\mu m \times 16\mu m$ pixel matrix, triggered at a frame rate $f_{CCD} = 16$Hz). The CCD camera uses an integration time of $t_{int} = 500$ ms and averages over 10 frames. The spectrometer which has a spectral range of $380 - 800$ nm and a resolution of 2 nm, consists of a 30 μm

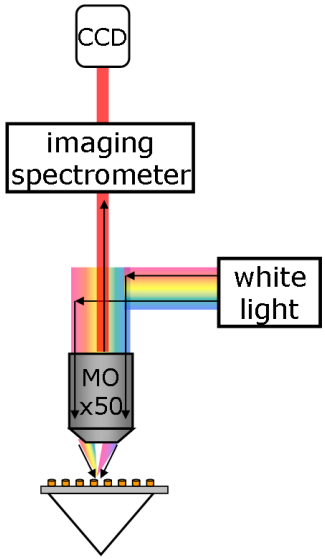

Figure 3.5 – Scheme of the setup for spectroscopy.

large slit and a diffraction grating which splits and diffracts light into several beams travelling in different directions. Therefore, by selecting a zone of interest on the sample using the slit, the CCD camera records a full-field image of the intensity of the scattered light as a function of the wavelength and of the position in the slit.

Calibration of the Spectral Images In order to analyse the recorded spectral images, in one column the corresponding wavelength has to be assigned to each pixel. This calibration is done using a spectrum recorded with a Hg spectral lamp. Hg has a discrete emission spectrum whose emission lines are known. The following linear relation between the wavelength λ and the pixel number has been experimentally established:

$$\lambda = 1.21 \cdot pixel_{column} + 272\ nm \tag{3.1}$$

White Light Source The spectral measurements are performed using a conventional tungsten halogen lamp as an incoherent white light source. The lamp has a spectral range between 450 and 800 nm. The scattering spectra recorded of the nanostructures have to be normalized in order to account for the spectral characteristics of the illumination source. For that a spectral image only of the lamp is recorded, denoted in the following as S_{Lamp}, using a homogeneous scatterer. Then, the spectral response of the tungsten lamp is extracted from the spectral image by integrating a total of 200 lines along the slit as shown in Fig. 3.6 (a) indicated by the dotted white lines. Figure 3.6 (b) plots the extracted scattered intensity as a function of wavelength, i.e. the spectrum of the illumination source. Note that the actual spectrum of the Hg lamp expands towards the larger wavelengths in the near-infrared spectrum range which is however not revealed by the spectrometer due to its limited spectral range.

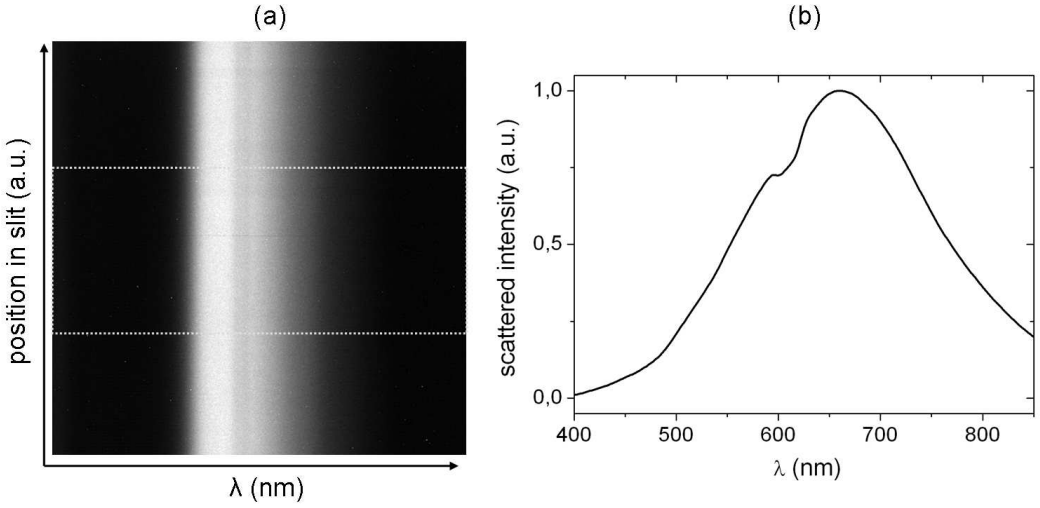

Figure 3.6 – (a) Spectral image of the tungsten halogen lamp. The white dotted lines indicate the zone of intensity integration. (b) Extracted spectrum from the left handed image by integrating over 200 lines. The scattered intensity is normalized to 1.

Extraction of Spectra of an Individual Nanoobject In a first step, the measured signal S_{meas} which contains the spectral response of the nanoobject together with the background has to be extracted from the spectral image. This is done by selecting and integrating over several lines containing the entity of the scattered photons of one nanoobject which are diffracted by the spectrometer grating on the camera. S_{meas} contains the spectral contribution of the lamp as well as of the background. To define the spectrum of the background, denoted as S_{BG}, the same procedure is applied by integrating this time over several lines in a zone next to the structure. To separate the spectral information of the nanoobject from the background, S_{BG} is subtracted from S_{meas}. Then, this difference is divided by S_{Lamp}, in view of normalizing the spectrum in wavelength. Hence, the final spectral response, S_{object}, containing only the information of the nanoobject of interest is calculated as follows:

$$S_{object} = \frac{S_{meas} - S_{BG}}{S_{Lamp}} \tag{3.2}$$

Figure 3.7 demonstrates an example of a spectral image which is overlaid with the corresponding calculated scattering spectrum S_{object}.

In order to calculate the uncertainties in all spectral measurements we evaluated the spectral width of the peak position. These uncertainties are solely related to measurement noise and will be presented as error bars in the presented graphs.

As the spectrum of the illumination source revealed, the spectrometer has a limited spectral range which leads to a cutting off of the recorded spectra in the near-infrared range. As a result, the spectrometer does not fully resolve any scattering spectrum that has a peak at wavelengths longer than 800 nm, and instead of the real scattering peak, a

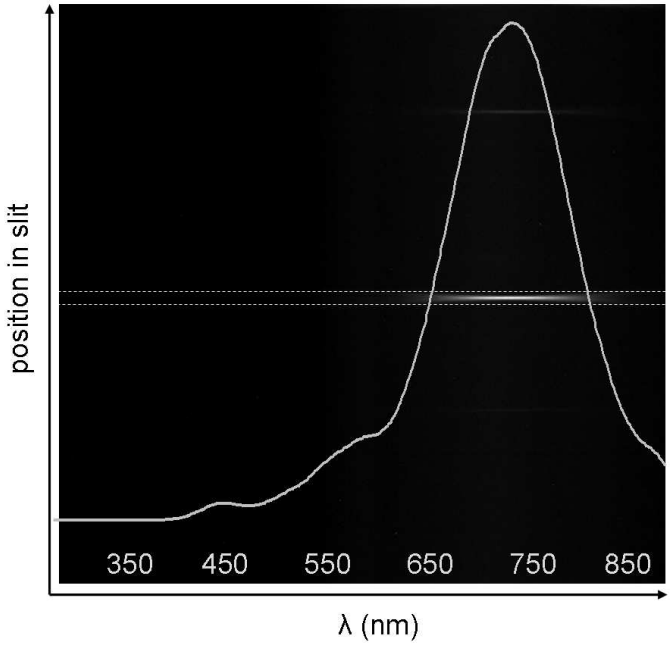

Figure 3.7 – Full-field image of an example spectrum of a nanostructure. The image displays the scattered intensity as a function of wavelength (horizontal axis). The corresponding, background corrected and normalized spectrum is superposed (white curve).

peak situated at lower wavelengths is measured. Hence, the scattering spectra measured of nanostructures of which we expect a scattering peak in the near-infrared spectral range, have to be analysed carefully.

Using this imaging spectroscopy technique, the spectra of various nanostructures have been measured and analysed in detail. The results are presented and extensively discussed in Ch. 4 and Ch. 5.

3.3 FEM Simulation of Plasmonic Nanoobjects

The study of the scattering by plasmonic nanostructures was completed by performing simulations. These numerical calculations were carried out using the commercial software package COMSOL Multiphysics (version 3.5a with incorporated RF module, installed on a Dual-Quad Core 12GB RAM workstation, http://www.comsol.com), which comprises an electromagnetic code based on the finite element method (FEM).

Initially, this thesis work was entirely oriented towards an experimental study of plasmonic nanoobjects. However, in the course of this work, we required additional insights into the scattering behaviour of the investigated nanostructures in order to understand better our experimental results. Therefore, we decided to develop a simulation model, which describes the optical properties of plasmonic nanoobjects in the far-field and as well in the near-field. Note that this kind of simulations did not exist at the Institut

Langevin before my thesis which thus constitutes a first effort towards the implementation of finite element methods in our laboratory. Finally, the development of these simulation models and the analysis of the simulated results occupied a major part of this thesis work.

Two different characteristics are examined numerically: the spectral scattering response in the far-field and the scattered intensity in the near-field. For all simulations, the refractive index of gold n_{Au} is taken from experimental values in literature (Palik 1998). The refractive indices for the substrate and for air are chosen as $n_{substrate} = 1.5$ and $n_{air} = 1$, respectively. The model we used has a spherical geometry. Figure 3.8 illustrates a cross section of the simulation geometry. The spherical geometry has been chosen to take potential advantage of symmetry planes in order to reduce the simulation volume. The lower half sphere ($\forall$ z $<$ 0) represents the substrate, $n_{substrate}$, and the upper half sphere ($\forall$ z $\geq$ 0) the air environment, n_{air}. The x-y plane at z=0 builds the dielectric-air interface. The nanostructures, sketched as yellow rectangles, are situated on top of the substrate. As Fig. 3.8 shows, the object is enclosed by four spheres, denoted as S1, S2,

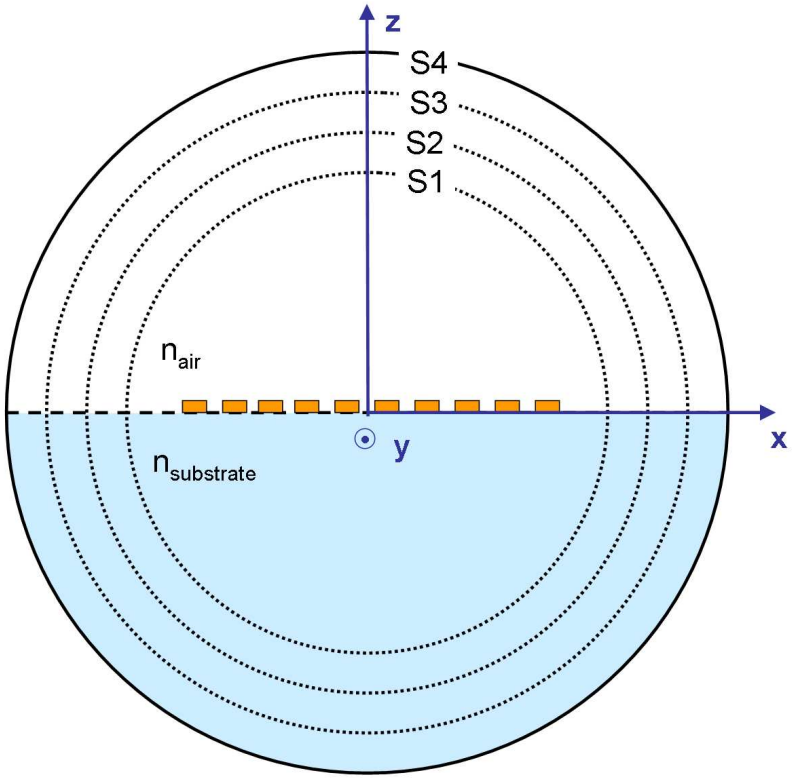

Figure 3.8 – Cross section (x-z plane) of the basic FEM model. The lower half space represents the substrate (light blue, $n_{substrate}$) and the upper half space the air environment (white, n_{air}). The nanostructure is situated on top of the substrate.

S3 and S4 which occupy different functions. The typical radii, R_{Si}, used for these spheres can be described by using the following rule of thumb:

- S1 (sphere surrounding the nanostructure): R_{S1} =(size of structure (in nm))/2 + 400nm
- S2 (auxiliary closed surface for additional postprocessing): $R_{S2} = R_{S1} + 100\text{nm}$
- S3 (air/perfectly matching layers (PML) boundary): $R_{S3} = R_{S2} + 100\text{nm}$
- S4 (exterior PML boundary): $R_{S4} = R_{S3} + 100\text{nm}$

The FEM model uses the 3-dimensional scattered harmonic propagation mode in RF module. The boundary conditions for boundaries perpendicular to the electrical field are defined as perfect electric conductor (PEC), and the boundaries perpendicular to the magnetic field are defined as perfect magnetic conductor (PMC). On the outermost boundary of sphere S4 we define a scattering boundary condition for a plane wave.

The meshing in a FEM simulation is very important, especially in the case of three dimensional simulations which need in general a great computational load. Here, we have to manage the balancing act between a sufficiently fine meshing net and an acceptable computation time to solve the problem. The meshing size is adjusted individually for each subdomain by using the free mesh parameters option. As a rule of thumb, the meshing size should be at least 7 elements per wavelength. The subdomain of the nanostructure has to be meshed very finely, since in this region the interaction with the incident light will be the strongest. A maximal meshing element size of 10 nm is applied which is more than five times smaller than the size of the smallest object.

This model was used to exploit either the scattering in the far-field or the scattering in the near-field for the purpose of comparing them to experimental results. Because in the experiments the scattering spectra have been measured in reflection, and the holograms have been obtained in transmission, both different illumination configurations have to be accounted for in the simulation model. Thus, different definitions of the incident electric field are used which will be further explained in the following.

3.3.1 Scattering in the Far-Field

To simulate the scattering spectrum of a nanostructure in the far-field, we define the incident light in the simulation model as a plane wave which propagates from air to the substrate, i.e. from +z to −z direction, normal to the interface. Its wave vector is denoted as ${k_{inc}}^{Refl}$. The corresponding electric field vector is oriented parallel to the x-axis, i.e. the long axis of the nanostructure. The geometry is sketched in Fig. 3.9 (a). In order to extract the scattering response in the far-field, the far-field variable E_{far} is defined on the boundary of sphere S2. Then, E_{far} is calculated using the in Comsol implemented Stratton-Chu formula by integrating over the upper boundary surface of sphere S1.

The Stratton-Chu formula does a near-field to far-field transformation, so that the modelling volume can be reduced into the near-field zone. This transformation is very

important, especially in the case of 3D simulations where the computational resources can easily reach their limit and where bigger model volumes mean longer computational times. The solution is computed for different wavelengths, λ, typically varied between 500 and 900 nm with a step $\Delta\lambda$ between 5 and 20 nm, depending on the size of the model volume. The far-field intensity is plotted against the wavelength.

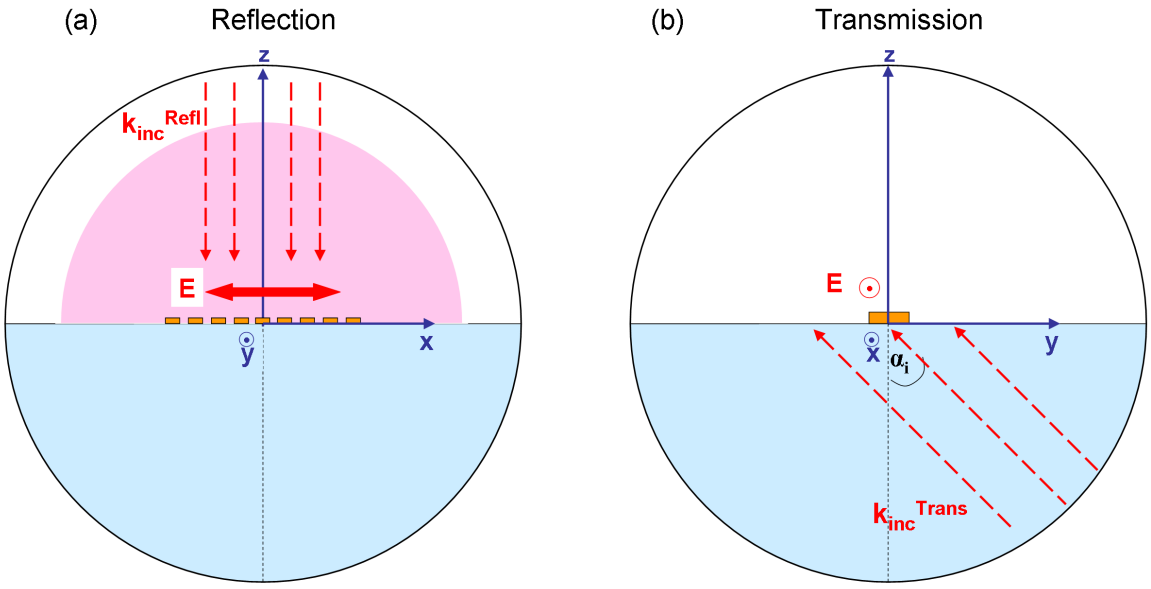

Figure 3.9 – (a) Reflection case: Cross section along the plane at y=0 of the model for the simulation of the scattering spectra in the far-field. The pink half sphere illustrates the surface over which the scattered (reflected) far-field is integrated. (b) Transmission case: Cross section along the plane at x=0 of the model illustrating the total internal reflection configuration. The incident k-vector $k_{inc}{}^{Trans}$ propagates in +z direction, under an incident angle of $\alpha_i = 45°$.

3.3.2 Scattering in the Near-Field

The scattered near-field is simulated in total internal reflection mode. The incident light hits the structure coming from the substrate, i.e. the k-vector of the incident electric field propagates from −z to +z under an angle of 45° between the z-axis and the plane of incidence (total internal reflection). Thereby, the electric field has to be defined in the whole simulation volume. This is done by analytically calculating the corresponding Fresnel coefficients in order to account for the different electric field components of reflection and transmission at the substrate-air interface.

In our experimental setup, different illumination configurations are possible: the electric field vector is oriented either parallel or perpendicular to the plane of incidence which is either the y-z or the x-z plane. Hence, four different configurations are possible of which each configuration requires another electric field description. The corresponding

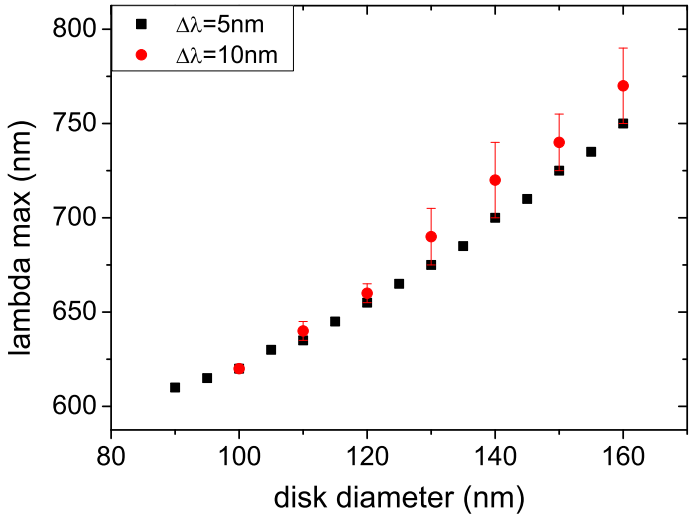

Figure 3.10 – Validation test of the scattering maxima for different wavelength steps $\Delta\lambda$. The graph plots the scattering maxima with changing disk diameter. The squares result from a simulation using $\Delta\lambda = 5$ nm and the circles from $\Delta\lambda = 10$ nm. Note that the error-bars correspond to the 2% deviation of the results (see the text).

analytical expressions describing the field in the total volume are found in Appx. A. The most common illumination configuration we used is the TE wave excitation, i.e. the electric field is perpendicular to the plane of incidence which is the y-z plane. Hence, the light is polarized along the long axis of the nanoobject. After solving the model, the scattered near-field intensity $I = |E^{sc}|^2$ is plotted in the x-y plane, 40 nm above the substrate, i.e. 10 nm above the nanostructure. The incident electric field amplitude $|E_0|$ is equal to 1 V/m, therefore the intensity I can be denoted in general as an intensity enhancement, because we have $I = |E^{sc}|^2/|E_0|^2 = |E^{sc}|^2$.

3.3.3 Tests for Validation

As remarked previously, all simulation models we used have been developed by ourselves. Hence, we had to perform several validation test, in order to validate the correctness of the models and thus the obtained results. These tests regarded several factors, i.e. the meshing size, the convergence of the solution, the correct definition of the exciting field, etc. All these tests had one common denominator: to find the best compromise between the most precise solution and an acceptable calculation time. Simulations of nanostructures, deposited on a substrate surface, are very time-consuming due to their complex geometry and the need of a three-dimensional model. As an example, the computation of the solution of a chain of 20 disks for one exciting wavelength can last up to several hours.

First, we performed several test simulations on basic structures, i.e. a nanosphere or a single nanodisk, by varying the meshing size of the simulation geometry, and compared the different solutions. For a too coarse meshing size, the solution deviates, and for a too fine meshing size, the solution time increases rapidly, and the RAM memory risks to be saturated. Another test consisted of varying the simulation volume, i.e. we varied the radii of the different surrounding spheres of the nanostructure. In particular the radius of the inner sphere $S1$ is of importance since its surface is used to calculate the scattered far-field of the nanostructure. Here, we have to find the compromise between a small simulation volume and a correct solution.

In order to calculate the scattering spectrum of a nanoobject, we simulated the far-field in a given spectral range with an increasing incident wavelengths. In this case, the step $\Delta\lambda$ between two wavelengths is important, because a too large step, i.e. $\Delta\lambda \geq 50$ nm, could result into a deviation of the scattering maximum. In fact, in the case of the calculated scattering spectra of single disks we observed a deviation of 2% of the spectral maxima when changing $\Delta\lambda$ from 5 to 10 nm (see Fig. 3.10). The deviation is expressed by the error bars in Fig. 3.10.

Furthermore, it is important to test if our definitions of the incident exciting field are correct (see Appx. A for details of the different exciting fields used). This is verified by simulating a model without any nanoobject, only the substrate-air interface is considered. By plotting the incident field, we can check if there are any errors in our excitation. For example, we verified that the wave fronts correspond to a plane wave, or if the wave is incident from the optically denser medium, we verified that the refracted wave emerges under a larger angle compared to the incident angle.
Another parameter that can indicate if the model works fine, is the scattered field. For a model that does not include any scattering objects, we expect a very small amplitude of the scattered field components in the order of 1% or less of the chosen excitation amplitude.

3.4 Conclusion

In conclusion, this chapter presented the geometry and the fabrication process of the nanostructures under study. The experimental setup for the measurement of the scattering spectra of single nanoobjects was described. We explained briefly the procedure to extract the spectra from the recorded full field images.

In the second part of this chapter, we described in detail the model we developed to perform simulations of plasmonic nanostructures. We pointed out that the initial field expressions in the simulation depend strongly on the chosen situation to simulate. Briefly, the reflection and the transmission cases were considered, and we described some of the tests we performed to validate the correctness of our models.

Chapter 4

Validation of Experimental Techniques on Elementary Nanoobjects

Table of contents

Das stolze Licht, das nun der Mutter Nacht
Den alten Rang, den Raum ihr streitig macht,
Und doch gelingt's ihm nicht, da es, so viel es strebt,
Verhaftet an den Körpern klebt.

Johann Wolfgang von Goethe, Faust I

The present chapter will discuss in detail the optical properties of elementary nanostructures. Here, these nanostructures are primarily studied in order to validate the experimental and simulation techniques we have developed.

First of all, what do we denote as *elementary nanostructures*? Elementary nanostructures are nanoobjects having a simple, preferably symmetric geometry, for example spherical or elliptical shaped nanoparticles. During the last decade, such elementary nanostructures have been studied to a large extent, both theoretically and experimentally. Because of their simple geometry, their physical properties can be described analytically using classical electrodynamics, and many important features observed experimentally can be understood theoretically.

From the experimental point of view, the widespread use of symmetric shaped particles, like spheres and rods, is mainly motivated by the easy and well-established chemical synthesis methods that allow producing single-crystalline nanoparticles in solution. Additionally, the state of the art electronic lithography and focused ion-beam techniques allow nowadays the fabrication of perfectly shaped metal nanostructures separated by a well defined inter-particle spacing of less than 10 nm. As a result, the optical properties of such basic particles are very well known and the documentation in literature is vast. Hence, an investigation of basic nanostructures enables us to put our results in the context of precedent studies.

Secondly, what do we want to *validate*? By means of validation we mainly refer to the validation of the techniques we used during this work and to the justification of their application for the study of plasmonic nanostructures. Concerning the technique of digital holography, it is well known that it is a powerful tool for various applications. So far, however, its use to detect the scattered far-field of plasmonic nanostructures in amplitude and phase in order to map the three dimensional pattern of scattered light is unique. In order to validate the application of digital holography to plasmonics, it is necessary to study in the first place basic nanoobjects. This study will allow us to fully understand and correctly interpret the 3D maps of the scattered light. Once the cartographies of the scattered field of basic structures are understood, the technique can then be applied to more complex nanosystems.

Another technique that we are interested in validating is the numerical simulation procedure. We used the finite element method (FEM) to simulate the far- and near-field scattering of nanostructures. To our knowledge, up to now, the FEM simulation method is less frequently used to simulate optics in nanosystems (Hoffmann *et al.* 2009; Liu *et al.* 2008; Liu *et al.* 2009; Lassiter *et al.* 2009; Zhang *et al.* 2010), compared e.g. to the finite-difference time-domain (FDTD) method (Nordlander *et al.* 2004; Schuck *et al.* 2005; Crozier *et al.* 2003; Hohenau *et al.* 2006; Huang *et al.* 2010; Girard and Quidant 2004; Schnell *et al.* 2010; Biagioni *et al.* 2009; Mohammadi *et al.* 2008; Yang and Crozier 2008; Liu *et al.* 2009; Smythe *et al.* 2007). The main advantage

that arises from simulations of elementary (here, strongly symmetric) nanoobjects is their lower computational resource consumption, which is notably due to the small model volume, compared to model volumes describing complex structures. The simulation of elementary objects is therefore important because it enables us on the one hand to test the simulation model and, on the other hand, to compare the results with our experimental measurements. Once the model has proved its accuracy in basic cases, the simulations can be extended to more complex structures.

Outline In this chapter we will extensively discuss the scattering properties of single and coupled disks and rods. We will compare measured and simulated scattering spectra of single disks. Furthermore, near-field simulations of single disks and far-field maps of the light scattered by single disks are presented.

Regarding the physics that underlies the coupling behaviour of nanoobjects, we introduce the plasmon hybridization model. In this context, experimental and numerical results of the scattering behaviour of coupled nanodisks and nanorods are presented. We investigate the dependence of the nanoparticle shape, size and inter-particle distance on the resonance wavelength position. Lastly, we will examine the spatial field characteristics of coupled nanodisks and rods. The characteristics of the near-field maps, obtained by simulation, will be discussed. Furthermore, recorded holograms of the light scattered by various coupled nanoobjects are presented, and we analyse their spatial scattering characteristics in the far-field. In this context, we discuss the angular scattering pattern of two coupled disks for different illumination configurations.

4.1 Single Nanodisks

The most basic optical antenna geometries are single and two-particles antennas. The single particle antennas consist of a single nanoparticle e.g. a sphere, a disk or a rod, whereas the two-particles antenna is composed of two identical nanoparticles that are separated by a small gap, e.g. two end-to-end aligned rods or two disks. Single nanoparticles have been successfully applied to enhance the sensitivity of fluorescence and Raman spectroscopy at the single molecular level (Anger *et al.* 2006; Kühn *et al.* 2006; Mohammadi *et al.* 2008). Elongated particles as opposed to spheres also show sensitivity to the polarization of the fields. Typically, the field enhancement and the confinement near the ends of nanorods is much larger than for a sphere, which can be attributed to the combined contribution of both a more favourable spectral location of the fundamental resonance and to the enhancement by lightning-rod effects.

A single disk is the basic structure from which more complex structures like two coupled disks or chains of coupled disks are built. Therefore, their optical properties are examined and discussed in the following.

4.1.1 Light Scattering by a Single Disk

First of all, we will discuss the scattering properties of single disks. Figure 4.1 (a) shows the measured normalized scattered intensity spectra of two single disks with disk diameters of 100 and 150 nm (blue and red spectra, respectively) whereas Fig. 4.1 (b) plots the surface plasmon resonance wavelength λ_{SPR} as a function of the disk diameter. The measured (dots, red) values are compared to the calculated values (squares, black), resulting from FEM simulations. The details of the simulation parameters are presented in detail in Ch. 3.3. The two spectra plotted in red in Fig. 4.1 (a) were obtained for the same single

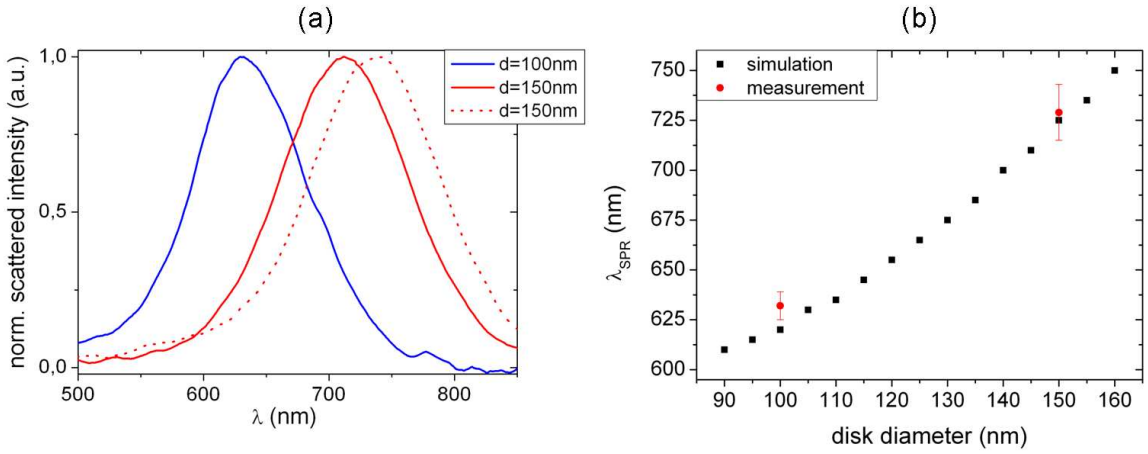

Figure 4.1 – (a) Measured normalized scattered intensity spectra of single disks. The dotted (continuous) spectrum of the large disk corresponds to a measurement with linear polarized light along the x- (y-) axis, along the horizontal plane of the disk. (b) Resonance wavelengths λ_{SPR} obtained by simulation and measurement as a function of disk diameter.

disk using two different linear polarizations, i.e. light polarized along the x-axis (continuous red line) and polarized along the y-axis (dotted line). A shift of $\Delta\lambda_{SPR} = 28$ nm is measured between both polarizations. In theory, supposing linear in-plane polarized light, no polarization dependence should be observed in the scattering spectrum for an ideally shaped disk. Regarding the results of the simulation in Fig. 4.1 (b) and following the quasi linear dependency of the single disk resonance on the disk size, we find that the measured 28 nm large shift in the resonance wavelength can be associated to a deviation in disk size of about $\Delta d = 12$ nm which corresponds to a 8% discrepancy. Assuming that the fabricated disk has not a perfectly round shape, but a realistic geometry, which may resemble a slightly elliptically elongated disk, we recognize that depending on the direction of the polarization, different longitudinal plasmon modes are excited in the particle, thus explaining a shift of the spectrum with changing polarization.

The spectrum of the 150 nm large disk is about 100 nm red-shifted compared to the spectrum of the 100 nm disk. We do not observe sharp peak resonances, but quite broad

resonances for both disks. A linewidth, which is defined as the full width at half maximum (FWHM) of the resonance, of 107 and 120 nm is obtained for the spectrum of the 100 nm and the 150 nm disk, respectively. This broadening of the resonance is due to increasing radiation damping for larger particles.

Comparing the measured and calculated λ_{SPR} values in Fig. 4.1 (b), we measure a resonance wavelength of $\lambda_{SPR,exp} = 632$ nm for a 100 nm disk compared to the simulated value of 620 nm. For the 150 nm disk, we obtain $\lambda_{SPR,exp} = 729$ nm, compared to $\lambda_{SPR,sim} = 725$ nm. We recognize that the agreement between measurement and simulation is excellent.

Furthermore, the linear scaling of the plasmon resonance wavelength with the disk diameter as predicted by theory is confirmed both by experiment and simulation. The slight change in the slope at larger disks towards lower resonance frequencies is explained by the transition from the quasi-static regime to the regime where retardation comes into play.

To sum up, the study of the scattering spectra of single disks have shown an excellent agreement between measured and simulated values. Hence, this consistency proves firstly the good quality of the fabricated nanostructures. The excellent sensitivity of the spectroscopic setup towards the detection of single nanoobjects is confirmed. Secondly, we conclude that the simulation model, although simulating an ideal case with ideal shaped nanodisks, reflects very well the expected behaviour.

4.1.2 Near-Field of Single Disks

Previously, we have seen that the simulated scattering spectra of single disks proved an excellent agreement with the measured values which led us to the conclusion that the developed simulation model describes well the scattering characteristics of an elementary nanostructure - in this case a nanodisk - when solving for the scattered electric field in the far-field range.

Aiming to validate further the simulation model in the range of the near-field, here, we are interested in studying the near-field of a single disk. The geometry is illustrated in Fig. 4.2 (b). The incident light, λ_{exc} propagates in the y-z plane under an angle $\alpha = 45°$ of total internal reflection (TIR). We use s-polarized light, hence the electric field has only a component along the x-axis, $E_{0,x}$. This configuration simulates the illumination used in the holographic setup with a s-polarized wave. We are referring to Ch. 3.3 and Appx. A for further details.

Figure 4.2 (a) shows the scattering spectrum of a single disk derived from simulation. The full circles demonstrate the magnitude of the scattering response of the disk at two different wavelengths, one off resonance and one at resonance, i.e. at $\lambda_{exc} = 720$ nm. It is seen that the scattered intensity off resonance is less than half of the scattered intensity at resonance. In Fig. 4.2 (c,d) the near-field of a single disk is plotted at these two excitation

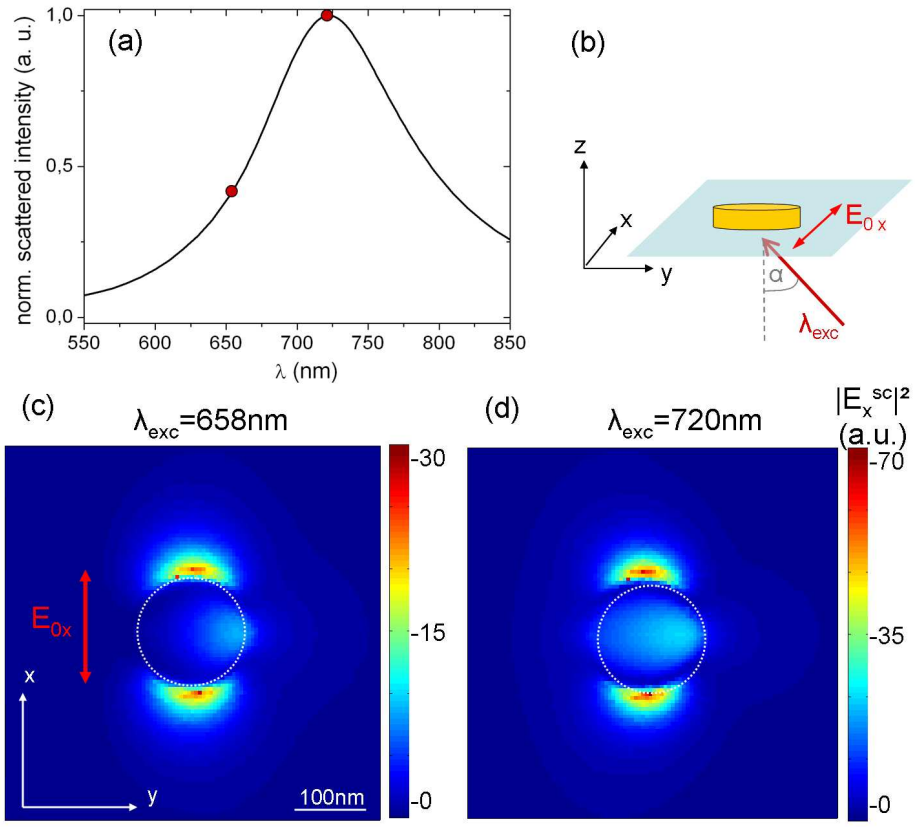

Figure 4.2 – (a) Simulated scattering spectra for a disk of 150 nm diameter. (b) Scheme illustrating the geometry of the simulation: the incident light propagates in the y-z plane under an angle $\alpha = 45°$; the electric field has only a x-component E_{0x}. (c)+(d) Corresponding calculated near-field intensity, $|E_x^{sc}|^2$, plotted 10 nm above the disk surface, for 2 incident wavelengths. The white dotted circle represents the disk position and the red arrow the orientation of the exciting electric field.

wavelengths: $\lambda_{exc} = 658$ nm (c) and $\lambda_{exc} = 720$ nm (d). In order to plot the near-field maps, the square modulus of the x-component of the scattered electric field, $|E_x^{sc}|^2$, is extracted at a plane 10 nm above the disk surface.

Analysing the near-field maps, it is seen that the near-field enhancement is highest close to the disk along the x-direction which is the direction of the external electric field $E_{0,x}$ (indicated by a red arrow). The disk behaves like a dipole. In fact, this behaviour is expected for a metal particle under a linear external field excitation. The external field induces a dipole moment inside the disk in opposite direction to $E_{0,x}$. The induced dipole then interacts with the external field leading to a near-field enhancement at the side of the disk. Note that the distribution of the near-field is slightly asymmetrical due to the asymmetric incident wave vector.

At first sight, the near-field images seem similar, but comparing the amplitudes the near-field enhancement at resonance is about 2.3 times higher than off resonance which is

in agreement to the scattering response in the far-field under the two different excitation wavelengths. Exciting the disk at resonance, it exhibits an enhancement of 70 with respect to the incident field, which is the highest near-field enhancement observed compared to other exciting wavelengths.

In summary, the single disk behaves like a dipole in a linear polarized excitation field. The amplitude of the near-field enhancement depends strongly on the exciting wavelength, and is maximal at resonance.

4.1.3 Holography of Single Disks

This part of the discussion of the scattering properties of elementary particles focusses on the three dimensional scattering maps which we obtained by numerical reconstruction of the recorded holograms.

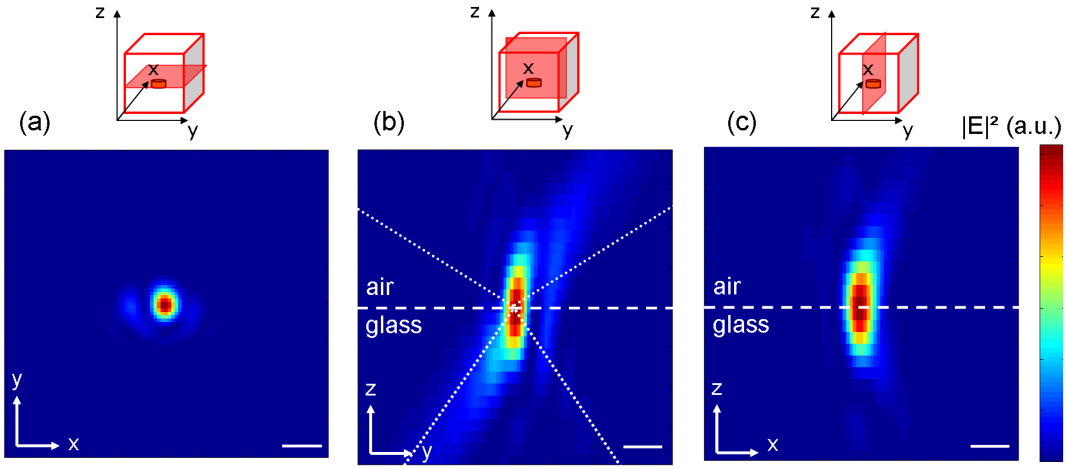

Figure 4.3 – Square modulus of the scattered field reconstructed from a single hologram at $\lambda_{exc} = 785$ nm of a single disk ($d = 150$ nm). Cross sections along different planes centred on the antenna: x-y (a), x-z (b) and y-z planes (c). The length of the scale bar is 1 μm and the color bar is the same for all images. The schemes on the top clarify the position of the disk with respect to the cross sections. The collection cone of the $NA = 0.95$ objective is shown on the glass side and on the air side in (b).

Figure 4.3 presents scattering cross sections along the three main reconstruction planes (x-y, x-z and y-z) of a single disk with 150 nm diameter. The hologram is obtained with s-polarized light at an excitation wavelength of $\lambda_{exc} = 785$ nm. In the x-y plane the scattered far-field of the single disk appears as a bright dot, whereas the planes containing the z-axis possess information on the forward scattered light of the nanodisk into air. The plane of incidence is the y-z plane, as Fig. 4.3 (b) reveals by the slight asymmetry of the scattered light. The nanodisk is hit by the incident beam under the TIR angle of 45°, in the y-z plane. The collection cone of the NA= 0.95 microscope forms a half-angle of 71.8°

in air and 39.2° in glass (illustrated as dotted lines in Fig. 4.3 (b)). Note that large NA immersion optics cannot be used, as they would forbid the use of TIR, which is necessary for dark-field operation. However, as can be seen from the bottom image in Fig. 4.3 (b), this cone is larger than the apparent angle of the scattered light, and we can safely assume that most of this light is collected by the large-NA objective.

Cross sections along the z-axis should be interpreted with care for negative z values: the holographic system only collects forward scattered light, and the intensity shown in the glass substrate (below the dotted line in Fig. 4.3) only corresponds to the back propagation of this light and does not carry other physical information.

Analysing the forward scattered light of the nanodisk we recognize a scattering along the z-axis in air with a spatial extension of about 1 μm. This extension is estimated using as a delimiter the $1/e$ decay of intensity. Assuming that the disk behaves like a dipole oriented in the x-y plane, as the near-field images revealed, this scattering behaviour is interpreted as a dipole-like scattering. For comparison, the emission diagram of a RF dipole antenna in free space is a slightly flattened torus perpendicular to the antenna axis.

Angular Scattering Pattern of a Single Disk In order to get further insight into the scattering characteristics of a single disk we are interested into analysing its angular scattering pattern. The emission pattern of an object can be recorded by collecting the emitted photons with an objective lens and by imaging the intensity distribution in the objective's back focal plane. These images, that display the Fourier plane, contain the angular distribution of the emitted light (Lieb *et al.* 2004). The intensity and the coordinates of the Fourier space are related to the angular radiation pattern (Curto *et al.* 2010):

$$I(\theta, \varphi) = I(k_x, k_y) \cos\theta \tag{4.1}$$

with $k_x = KR \sin\theta \cos\varphi$ and $k_y = KR \sin\theta \sin\varphi$ where θ is the polar angle and φ the azimuthal angle. The cosine factor in Eq. 4.1 is an apodization factor, K is a calibration constant and R the radius in pixels of a given point in the Fourier space image. The scheme shown in Fig. 4.4 (a) clarifies the signification of the angles. A dipole placed on a surface has the dipole moment p, and its orientation is described by the angles Θ and Φ in the real space. The dipole scatters light which is collected by an objective under a limiting angle θ_{NA}. In the Fourier plane, a circular angular scattering pattern is observed whose coordinates are directly linked to θ and φ, see Eq. 4.1. Lieb *et al.* have studied single molecules near a planar surface by calculating and imaging their emission patterns giving direct access to the three-dimensional dipole orientations of the molecules. The authors showed that an angular distribution exhibiting two lobes is characteristic for a dipole oriented parallel to a dielectric interface.

In digital holography, which records the amplitude and phase information of an object,

the Fourier plane can be attained via Fourier transformation, and thus, the angular intensity information can be accessed. However, it is remembered that in our setup only forward scattered light is collected, hence, the Fourier space contains only information on the angular scattering pattern in air.

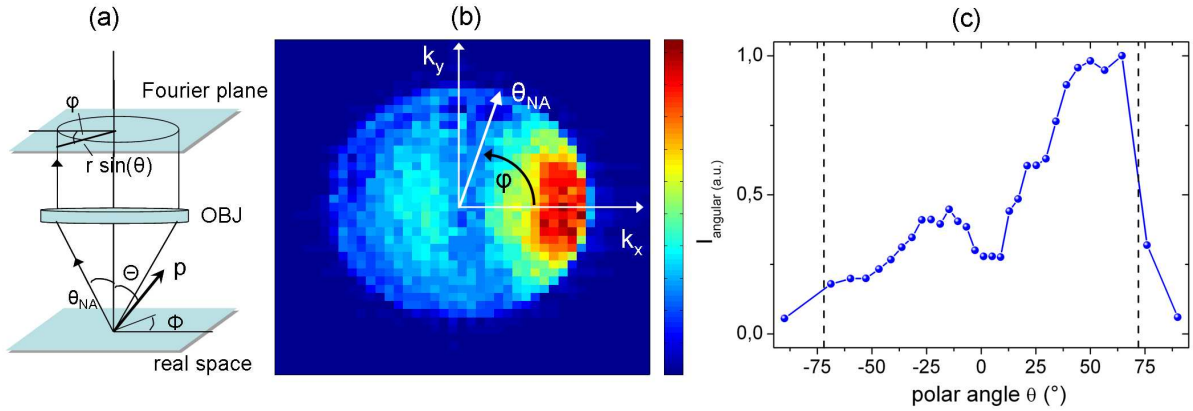

Figure 4.4 – (a) Scheme illustrating the orientation angles for the dipole p. (b) Fourier plane of the single disk hologram showing the radiation pattern. The numerical aperture angle (θ_{NA}) is indicated. (b) Angular distribution of the scattering as a function of the polar angle θ for the single disk. The vertical dashed lines indicate the maximum collection angle of the objective.

Figure 4.4 (b) displays the calculated Fourier plane of the recorded single disk hologram, i.e. its angular scattering pattern. The numerical aperture angle θ_{NA} corresponds to the maximum collection angle of the objective, thus, limiting the recorded angular scattering at an angle of 71.8°. We observe one distinctive lobe. The graph in Fig. 4.4 (c) plots the normalized angular scattering intensity as a function of the polar angle for the single disk. The vertical dashed lines indicate the maximum collection angle of the objective. Due to the pixelation of the Fourier plane we achieve an angular resolution of 5°. It is seen that the scattering is mainly distributed asymmetrically at an angle of around 55°. The angular distribution of the intensity scattered by a single gold nanoparticle have been measured and calculated previously (Huang *et al.* 2008). Similar images have been obtained, though displaying two lobes instead of one. This one lobe feature may be due to the asymmetric TIR illumination resulting into an asymmetric scattering of the single disk. However, the one lobe observed in the Fourier plane image confirms that the single disk behaves like a horizontal dipole on a glass interface.

4.1.4 Conclusion on the Scattering Behaviour of Single Disks

We measured the scattering far-field response of two types of single disks: nanodisks having a diameter of 100 nm and 150 nm. The resonance wavelength of the latter is about 100 nm red-shifted compared to the former one. The simulation of the scattering

spectra proved an excellent agreement with the measured values with an accuracy of about 1%. Hence this agreement confirms at the same time the excellent sensitivity of the spectroscopic setup in view of the detection of scattered light by nanoobjects, and further validates our developed FEM model with regard to simulations of basic plasmonic nanostructures on a substrate-air interface.

Near-field simulations revealed a dipole-like behaviour of a single disk under a linear polarized field excitation. The near-field enhancement is maximal at resonance. Furthermore, we presented the first hologram of a single disk showing the far-field map of the scattered light. Cross sections along the three main axes revealed an elongated shape perpendicular to the disk surface which is interpreted as a dipole-like scattering. This assumption was confirmed by an analysis of the Fourier space of a single disk which represents the angular scattering intensity pattern. The scattering is characterized by one lobe, at a 55° polar angle confirming the scattering behaviour of a horizontal dipole on an interface.

Overall, we have shown that the technique of holography is capable to image three dimensional far-field maps of the scattered light by nanostructures.

4.2 Coupling of Two Nanodisks

The coupling of two nanoparticles plays an important role in the context of plasmonics because of the increased near-field enhancement and confinement that occurs in the gap. Two factors are related to the enhancement: the interaction of localized plasmons and the interference of the electromagnetic fields generated by these plasmons. The coupling enables a further degree of freedom by the possibility to tune the resonance frequency.

In order to get a deeper understanding in the physics of the coupling phenomena of those so called plasmonic dimers, and in particular, to comprehend the dependence on the inter-particle separation, the plasmon hybridization model was introduced by Nordlander and co-workers (Prodan *et al.* 2003; Nordlander *et al.* 2004). In general, for ensembles of plasmonic particles one may state that whenever modes are spectrally and spatially overlapping, their coupling generates new resonances with an energy splitting, analogous to atomic orbital hybridization.

The type of coupled nanoparticles which we will present in the following, is composed of two disks or disk shaped particles. Two coupled disks have been studied extensively in the past by several groups, in most cases by measuring or calculating the scattering, transmission or extinction spectra of either single or arrays of nanostructures (Rechberger *et al.* 2003; Su *et al.* 2003; Nordlander *et al.* 2004; Atay *et al.* 2004; Romero *et al.* 2006; Jain *et al.* 2007; Olk *et al.* 2008; Huang *et al.* 2008; Yang *et al.* 2010). The most important results on two coupled nanoparticles, of theoretical and experimental nature, will be presented in the following.

4.2.1 Introduction to the Study of Two Coupled Disks

Dipolar-Coupling Model Rechberger *et al.* were one of the first to investigate arrays of gold nanodisk pairs fabricated by electron lithography using optical transmission spectroscopy (Rechberger *et al.* 2003). They found that with decreasing inter-particle distance the surface plasmon resonance shifts to longer wavelengths for a polarization direction parallel to the long particle pair axis whereas they observed a blue-shift for the orthogonal polarization. They explained these experimental findings by a simple dipolar interaction mechanism.

Simultaneously, Su *et al.* investigated the coupling between individual pairs of elliptical gold particles by discrete dipole approximation (DDA) simulation and optical scattering spectroscopy (Su *et al.* 2003). Their results are conform with the findings from the Rechberger group. They demonstrated that the resonant wavelength peak of two interacting particles is red-shifted from that of a single particle which they attributed to near-field coupling. They showed that the shift decays approximately exponentially with increasing particle spacing and becomes negligible when the gap between the two particles exceeds about 2.5 times the particle short-axis length. Furthermore, they found that the exponential decay is size independent when the peak shift and particle gap are scaled respectively by the resonant-peak wavelength and the short axis length of the individual particles. The decay constant, however, is found to be particle-shape-dependent.

The Regime of Touching Nanoparticles The group around Atay studied the optical transmission of periodic arrays of nanodisks (Atay *et al.* 2004). By varying the inter-particle separation from strongly coupled disks to touching, overlapping particles, they observed an abrupt, large renormalization and a splitting of the plasmon-polariton energy. These spectral anomalies are ascribed to a transition whereupon the inter-particle dipole-dipole interaction is shunted and the plasmon polaritons exhibit multipolar behavior, including a very high local concentration of electromagnetic energy in the vicinity of their conductive contact.

Romero *et al.* analysed theoretically the nearly touching regime of two metallic nanospheres and explained how long-wavelength resonances occur both for approaching particles and after particle overlap (Romero *et al.* 2006). Both of these regimes are characterized by a large pileup of induced charge at the gap or overlap region. However, the charge at the gap and the lowest-frequency modes are distinctly different for these two regimes and are not connected via the transition through the limit where the spheres are just touching. Furthermore, they found that dimers with small overlap regions produce larger enhancement than non-touching particles in close vicinity.

The Plasmon Ruler Equation Jain *et al.* investigated lithographically fabricated arrays of gold nanodisk pairs by absorption spectroscopy and electrodynamic simulations,

using the DDA (discrete dipole approximation) method (Jain *et al.* 2007). In agreement with previous works, they found that the plasmon wavelength decays exponentially with increasing inter-particle gap. In addition, they obtained an universal scaling behaviour of the inter-particle plasmon coupling, i.e. a decay constant that was about 0.2 in units of the particle size for different nanoparticle size, shape, metal type, or medium dielectric constant. They attributed this universal scaling behaviour to the interplay of two factors: the direct dependence of the single particle polarizability on the cubic power of the particle dimension and the decay of the plasmonic near-field as the cubic power of the inverse distance. Hence, the authors derived a "plasmon ruler equation".

The Far-Field of Two Coupled Nanoparticles Olk *et al.* studied the far- and near-field interactions of two spherical nanoparticles by attaching one to a scanning fiber probe and the second to a scanning substrate (Olk *et al.* 2008). Using this configuration the spectral properties were examined with regard to the inter-particle distance and the polarization of the excitation light. They found a periodic modulation of the coupled plasmon resonance for separations smaller than 1.5 μm.

Coupled Nanodisks as a Nanoantenna It is known that metal nanoparticles can be viewed as a nanoantenna in the optical regime due to their capability to localize and redirect electromagnetic fields. In this context, Huang *et al.* investigated coupled gold nanoparticles, seen as an antenna (Huang *et al.* 2008). They developed experimental techniques to measure various parameters defining the characteristics of an antenna, i.e. the resonant frequencies, the gain and the detuning factors. They also recorded radiation patterns and found a radiation pattern of coupled nanoparticles being essentially dipolar in nature.

Excitation of Bright and Dark Modes The hybridization model introduced by Nordlander *et al.* results in a mode splitting between the bonding and anti-bonding modes, also referred as "bright" and "dark" modes. The anti-bonding modes are not always observed in white-light scattering experiments since their excitation is symmetry-forbidden for normally incident plane waves. However, the dark mode can be excited if the symmetry of the system is broken either by the shape of the structure (Hao *et al.* 2008) or by the excitation geometry (Liu *et al.* 2009). Another mechanism for exciting non-dipole active multipolar plasmons is the retardation effect (Kottmann and Martin 2001). For nanoparticles of a size comparable to a quarter of the wavelength of the incident light, the electric field can no longer be assumed uniform across the nanoparticle. For such a system the higher multipolar components of the incident wave can directly couple to the corresponding multipolar plasmon modes (Kelly *et al.* 2003).

To study bright and dark modes, Yang *et al.* used in a total internal reflection geometry TM polarized light either polarized parallel or perpendicular to the dimer axis to excite

and observe transverse modes in two coupled nanocrystal having a size of 150 nm and separated by a distance of 65 nm (Yang *et al.* 2010) . According to the authors these geometries are in the right spatial range to allow anti-phase coupling.

In this context, we would like to mention the recent theoretical study of Devilez *et al.* on a nanoantenna consisting of three aligned nanospheres. The authors demonstrated that anti-symmetric modes can be excited by a propagating plane wave under an incident angle of 45° (Devilez *et al.* 2010b). Furthermore, they showed that in a narrow frequency range, symmetric and anti-symmetric mode balancing induces a strong enhancement of the near-field intensity in one gap while the other gap is "turned off".

Outline We have seen that there are various studies investigating the optical properties of coupled disk-shaped nanoobjects. The dependence of the resonance shift on the inter-particle gap has been successfully explained by means of a dipolar-coupling model. It has been demonstrated that a nanoparticle pair can be seen as a nanoantenna exhibiting a dipolar radiation pattern. Furthermore, it has been shown recently that in a total internal reflection configuration the excitation of dark modes is possible.

In this context, we will present only the major results that we obtained. Firstly, we will briefly introduce the plasmon hybridization model which explains the energy shift that occurs when two nanoparticles are strongly coupled. We discuss measurements and calculations of the scattering spectra of two coupled disks which results into a blue-shift of the resonance wavelength with increasing inter-particle distance which is in agreement with previous works and explained by the dipolar-coupling model. Then, we discuss far-field scattering maps obtained by holography on two coupled nanodisks and our preliminary attempts to study the bright and dark modes excited in a nanodisk pair.

4.2.2 Plasmon Hybridization Model

In the plasmon hybridization model the plasmon mode of a nanoparticle dimer can be understood in terms of hybridization of the individual nanoparticle plasmon modes due to the coupling over the small inter-particle distance. Such coupling causes a mode splitting into a lower-energy bonding mode and a higher-energy anti-bonding mode (Nordlander *et al.* 2004). This energy splitting is depicted in Fig. 4.5. The bonding resonance modes are caused by an in-phase dipole coupling. Due to its dipolar character, this oscillation mode interacts strongly with incident, plane wave radiation. For that reason, these modes are also named *bright* modes. The anti-bonding modes have an anti-phase dipole coupling. As a consequence, the anti-bonding mode does not efficiently emit into the far-field since both individual dipoles oscillate out of phase and therefore cancel each other out in far-field. Thus, they are also called *dark* modes. Due to reduced radiation damping, dark

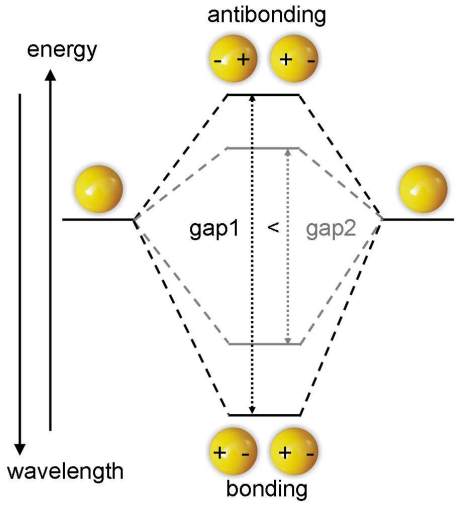

Figure 4.5 – Schematic picture illustrating the plasmon hybridization model. Here the dimer is represented by two spheres, but they can be replaced by any other form of nanoparticle (rods or disks). Gap1 is smaller than gap2 which causes a smaller energy splitting (grey lines).

modes are expected to have a higher quality factor [1] (Huang *et al.* 2010). It is found that for large inter-particle distances, the energy shifts of the dipolar dimer plasmons essentially follow the interaction energy between two classical dipoles, i.e. $1/D^3$. With decreasing distance, the shifts of the dipolar plasmons become much stronger, due to the interaction and mixing with higher multipole oscillations (Nordlander *et al.* 2004). Thus, a significant energy splitting between the bonding and anti-bonding modes is only achieved with small inter-particle gaps.

4.2.3 Scattering Spectra of Two Coupled Disks

On our sample, two different disk diameters (100 and 150 nm) and various gap widths were available which permitted us to examine both the influence of the disk size and the inter-particle distance on the resonance wavelength.

Resonance as Function of Disk Diameter First, we studied the scattering spectra of two coupled disks as a function of the disk diameter. The simulations we performed reveal a linear dependency, plotted in Fig. 4.6. With a fixed inter-particle gap, the resonance energy of the structure shifts with increasing disk diameter energetically to lower values.

This common feature has been also observed studying nanoantennas composed of two rod shaped nanoobjects (Muskens *et al.* 2007; Wissert *et al.* 2009). It can be interpreted

[1] The quality factor Q can be approximately calculated as: $Q \simeq \frac{\lambda_{res}}{\Delta\lambda_O}$ where $\Delta\lambda_O$ is the linewidth of the resonance at λ_{res}. The higher the quality factor, the longer the energy can be stored inside the resonator.

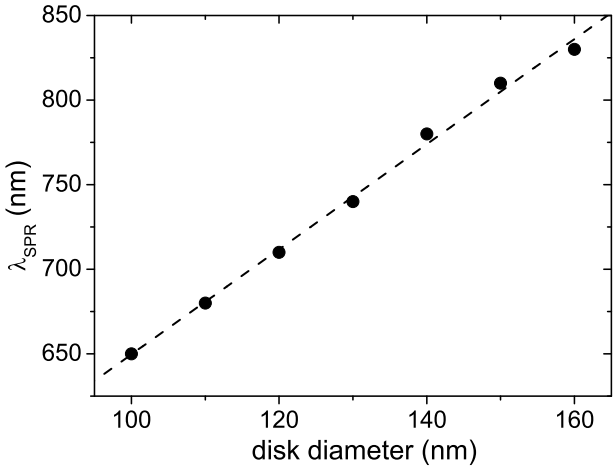

Figure 4.6 – Simulated plasmon resonance wavelengths of two nanodisks, separated by a 30 nm gap, as a function of the disk diameter.

as an increase of the charge separation localized at the ends of the antenna arms (here, the disks form the antenna arms) due to the interaction with the external driving electromagnetic field. This results therefore, in a reduced internal Coulomb field parallel to the long axis of the nanoantenna (note that the internal electromagnetic field is anti-parallel to the driving external electromagnetic field). Thus the restoring force of the free electrons in the metallic antenna arm reduces with increasing arm length, which in consequence results in a spectral red-shift of the scattering peak resonance.

Resonance as a Function of Inter-Disk Gap In a next step, we simulated the scattering resonance of two coupled disks as a function of the gap size. The results are plotted in Fig. 4.7 together with the results from measurements. The dependency of the resonance on the gap size that we found both by calculations and measurements reflects qualitatively very well the results that were obtained by calculations using the plasmon hybridization method (Nordlander *et al.* 2004).

With increasing gap, the plasmon resonance of the coupled disks approaches the single disk resonance. Overall, we observe an exponential decrease with increasing gap width.

The calculated values reveal that two coupled disks of 100 nm disk size reach the single disk resonance at a gap of 50 nm, whereas two coupled disks composed of 150 nm disks still exhibit a small red-shift at a 75 nm disk separation which is equal to a weak coupling between the disks. This effect is explained by the gap-diameter ratio which has to be taken into account (and not only the gap size): Larger disks can be coupled over larger distances than smaller ones. As a rule of thumb, it can be assumed that the limit of the coupling regime is reached when the diameter-gap ratio reaches a value of 2. In both

cases (diameter of 100 and 150 nm), the decoupling distances ($d_{decoupl}$ = 50 and 75 nm, respectively) correspond to this value.

Comparing simulations and measurements, several comments are made: Qualitatively, the resonance wavelength's behaviour follows a similar dependency as observed by calculations. In particular, the accordance between both curves of the 150 nm disk dimers is very good. The decrease of the wavelength with increasing gap is very well reproduced. However, it must be noted that we have a large discrepancy between simulated and measured λ_{SPR} values of both types of coupled disks at a gap of 10 nm.

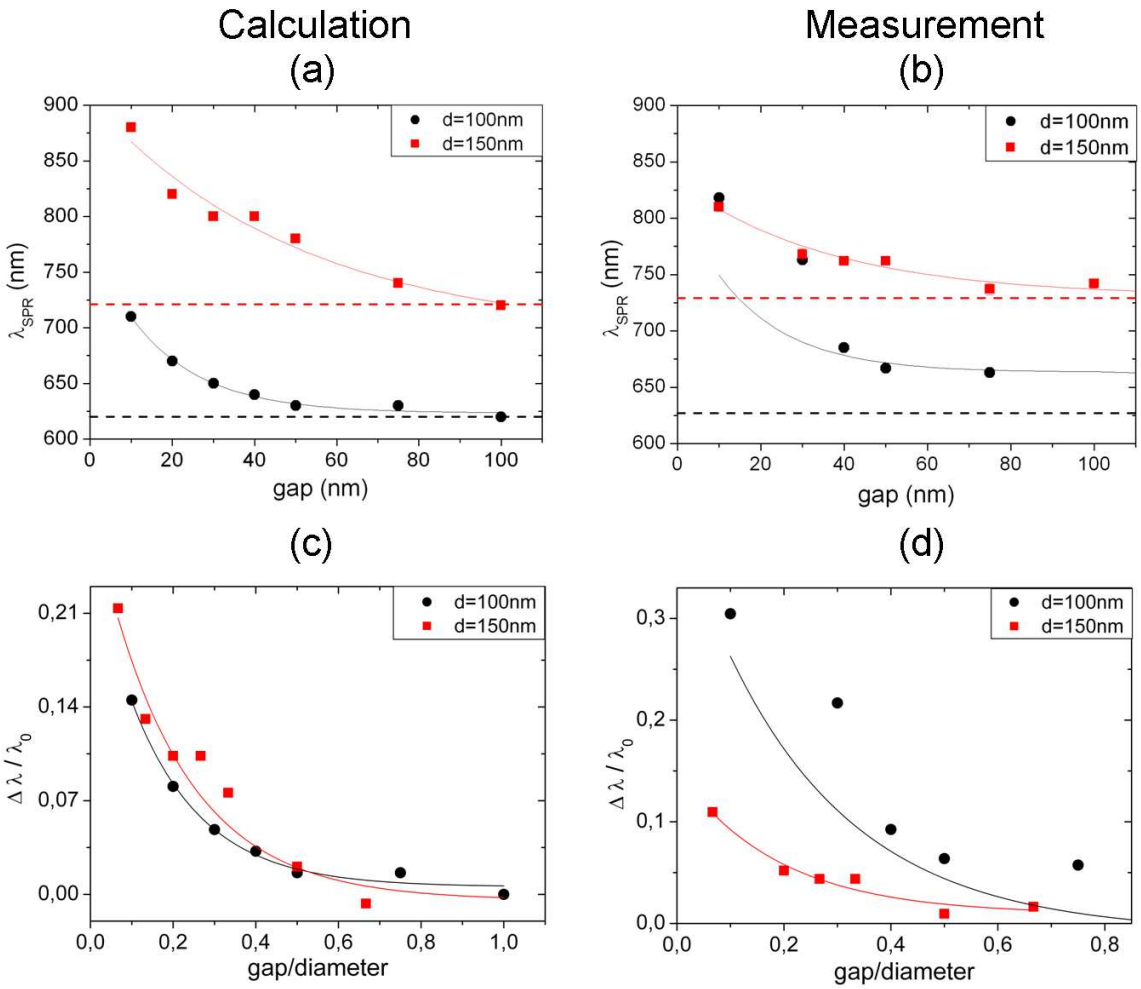

Figure 4.7 – Computed (a,c) and measured (b,d) plasmon resonance wavelengths / fractional plasmon shift of disk dimers as a function of the gap/ gap-diameter ratio. The circles and the squares correspond to dimers of 100 nm and 150 nm diameter, respectively. The dashed lines correspond to the calculated and measured single disk resonances, respectively. The continuous lines are exponential decay fits of type $y(x) = a \cdot exp\,(-x/\tau) + y_0$.

Examining the curve obtained for two small (d = 100 nm) coupled disks, the measured resonance of the structure with the smallest spacing is quite red-shifted with respect to the

calculated value. This effect may be explained by assuming that not all nanostructures with an expected inter-particle spacing of 10 nm are fully separated, but composed rather of two touching or overlapping nanodisks. In fact, it is not straightforward to obtain by electronic lithography gap distances of less than 10 nm. In addition, SEM observations revealed in some cases touching objects instead of 10 nm sized separations. The resonance of touching particles behaves differently, as analysed experimentally and theoretically by Atay *et al.* and Romero *et al.* (Atay *et al.* 2004; Romero *et al.* 2006). Touching particles are at the instance of "point contact" and this geometry can favour the quadrupole mode which is characterized by a higher energy (blue-shift of the plasmon resonance). In the case of overlapping particles, the two disks merge into a single ellipsoidal particle, and the dipole mode of a single particle establishes, which is characterized by a red-shift.

We can have strong assumptions that the measured resonance wavelength in the case of two 10 nm spaced 100 nm sized disks is actually the resonance of two overlapping disks. In the case of 150 nm disks, the associated resonance would be located in the infrared, i.e. beyond our spectral sensitivity because the spectrometer does not fully resolve any scattering spectrum that has a peak at a wavelength longer than 800 nm. As a result we measure a resonance at 810 nm, instead of the expected value of 880 nm derived from simulation.

The Decay Constant Both simulations and measurements confirmed an exponential decay of the resonance wavelength with increasing gap width. Therefore, on the basis of the scaling behaviour found by Jain *et al.*, we performed a quantitative analyse of the decay constant. For this we analysed the "fractional" plasmon shift $\Delta\lambda/\lambda_0$ versus the gap-diameter ratio where $\Delta\lambda$ is the plasmon shift of the coupled particle system with respect to the single particle resonance λ_0. In the case of simulation, for both disk types, we can apply an exponential fit of the type $y(x) = a \cdot exp\,(-x/\tau) + y_0$ with a decay constant τ. The parameter y_0 is expected to be zero, since $\Delta\lambda$ approaches zero for large gaps.

	literature	simulation		experiment	
	d=88 nm	d=100 nm	d=150 nm	d=100 nm	d=150 nm
τ	~ 0.20	0.17 ± 0.02	0.20 ± 0.03	0.25 ± 0.06	0.19 ± 0.06
a	~ 0.10	0.25 ± 0.02	0.29 ± 0.02	0.41 ± 0.05	0.14 ± 0.02
y_0	0.00	0.01 ± 0.00	0.00 ± 0.00	-0.01 ± 0.02	0.00 ± 0.01

Table 4.1 – Exponential fit values τ, a and y_0 derived from simulation and experiment. For comparison we gave the values from a study on two coupled disks taken from literature (Jain *et al.* 2007) on the left column.

The values τ, a and y_0 derived from the exponential fits are given in Tab. 4.1. Note that these values are without unit. The authors Jain *et al.* studied a similar system, i.e.

coupled gold nanodisks with a diameter of 88 nm and a thickness of 25 nm, deposited on a glass substrate (Jain *et al.* 2007), and found experimentally the values given on the left column. Comparing with our obtained values, we conclude that our simulations are in very good agreement with the previous study.

The observed exponential decay can be qualitatively explained by the dipolar-coupling model. This model describes the interplay of two factors: the dependence of the single-particle polarizability on the cubic power of the particle dimension and the decay of the particle plasmon near-field as the cubic power of the inverse distance (Jain *et al.* 2007).

We conclude that our measurements are in good agreement with simulations. Our results are entirely explained in the frame of the dipolar coupling model. Furthermore, we state an excellent agreement with previous studies on similar nanoobjects.

4.2.4 Study of Different Modes Excited in Two Coupled Disks

The recent studies of Yang *et al.* and Devilez *et al.* have shown that the excitation of anti-symmetric modes in two coupled nanocrystals or in three aligned nanospheres is possible using a total internal reflection geometry due to the broken symmetry of the system (Yang *et al.* 2010; Devilez *et al.* 2010b). In the case of the coupled nanocrystals, the use of an incident TM polarized [2] light wave either perpendicular or parallel to the dimer axis allowed the observation of both in-phase and anti-phase transverse modes. The dark mode resulted into a dumbbell scattering pattern, while the bright mode showed a spheroid pattern centred at the dimer junction.

The dark-plasmon modes do not couple to incident far-field radiation, however, it can couple to a localized dipole, and has to be included when considering emission modification. Hence, one would expect a change in the far-field scattering characteristic when exciting a dark mode compared to the scattering characteristics of a bright mode.

Inspired by this, we were interested to investigate the far-field scattering pattern of two coupled nanodisks under different illumination and polarization configurations. This experimental study awaits a full confirmation by the analytical calculations from the team of Nicolas Bonod at the Institut Fresnel.

Far-Field Scattering Maps of Two Coupled Disks Figure 4.8 presents cross sections of far-field scattering images obtained by holography on two coupled disks. We differentiate between 4 different illumination configurations:

(a) dimer axis $\perp$ to the plane of incidence, s-polarization (Fig. 4.8 (a))

(b) dimer axis $\parallel$ to the plane of incidence, p-polarization (Fig. 4.8 (b))

[2] In a TE (transverse-electric) wave, the electric field component is perpendicular to the plane of incidence, also denoted as *s-polarization*, and in a TM (transverse-magnetic) wave, the electric field component is parallel to the plane of incidence, also denoted as *p-polarization*.

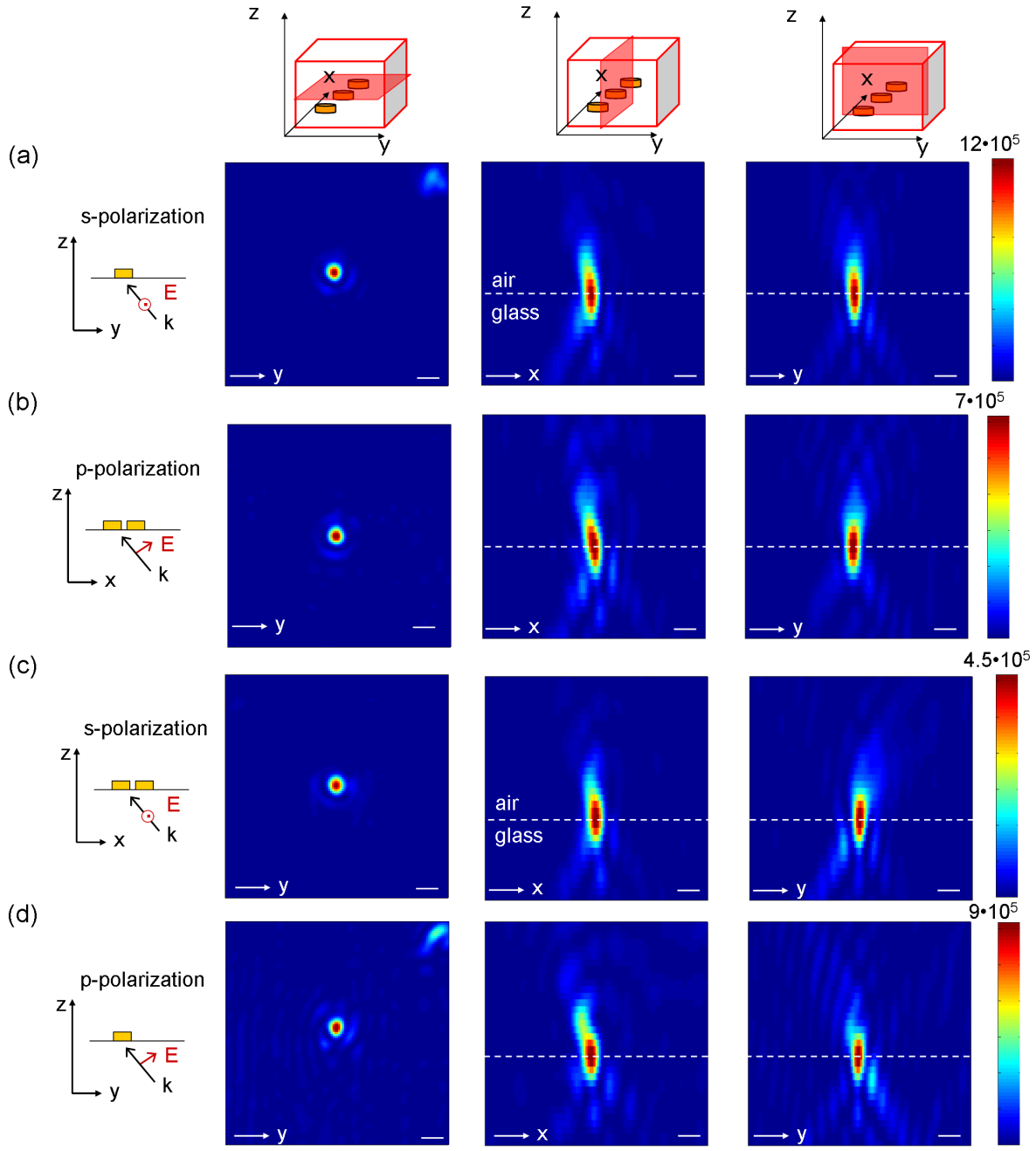

Figure 4.8 – Far-field scattering images of longitudinal (a,b) and transverse (c,d) modes excited in two coupled nanodisks ($d = 150$ nm, gap$= 40$ nm): Cross sections along the three main planes (from left to right: x-y, x-z and y-z plane) of a hologram recorded at $\lambda_{exc} = 785$ nm at 4 different illumination configurations (see schemes on the left): (a) s-polarized excitation with the wave vector perpendicular to the dimer axis, (b) p-polarized excitation with the wave vector parallel to the dimer axis, (c) s-polarized excitation with the wave vector parallel to the dimer axis, and (d) p-polarized excitation with the wave vector perpendicular to the dimer axis. The length of the scale bar is 1μm.

(c) dimer axis ∥ to the plane of incidence, s-polarization (Fig. 4.8 (c))

(d) dimer axis ⊥ to the plane of incidence, p-polarization (Fig. 4.8 (d))

It is clear that in the case of s-polarized light in total internal reflection configuration, the excitation electric field has only one component, i.e. the component E_x for case (a) and E_y for case (c). For an illumination beam polarized parallel to the principal axis, the two disks interact by means of near-field coupling, the in-phase longitudinal mode is excited. The near-field coupling manifests in a strong field enhancement in the gap. For an illumination polarized perpendicular to the principle axis, the near-field coupling of the two particles is weak, as the surface-adjacent regions of high near-fields are pointing away from the neighbouring disks. The transverse mode is excited. Alas, the orientation of the induced dipoles facilitates far-field interaction of the disks, as the two disks are located in the dipolar emission field of its neighbouring particle. Olk *et al.* showed that this far-field coupling leads to a periodic modulation of the spectral properties (Olk *et al.* 2008). The authors assigned this spatial periodicity to the phase relation between different components of the detected light: the interference of light directly scattered by a selected nanoparticle, and light that was scattered by the other particle and then re-scattered by the first one.

Analysing the scattering characteristics in the three reconstruction planes, in the case of s-polarized excitation light (see Fig. 4.8 (a)) it is seen that in both images containing the z-plane, the scattered light is distributed along the z-axis into air. We have a dipolar like scattering behaviour which results from the induced in-phase longitudinal mode that couples to the far-field. Regarding the case (b), which is plotted in Fig. 4.8 (b), it is seen that the electric field has two components, one along the x-axis and one along the z-axis. Since the height of the disk is very small (30 nm) compared to the disk size, the component E_z can be neglected compared to E_x. The resulting far-field scattering images have the same characteristics as the top images, and we assume that we have a dipolar like scattering, as well, and the excitation of a (weaker) longitudinal mode.

Analysing the images corresponding to the case of a s-polarized wave with a wave vector parallel to the principal axis (see Fig. 4.8 (c)), we observe that the scattering cross sections resemble the scattering images that we obtained with the longitudinal modes. Hence, we can conclude that the far-field scattering pattern of the transverse mode in two coupled disks does not differ from that of a longitudinal mode.

Using an illumination configuration corresponding to case (d), with p-polarized light incident perpendicular to the principle axis, we observe a notable change in the far-field scattering pattern: In the x-z plane additional to the scattering along the z-axis we observe a slightly inclined branch of scattered light, and in the y-z plane it is seen that the elongation of the scattering along the z-axis is smaller. Analysing the exciting electric field, we have in case (d) two electric field components, E_y and E_z, where the

latter component can be neglected. Hence, we can speculate that this configuration leads to the excitation of a transverse mode in the two disks structure.

The question that arises is if one of those configurations can lead to an anti-phase, a dark mode. However, the analysis of the far-field scattering images is not straightforward, and the question can not be answered directly.

Near-Field of Two Coupled Disks In order to get a further understanding of the scattering behaviour of two coupled disks under different excitations, simulations of the scattered near-field have been performed. The resulting near-field images are plotted in Fig. 4.9. First, the near-field image (a) confirms the excitation of the in-phase longitudinal mode. We achieve a near-field enhancement of 140 and a strong field confinement in the gap.

However, the analysis of the other images is not so easy. Image (c) reveals the excitation of a transverse mode, no field confinement in the gap is observed. However, the near-field enhancement close to the disks along the y-axis is slightly asymmetric. This feature may be an indication of the excitation of an asymmetric transverse mode (see sketch in Fig. 4.9 (c)).

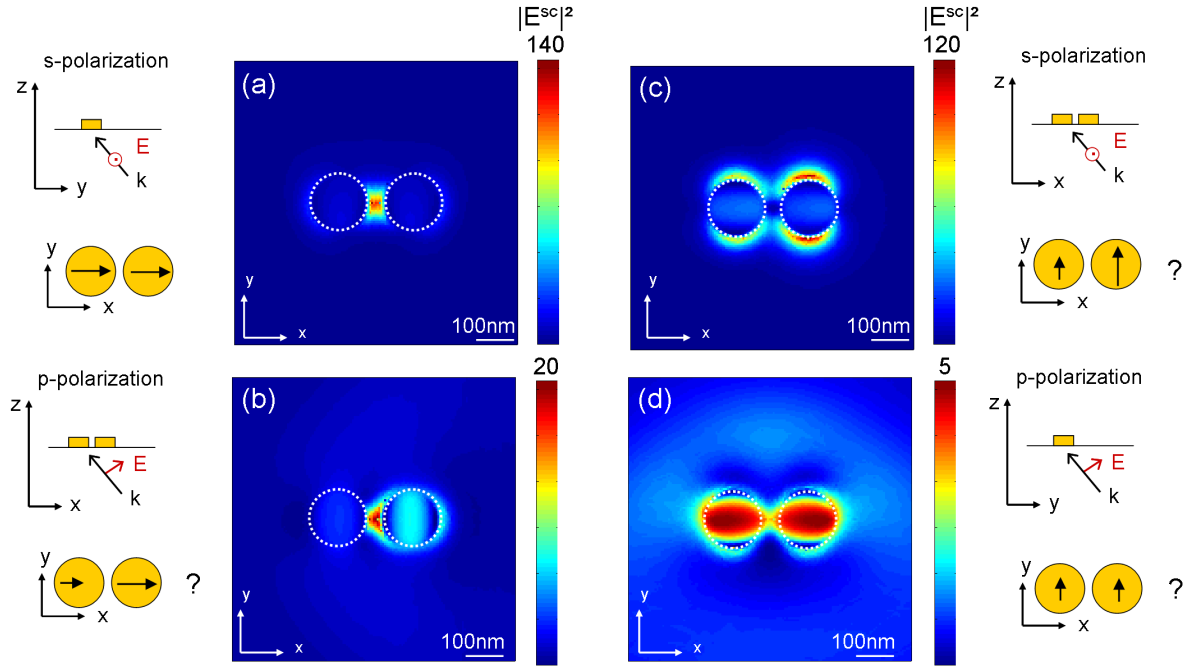

Figure 4.9 – Simulation of the near-field intensity $|E^{sc}|^2$ of two coupled disks ($d = 150$ nm, gap$=$ 40 nm). The near-field in the x-y plane is plotted 10 nm above the surface of the disks for 4 different illumination configurations: (a) wave vector $\perp$ to dimer axis, s-polarization, (b) wave vector $\parallel$ to dimer axis, p-polarization, (c) wave vector $\parallel$ to dimer axis, s-polarization, and (d) wave vector $\perp$ to dimer axis, p-polarization. Note that only the in-plane components are plotted, i.e. the x- and y-components.

The image in Fig. 4.9 (b) reveals a near-field enhancement by a factor of 20 in the gap between the disks which is an indication for the excitation of a longitudinal mode. The smaller enhancement, compared to configuration (a) is due to the smaller amplitude of the component $E_x{}^{sc}$. Note that the out-of plane component, i.e. $E_z{}^{sc}$, amounts to an enhancement of 80, which is due to its significant contribution in this configuration. We observe a strong asymmetry of the field confinement compared to the in-phase longitudinal mode observed in image (a).
Regarding the near-field map shown in image (d) it is seen that here the field is only weakly scattered in the near-field, we have an enhancement factor of 5 for the in-plane components. The out-of plane component results into an enhancement factor of 30, hence it constitutes the major part of the near-field, as it is expected. This near-field map does not reveal any asymmetry, and there is no field confinement in the gap. The particular feature of an additional branch appearing in the far-field scattering images (see Fig. 4.8 (d)) may be due to the near-field, mainly concentrated above the disks structure.

Angular Scattering Pattern of Two Coupled Disks In Sec. 4.1.3 we have seen that the Fourier space contains information on the angular distribution of the scattered light, and we have shown that a single disk behaves like a horizontal dipole. In order to get a deeper insight into the scattering behaviour of two coupled disks illuminated under four different configurations, we analyse the Fourier planes of their holograms. The resulting images are presented in Fig. 4.10.

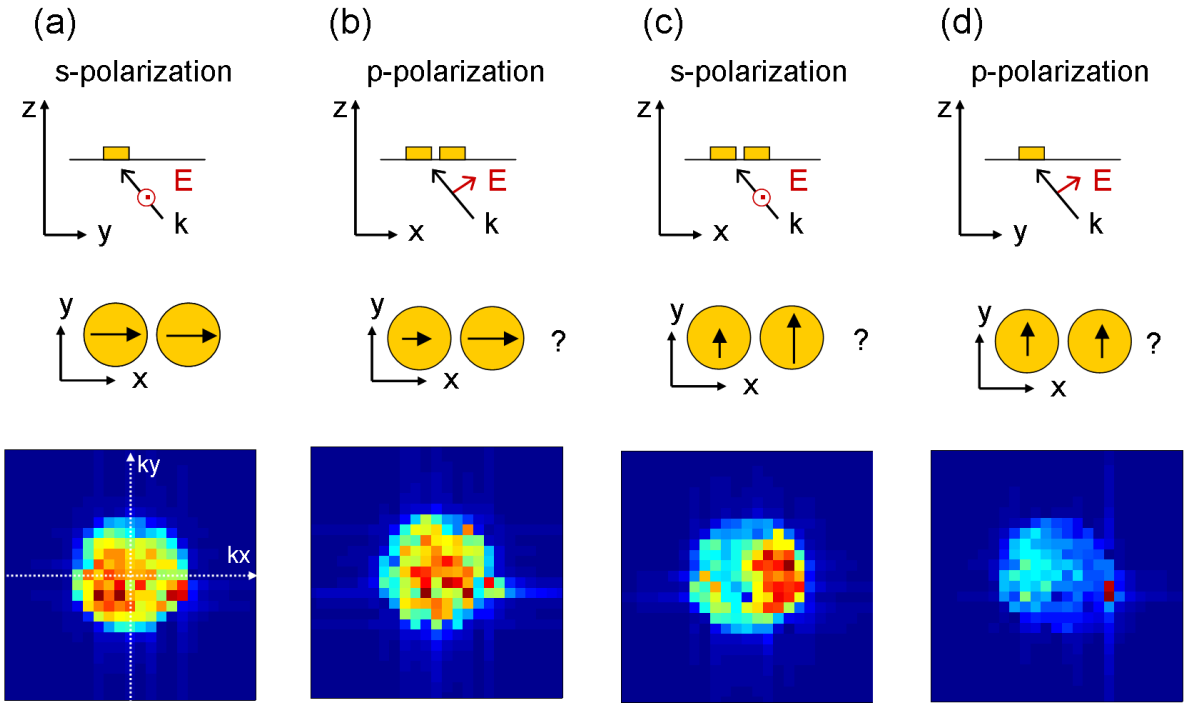

Figure 4.10 – Fourier planes of four different illumination configurations of two coupled disks.

Let us first have a look at the Fourier plane images (a) and (c) which correspond to the longitudinal and transverse modes in the two disks, respectively. Image (c) exhibits one lobe along the k_x-axis and shows some pixels of higher intensity in its opposite direction. Overall it strongly resembles the Fourier plane image that we obtained with a single disk (see Fig. 4.4). Hence, this feature indicates that configuration (c) excites a transverse mode, resulting into two disks behaving like two horizontal dipoles. In configuration (a) it is recognized that most of the intensity is distributed in the bottom left k-space, containing the negative k-values. This angular scattering pattern differs from the one observed in (c) which is not surprising since we expect the excitation of a different mode. In configuration (a) we excite a longitudinal mode of the two disks with a strong near-field coupling. The discrepancy in the Fourier planes between (a) and (c) is attributed to the influence of the strong near-field coupling. We observe in the angular scattering pattern that the scattering is distributed around negative polar angles, thus in opposite direction compared to the scattering of configuration (c) and around smaller angles, indicating a more directional scattering along the z-axis.

Illumination configuration (b) results into a relatively homogeneous distribution of the intensity in k-space, similar to configuration (a), but more centred in the k-space. Lastly, configuration (d) exhibits a weak lobe oriented along the $-k_x$ axis. The two high intensity pixels on the right in the image result from the scattering of the gold frame on the sample which is in this kind of configuration more evident due to the weak scattering signal. [3] Images (c) and (d) are very different, which supports the assumption that in each case, a different transverse mode is excited.

Du to the pixelation in the k-space, we obtain a relative coarse angle resolution of around 8°, therefore the graph in Fig. 4.11 can give only indications of the scattering directions. Overall the graph confirms qualitatively the previous observations of the Fourier space images.

We have seen that each hologram obtained under a different illumination configuration is characterized by a different angular scattering intensity distribution. This observation indicates that different modes are excited in the two coupled disks structure by varying the polarization and the propagation direction of the incident wave, thus confirming our previous interpretations.

Interpretation and Conclusion The two disks system that we have studied here has a resonance at a wavelength of 800 nm, thus near the excitation wavelength used. This resonance wavelength corresponds to the plasmon resonance of the in-phase longitudinal

[3] Note that the in all k-space images continuous vertical and horizontal lines are recognized, particularly evident in image (d). These lines in the k-space correspond to the scattering of the gold frame situated at a distance of 25 μm from each nanostructure. This gold frame has been introduced in the fabrication process and serves for better identification of the single nanostructures on the sample. See Ch. 3.1 for details.

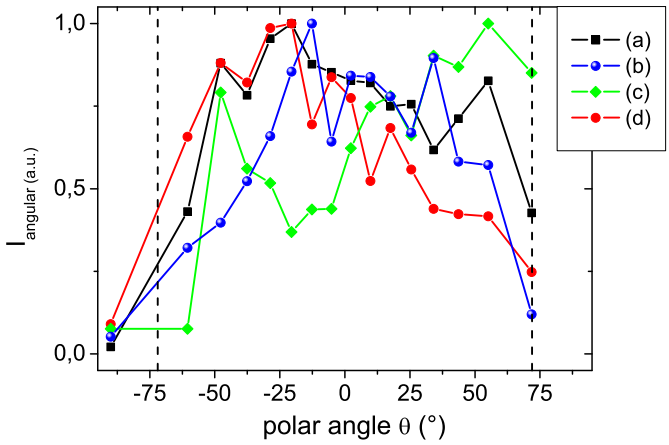

Figure 4.11 – Angular normalized intensity distribution $I_{angular}$ as a function of the polar angle θ for four different illumination configurations of two coupled disks.

mode. Usually, the anti-bonding mode has a higher energy than a bonding mode, and its plasmon resonance is therefore expected at lower wavelengths. However, the exact resonance positions of the anti-phase modes in our nanosystem is not known due to the symmetric illumination that was used both to record and to simulate the scattering spectra. Experiments or simulations would be needed for the study of the scattering in an anti-symmetric configuration that allows the excitation of anti-phase modes.

The presented study of the excitation of different symmetric and asymmetric modes is of preliminary nature. The results of experiments and simulations give good indications towards their interpretation, but most of our interpretations remain speculative since we do not have a complete insight into the scattering behaviour. Therefore, an analytical description would be necessary to analyse the scattering behaviour completely and to fully understand the physics. An analytical study is intended with the theoretical expertise of the group around N. Bonod. However, it is remarked that the features derived from the near-, far-field scattering maps and the angular scattering analysis are in their ensemble coherent and, thus, support our interpretations.

4.2.5 Conclusion on Two Coupled Nanodisks

In this section, we have studied the spectral and the spatial scattering behaviour of two coupled nanodisks. The coupling of two nanoparticles results into an increased near-field enhancement in the gap. We have summarized the results on different experimental and numerical studies on the two coupled nanodisks system. A simple dipolar model was introduced to explain the red-shift of the plasmon resonance with decreasing inter-particle distance. The plasmon hybridization model was briefly described to explain the effects of coupling of two nanoparticles. The coupling results into a mode-splitting, a lower-energy

in-phase mode and a higher-energy anti-phase mode.

We presented the results of measured and simulated scattering spectra of two disks. The resonance wavelength decays exponentially with increasing gap width. This observed exponential decay can be qualitatively explained by the dipolar-coupling model which describes the interplay of two factors: the dependence of the single particle polarizability on the cubic power of the particle dimension and the decay of the particle plasmon near-field as the cubic power of the inverse distance. Overall, the accordance between measurements and simulations is very good. Our obtained results agree well with former studies and are well in line with theoretical descriptions.

We studied further the spatial scattering characteristics obtained by holographic measurements and near-field simulations. Different illumination configurations have been studied and analysed. Furthermore, we have presented an analysis of the Fourier space in order to get insight into the angular scattering pattern of two coupled disks under different illumination configurations.

4.3 Two Coupled Nanorods

A typical nanodimer geometry that has been extensively studied during the past years is composed of two end-to-end coupled nanorods (Aizpurua *et al.* 2005; Smythe *et al.* 2007; Muskens *et al.* 2007). The strong coupling between the rods over a narrow gap creates highly localized and strongly enhanced optical near-fields in the gap. This effect makes this structure ideal for an efficient antenna for light.

4.3.1 Light Scattering of Coupled Rods

In order to simulate the scattering response of a rod-like rectangle, a rectangle with dimensions $L \times w \times h$ (L =length, w =width, i.e. 40 nm, and h =height, i.e. 30 nm) is designed. To take into account the actual rod shape which is fabricated, due to the finite size of the electron beam and the resolution of the lithography resist, rounded edges are introduced on the rectangle's ends using a hemispherical cap of 20 nm radius.

For the study of the coupling behaviour of the gold nanorods, various scattering spectra have been simulated by changing the gap distance from 2 nm to 100 nm and varying the length L of each antenna arm from 70 nm to 170 nm. As Fig. 4.12 reveals, the obtained plasmon resonance wavelengths are located in the visible and near IR regime, i.e. between 600 nm and 1000 nm.

Several observations are made: The simulated resonance wavelength dependency of a single rod on the rod length is approximately linear. This result is in accordance with precedent studies on a similar system (Muskens *et al.* 2007; Wissert *et al.* 2009) and well understood in the frame of the quasi-static model. Regarding the evolution of the

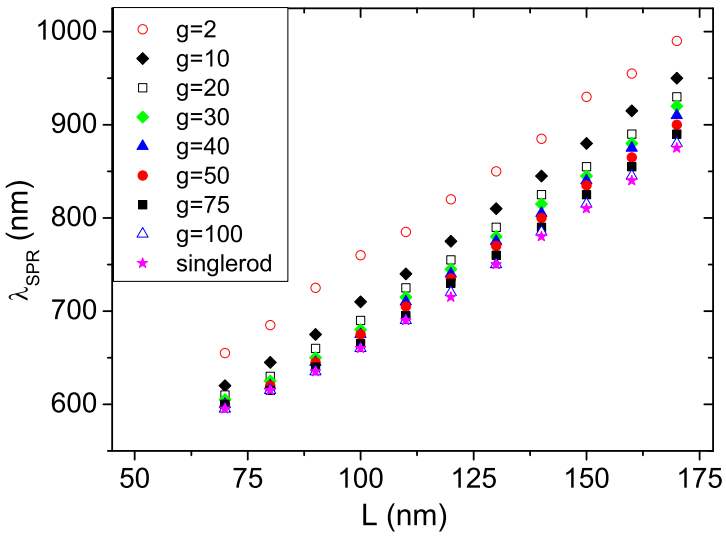

Figure 4.12 – Plasmon resonance wavelengths λ_{SPR} of simulated scattering spectra as a function of rod length of single rods (stars) and coupled rods with varying gap distance (gap g is in nm).

resonance wavelength of two coupled rods with a fixed gap size for increasing rod length, we observe as well a linear dependency. The same linear behaviour has already been observed in the case of two coupled disks when changing the disk diameter, see Ch. 4.2.3.

Secondly, the resonance wavelength of rods with a narrow gap distance of 2 nm are strongly red-shifted (about 40 nm) compared to a 10 nm large gap, indicating a strong coupling. Increasing the gap further results into an increased shift of the resonance towards lower wavelengths, i.e. towards higher energies. At a gap of 100 nm the resonance peak superimposes on that of a single rod, which indicates that the regime where the two rods are completely uncoupled is reached, and only the single rod resonance dominates.

The plasmon hybridization model predicts a vanishing energy splitting with increasing gap. Hence, the bonding mode which we observe in this case due to the symmetric illumination, increases in energy until the splitting is zero at large gaps, i.e. for uncoupled rods. This effect is nicely reproduced by the simulations. Another interesting feature we observed is that for short rod lengths the shift in the resonance peak for decreasing gap is smaller than for long rod lengths (change of slope). While two 10 nm spaced rods of 70 nm length experience a shift of 35 nm compared to the single rod resonance, the resonance of a single rod of 170 nm length shifts the double, about 75 nm for two 10 nm spaced rods. This is explained by the fact that for small rod lengths, the rod is nearly spherical and edge effects become more important which results into a lowering of the frequency shift.

Since we are interested in studying the interaction of nanorods with frequencies in

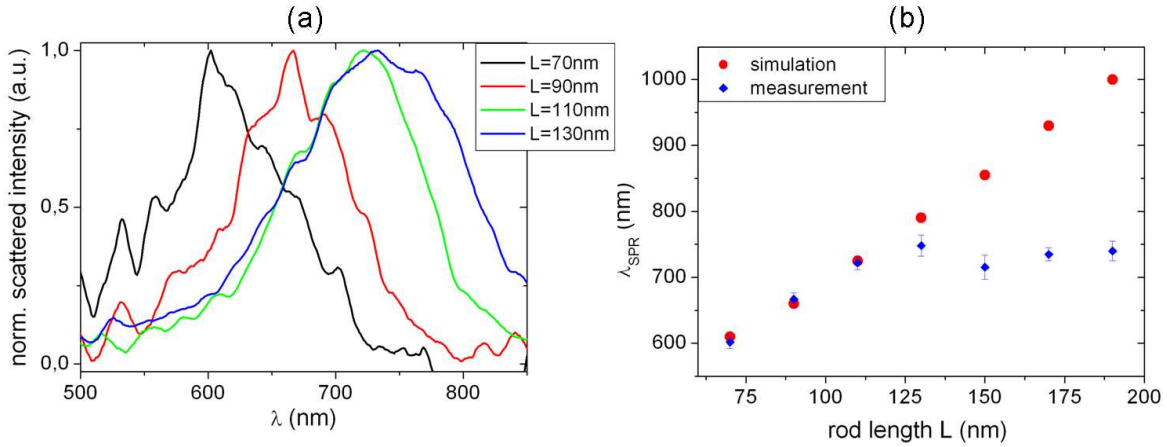

Figure 4.13 – (a) Measured normalized scattered intensity spectra of coupled rods (gap=20 nm) with varying rod length. (b) Comparison of resonance peaks between simulation and measurements.

the visible range, we performed our spectroscopic measurements on short rod lengths. Figure. 4.13 (a) shows the measured normalized scattered intensity spectra of 4 different coupled rods. If we compare the resonance variation due to a change in gap to the variations induced by varying rod length, the simulation reveals that the strongest shift is observed when changing the rod length L. Thus, for the spectral measurements we varied the rod length and fixed the gap size at 20 nm for the structures under investigation. The choice of this gap size is a good compromise between a strong coupling of the two rods and the certainty of a well defined gap. We see that for increasing rod length the scattering spectrum shifts to red as expected. However, both spectra corresponding to rod lengths $L = 110$ nm and $L = 130$ nm overlap. In fact, this feature unveils the upper limit of the spectral sensitivity of the spectrometer. As a result, at longer lengths L the value of the measured resonance wavelengths appears to remain constant, at about 750 nm.

A direct comparison of λ_{SPR} between measurement and simulation is shown in Fig. 4.13 (b). For short rod lengths, the accordance between measurement and simulation is excellent. This reveals at the same time the high quality and great accuracy of the nanofabrication, the excellent sensitivity of the spectroscopic measurements for the recording of spectra of single nanoobjects and, moreover, the good functionality of the FEM model.

4.3.2 Near-Field of Single and Coupled Rods

The calculated near-field maps of one single and two coupled (gap= 20 nm) nanorods at two different excitation wavelengths ($\lambda_1 = 658$nm and $\lambda_2 = 785$nm) are displayed in Fig. 4.14. We plotted the intensity $I = |{E_x}^{sc}|^2$, i.e. the scattered near-field intensity along the long rod axis. The excitation light is polarized along the rod axis and the near-field

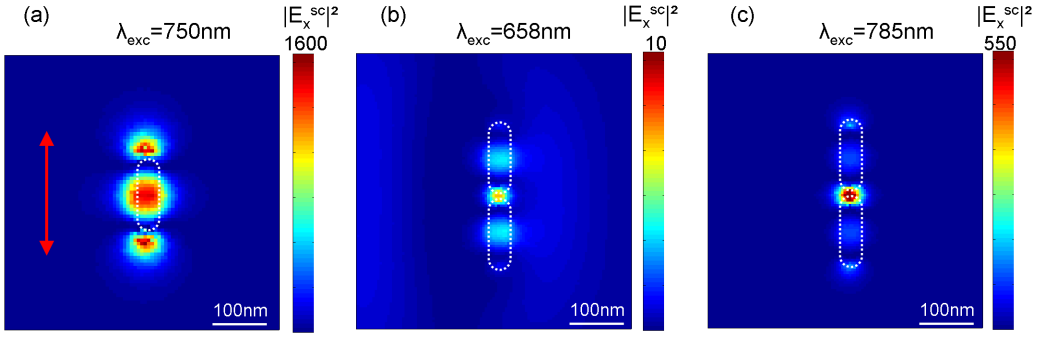

Figure 4.14 – Simulated near-field of a single rod (a) and two coupled rods ($L = 130$ nm, gap= 20 nm) at $\lambda_{exc} = 658$ nm (b) and $\lambda_{exc} = 785$ nm (c) 10 nm above the structure. The red arrow indicates the orientation of the electric field and the white dotted lines the position of the nanorods. The length scale is equal for all images. Note that the intensity $I = |E_x^{sc}|^2$ is plotted.

is calculated 10 nm above the objects. According to Fig. 4.13 (b), the dimer structure resonates at a wavelength of 790 nm, whereas the single rod is at resonance at a slightly lower wavelength, notably at 750 nm (see Fig. 4.13).

The single rod exhibits strong near-field enhancements at each rod end, centred above the rod. We note that the single rod is not excited at resonance, but near to it. The highest near-field enhancement of the dimer is situated in the gap at an excitation wavelength close to its resonance wavelength. An intensity enhancement of up to 500 is reached on the dimer structure at $\lambda_2 = 785$ nm, compared to an enhancement of 10 at an excitation wavelength of $\lambda_1 = 658$ nm. This concentration of intensity in an area of subwavelength size is usually called *hot spot*. Furthermore, from Fig. 4.14 (c) it is seen that there is also a concentration of intensity close to the rod's ends opposite to the gap. This intensity enhancement is attributed to the single rod near-field enhancement which is usually found at both rod ends as Fig. 4.14 (a) reveals. However, the gap enhancement in the dimer exceeds largely the field enhancement on the rod's ends.

4.3.3 3D Far-Field Images of Light Scattered by Coupled Rods

The near-field images in Fig. 4.14 showed us that a two-coupled-rods system, excited at its resonance wavelength, resonantly enhances the near-field in the gap, up to an enhancement factor of 500. We may also expect a difference in the far-field when a dimer is excited at resonance or off resonance. Therefore, we investigated the scattered far-field, by recording holograms of the scattered light of different rod dimers. In order to excite the rod dimer close to its resonance or far from it, we chose to study dimers with various rod lengths, since the position of the resonance varies stronger as a function of length than of gap size. The holograms were recorded with an excitation wavelength of 785 nm.

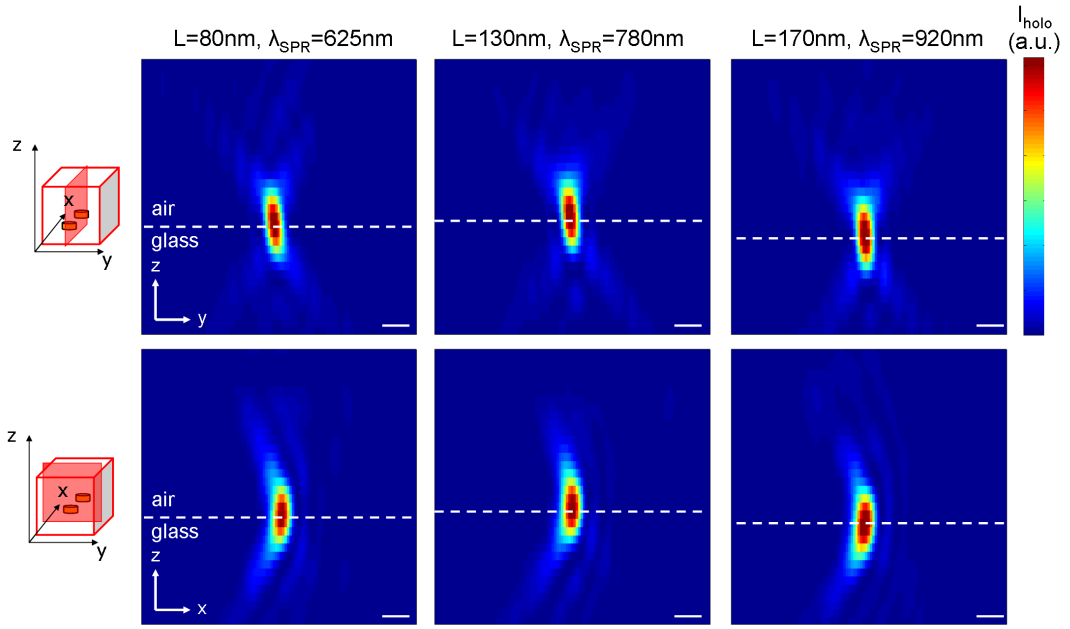

Figure 4.15 – Scattering cross sections of holograms recorded at $\lambda_{exc} = 785$ nm of different rod dimers, gap= 20 nm. The rod length changes, from left to right: L= 80, 130 and 170 nm. The corresponding resonance wavelengths determined by measurement/calculation are given on top of each image pair. The top images show the y-z plane, and the bottom images the x-z plane of the scattered light. The length of the scale bar is 1μm.

Figure 4.15 displays scattering cross sections of three different rod dimers, i.e. the y-z (upper images) and x-z (bottom images) planes. The rod length in each dimer is 80 nm (left images), 130 nm (middle images) and 170 nm (right images). The corresponding resonant wavelengths which were derived from Fig. 4.12 are 625 nm, 780 nm and 920 nm, respectively. That means that the dimer composed of 130 nm long rods is excited at resonance, whereas the other two dimers are off resonance. Like in the case of single disk holograms a dipole-like scattering is recognized. At first sight unexpectedly, no particular variation in the emission pattern is seen comparing the different holograms.

In order to understand this, we have to analyse the conditions under which we measure the detected scattered light. At each measurement of a hologram the density filters in the object beam are adjusted in order to obtain always a maximum of detected signal on the CCD camera which is crucial if we want to record the scattered light of nanoobjects with good accuracy. The outcome of this is that a direct comparison of the amplitude of different measurements is not possible, especially in the case of measurements under different conditions (e.g. change of nanoobject, polarization or wavelength).

Bearing in mind this consideration, two explanations are possible when discussing the scattering maps in Fig. 4.15. Firstly, regarding the near-field scattering behaviour, the near-field reveals that even a dimer excited off-resonance behaves like a dipole. The most

important difference is the amplitude of the near-field enhancement. But as we have seen, a direct absolute comparison of the scattered field amplitude is not possible in this kind of holography technique. Therefore, considering that the most important change resulting from a change in excitation is a variation in the scattered field amplitude, which we cannot measure reliably, we must conclude that the shape of the scattering patterns of rod-dimers, being at or off resonance, do not vary significantly in the far-field to be detected. Considering this explanation, we conclude that the far-field scattering maps are in coherence with the near-field scattering maps. In order to study this in more detail, a measurement of the absolute intensity is necessary. Another possible explanation assumes an existing modification of the scattering pattern in the far-field, but with a variation beyond the spatial resolution of our setup, hence undetected.

In summary, the 3D images of scattered light of nanorod dimers reflect a dipole-like scattering, but no influence of the excitation wavelength on the scattering patter is detected which leads us to the conclusion that the change in the far-field scattering under a different excitation wavelength, is either too small to detect or not significant in the far-field scattering.

4.3.4 Conclusion on Coupled Rods

We have characterized the scattering properties of two coupled nanorods, which is an ideal structure for a nanoantenna. Measured and simulated scattering spectra have been analysed. The resonance wavelength of a single rod and as well of two coupled rods is approximately linear with the rod length, and it blue-shifts with increasing gap size. The resonance for largely spaced rods approaches the single rod resonance. These observations are explained in the frame of the quasi-static model and the plasmon hybridization model.

Near-field simulations revealed a strong increase in intensity located in the gap at an excitation wavelength, as it is expected in such kind of structure. However, we observed a big difference in the enhancement factor: for an excitation wavelength near the resonance wavelength of the structure, a factor of 550 is obtained, compared to a factor of 10 for an excitation wavelength far from its resonance. The far-field scattering images that we obtained by holography reflect well a dipole-like scattering, but no influence of the excitation wavelength on the spatial repartition has been observed. This led us to the conclusion that either different excitation wavelengths do not result into a significant change in the far-field scattering pattern or that its effect is too small to be detected.

4.4 Conclusion

In this chapter we have presented a detailed study of elementary nanoobjects, notably single and coupled nanodisks and nanorods. The main purpose of this study was the

validation of our experimental and simulation techniques and their justification for the application of plasmonic nanostructures.

The comparison of simulated and measured scattering spectra resulted into an excellent agreement between both, confirming the excellent sensitivity of the spectroscopic setup in view of the detection of scattered light by single nanoobjects, and validating our developed FEM model with regard to simulations of basic plasmonic nanostructures on a substrate-air interface.

The coupling of two nanoparticles is characterized by a near-field enhancement and confinement in the gap, and a red-shift of the resonance wavelength. Generally, the plasmon resonance decays exponentially with increasing gap towards the single particle resonance. Those features can be explained within the framework of the plasmon hybridization model, which we introduced briefly, and the dipolar-coupling model. Overall we state that our experimental and calculated results are in excellent agreement with theoretical predictions and previous studies, thus justifying and validating our experimental and numerical know-how for single plasmonic nanoobjects.

Holographic measurements of coupled nanoparticles resulted into three dimensional scattering maps from which we derived a dipole-like scattering behaviour: The cross-sections parallel to the z-plane reveal forward scattered light along the z-axis having an elongated ellipsoidal shape.

We performed a preliminary study of different modes that can be excited in a system of two coupled disks, especially with regard to the excitation of so called *bright* and *dark* modes. We analysed far-field scattering images from holographic measurements, their corresponding angular scattering images and near-field maps obtained from simulations. We have shown that each illumination configuration resulted into the excitation of a different mode. An analytical description is necessary, which is being carried out at the Institut Fresnel.

In addition, we examined the spectral and spatial (both in the far- and near-field) properties of two coupled rods. Overall, all results obtained on the coupled rod system are confirmed both by theoretical predictions and precedent studies of similar structures.

We have shown that both our experimental and numerical techniques to characterize the far- and near-field scattering of a plasmonic nanostructure result into an excellent agreement with theoretical predictions. Therefore, by the study of elementary plasmonic nanoobjects we have validated and justified the techniques all along the line.

Chapter 5

Extensive Study of Plasmonic Nanostructures

Table of contents

The world in a grain of sand.

William Blake

There is a theory which states that if ever anyone discovers exactly what the Universe is for and why it is here, it will instantly disappear and be replaced by something even more bizarre and inexplicable. - There is another theory which states that this has already happened.

Douglas Adams

The results presented in Ch. 4 on fundamental nanoobjects, demonstrated on the one hand our capability to measure and simulate scattering spectra of nanoobjects and on the other hand our ability to record three dimensional images of the scattered light by nanostructures. This chapter addresses the study of more sophisticated nanoobjects, i.e. nanostructures of complex geometry with scattering characteristics which are more difficult to model and to understand intuitively. The aim of this chapter is to apply our developed imaging technique to a novel set of plasmonic objects. An extensive study on chains of nanodisks will be presented. Furthermore, the coupling behaviour in triangular structures will be examined.

Nanoparticle chains have attracted a lot of attention for their ability to confine (Krenn *et al.* 1999) and guide light through subwavelength cross-sections (Quinten *et al.* 1998; Maier *et al.* 2003). Moreover, under an extended illumination, intense and sub-lambda free-space hot spots of similar magnitude as reported for nanometer gap systems can be achieved (Ghenuche 2009). Most of the recent studies on metal nanoparticle chains are of numerical nature (Quinten *et al.* 1998; Girard and Quidant 2004; Ghenuche *et al.* 2005; Koenderink and Polman 2006; Lévêque and Quidant 2008; Devilez *et al.* 2010a; Willingham and Link 2011; Lester and Skigin 2011), but some experimental investigations are also found (Krenn *et al.* 1999; Maier *et al.* 2002; Maier *et al.* 2003; Ghenuche *et al.* 2007; Suck *et al.* 2011). However, a systematic study of their resonance spectra and scattering patterns is still missing. Inspired by Ghenuche *et al.* 2007, who investigated chains of nanoparticles by two photon luminescence spectroscopy, we are interested in studying the scattering of chains of nanodisks by numerical heterodyne holography, a technique that is not yet well known in the domain of plasmonics. Using direct holography we will examine the scattering characteristics of a nanodisk chain under the viewpoint of an optical antenna. An optical antenna can be apprehended in different ways, i.e. as a device which can direct the emission of a source in a given direction or, conversely, concentrate radiation coming from a given direction to a confined region of subwavelength size. In this context the directivity is a measure of an antenna's ability to concentrate or collect radiated power into a certain direction. We will show that a nanodisk chain has the ability to scatter light directionally perpendicular to the chain axis.

Furthermore, we will show that, taking advantage of heterodyning, photothermal holography is a technique that gives direct insight into the temperature of an alternatively heated nanostructure and its modulated temperature distribution. In direct or photothermal holography, the polarization of the incoming illumination is of course essential: the behaviour of an antenna in parallel or perpendicular polarization is extremely different. We will show that this difference reveals the coupling strength between various structures.

Another geometry that is examined is the novel triangular structure presented in Ch. 3.1. This structure is composed of two very long and very thin coupled right-angled triangles. In this way, under an incident light polarized parallel to the short legs of the tri-

angles, the small gap-spaced structure behaves essentially as two coupled rectangles with changing length. We will show that this structure permits to examine different resonance conditions that appear on different sites on the structure, depending on the length of the rectangles. Its main advantages are (i) a continuously varying "pseudo-rod" length, and (ii) a larger available metal surface allowing easier far-field measurements.

5.1 Probing the Coupling of Nanodisk Chains by Spectroscopy

Before we begin with the analysis of the scattering images of nanodisk chains, it is important to get a detailed knowledge of the scattering spectra of these structures. This will help us later to fully understand the holographic images of the scattered light. In this section we study extensively the scattering spectra of a great variety of nanodisk chains by far-field spectroscopy. Far-field spectroscopy has proven its ability to detect scattering spectra of single nanodisks with high accuracy (see Ch. 4.1.1). We will experimentally show that nanochains exhibit longitudinal and transverse modes. Furthermore, we will demonstrate that near-field coupling between the disks influences the far-field scattering spectrum of the chain. The experimental results will be qualitatively compared to results from simulations.

5.1.1 Longitudinal and Transverse Modes in Nanodisk Chains

First of all, we are interested in studying the influence of the polarization of the incident light on the scattering response of the chain. Maier and co-workers have demonstrated that far-field spectroscopy on chains of gold nanoparticles revealed the existence of longitudinal and transverse plasmon modes (Maier *et al.* 2002). For this experiment, they used a white light illumination with a polarization either in the direction of the chain axis or perpendicular to it. The authors showed that the plasmon resonance of the longitudinal mode was red-shifted with respect to the transverse plasmon mode resonance. The shift diminishes with increasing gap and is directly related to the near-field coupling between the nanoparticles in the chain. Maier et al. understood the polarization dependence of the plasmon resonance from a model treating the Au particles as point dipoles (Brongersma *et al.* 2000; Maier *et al.* 2001). The excitation of transverse and longitudinal modes has been also reported in nanoantenna structures, such as coupled nanorods (Muskens *et al.* 2007; Wissert *et al.* 2011).

Figure 5.1 shows the results of our measurements on one chain type where we plotted the normalized scattering spectra of two chains for polarizations parallel (continuous lines) and perpendicular (dashed lines) to the chain axis. Two observations can be made:

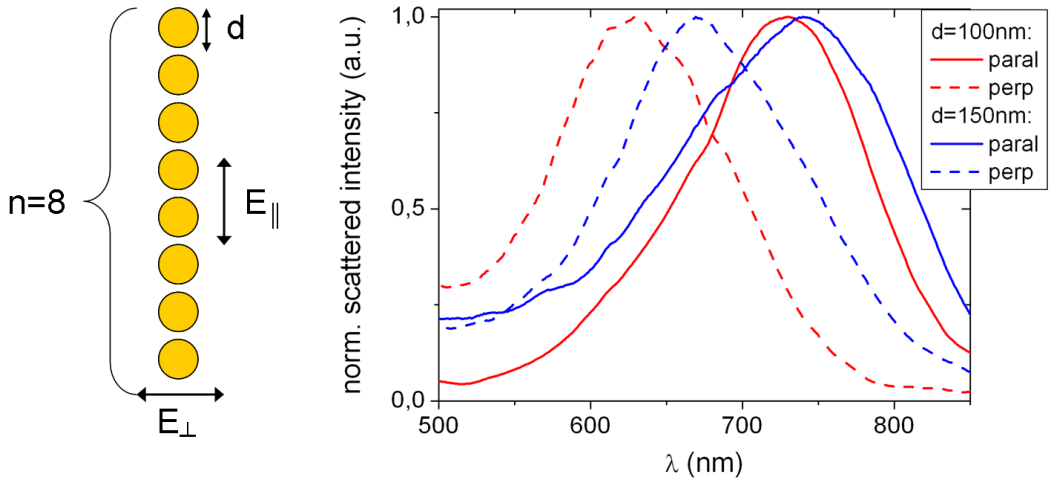

Figure 5.1 – Normalized scattering spectra of two different chains consisting of 8 disks (gap = 20 nm) with a diameter of 100 nm (red curves), or 150 nm (blue curves), respectively, obtained with parallel (continuous lines) or perpendicular (dashed lines) polarized light with respect to the chain axis. Scheme on the left clarifies the situation.

(i) The scattering spectra of chains with large disks are red-shifted with respect to the spectra of chains with smaller disks (blue curves versus red curves).

(ii) The scattering spectra obtained with light polarized perpendicular to the chain axis are shifted towards lower wavelengths compared to spectra obtained with parallel polarized light (dashes curves versus continuous curves).

Both effects can be qualitatively understood considering that small objects (small disks, or disk chains illuminated perpendicularly, i.e. weakly coupled) resonate at shorter wavelengths than larger objects.

In order to examine more closely the excitation of these different modes, polarization dependent measurements on various disk chains are performed. The results are summarized in Fig. 5.2 where we plotted the measured resonance wavelengths as a function of disk number and polarization. Once again, we must keep in mind that the fabrication of such precise nanostructures does not have a perfect yield: some structures have imperfections which induce variations. Superimposed with measurement noises, this can strongly influence the results. Several interesting features can nevertheless be identified with good certainty: Firstly, the plasmon resonances of chains consisting of disks with a diameter of 150 nm are red-shifted compared to the resonances of chains with a 100 nm disk diameter. This feature has already been observed in Fig. 5.1, and is attributed to the linear scaling of the plasmon resonance wavelength with the size of the nanostructure.

Secondly, we confirm the second observation made in Fig. 5.1 and note that for all chains the resonance wavelengths obtained with perpendicular polarized light (empty symbols)

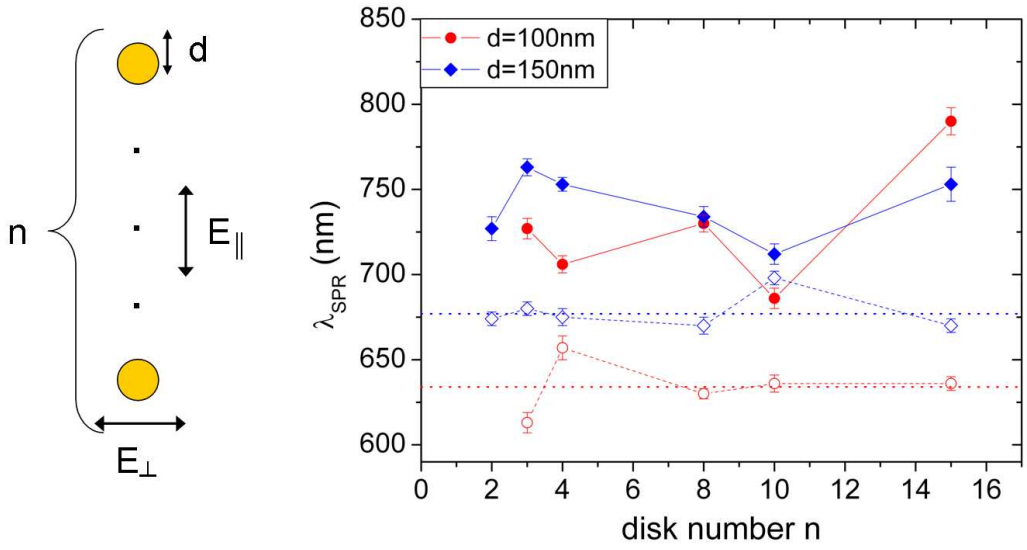

Figure 5.2 – Dependence of the plasmon resonance on disk number and polarization: polarization parallel to chain axis (full symbols) and perpendicular to chain axis (empty symbols). The red (blue) symbols correspond to 100 nm (150 nm) large disks. For better comparison, the disks in all chains are spaced by the same gap of 20 nm. The lines are guides to the eye.

are blue-shifted with respect to those measured with parallel polarized light (full symbols). The difference in λ_{SPR} between the two polarizations ranges from 14 nm (chain: $n = 10$, $d = 150$ nm) to 154 nm (chain: $n = 15$, $d = 100$ nm).

Thirdly, analysing the transverse mode of the different chains it is evident that its resonance position does not depend on the chain length (see empty symbols in Fig. 5.2). Within the experimental accuracy, all transverse modes are situated around the same wavelength, at 634 nm (for 100 nm disks) and 677 nm (for 150 nm disks). These values are indicated by the dotted lines in Fig. 5.2. It has to be emphasized that the transverse modes do not coincide with the single disk mode. This is due to the fact that the investigated chains have a disk spacing of 20 nm, the disks are still coupled and near-field interactions induce a frequency shift away from the single disk plasmon mode, towards higher energies (Maier *et al.* 2002).

Lastly, it is remarked that Fig. 5.2 does not reveal any clear tendency in the correlation between the plasmon peak position of the longitudinal mode and chain length. This observation may allow the assumption that the plasmon mode is not directly correlated to the disk number in the chain but follows more complex laws. A similar behaviour in nanoparticle chains has been mentioned before mostly in numerical studies (Ghenuche *et al.* 2005; Ghenuche *et al.* 2007), and thus confirms our observations. In this context, we would like to remark that up to our knowledge we are the first group providing such an exhaustive, fully experimental study about the influence of disk number on the resonance

modes in a disk chain.

In conclusion, we have shown that the polarization of the incident light has a strong influence on the resonance position of the scattering spectrum of the chains. Depending on the polarization of the incident light, nanodisk chains exhibit longitudinal or transverse modes. Whereas the resonance of the longitudinal mode fluctuates with changing chain length, the resonance of the transverse mode is mostly independent of the disk number. Compared to the longitudinal mode, the transverse mode has a higher energy.

5.1.2 Far-Field Scattering Revealing Near-Field Coupling in Nanodisk Chains

We have seen that the longitudinal modes in a chain reveal the near-field coupling between the disks. Therefore, we were interested in examining more closely the coupling behaviour by far-field spectroscopy. We measured scattering spectra of different chains as a function of gap width. The resulting resonance wavelengths are shown in Fig. 5.3 (a) where the resonance wavelength λ_{SPR} is plotted as a function of the gap for various chains. The blue-coloured symbols correspond to the plasmon resonances of chains with 100 nm disks and the red-coloured symbols to those of chains consisting of 150 nm disks.

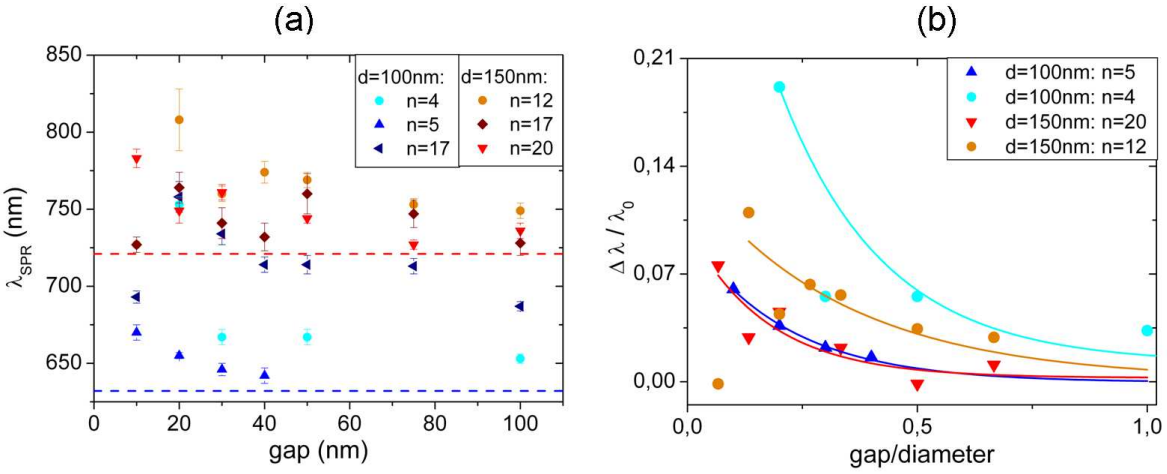

Figure 5.3 – (a) Surface plasmon resonance wavelengths as a function of the gap between the disks for various chains. The red (blue) symbols correspond to chains with 150 nm (100 nm) large disks. The upper (red) and the lower (blue) dashed lines correspond to the (measured) resonance wavelength of a single disk of 150 and of 100 nm diameter, respectively. (b) Fractional plasmon shift $\Delta\lambda/\lambda_0$ for 4 chosen chains as a function of gap-diameter ratio. The continuous lines are exponential decay fits of type: $y = a\,exp(-x/\tau) + y_0$.

Whereas the 17 disks chain (d = 100 nm) exhibits globally a large red-shift of λ_{SPR} compared to its corresponding single disk mode, the other chains exhibit smaller red-shifts.

This effect may be attributed to the chain length. Although not entirely evident for all chains, we observe that an increasing gap leads to a decrease in the resonance wavelength. For large gaps (100 nm) the resonance wavelengths for both chain types approaches the single disk modes (indicated by the dashed lines). The resonance dependence on the gap exhibits an exponential decay behaviour. Such an exponential decay has been already observed in the case of two coupled disks and is qualitatively explained by the dipolar-coupling model. In fact, it has been shown that this model is also valid for disk chains or waveguides (Brongersma *et al.* 2000).

It must be remarked that the strong deviation of the measured values for the smallest gap from the expected tendency can be attributed to two factors: the nanofabrication and the sensitivity of the spectrometer. The fabrication of very small gaps less than 20 nm is very delicate. Therefore, disks which are expected to be spaced by a gap of 10 nm may be connected. It has been shown that this overlapping leads to a strong change in resonance (Atay *et al.* 2004) which has been discussed in Ch. 4.2.3. The second factor, that may be relevant, is the upper limit of the wavelength sensitivity of our spectrometer which cuts off spectral peaks situated in the near-IR spectrum. This may explain the unexpected, relatively short resonance wavelengths for small gaps in the chains of 150 nm sized disks. This feature has been discussed previously in Ch. 4.2.3.

The Decay Constant of Finite Disk Chains In order to examine the feature of the resonance wavelength decay more closely, we analysed quantitatively the decay constant τ. For this, we plotted the fractional plasmon shift, i.e. $\Delta\lambda/\lambda_0$ with $\Delta\lambda = \lambda_{SPR} - \lambda_0$ where λ_0 denotes the single disk resonance, against the gap-diameter ratio for 4 chosen chains. The results and their exponential fits of type $y(x) = a \cdot exp(-x/\tau) + y_0$ are plotted in Fig. 5.3 (b). The numerical values of the decay constant of each analysed chain are presented in Tab. 5.1.

	d=100 nm			d=150 nm		
	n=2 (exp.)	n=4	n=5	n=2 (exp.)	n=12	n=20
τ	0.25 ± 0.06	0.23 ± 0.10	0.21 ± 0.02	0.19 ± 0.06	0.33 ± 0.30	0.17 ± 0.10
a	0.41 ± 0.05	0.43 ± 0.16	0.10 ± 0.00	0.14 ± 0.02	0.13 ± 0.04	0.10 ± 0.03
y_0	-0.01 ± 0.02	0.01 ± 0.02	0.00 ± 0.00	0.00 ± 0.01	0.00 ± 0.03	0.00 ± 0.01

Table 5.1 – Exponential fit values τ, a and y_0 of 4 different disk chains. For comparison we included the experimental values from our two disks study.

Comparing the values of the three constants, we notice that they correspond roughly to each other, meaning that the decay trend becomes independent of the nanoparticle size on account of this scaling. We derived the averaged constants: $\overline{\tau} = 0.23$, $\overline{a} = 0.22$ and $\overline{y_0} = 0$. Figure 5.3 (b) reveals that the fits corresponding to the 5 and 20 disks chain superpose, whereas the other two fits diverge from this trend resulting into a deviation of

τ and a from the averaged constants. These large deviations for the 4 and 12 disks chain are ascribed to an imperfect geometry of the structures.

Additionally, we included in Tab. 5.1 the values derived from our experimental study with two coupled disks from Ch. 4.2.3. The comparison shows a good agreement between two coupled disks and chains of a higher number of disks, meaning that the dipolar model on which the scaling is based, fits also very well for the description of finite nanodisk chains.

In conclusion, we have shown that the decay trend of nanodisk chains follows the same behaviour than that of two coupled disks. We derived a decay constant $\overline{\tau}$ of 0.23 valid for all chains, meaning that the decay trend is independent of the nanoparticle size, but dependent on the spacing-size ratio. As a result, the dipolar coupling model describes as well the resonance wavelength dependence of finite nanodisk chains. Overall, we have demonstrated that the resonance exhibits an exponential decay of equal constants regardless of disk length or disk size.

Simulation of Scattering Spectra of Nanodisk Chains

In literature, not many numerical studies on metal nanoparticle chains are found that investigate the influence of the particle numbers (Ghenuche *et al.* 2005; Girard and Quidant 2004). Ghenuche *et al.* investigated the scattering spectrum as a function of the particle number in a chain using the Green Dyadic Method. Girard and Quidant developed a self-consistent model to calculate the near-field transmittance of metal particle chains with increasing particle number. Both studies found different scattering/transmittance amplitudes with changing particle number, but no clear dependency of the resonance peak position on the particle number was stated. Ghenuche *et al.* found a peak difference of 25 nm for varying the chain length from 5 to 20 particles.

However, a numerical study investigating the influence on the gap on the scattering spectrum is missing. Additionally to our experimental investigations, we performed FEM simulations to determine the scattering spectra of various chains with changing gap and varying disk number. Fig. 5.4 shows the simulated scattering spectra of chains consisting of 12 disks. Two parameters are varied: the disk diameter (100 and 150 nm) and the interdisk spacing (10, 30 and 50 nm). For the purpose of comparison, the scattering response of the single disks is added in the graph.

Again, three observations can be made: (i) The spectra of chains with larger disks are red-shifted. (ii) An increasing gap induces a blue-shift of the spectrum. (iii) The resonance wavelength of the chains approaches that of the single disk resonance for large inter-disk spacings. Whereas the chain with 100 nm disks already reaches the single disk resonance for a gap of 50 nm, the resonance position of the chain with larger disks of 50 nm spacing is still about 80 nm red-shifted compared to the corresponding single disk resonance. This means that the coupling in disk chains is dominated by the diameter-gap

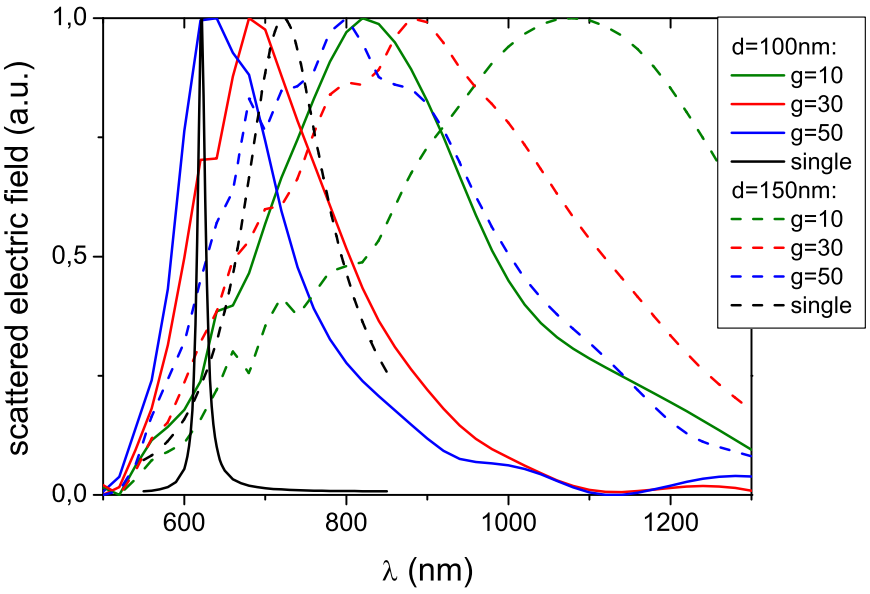

Figure 5.4 – (a) Scattering spectra from simulations of various chains consisting of 12 disks with disk diameter of $d = 100$ nm (continuous lines) and $d = 150$ nm (dashed lines), respectively, and varying spacing. The black spectra correspond to the single disks.

ratio and not only by the gap size alone, as observed previously. Overall, these features are in excellent agreement with the observations that have been made earlier when analysing our experimental results.

Further simulations were performed in order to investigate the gap dependency of the plasmon resonance for chains of various lengths. The results are summarized in Fig. 5.5, where the plasmon shift $\Delta\lambda$ is plotted against the gap for a set of different chains. For better comparison, the disk diameter is constant for all plotted chains.

First of all, the simulations confirm the exponential decay of the plasmon resonance with increasing disk spacing. The second important message derived from Fig. 5.5 is that the number of disks in a chain on the resonance position has no significant influence. The strongest shift in the resonance position underlies the gap spacing. For various disk numbers we find a small variation of about 60 nm on the resonance position, but no explicit correlation is observed. This variation may be due to the broadening of the calculated spectrum which increases the inaccuracy to determine the peak position of the wavelength.

Taken into account the considerations above, we derive the decay constant from exponential fitting over all points of all chains, and we obtain $\tau_{sim} = 0.13 \pm 0.01$, $a_{sim} = 0.76 \pm 0.03$ and $y_{0,sim} = 0.00 \pm 0.01$. These values, however, differ strongly from the values derived from measurements. This discrepancy is attributed to the large resonance shifts

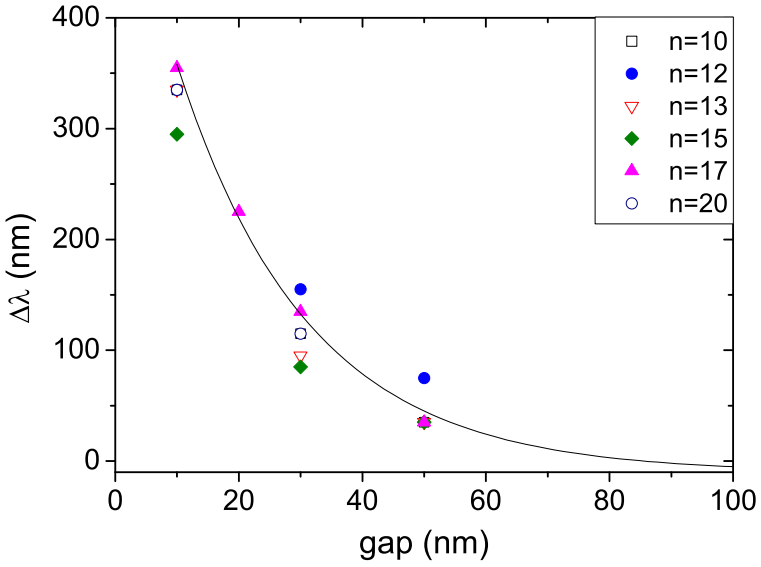

Figure 5.5 – Plasmon shift of different chains ($d = 150$ nm) as a function of gap deduced by simulations. The continuous line corresponds to an exponential decay fit.

$\Delta\lambda$ up to 350 nm. For comparison, in the case of two coupled disks we calculate a resonance shift of maximal 200 nm. In fact, these observations led us to the conclusion that the resonance of a disk chain depends however on the chain length. For strongly coupled chains, composed of more than 10 disks, the resonance is strongly red-shifted compared to a chain of two disks.

Regarding the congruence of our experiments and simulations, we recognize that a direct, quantitative comparison is not possible. However, the trends exhibited in each are the same. The resonances found in our simulations, particularly for the small gap widths, are generally more red-shifted than those we measured from disk chains of equal size and spacing. In fact, these discrepancies are attributed to differences between the simulations and our experimental situation. Our fabricated nanostructures have imperfections: electron beam lithography and lift-off leave the disks with slightly different diameter, rough sides and non-uniform heights. Consequently, the gaps in-between the disks vary in size. In the simulations we performed, the disks in the chain were all smooth and uniform in shape, and the spacing between the disks was identical. These assumptions cannot be made for the real structures. Furthermore, the sensitivity of the spectrometer has an upper and a lower limit of the detectable wavelength. Thus, if a chain exhibits a resonance above or below this limit, the detected spectral maximum does not correspond exactly to the real resonance peak of the chain. As a result, the simulated and experimental resonances cannot coincide quantitatively.

It is important, however, to stress the fact that we observed the same general trends both in experiment and in simulation. The qualitative agreement is excellent, and the

results reflect very well the underlying physics.

5.2 Far- and Near-Field Maps of Scattered Light by Nanodisk Chains

Far-field spectroscopy measurements revealed a strong gap and polarization dependence on the plasmon resonance wavelength of the nanodisk chains. Similar observations have been documented by previous studies, and the results can be understood qualitatively with the dipolar coupling model. We are interested to study if similar dependencies can be observed by studying the *spatial* far-field scattering properties. Fourier-space analyses obtained in the back focal plane of an object reveal directionality, but cannot deliver a full 3D reconstruction since the phase is not measured. Up to now, no studies of 3D images of scattered light by plasmonic chains can be found in the literature.

In this context, we will present and analyse maps of scattered light recorded on chains under various conditions. We investigated the impact of both extrinsic and intrinsic factors on the scattering pattern, e.g. the polarization of the incident light and its wavelength, the disk number and the coupling strength. We will show, that all those factors have a different impact on the far-field scattering pattern of the chains. Measured far-field scattering images and simulated near-field maps will be discussed in detail.
Furthermore, it will be shown that the concept of an optical antenna can be applied to nanodisk chains. An optical antenna is a structure that strongly enhances the interaction of light with nanoscale matter and with a well defined emission pattern. Ideally an antenna concentrates the emitted light into a certain direction. We will show that resonant nanodisk chains can scatter light directionally.

5.2.1 The Influence of the Chain Length on the Far-Field Maps

Having a great variety of chains at disposition, we were firstly interested into investigating how the number of disks n in a chain influences the holograms of the scattered light. Figure 5.6 shows cross sections along the x-z planes of different chains. For a better comparison, the disk diameter is 150 nm in all presented chains and the disk separation is 20 nm. In this case, the holograms were recorded at a wavelength of 658 nm. The disk number increases from left to right in Fig. 5.6. With increasing chain length, several features are observed: The scattering map of a 4 disks chain exhibits one hot spot. [1] This

[1] For the purpose of simplifying the description of the scattering maps for the following, we will denote the observed intensity accumulations on the chains as *hot spots*. It has to be noted, however, that this expression used in this context does not have the same meaning as usually used in near-field optics where a hot spot denotes a field concentration in a subwavelength sized area. When describing holograms, we always analyse far-field images, i.e. the so called hot spots are not limited to a sub-lambda zone, but

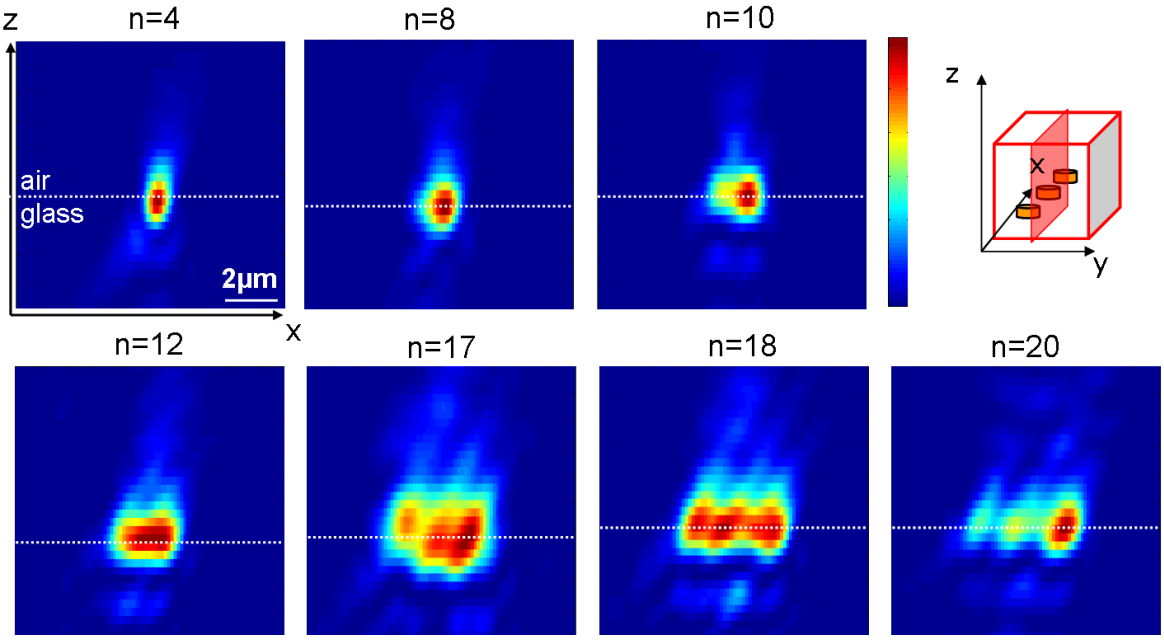

Figure 5.6 – Cross sections along x-z plane of holograms of disk chains, $d = 150$ nm, gap$= 20$ nm. The exciting wavelength is 658 nm. From left to right, the disk number, i.e. the chain length, is increasing.

scattering feature resembles the scattering characteristics observed with two coupled rods or disks. Increasing the disk number to 8, the hot spot becomes broader in latitude, i.e. along the x-axis which corresponds to the axis of the chain. This observation is consistent with the increase in length. The length of a chain of 8 disks increases to 1.34 μm about the double compared to a chain of 4 disks (length$=$ 0.66 μm). Increasing the length furthermore, a second hot spot develops (at $n = 12$). The two hot spots become broader and more distinctive, until a third hot spots appears for a 18 disks chain. The scattered map of a chain of 20 disks consists of three hot spots. Hence, three main regimes were observed in the scattering maps: appearance of one, two and three hot spots.

In view of explaining these features, two interpretations are considered. Studying the intrinsic properties of a gold particle chain by computing the local density of electromagnetic states (ELDOS), Ghenuche *et al.* introduced the hypothesis that a particle chain can behave like a linear cavity (Ghenuche *et al.* 2005). Due to constructive interference of counterpropagating fields, resonances build up in the chain, with periods independent from the pitch of the particles, but dependent on the incident wavelength. Bearing this hypothesis in mind, the scattering maps could therefore indicate that, depending on the disk number, resonant modes build up in the chain which are then expressed by hot spots in the far-field. Since in our case the resonant modes depend on the disk number, it is concluded that an increase in chain length results into the creation of an additional

extend into the far-field.

resonance observable in the far-field.

Another interpretation is based on the near-field coupling. We will see later that a long chain composed of touching disks exhibits a scattering map similar to that of a long single rod. No hot spots are observed. Hence, it may be concluded that multiple hot spots arise mainly in chains with separated disks. In Ch. 4.1.3, we have seen that the far-field images obtained from the scattering of a dipole are characterized by a bright dot in the x-y plane and a forward scattering into air for the planes along the z-axis. The far-field images shown in Fig. 5.6 revealed similar features, but multiple, slightly broader hot spots are observed. Intuitively, this effect could be understood as the creation of multiple dipoles along the chain. It is known that the coupling between the disks induces a near-field enhancement in the gaps. Due to the asymmetric illumination this near-field enhancement is not symmetrically distributed over the chain (Ghenuche *et al.* 2005). Assuming that the external electric field interacts with the near-field induced by the coupling between the disks, multiple dipole modes may be created along the chain depending on the distribution of the near-field enhancement along the chain. Hence, this coupling may result in the observed multiple hot spots in the far-field.

5.2.2 TE Wave and TM Wave Excitation

As the investigation of the scattering spectra of the chains revealed, it is evident that the orientation of the electric field component with respect to the chain has an important impact on the mode excitation. The analysis of the scattering spectra revealed that depending on the polarization, either longitudinal or transverse modes of the chain are excited.

To study this influence from a different point of view, holograms were recorded using different configurations for the excitation. Here, we discuss the resulting scattered field maps for either a TE wave excitation (s-polarization) or a TM wave excitation (p-polarization). For a p-polarized incident wave, illuminating the structure under a 45° angle, the electric field has two components, one along the y- and a second along the z-axis. These two illumination configurations are illustrated in the left-handed schemes in Fig. 5.7 which presents the resulting holographic images of two different chains excited with either a TE (upper images) or a TM wave (bottom images).

Far-Field Scattering Maps Comparing the scattering images some differences are denoted: In the x-y plane under TE excitation, the whole chain scatters light, and two distinctive spots of high intensity concentrations are observed on the chain, whereas a TM wave excitation results into a homogeneous scattering along the chain. Only one more intense spot is revealed at the chain end. This feature becomes more evident in the images of the x-z planes on the right hand side. Another interesting feature is the slight change in scattering if comparing the y-z plane images in the middle. The scattering

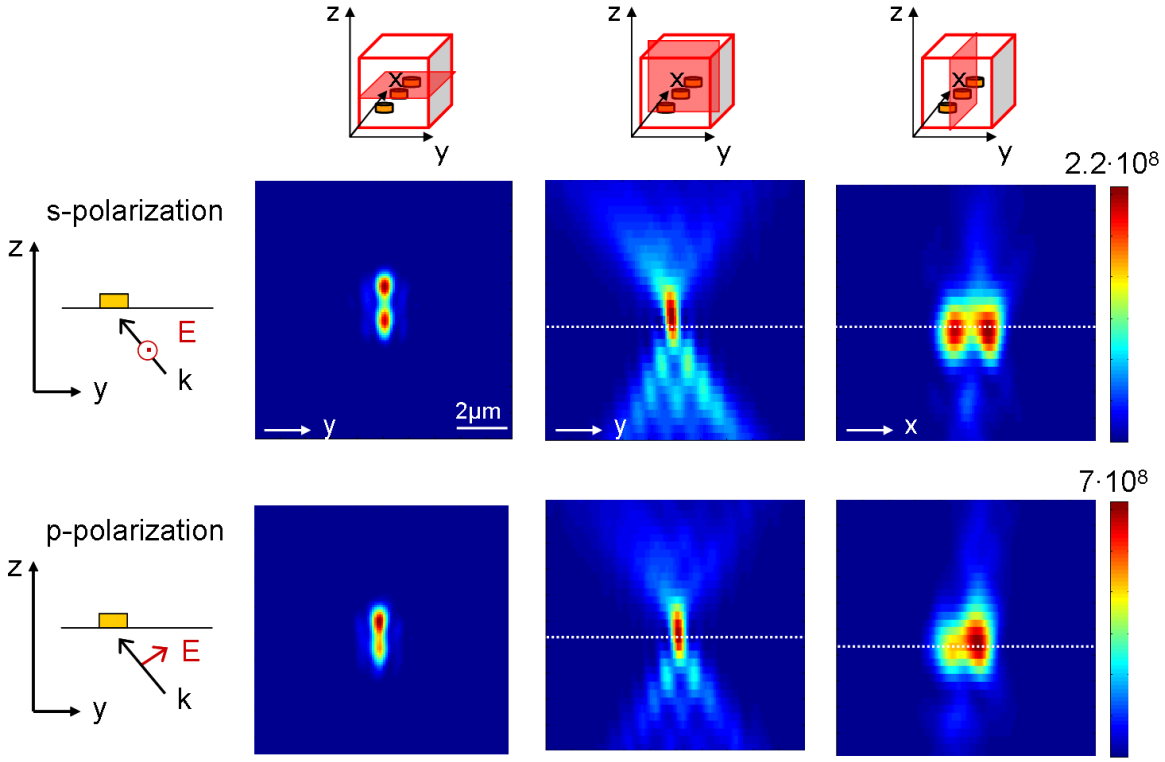

Figure 5.7 – Influence of polarization of exciting E-field on a chain ($n = 20$, $d = 100$ nm, gap$= 20$ nm): Cross sections along different planes centred on the antennas: x-y (left column), x-z planes (column in the centre) and y-z planes (right column). Schemes on the left clarify the two different illumination configurations. The spatial scale bar is the same for all images.

into air along the z-axis is globally more intense in the case of s-polarization than for p-polarized incident light. Evidently, if a chain is excited with a s-polarized wave, incident perpendicular to the chain axis, longitudinal modes are excited (see left-handed insets in Fig. 5.7). The interaction of the chain with the light is more effective, and an increase in scattering is expected.

Figure 5.8 shows a second example of the polarization influence on a chain, and another interesting feature is revealed. Here, the influence of p-polarized incident light on the scattering images is more evident. Whereas the hologram obtained under s-polarized illumination reveals a scattering over almost the entire chain length, a p-polarized illumination results into 4 separate spots of scattered light along the chain.

This particular feature may be explained by considering that the incident electric field of a TM polarized light has two components, $E_{0,y}$ and $E_{0,z}$. The electric field component along the z-axis does not induce any considerable dipole moment since the disk thickness is very small (30 nm). Therefore, the component perpendicular to the chain axis will dominate, and mainly a transverse mode of the chain will be excited.

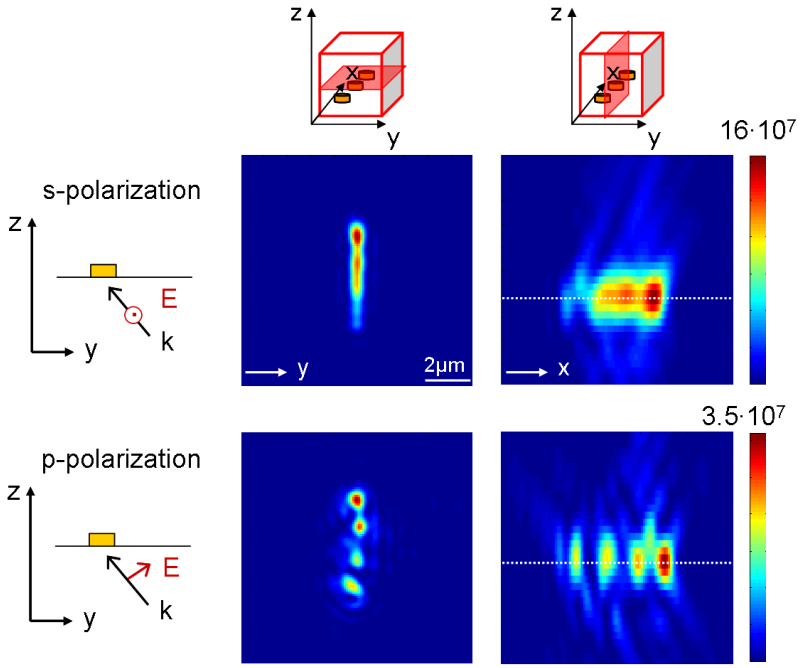

Figure 5.8 – Influence of polarization of incident beam on a chain ($n = 20$, $d = 150$ nm, gap= 40 nm): Cross sections along different planes centred on the antennas: x-y (left column) and y-z planes (right column). Scheme on the left clarifies the two different illumination configurations. The scale bar is the same for all images.

Near-Field Scattering Maps In order to obtain a deeper insight into the far-field scattering images, we performed near-field simulations. The resulting near-field images are plotted in Fig. 5.9 and 5.10, where the scattered intensity $I = |\vec{E}^{sc}|^2 = |E_x^{sc}|^2 + |E_y^{sc}|^2 + |E_z^{sc}|^2$ is plotted 10 nm above the surface of the chains.

Regarding the distribution of the near-field with s-polarized light, it is seen that in both cases the chain exhibits a strong field accumulation in several gaps in the middle of the chain. In Fig. 5.9 we identify two peak field concentrations that are positioned symmetrically around the middle of the chain. Hence, the two intense spots observed in the far-field images may be attributed to these two zones of near-field accumulations. In Fig. 5.10, we observe two zones with a near-field accumulation, in this case situated closer to the chain extremities.

Both simulations of p-polarized illumination result in strongly changed near-field distributions compared to a s-polarized incident wave. No scattered field in between the disks is revealed, hence, no near-field coupling exists between the disks. The amplitude of the scattered intensity from the disks is very weak. The near-field is uniformly distributed along the chain. This uniform scattering is assumed to arise from a collective scattering by single disks.

The simulations reveal a strong discrepancy between the near-field amplitudes due to s-

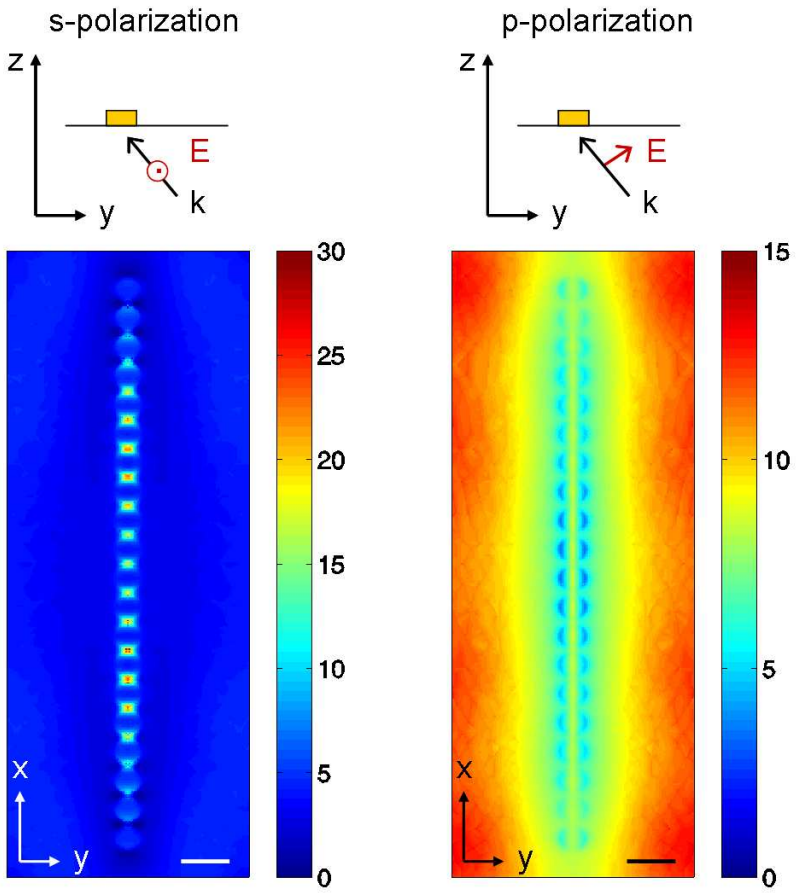

Figure 5.9 – Simulated scattered near-field intensity 10 nm above a 20 disks ($d = 100$ nm, gap$=$ 20 nm) chain for two different incident light configurations. Left: s-polarized light. Right: p-polarized light. The scale bar is 200 nm, and the color bars are normalized with respect to the maximum scattered light in the p-polarized case.

and p-polarized excitation. This behaviour could not be confirmed by the measurements. This may be explained by the fact that when changing the polarization of the illumination beam we change as well the intensity of the incident light. Hence, a direct comparison of the amplitudes is not feasible.

Although a direct comparison between simulation and measurement is not possible, the strong difference of the scattering characteristics due to different polarizations is evident in both cases. The near-field simulations show a strong change in the induced near-field depending on the polarization of the incident light. The near-field enhancement and confinement is strongest for an electric field component parallel to the chain axis, whereas a p-polarized wave does not result in any field confinement in between the gaps. As a result, we expect a difference in the scattering pattern as well in the far-field, keeping in mind that propagation to the far-field behaves as a low-pass filter on spatial frequencies.

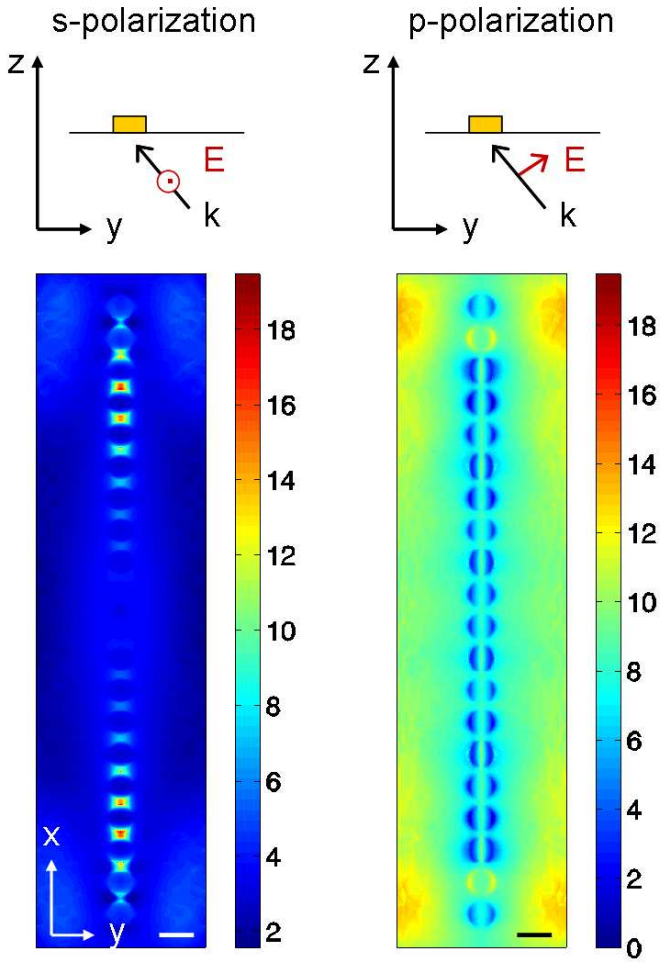

Figure 5.10 – Simulated scattered near-field intensity 10 nm above a 20 disks (d=150nm, gap=40nm) chain for two different incident light configurations. Left: s-polarized light. Right: p-polarized light. The scale bar is 200nm.

In summary, the polarization of the incident light exhibits a strong influence on the type of the excited mode in the chain: longitudinal modes, or a melange of weakly coupled transverse and single disk modes. While near-field simulations reveal a strong difference in amplitude and near-field distribution depending on the excitation, the scattering images exhibit a visible change in shape.

5.2.3 Imaging of Longitudinal and Transverse Modes in a Chain

In the preceding section we have shown that the orientation of the exciting electric field has a crucial impact on the resulting scattering map. In this section, we focus our attention on TE wave excitation, but with an electric field oriented either parallel or perpendicular to the antenna chain axis in order to excite longitudinal or transverse modes in the chain. It is expected that these modes will result into a different scattering of the disk chains.

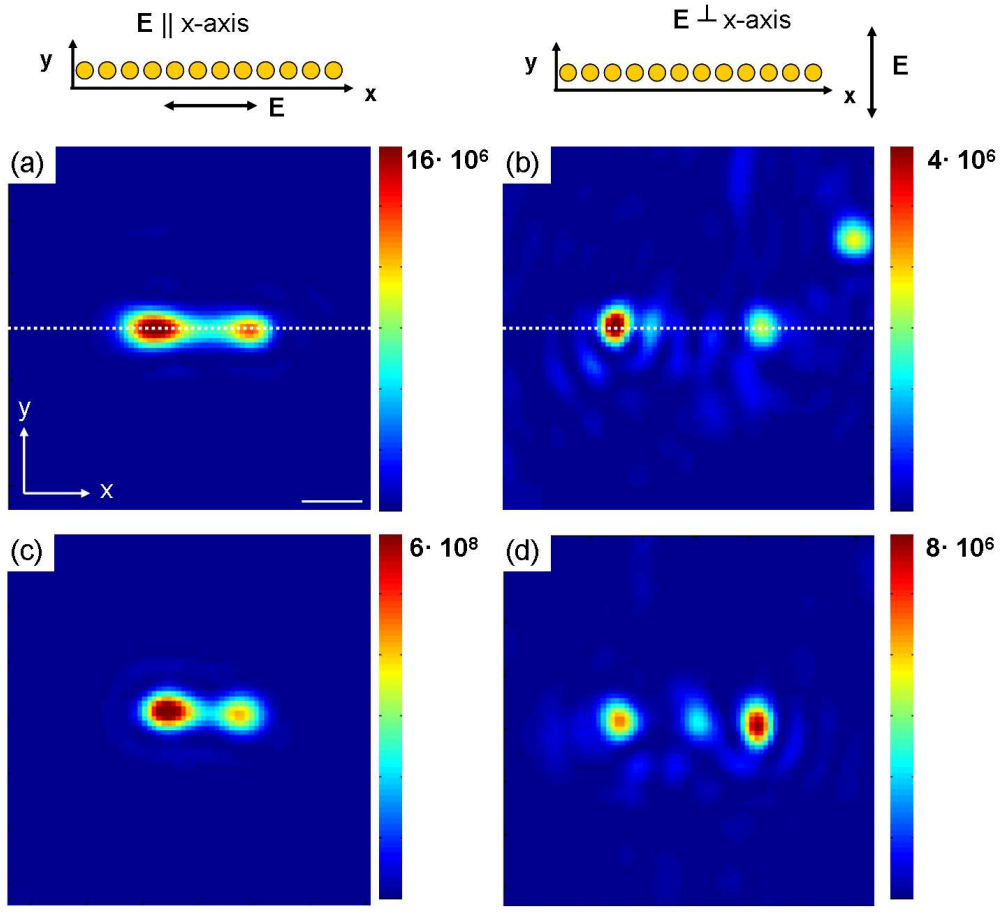

Figure 5.11 – The x-y planes of holograms obtained on two chains: $n = 12$, $d = 150$ nm, gap$=$ 30 nm (a and b) and $n = 17$, $d = 100$ nm, gap$=$ 20 nm (c and d). The holograms are obtained under two different configurations: E-field parallel to chain axis (left column) and perpendicular to chain axis (right column). See insets on top for clarification of the illumination configuration. The scale bar is 1 μm and the same in all images.

Far-Field Imaging We performed polarization dependent holographic measurements on various chains. Figure 5.11 presents the resulting images of two chosen chains. When exciting the longitudinal modes of the chain (left column), the scattering pattern has the form of an elongated 8, two connected hot spots are identified. When the transverse modes are excited in the chain, two distinct scattering spots are recognized, but no significant scattering on the chain itself is found. These features are observed in the case of both chains, the chain with 12 disks (upper images) and the chain with 17 disks (bottom images).

The positions of the hot spots on the chains were analysed more precisely by plotting the measured intensity along the chains as indicated by the white dotted lines in Fig. 5.11. The resulting line profiles are shown in Fig. 5.12. Analysing the line profiles, it is revealed

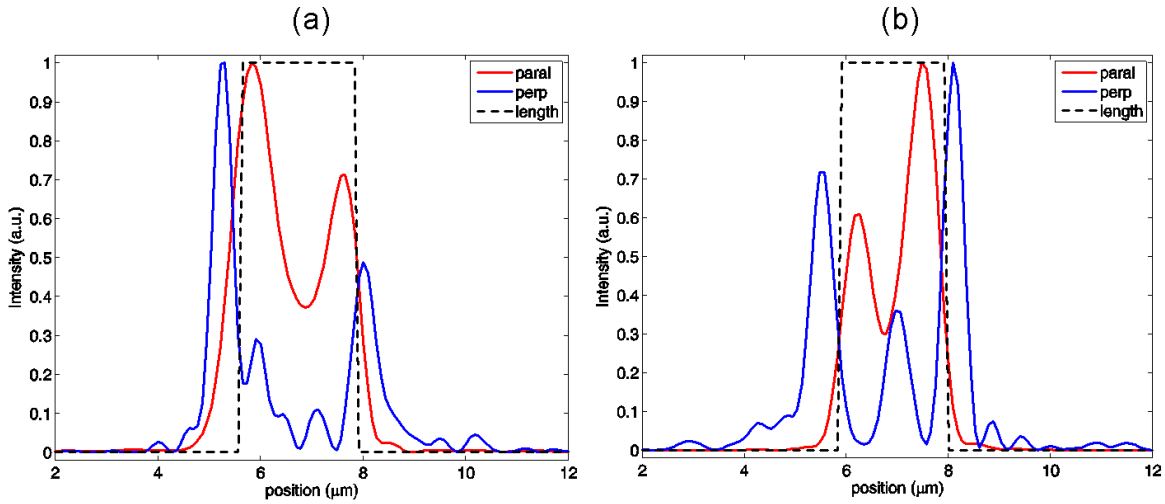

Figure 5.12 – Measured intensity is plotted as a function of position along the chains. Graph (a) corresponds to the images in Fig. 5.11a,b and graph (b) corresponds to the images in Fig. 5.11c,d. The black dashed line represents the length of the total chain. All line profiles are normalized to 1.

that the hot spots resulting from longitudinal modes in the chain are situated on the chain, near the chain extremities (red curves). On the other hand, the hot spots due to transverse modes excited in the chain, are situated close to the chain ends (blue curves). In order to investigate quantitatively the position of the hot spots, the exact values of the chain lengths are compared to the distances between the hot spots, as shown in Tab. 5.2. It is confirmed that the hot spots due to transverse modes are found next to the chain extremities.

Regarding the amplitude of the scattered intensity on the chain, in the case of longitudinal modes, it is seen that the scattered intensity between the hot spots does not drop to zero, but remains at about half the maximal intensity. On the contrary, the scattered intensity between the two hot spots on the chain ends drops almost to zero in the case

	l_{chain}	$D^{\parallel}$	$D^{\perp}$
Fig. 5.12 (a)	2.13 μm	1.83 μm	2.78 μm
Fig. 5.12 (b)	2.02 μm	1.21 μm	2.60 μm

Table 5.2 – Chain lengths, l_{chain}, and hot spot extensions for parallel, $D^{\parallel}$, or perpendicular polarization, $D^{\perp}$, measured in the profiles of Fig. 5.12

of transverse mode excitation. This feature may be an indication that a chain, excited in transverse mode, does not scatter light strongly enough to be detected.

A similar feature has been observed by Baffou *et al.* when measuring the two photon luminescence (TPL) of two coupled long rods (Baffou *et al.* 2010). In the case of longitudinal polarization, a strong optical signal was observed in the gap region, while under perpendicular polarization the maximal TPL signal was measured at the ends of the rods. The authors attributed this effect to the tip effect which is stronger on the rod's external ends under perpendicular polarization.

Near-Field Maps Additionally, we performed near-field simulations with the purpose of explaining the origin of the observed scattering characteristics.

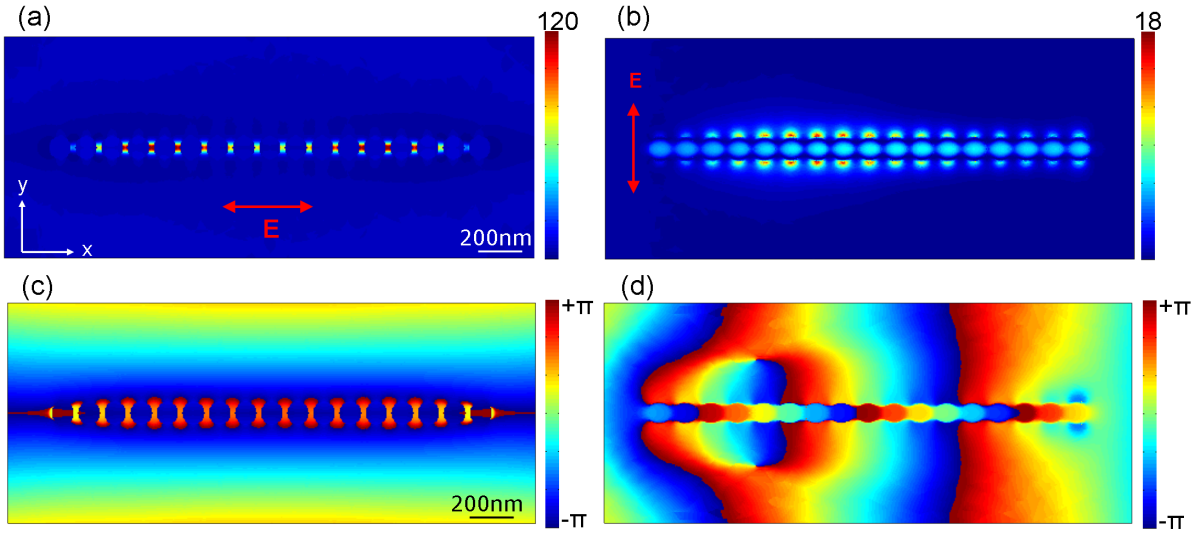

Figure 5.13 – Simulated near-field of longitudinal (a) and transverse modes (b) of a 17 disks chain. $|{E_x}^{sc}|^2$ is plotted 15 nm above the substrate. The exciting electric field is in (a) parallel to the x-axis and in (b) parallel to the y-axis. The corresponding phase images are plotted in images (c) and (d).

Figure 5.13 (a) shows the near-field intensity induced by an electric field excitation parallel to the chain axis, while Fig. 5.13 (b) gives the near-field with an exciting electric field along the y-axis, i.e. perpendicular to the chain axis. In the case of a longitudinal mode excitation, the near-field is concentrated exclusively between the disks in the gaps.

The near-field distribution is not uniform, and maxima of the near-field scattering are found which are distributed on two zones on the chain, symmetrically around the chain center. The near-field enhancement is up to 120. Comparing this simulated near-field map to the corresponding measured far-field image in Fig. 5.11 (c), the similarity between both intensity distributions is recognized. Figure 5.13 (b) indicates that each disk in the chain acts like an dipole oriented along the y-axis. As a result, their far-field scattering cancels out in the inner part of the chain, but not at the chain extremities which would explain the observed far-field images.

Figure 5.13 (c) and (d) represent the corresponding phase images. It is seen that in the longitudinal mode all induced dipoles in the disks are in phase along the chain which is expected under a homogeneous illumination. The case of an electric field excitation perpendicular to the chain axis, Fig. 5.13 (d), reveals a different much more complex phase-image. Here, it is seen that phase jumps are present along the chain due to the illumination parallel along the chain axis which induces retardation effects.

This study proves that phase effects have an influence on the resulting near- and far-fields of a nanodisk chain.

For better clarity, Fig. 5.14 compares the intensity profiles of the measured far-field (Fig. 5.11 (c)) and the near-field (Fig. 5.13 (a)). The numerous peaks in the latter correspond to the field enhancement in the gaps. Although a direct relation of the far-field images to the near-field maps is not possible, Fig. 5.14 reveals a good agreement in the positions of the maximal scattered field. One is conducted to conclude that the two hot spots observed in the far-field are related to the two near-field accumulations after far-field propagation, which is equal to low-pass filtering.

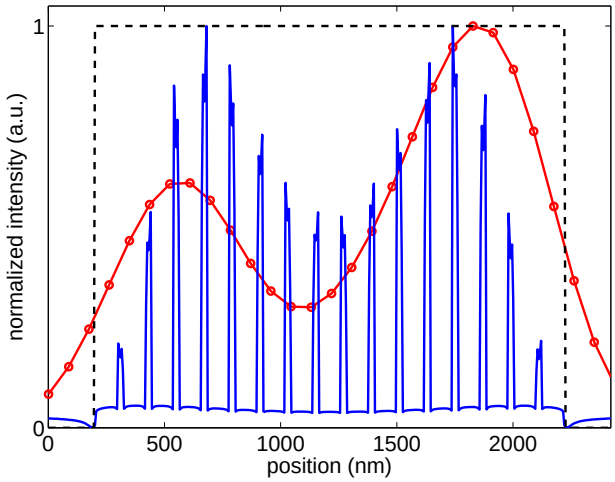

Figure 5.14 – Corresponding line profiles along chain axis of measured far-field (red) and simulated near-field (blue). The black dashed line represents the length of the total chain which is 2.02 μm.

Regarding the near-field maps obtained with excitation perpendicular to the chain axis

(see Fig. 5.14b), firstly, we observe that the field enhancement is 6 times lower than in the case of parallel polarization. There is no near-field in the gaps, but a field enhancement at the side of the chain on each disk, alongside the direction of excitation, similar to the near-field of a single disk observed in Ch. 4.1.2. However, all disks do not scatter the light in the same way. We observe that near the middle of the chain, the scattering is enhanced. Considering the results of both experiment and simulation, the interpretation of the observed features may be the following. When longitudinal modes are excited in the chain, the enhanced near-fields that develop in the gaps, couple to the far-field which results into a strong scattering of the chain. Hence, we observe a scattering characterized by connected hot spots in the far-field.

With an excitation of an electric field perpendicular to the chain axis the near-field enhancement in the chain is 6 times lower, as well as the scattering of light in the far-field. The excited transverse mode provides almost no near-field enhancement and confinement in the gaps. Although not revealed from the simulations, we conclude that the disks situated at the chain extremities are the only disks that couple efficiently to the far-field, resulting in a strong scattering next to the chain extremities.

In conclusion, we have shown that the scattering images of excited longitudinal and transverse modes differ strongly. While the scattering of longitudinal modes is characterized by hot spots originating from the chain, the far-field scattering of the transverse modes originates mainly due to the scattering of the light at the chain ends.

5.2.4 Influence of the Exciting Wavelength

We have seen that the nature of the illumination beam is crucial for the characteristics of the scattering response of the chain. Now, we will show that also the wavelength of the incident light influences the scattering behaviour significantly.

The graph on the left-hand side in Fig. 5.15 shows the scattering spectrum of a chain consisting of 15 disks with a diameter of 150 nm and spaced by a gap of 20 nm. The spectrum reveals that the chain has a resonance position at around 770 nm. We recorded two holograms of the same chain using a s-polarized illumination at a wavelength of $\lambda_{exc,1} = 658$ nm and $\lambda_{exc,2} = 785$ nm, where $\lambda_{exc,2}$ is in this case close to the chain's resonance. Figure 5.15 presents the scattering cross sections along the three main reconstruction planes (x-y, x-z and y-z planes) of the chain. The position of the chain with respect to each plane is schematically shown on the left-hand side insets.

The antenna is hit by the incident beam under the TIR angle (45°), in the y-z plane. The holographic signal is, of course, influenced by the laser intensity, system transmission, and detection efficiency, which are wavelength sensitive. In order to compare the intensities of the holographic signals in Fig. 5.15, we have therefore multiplied the normalized images at each laser wavelength by the spectrometric intensities, which do not depend on the wavelength sensitivity of the holographic setup.

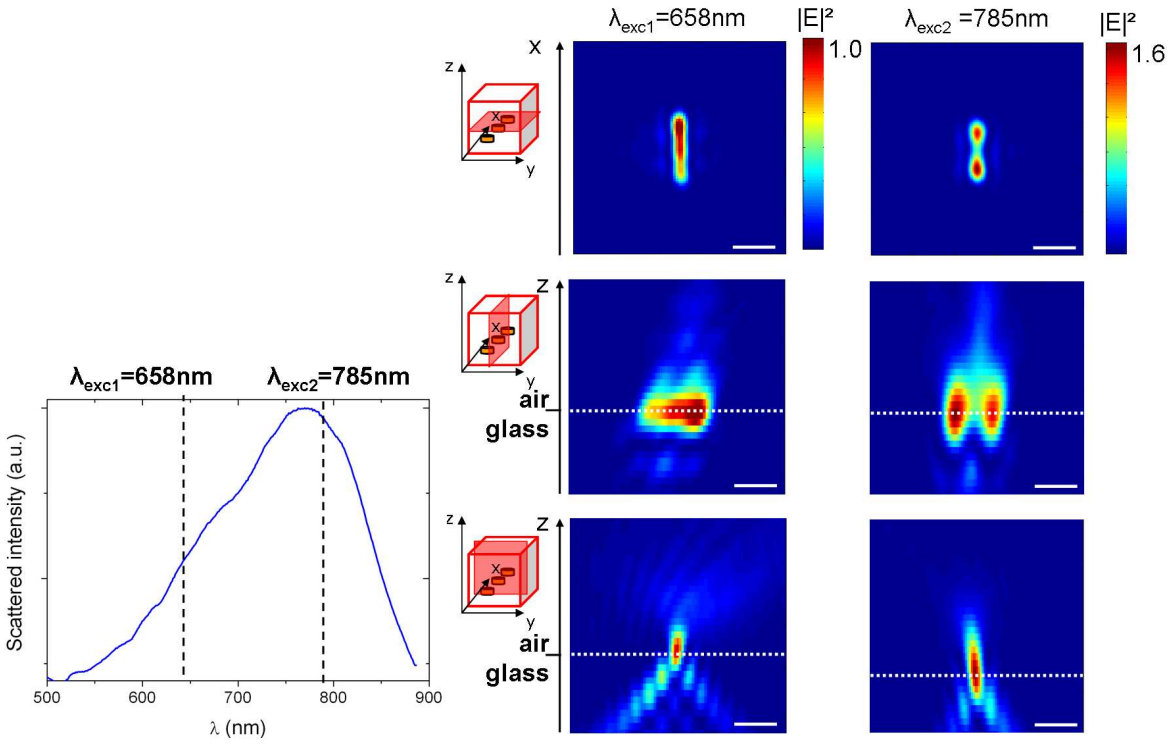

Figure 5.15 – Influence of the excitation wavelength. (a) Measured scattering spectrum of a chain ($n = 15$, $d = 150$ nm, gap$= 20$ nm). (b) Intensity of the scattered field reconstructed from a single hologram at $\lambda_{exc,1} = 658$ nm (left column) and at $\lambda_{exc,2} = 785$ nm (right column). The scale bar is 2 μm.

Analysing the scattering maps of the top views (x–y plane), the shape of the disk chain is recognized. Its length is estimated from the image as 2.9 ± 0.1 μm, slightly larger than the expected length (2.5 μm). At $\lambda_{exc,2}$ two hot spots on the chain are recognized, a similar scattering behaviour that was observed before when studying the influence of linear polarized light on the chain. Considering that the scattering spectrum exhibits a peak close to 785 nm, the chain is considered to be excited at resonance.

Comparing the cross sections in planes containing the z-axis (middle and bottom images), a clear difference is perceivable for the two different illumination wavelengths. At $\lambda_{exc,1}$ we observe in the x-z plane an angular radiation pattern featuring a uniformly scattered field along the chain axis, whereas in the case of $\lambda_{exc,2}$, close to the chain's resonance wavelength, two distinctive hot spots are identified. The existence of such resonant hot spots and their wavelength dependence has already been observed in similar systems (Ghenuche *et al.* 2007). Furthermore, the scattering in the y-z plane exhibits an interesting feature: With an illumination at resonance it is recognized that the disk chain strongly scatters light into air, in a direction along the z-axis.

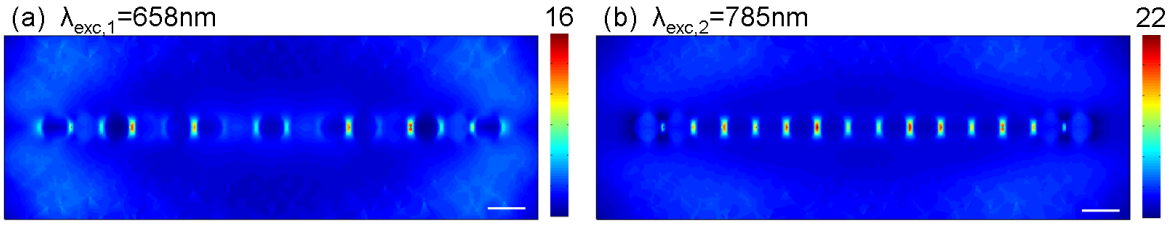

Figure 5.16 – Simulated near-field 10 nm above a chain of 15 disks (d=150 nm, gap=20 nm) for two exciting wavelengths: 658 nm and 785 nm. The scale bar is 200 nm.

Additionally we performed near-field simulations, which are shown in Fig. 5.16. The near-field maps reveal a pronounced difference in amplitude and distribution of the near-field intensity. On the example of the 15 disks chain, the near-field enhancement is highest, 22, for an excitation at $\lambda_{exc,2} = 785$ nm. The magnitude of the near-field intensity in the gaps changes along the chain. Whereas at an excitation wavelength of $\lambda_{exc,1} = 658$ nm every second gap is "switched off", i.e. no near-field is found, in the case of a larger illumination wavelength (i.e. at $\lambda_{exc,2}$) a near-field confinement is observed in every gap. Furthermore, the positions of the gaps where the maximal near-field intensities are situated, differ with changing excitation wavelength.

Another example is presented in Fig. 5.17 where we show the far-field scattering characteristics of a chain consisting of 17 150 nm large disks, having a disk spacing of 20 nm. Here, it is seen that the resonance of the chain is found at 670 nm, i.e. close to $\lambda_{exc,1}$. From the top-view images, the chain length is estimated as 3.0 ± 0.1 μm, in agreement with the expected length (2.9 μm). Comparing the cross sections in planes containing the z-axis, a clear difference is perceivable for the two different illumination wavelengths.

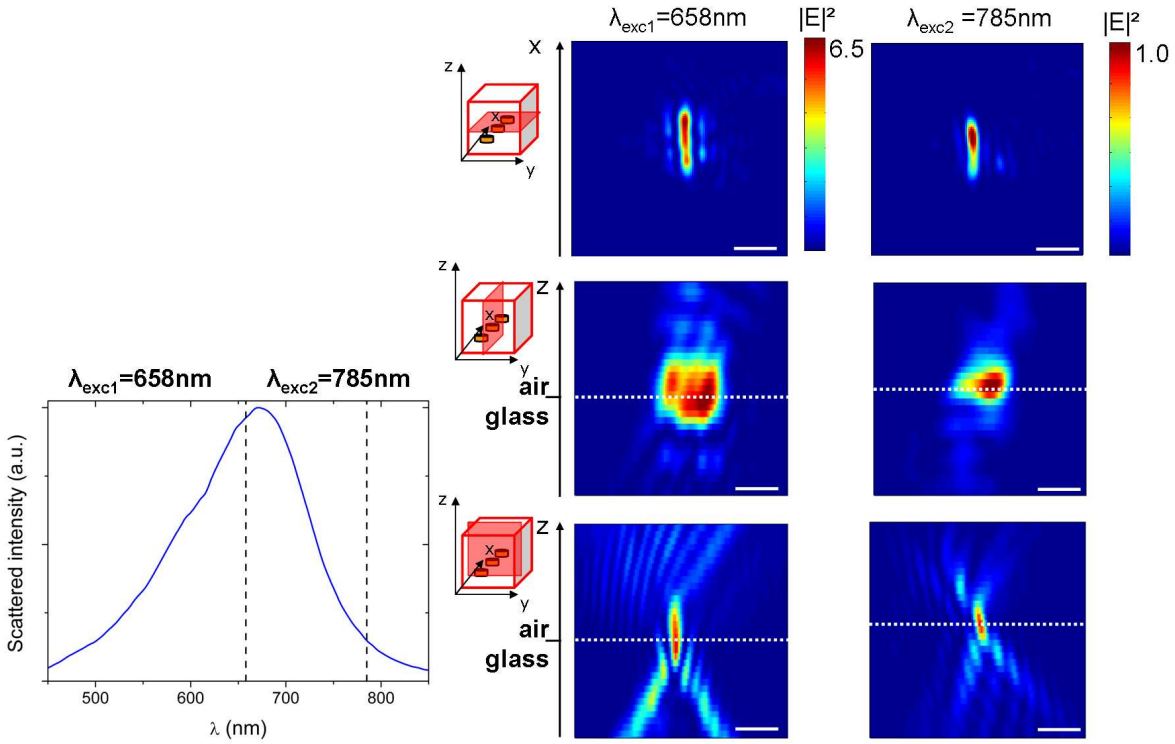

Figure 5.17 – Influence of the excitation wavelength. (a) Measured scattering spectrum of a chain ($n = 17$, $d = 150$ nm, gap$= 20$ nm). (b) Intensity of the scattered field reconstructed from a single hologram at $\lambda_{exc,1} = 658$ nm (left column) and at $\lambda_{exc,2} = 785$ nm (right column). The scale bar is 2μm.

In the y-z plane, we observe an angular radiation pattern featuring two relatively indistinct hot spots at $\lambda_{exc,2}$, whereas in the case of the resonance wavelength $\lambda_{exc,1}$, three hot spots are identified (along the z-axis). In addition, the angular shape of the three hot spots is recognized again in the corresponding x-y plane of the chain. The size of the hot spots along the z-axis is evaluated as 2.9 ± 0.2 μm. In Fig. 5.17 (right column), in the x-z planes using $\lambda_{exc,2}$ illumination, i.e. far from the antenna's resonance wavelength, we notice that the distribution of the scattered light intensity is mostly uniform. At the resonance wavelength, we again observe a directional scattering along the z-axis. The maximum intensity is found along the z-axis, coincidentally with the hot spots measured in the y-z plane. Furthermore, it is expected that the system behaves differently when excited with a wavelength shorter than its resonance wavelength than when excited with a larger wavelength because. In the latter case, the system does not follow anymore the oscillations imposed by the external electric field. In fact, these considerations may be an explanation for the strong differences in the characteristics between the holographic images in Fig. 5.15 and Fig. 5.17.

Strong directional scattering and a higher number of hot spots are observed only in the case of an illumination wavelength close to the resonance of an antenna chain. Thus, these features are interpreted as strong evidence for a resonating chain. Furthermore, a strong directional scattering is one of the characteristics of a resonating antenna (Bharadwaj *et al.* 2009; Suck *et al.* 2011), hence we can speak of the nanodisk chain as a nanoantenna.

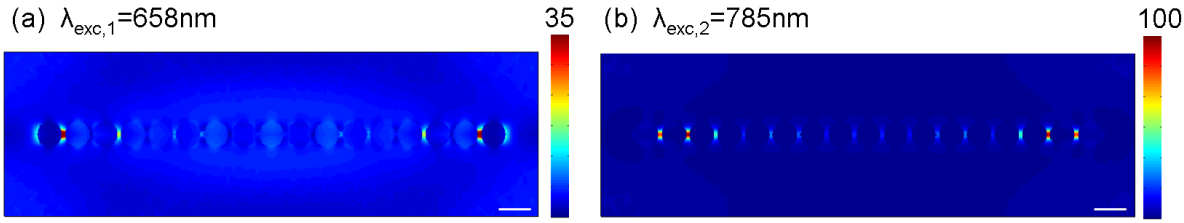

Figure 5.18 – Simulated near-field 10 nm above a chain of 17 disks (d=150 nm, gap=20 nm) for two exciting wavelengths: 658 nm and 785 nm. The scale bar is 200 nm.

However, when simulating the spatial scattering characteristics of this chain, the resulting near-field maps, shown in Fig. 5.18, reveal a contrary trend compared to the measured far-field images. The near-field enhancement is seen to be higher in the case of an excitation using $\lambda_{exc,2}$. Hence, it is assumed that the chain is nearer to its resonance for an excitation at 785 nm. In both illumination cases, the near-field distribution are similar, and the gaps with the highest near-field magnitude are close to the chain ends. This large discrepancy between measurement and simulation may be due to imperfections in the fabrication process, resulting in a different resonance position than for a perfect nanodisk chain.

In conclusion, both far-field images and near-field intensity maps change strongly their

scattering characteristics with the length of the exciting wavelength. The smaller the difference between excitation and resonance wavelength, the stronger the near-field enhancement and the far-field scattering.

5.2.5 Probing the Coupling of Nanodisk Chains by Holography

In conjunction with the discussion of the scattering spectra, we have seen that a strong coupling between disks in a chain induces a red-shift of the scattering resonance. By analysing the holograms, we were interested in verifying if the coupling also has an impact on the far-field scattering pattern. Figure 5.19 presents x-y and x-z plane images of holograms that were obtained on chains consisting of 20 disks. The gap increases from

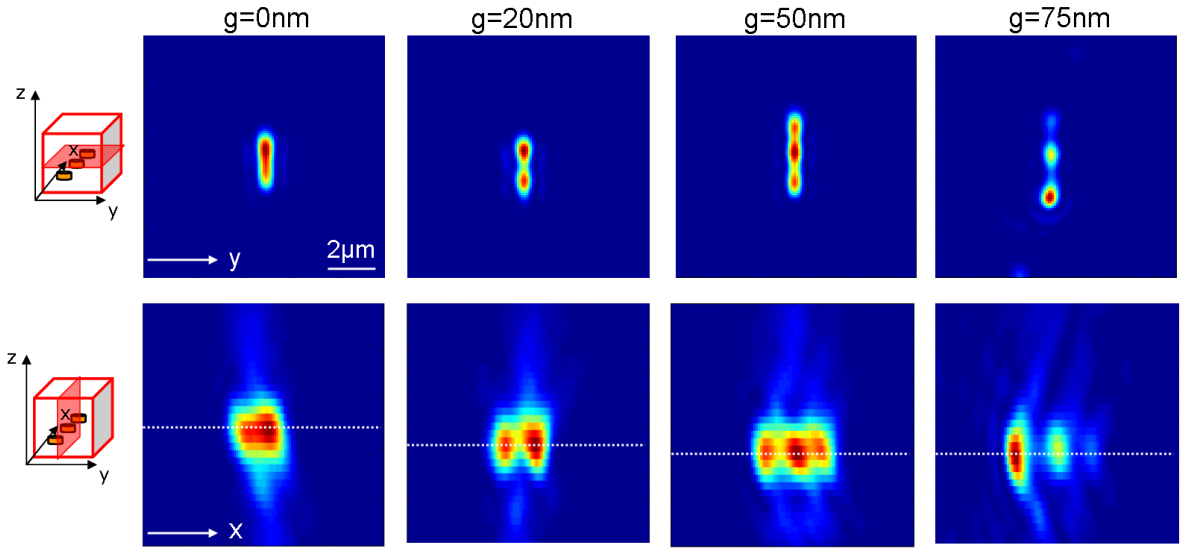

Figure 5.19 – Influence of the inter disk spacing on a chain: $n = 20$, $d = 100$ nm, varying gap: Cross sections along different planes centred on the antennas: x-y (top) and y-z planes (bottom). The scale bar is 2μm in all images. From left to right, the gap is increasing.

left to right, from touching disks (gap= 0) to 75 nm separated disks.

Regarding the x-y plane of the touching disks, the shape of the chain is recognized, its length is estimated from the image as 1.9 ± 0.1 μm. The scattering of this structure is uniformly distributed along the chain which is also revealed from the x-z plane image. A chain with touching disks can be considered like a single rod, in this case a 2 μm long structure, thus confirming the length estimation. By using a linearly polarized illumination along the chain axis, the rod-like structure behaves like a single dipole, resonating at this length in the microwave range.

When passing from the touching disks regime to the regime of strongly coupled disks (gap= 20 nm), the scattering map changes strongly. Now, two well distinctive hot spots

are recognized along the chain. Increasing further the gap distance, a third hot spot develops in the middle of the chain. Here, the highest field enhancement is observed at the chain centre. At a gap of 75 nm we can consider the disks in the chain as nearly uncoupled, as previously confirmed both by measured and simulated scattering spectra. Analysing the corresponding images, we notice that the scattered field of the hot spots becomes less intense, the scattering is strongest at one chain extremity, and the scattered field between the hot spots drops almost to zero. Hence, these features are considered as characteristics of a chain with (almost) uncoupled disks. Note that this feature is similar to the characteristic of a chain illuminated with transverse polarization (see Ch. 5.2.2).

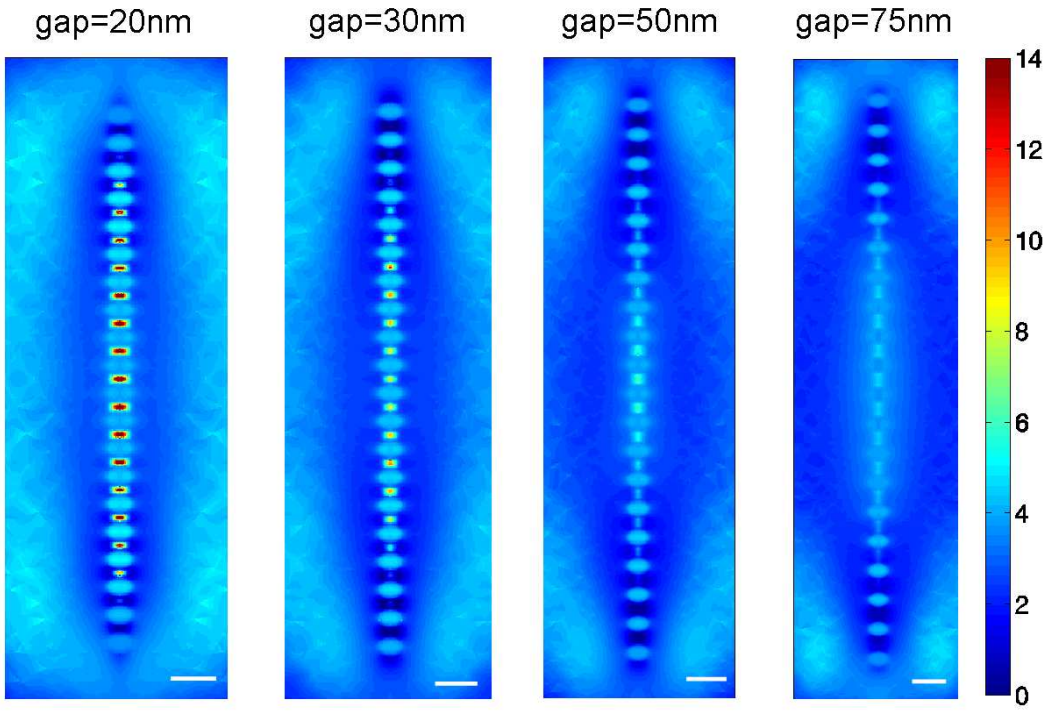

Figure 5.20 – Simulated scattered near-field, plotted 10 nm above the chain (20 disks, d=100 nm) for an exciting wavelength of 785 nm with varying gap spacing. The scale bar is 200 nm.

To complete our study of the influence of the coupling on the scattering characteristics, the corresponding intensity maps of near-field simulations are presented in Fig. 5.20. The color scale is the same for all images allowing a direct comparison between the images. Evidently, the near-field enhancement which is located in the gaps between the disks is strongest for the smallest gap width. The maximal near-field intensities are situated at the chain center. Increasing the spacing between the disks to 30 nm, the position of the maximal near-field enhancement shifts and is situated symmetrically around the chain center. The amplitude of the near-field decreases. Increasing the gap further, the near-field magnitude drops again. At a gap of 75 nm, no significant near-field enhancement is

observed any longer.

In summary, the near-field enhancement modifies its magnitude and its distribution on the chain with increasing gap size, i.e. decreasing coupling between the disks. Even though a direct comparison between the far-field maps and the near-field images is not feasible, the near-field simulations show that the coupling between the disks, expressed by the amount of the near-field intensity enhancement, vanishes at large gap widths. This characteristic supports strongly our observations in the far-field maps.

5.2.6 Imaging of Directional Scattering

Previously it has been observed that nanodisk chains scatter light in the direction perpendicular to their long axis which was revealed when analysing the scattering cross section of the y-z plane. One of the characteristics of an antenna at resonance is its directional scattering behaviour (Bharadwaj *et al.* 2009). Hence, under this point of view the nanodisk chain can be considered as a nanoantenna. In order to justify this, we will scrutinize in the following the feature of the directional scattering.

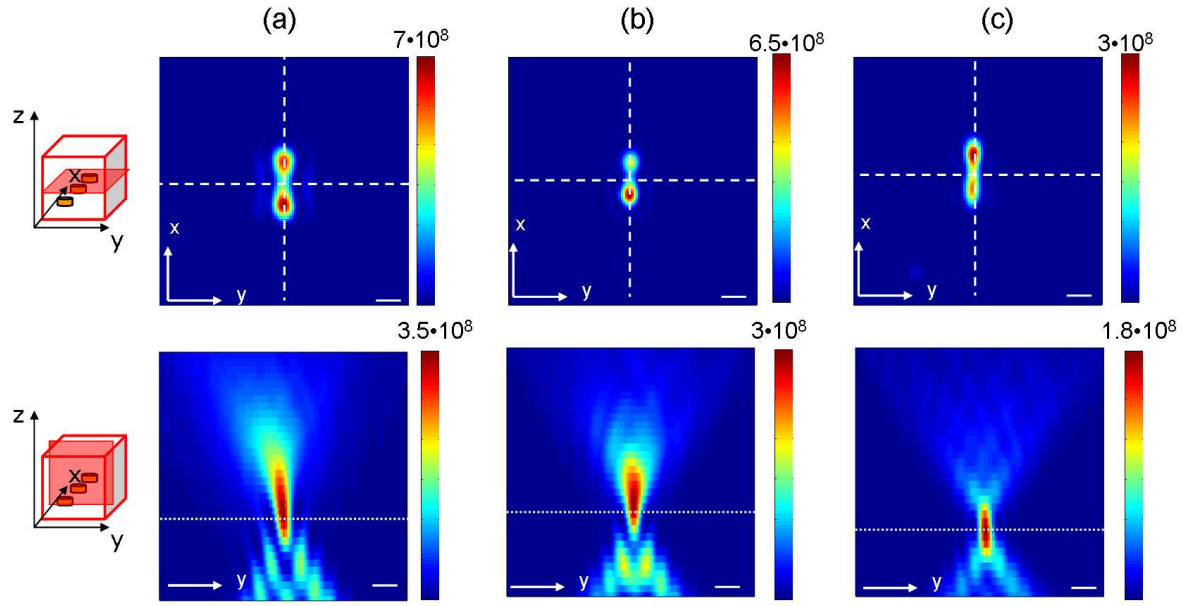

Figure 5.21 – Cross sections along the x-y and y-z planes of various chains: (a) n=15, gap=20 nm, d=150 nm (b) n=17, gap=20 nm, d=100 nm and (c) n=12, gap=100 nm, d=100 nm. The scale bar is 1 μm.

Figure 5.21 compares the scattering characteristics of three different chains. It is seen that the scattering in the y-z plane strongly differs between the chains. Whereas columns (a) and (b) reveal a strong scattering of light in the direction of the z-axis, the scattering observed in column (c) is rather weak. It is assumed that the latter feature is caused by the weak coupling between the disks due to the large gap.

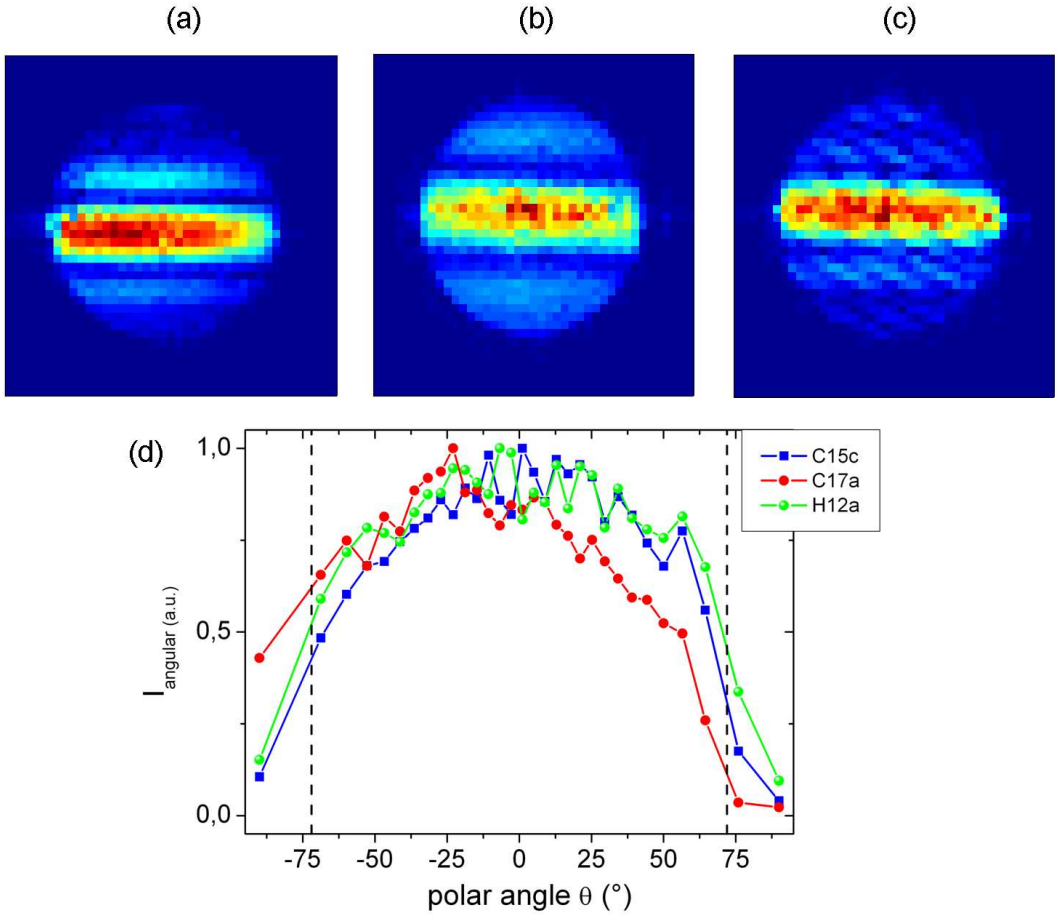

Figure 5.22 – Angular scattering pattern of three nanodisk chains: (a) n=15, gap=20 nm, d=150 nm (b) n=17, gap=20 nm, d=100 nm and (c) n=12, gap=100 nm, d=100 nm. (d) Angular normalized intensity $I_{angular}$ plotted against the polar angle θ.

Angular Scattering Pattern of Nanodisk Chains In order to analyse this directional scattering behaviour in more detail, we have plotted in Fig. 5.22 the Fourier planes corresponding to the three holograms. In Ch. 4 we have shown that the Fourier space contains the angular distribution of the scattered light, and used it to analyse the angular scattering of a single and two coupled disks. The three Fourier space images of the nanodisk chains are very similar. All images reveal a scattering intensity that is mostly distributed around the k_x-axis. The graph, displaying the angular normalized scattering intensity as a function of θ in Fig. 5.22 (d), shows in all three cases a scattering, homogeneously distributed around $\theta = 0°$, thus around the z-axis. Due to the low angular resolution of 5° it is difficult to reveal further angular features. The angular scattering images are dominated by the scattering of the disks itself, thus leading to the observed horizontal structure in the k-space.

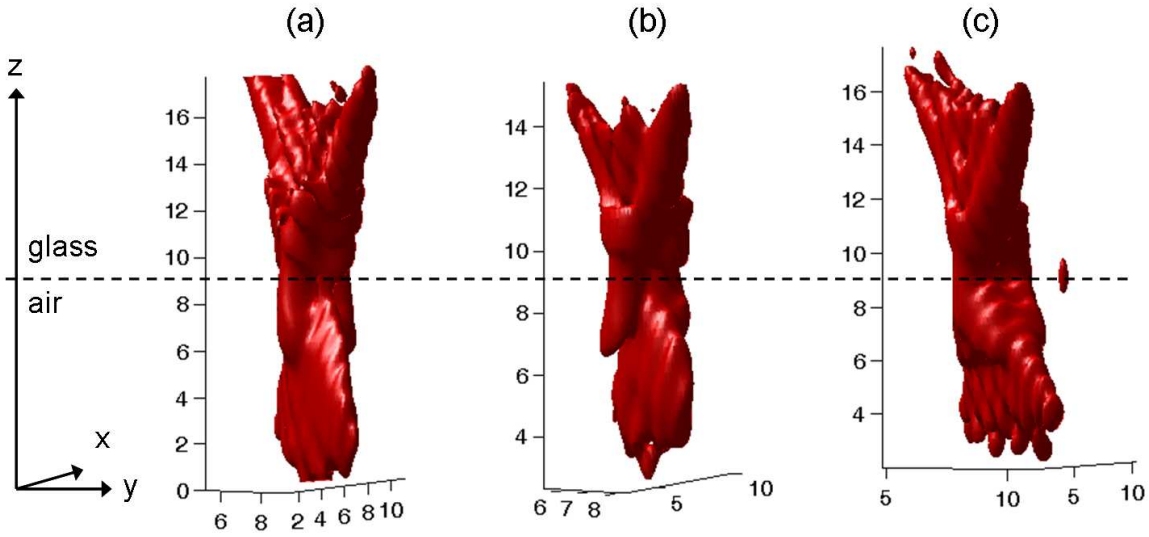

Figure 5.23 – Three dimensional surface plots of the scattered light by three nanodisk chains: (a) n=15, gap=20 nm, d=150 nm (b) n=17, gap=20 nm, d=100 nm and (c) n=12, gap=100 nm, d=100 nm. The images plot the surface at the threshold value of the intensity ($I = |E^{sc}|^2$) of $I_{max}/20$. The axes are given in μm. The position of the chains is found at a value of 9 μm at the z-axis, whereas lower z-values correspond to scattering in air and higher z-values to scattering in the substrate.

Three-Dimensional Surface Plots On this account, we examine the three-dimensional structure of the scattering maps of the three chains by drawing the three-dimensional shaded surface from a constant intensity of the scattered field by the three nanodisk chains, presented in Fig. 5.23. Note that in the following we will consider only the scattering into air, i.e. the scattering along z-values from 2 to 9 μm, the value at which the interface is situated. Firstly, comparing the values of the z-axis, we recognize that the scattering of chain (a) extends along a distance of about 9 μm, whereas the scattering surface of the other two chains terminates at 6 μm, which indicates a weaker scattering.

Analysing the scattering surfaces in more detail it is observed that the chains in Fig. 5.23 (a) and (b) reveal three connected lobes. Two lobes are situated near the ends of the chains and correspond to the point-like features observed in the x-y plane of Fig. 5.21. The third large lobe emerges in between the two former lobes and propagates further towards lower z-values. In particular, Fig. 5.23 (b) reveals the detachment of the large lobe at a z-value of about 7 μm. In comparison to the case of antenna (c), the latter features are less evident, the scattering is broader and less directive.

We conclude that the distinction between directional and non-directional scattering chains is not evident. The Fourier space images reveal an angular scattering distributed lobe-like around the z-axis, but due to the low angular resolution it is not possible to distinguish any further feature. An analysis of three-dimensional surface plots revealed three

lobes of scattered light into air, with a stronger central lobe propagating to further distances for a longer scattering chain. This feature thus confirms our previous observations in the three cross-sections of the far-field maps.

5.2.7 Conclusion on the Far- and Near-Field Maps of Nanodisk Chains

We have presented an extensive study of far-field and near-field scattering maps of nanodisk chains, revealing several scattering characteristics. It was shown that these characteristics depend strongly on extrinsic factors, such as the exciting wavelength or polarization, but also on intrinsic factors, characterized by the geometric structure of the chain, such as the disk spacings and the chain length. All these factors have an impact on the far-field scattering pattern and near-field maps. Typical features of a resonant chain are identified. The far-field scattering maps revealed so called "hot spots", zones on the chain that scatter light more intensely than others. FEM simulations have shown that a nanochain concentrates light in sub-lambda sized zones, notably the gap between the disks. This near-field concentration is not uniform, but the near-field on the chain reveals more and less intense zones. Such characteristics are reflected as well in far-field images, indicating that the hot spots in the near-field couple to the far-field. In general, the obtained results of the near-field simulations confirmed qualitatively the observed far-field characteristics. Coupling effects in the nanodisk chains were revealed by demonstrating that the near-field intensity changes in amplitude and in distribution when increasing the spacing between the disks. A similar feature was shown in the far-field scattering maps. When excited at resonance a nanodisk chain exhibits a strong directional scattering perpendicular to its axis. This observation leads one to the conclusion that a resonating nanodisk chain behaves like a nanoantenna. This property has been examined more closely by discussing the features of Fourier space images and by analysing three-dimensional surface plots of different chains. We have shown that the technique of heterodyne holography proves to be an excellent tool to map the scattered field of plasmonic structures which has the ability to reveal various characteristics.

5.3 Probing the Plasmonic Coupling of Disks by Heating

The precedent section demonstrated that the coupling strength between the disks in the chain has a crucial impact on the scattering distribution both in the far-field and in the near-field. However, holographic measurements do not allow a direct comparison of the measured amplitudes as explained in Ch. 4.3.3, and a qualitative study of the coupling strength is not feasible.

The technique of photothermal heterodyne holography has lately proven its capability to map the scattered fields of heated metal nanoparticles (Absil *et al.* 2010) and to perform frequency resolved temperature imaging in integrated circuits (Suck *et al.* 2010). Photothermal excitation is a well established technique for the sensitive detection of absorbing objects. A modulated optical beam is sent on the sample, creating a localized heating, which in turn induces a variety of phenomena including e.g. infrared emission, thermal expansion, refractive index changes (Rosencwaig *et al.* 1985) or photon absorption in the case of a heated metal. Hence, in the case of metallic nanostructures, the optical beam induces a heating which is maximal if the heating beam is tuned to the localized plasmon band of the nanostructure. For example, Baffou *et al.* developed recently a thermal imaging technique based on fluorescence polarization anisotropy measurements, which enabled the mapping of the local temperature near nanometer-sized heat sources, and applied it to plasmonic structures (Baffou *et al.* 2009; Baffou *et al.* 2010).

Relying on absorption, which scales as the volume of the particle, is clearly an advantage for the detection of very small particles in comparison to scattering, which varies as the square of the particle volume. A detailed description of the photothermal holography technique is found in Ch. 2.4.

For the purpose of a qualitative and quantitative investigation of the coupling strength between nanodisks in a chain, we use here the technique of photothermal holography to heat the plasmonic chains and to map the resulting absorption of photons. In the present case the clear advantage of photothermal holography to direct heterodyne holography is the measurement of the signal due to absorption which does not depend on scattering fluctuations. Thus, a direct comparison of the measured photothermal signals between different configurations is feasible. Moreover, photothermal images obtained in this way deliver a signal which can be considered - in good approximation as we will show later - directly proportional to the temperature.

This section will demonstrate maps of the photothermal signal of nanoparticle chains and compare them to purely scattered field maps. The influence of the polarization of the heating laser beam will be revealed. Furthermore, we will show that the magnitude and the spatial distribution of the photothermal signal is directly related to the coupling strength between the disks in a chain.

5.3.1 Comparison of Holographic and Photothermal Images

In comparison with holographic imaging which relies on the measurement of scattered photons, photothermal detection images effects induced by absorbed photons. Hence, the two imaging techniques originate from different physics, and a significant difference in the resulting intensity maps is expected. In this section, we will compare qualitatively photothermal images to corresponding holographic intensity maps. Furthermore, the impact of the polarization of the heating beam on the resulting images will be examined.

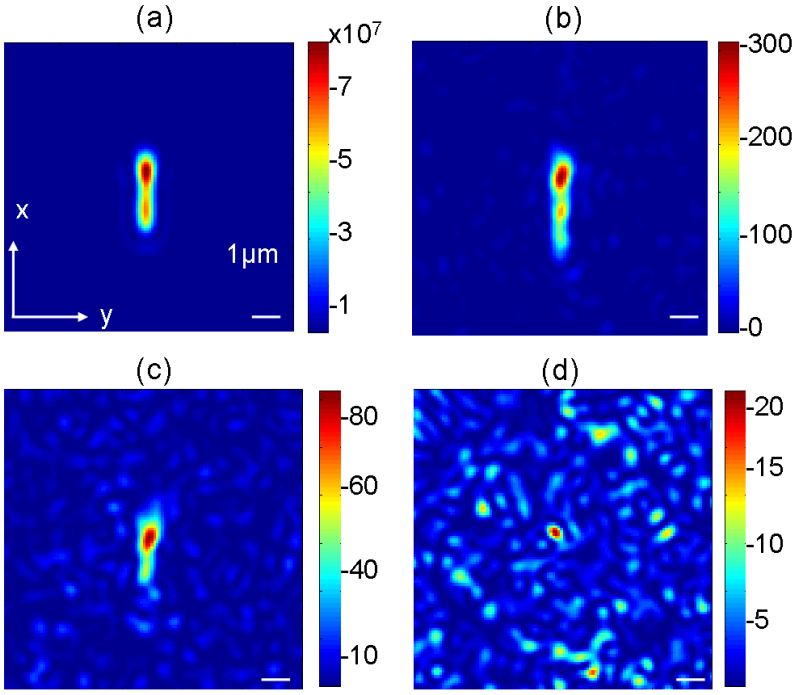

Figure 5.24 – (a) A holographic intensity image of a chain of 17 disks (d=150 nm, gap=10 nm). (b-d) Photothermal holograms of the same chain heated up by a λ=532 nm laser modulated at F_H=1011 Hz with an average power of 0.55 mW. In (b) the polarization of the heating beam is parallel to the chain axis and in (c) perpendicular to the chain axis. (d) The heating laser is switched off (d). The length scale is 1 μm.

Figure 5.24 presents different top view images (x-y plane) of the same chain (17 disks, d=150 nm, gap=10 nm), each image was recorded under a different configuration:

(a) scattered intensity map

(b) photothermal image using a heating beam polarized parallel to the chain axis

(c) photothermal image using a heating beam polarized perpendicular to the chain axis

(d) photothermal image without heating

Direct holography is performed using a laser at a wavelength of 785 nm, and photothermal holography was carried out with a 532 nm laser modulated at a heating frequency of F_H = 1011 kHz. The laser beam had an average power of P_{Heat} = 0.55 mW, reaching a region of about 44 μm^2 of the sample. This results in a mean power density of 1250 Wcm^{-2}. This value has been maintained during all photothermal measurements.

Regarding Fig. 5.24, it is evident that the photothermal maps differ strongly from the holographic image. This discrepancy reflects well the difference between both techniques.

Whereas holography records the amount of scattered light, photothermal holography is sensitive to the information of optical absorption by the heated structure. Comparing the maps shown in Fig. 5.24 (a) and (b), the shape of the chain is well reproduced in both cases. The photons scattered by the chain reveal an elongate structure with around 2.3 μm length, whereas the photothermal signal forms a structure of approximately 2.7 μm length. This length corresponds to the actual chain length, i.e. 2.7 μm. Furthermore, the image in Fig. 5.24 (b) displays a non-uniform photothermal signal. Two hot spots are detected which may correspond to zones that have a different temperature.

Comparing the photothermal maps of Fig. 5.24 (b) and (c), it is observed that the shape strongly changes with the polarization of the heating beam. In Fig. 5.24 (c) a length of about 1.7 μm is recognized, much less than in Fig. 5.24 (a) or (b) due to a lower signal. Regarding the amplitudes, it is clear that the photothermal intensity amplitude with parallel heating is more than 3.5 times higher than with heating perpendicular to the chain. This polarization dependence has been also reported elsewhere (Baffou *et al.* 2010). Evidently, a chain heated with a beam perpendicular to the chain axis exhibits a different heating distribution and heats less. In Fig. 5.24 (d), no photothermal signal at all is perceivable. We detect only the noise which is expected for a photothermal detection without any heating. Images obtained in this way serve us primarily to control the correct functioning of the photothermal detection.

In conclusion, the images in Fig. 5.24 have shown a great discrepancy between the holographic and photothermal maps which confirms that the two techniques underlie different physical origins. Whereas "pure" holography records scattered photons, photothermal holography records the absorption of photons due to optical heating.

5.3.2 Photothermal Imaging of Nanostructures - An Analytical Analysis of the Photothermal Signal

We have seen that photothermal images taken from a metallic nanostructure differ strongly in amplitude and shape from the corresponding scattering image proving that those images carry different kinds of information on the nanoobject. In order to understand qualitatively the origin of the photothermal images of nanostructures, with the help of Rémi Carminati we performed an analytical analysis of the photothermal signal obtained by heterodyne photothermal imaging.

We consider the following situation, illustrated in Fig. 5.25. A metallic nanostructure of volume V and with dielectric constant ε is illuminated by an incident field E_0 which corresponds to the object beam of the holographic setup. The resulting scattered field $E_S(\vec{r}, \Omega)$ is then detected at point $\vec{r}$ in the far-field. Due to the heterodyne detection, the scattered field is modulated at the frequency Ω.

For an analytical description of the electric field, we use the Green function formalism.

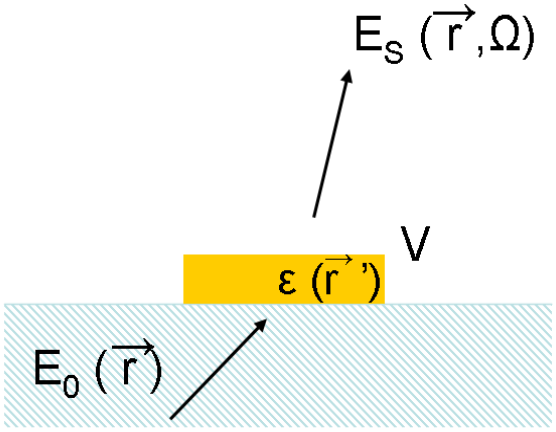

Figure 5.25 – Sketch clarifying the detection of the photothermal signal by holography. V denotes the volume of the heated nanoobject with the dielectric constant ε, E_0 is the incident field (the object beam) and $E_S(\vec{r},\Omega)$ denotes the photothermal signal, modulated at the frequency Ω, which is detected at point $\vec{r}$.

In electromagnetic theory, the dyadic Green function $\mathbf{G}(\vec{r},\vec{r'})$ renders the electric field at the field point $\vec{r}$ due to a single point source $\vec{j}$ at the source point $\vec{r'}$ (Novotny and Hecht 2006). The solution of the situation depicted in Fig. 5.25, describing the total electric field at point $\vec{r}$, is written as follows:

$$E(\vec{r}) = E_0(\vec{r}) + k^2 \int_V \mathbf{G}(\vec{r},\vec{r'})[\varepsilon(\vec{r'}) - 1]E(\vec{r'})d^3\vec{r'} \tag{5.1}$$

with k the wave vector, i.e. $k = 2\pi/\lambda$. The first term $E_0(\vec{r})$ denotes the incident field which is used to probe the light scattered by the nanoobject. The second term describes the field scattered by the object. The dielectric constant is wavelength and temperature dependent. When a metallic nanostructure is heated, the temperature difference will result into a variation of the dielectric constant:

$$\varepsilon(\vec{r'}) = \varepsilon(\vec{r'},T_0) + \frac{\partial\varepsilon}{\partial T}\Delta T(\vec{r'}) \tag{5.2}$$

The first term stands for the initial dielectric constant at the initial temperature T_0, and the second term denotes the dielectric constant variation which is proportional to the local heating $\Delta T(\vec{r'})$.

In photothermal heterodyne holography, a modulated heating beam is used, which creates a temperature modulation at the frequency Ω. As a result, the field $E(\vec{r})$ at point $\vec{r}$ is composed of a non-modulated and a modulated term:

$$E(\vec{r}) = E(\vec{r},\Omega = 0) + E(\vec{r},\Omega) + \cdots \tag{5.3}$$

The dots stand for modulations at higher harmonics, which are not detected due to the heterodyne detection at frequency Ω and can therefore be neglected.

In holography, the signal is given by the interference term $E_H = E_S \cdot E_R^*$, with E_R as the reference wave, therefore, the scattered field $E_S(\vec{r}, \Omega)$ (Eq. 5.1) which is detected, results into:

$$\begin{aligned} E_S(\vec{r}, \Omega) &= k^2 \int_V \mathbf{G}(\vec{r}, \vec{r'})[\varepsilon(\vec{r'}, T_0) - 1]E(\vec{r'}, \Omega)d^3\vec{r'} \\ &\quad + k^2 \int_V \mathbf{G}(\vec{r}, \vec{r'}) \frac{\partial \varepsilon}{\partial T} \Delta T(\vec{r'}) E(\vec{r'}, \Omega = 0) d^3\vec{r'} \end{aligned} \tag{5.4}$$

The first term in Eq. 5.4 corresponds to the scattered field due to multiple scattering which results from the "normal" holographic detection. This term is also affected by the Ω modulation. The second term denotes the field that corresponds to the temperature increase ΔT which is caused by the modulation of the dielectric constant of the nanostructure $\partial\varepsilon/\partial T$.

As Eq. 5.4 shows, photothermal holography detects both the scattering and the photothermal term. Therefore, the signal that is detected by photothermal holography is a superposition of the light scattered by the nanostructure and of the electromagnetic field which results from the change in the dielectric constant. Since the aim of this analytic study is to analyse the photothermal signal, we will restrict the following analysis on the second term in Eq. 5.4.

Firstly, we consider the dielectric constant. The variation of the dielectric constant with temperature is very small, typically between $10^{-3} - 10^{-2}$, and we can assume: $|\partial\varepsilon/\partial T|\ |\Delta T| \ll 1$. Hence, the modulated part of the dielectric constant describes a weakly scattering object. As a result we have an effective scatterer, and the Born approximation can be applied which consists of taking the incident field in place of the total field as the driving field at each point in the scatterer, i.e.:

$$E(\vec{r'}, \Omega = 0) \simeq E_0(\vec{r'}) \tag{5.5}$$

Secondly, we regard the conduction timescale, described by $\tau_{cond} = L^2/\alpha_{th}$ with the characteristic length L (in this case L corresponds to the size of the nanostructure) and the thermal diffusivity α_{th}. The conduction time τ_{cond} is very small compared to the frequency modulation, i.e. $\tau_{cond} \ll 1/\Omega$. [2] Under this assumption, the temperature variation ΔT is uniform and independent on $\vec{r'}$.

Taken these considerations into account we can re-write the photothermal term in Eq. 5.4, and we obtain the following equation where it can be safely assumed that the detected photothermal signal is proportional to the temperature increase ΔT in the nanostructure:

$$\boxed{E_S(\vec{r}, \Omega)_{phth} \simeq k^2 [\int_V \mathbf{G}(\vec{r}, \vec{r'})\ \frac{\partial \varepsilon}{\partial T}\ E_0(\vec{r'}) d^3r']\ \Delta T} \tag{5.6}$$

[2] The thermal diffusivity of gold is ${\alpha_{th}}^{Au} = 1.27 \cdot 10^{-4}$ m^{2}sec^{-1}. The smallest nanostructures under study have a typical size of around $L = 100$ nm (considering a single disk). Hence, we calculate a conduction time of ${\tau_{cond}}^{singledisk} \cong 8 \cdot 10^{-11}$ sec which is indeed very small compared to a typical modulation of 1000 Hz, i.e. $1/\Omega = 1 \cdot 10^{-3}$ sec.

It follows directly from Eq. 5.6 that the recorded interference term $|E_H| = |E_S \cdot E_R^*|$ is proportional to the temperature increase ΔT. Therefore, the reconstructed hologram $I_{Heat} = |E_O|^2$, which is given by the square modulus of the reconstructed field (E_O), is proportional to $|\Delta T|^2$.

In summary, we have shown that the technique of photothermal holography probes indeed the temperature increase of a nanostructure. Therefore, it results that the temperature spatial distribution can be probed with a resolution equal to the spatial resolution of the holographic setup which is near the diffraction limit.

5.3.3 Photothermal Signal and Absorption Cross Section

In the previous section we have shown by an analytical approach that the photothermal signal is proportional to the induced temperature increase in the nanostructure. Here, we are interested into verifying experimentally this proportionality of the photothermal signal.

We have seen that the measured photothermal intensity I_{Heat} is proportional to $|\Delta T|^2$. The temperature increase ΔT itself is proportional to the absorption cross section and the heating power, i.e. $\Delta T \propto C_{abs} P_{Heat}$.

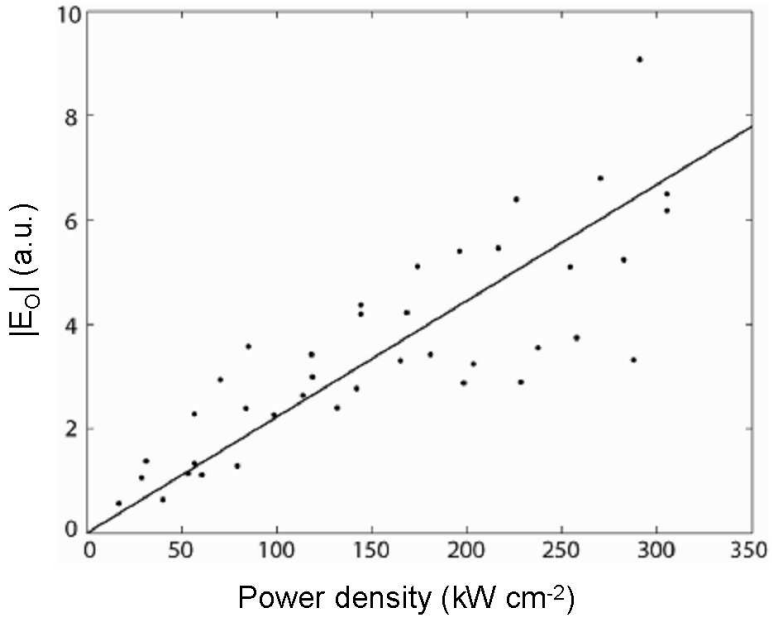

Figure 5.26 – Power density dependence of the reconstructed photothermal holographic signal $|E_O|$ (a.u.) from a single 50 nm particle, averaged over pixels located in the vicinity of the particle, for a heating frequency $F_{AOM3} = 5$ kHz. The graph is taken from Absil et al. (2010).

In a precedent study, our group has investigated the photothermal signal of 50 nm gold

beads, spin coated on a glass substrate and immobilized in a Poly Vinyl Alcohol (PVA) matrix (Absil *et al.* 2010). In this study, an analysis of the photothermal holographic signal has been presented by plotting $|E_O|$ against the heating power density. Figure 5.26 plots the corresponding graph which is taken from Absil *et al.*. The graph reveals the proportionality of the photothermal signal to the heating power. Thus, assuming that the heating power is proportional to the induced temperature increase, we confirm the photothermal origin of the observed signals.

Here, we intend to prove the proportionality on the example of the nanostructures. It has to be noted that due to the lack of time to perform an exhaustive time-consuming study and a complete analysis of the photothermal signal, the following analysis is limited to a small number of measurements and is therefore of preliminary nature. A complete study is planned as soon as possible.

All measurements are performed at a fixed heating laser power in order to avoid damaging the nanostructures due to elevated power densities. Therefore, only C_{abs} has to be considered as a changing variable. The absorption cross section scales with the volume of the heated structure. Because the height of the disks is constant, it is expected that the temperature increase is proportional to the surface of the nanostructure, A.

In order to exclude any coupling effects that may have an impact on the photothermal signal, only chains with touching disks are considered here. In this case we have rod-like nanostructures where the proportionality stated above (Eq. 5.7) is valid. As a result, the following proportionality has to be verified on these nanostructures:

$$I_{Heat} = |E_S \cdot E_R^*|^2 \propto A^2 \tag{5.7}$$

where I_{Heat} denotes the measured photothermal intensity.

Previously, by analysing holographic scattering images (e.g. see Ch. 4), we have learnt that the amplitude of the scattered intensities cannot be directly compared, which is due to the high sensitivity of the resulting holograms towards the property of the object beam. Although photothermal holography probes the temperature increase in the heated nanostructures, we have seen from Eq. 5.4 in Ch. 5.3.2 that the detected signal in photothermal holography results from a superposition of the purely scattered field and of the photothermal field which is proportional to the modulation of the dielectric constant.

Hence, in order to extract the photothermal signal, we performed the following operation: Firstly, assuming that the temperature increase is homogeneous over the entire chain of the touching disks, we calculate the average intensity signal of the photothermal images over the chain surface, and we obtain $\overline{I}^S_{Heat}$. The background intensity $\overline{I}^{BG}_{Heat}$ which is calculated by integrating over an equal sized zone next to the structure, is subtracted from $\overline{I}^S_{Heat}$. Next, we have to consider that the photothermal signal is however correlated to the scattering signal. In order to take this correlation into account, we therefore average the scattered intensity obtained from the direct hologram of the structure over

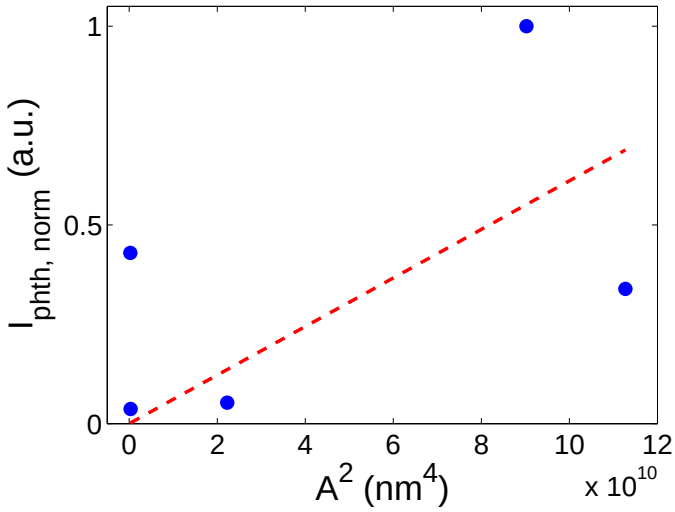

Figure 5.27 – Normalized photothermal intensity I_{phth} as a function of the square surface A^2 of different chains composed of touching disks. The dashed line is a linear fit of type $y = a \cdot x$.

the same surface used for the photothermal signal, and $\overline{I}^S_{holo}$ is obtained. This value is also corrected from the background by subtracting $\overline{I}^{BG}_{holo}$. Finally, we divide the background corrected photothermal signal by the background corrected scattered signal, and the corrected photothermal intensity I_{phth} is calculated which will be used in the following.

$$I_{phth} = (\overline{I}^S_{Heat} - \overline{I}^{BG}_{Heat})/(\overline{I}^S_{holo} - \overline{I}^{BG}_{holo}) \tag{5.8}$$

In Fig. 5.27 the normalized photothermal intensity, $I_{phth,norm}$, (normalized to 1) is plotted as a function of the square surface A^2 for several chains. The present values give an approximate indication of the expected behaviour. However, we notice that the values deviate from an expected linear behaviour. This is due to the small number of measurements, but also to fluctuations of the heating laser power which is not actively stabilized [3]. Small fluctuations in the heating power may be expected. Furthermore, potential fabrication defects of a heated chain (e.g. missing disks, residues of the resist, supplementary metallic material, etc.) would result into a strong variation of the heated signal since the distribution of heat is expected to change abruptly. A statistical approach is missing at this stage to validate properly the expected proportionality.

5.3.4 Photothermal Holography Reveals Coupling of Nanodisk Chains

The main result of the analytical analysis in Ch. 5.3.2 stated that photothermal holography probes directly the increase in temperature of a heated nanostructure. However, the

[3] The manufacturer announces a variability of 10%

proportionality of the photothermal signal to P_{Heat} is only valid in the case of uncoupled disks. When the coupling strength begins to play a significant role, it affects the photothermal signal in amplitude and distribution on the heated nanostructure. A different distribution of heat must be taken into account resulting into a change in temperature.

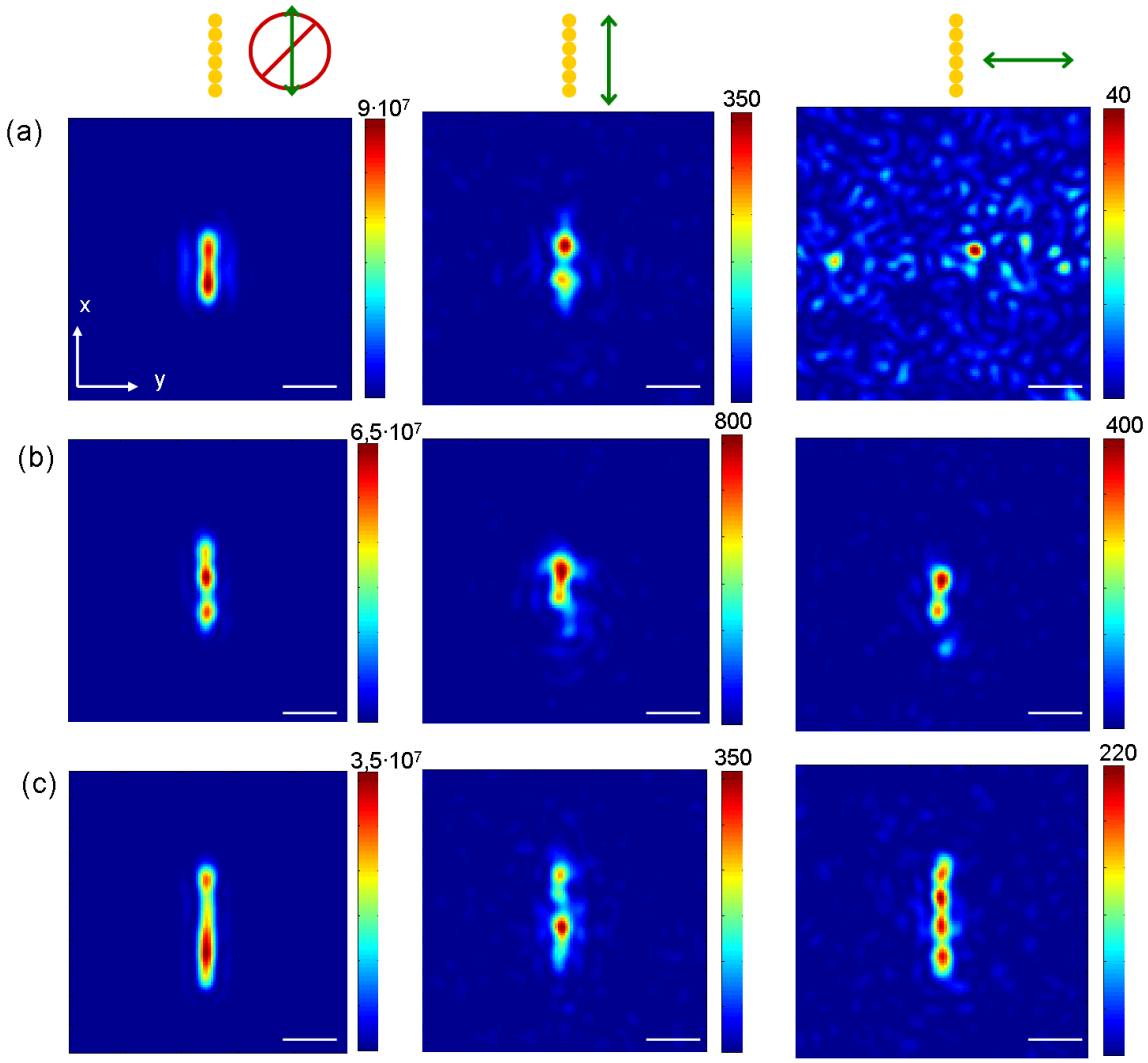

Figure 5.28 – x-y planes of holographic (left column) and photothermal images (with a modulation of $F_H = 1011$Hz) of a chain consisting of 17 disks of 150 nm diameter. The interdisk spacing changes from 0 nm (a) over 20 nm (b) to 75 nm (c). The central (right) column represents the photothermal images obtained with parallel (perpendicular) polarized heating laser. The length of the scale is 2 μm.

In order to study in detail the absorption behaviour of differently coupled nanodisk chains, series of photothermal measurements of chains are performed and compared to the corresponding scattering maps. Photothermal intensity maps are recorded with either a heating beam polarized parallel or perpendicular to the chain, i.e. denoted in the following as $Heat \parallel$ or $Heat \perp$. Chains consisting of 17 and 19 disks are investigated. The resulting

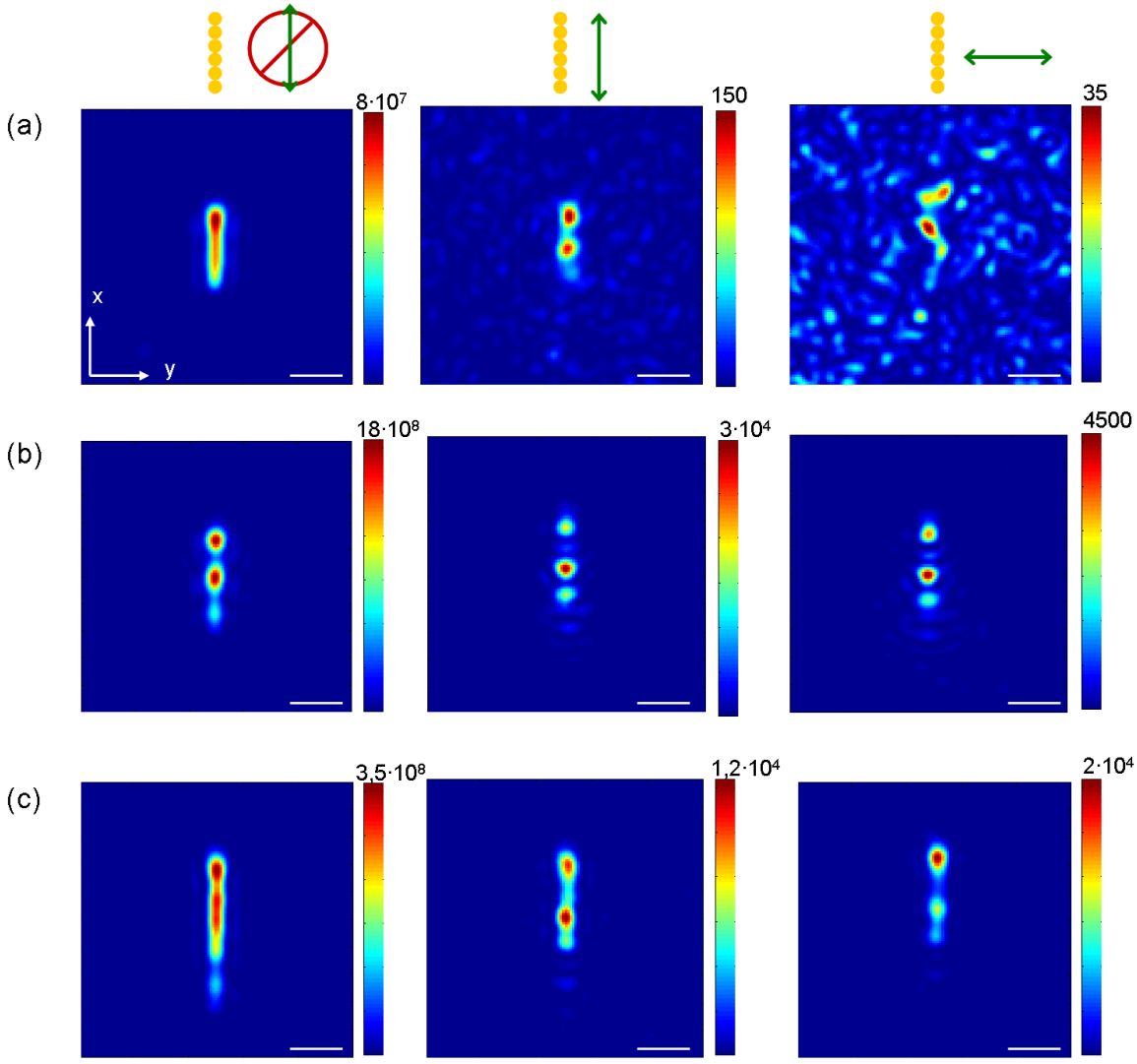

Figure 5.29 – x-y planes of holographics (left column) and photothermal images (the modulation is $F_H = 1011$ Hz) of a chain consisting of 19 disks of 150 nm diameter. The interdisk spacing changes from 0 nm (a) over 20 nm (b) to 100 nm (c). The length of the scale is 2 μm.

images are plotted in Fig. 5.28 and 5.29. Analysing the images, we observe three main features:

(i) The photothermal maps (central and right columns) distinguish themselves strongly from their corresponding scattering field maps (left columns).

(ii) The magnitude of the photothermal images obtained with parallel heating is in general larger than with perpendicular heating.

(iii) Comparing parallel and perpendicular heating maps, both photothermal maps of coupled disks (see Fig. 5.28(b) and Fig. 5.29(b)) are similar, while the photothermal maps of chains with touching (Fig. 5.28(a) and Fig. 5.29(a)) or largely spaced disks (Fig. 5.28(c) and Fig. 5.29(c)) are very different from each other.

The first two features have been observed already previously (see in Ch. 5.3.1). The last feature, however, is new and an interesting one. It means that the heat distribution in a coupled nanostructure is mostly independent from the polarization of the heating beam, and mainly the magnitude of the photothermal signal, i.e. the temperature increase changes.

Figures 5.28 and 5.29 present a selection of photothermal maps of a series of measurements as a function of the gap, and we are interested into studying quantitatively the influence of the coupling between the disks on the induced temperature increase. Therefore, we calculated for both heating polarizations the corrected photothermal intensities I_{phth} for different disk spacings in a chain. The results for two different chain types are shown in Fig. 5.30 (a,b) where I_{phth} is plotted as a function of the gap. Analysing the graphs, we note that I_{phth} rises with increasing gap and then exhibits a maximum between a gap of 20 nm and 30 nm, before the amplitude drops again. Independently of the chain length or heating polarization, the trends are the same in both graphs. The main difference lies in the amplitudes which are lower in the case of $Heat\ \perp$, as it was already observed before by analysing the photothermal images.

In order to account for the coupling strength between the disks in the chains, we chose to plot the difference between both curves, i.e. $(I_{Heat,\parallel} - I_{Heat,\perp})$ denoted as ΔI_{phth}. The resulting values are plotted in Fig. 5.30 (c,d). Both graphs exhibit a global maximum at a gap of 20 nm. Under the assumption that the coupling strength between the disks in a chain is proportional to ΔI_{phth}, the observed characteristics in Fig. 5.30 (c,d) reflect well the expected coupling behaviour in a nanodisk chain: In the regime of touching disks (gap=0nm) any near-field coupling can be excluded. The chain behaves like a large rod-like structure. An example of a chain with touching disks is given in Fig. 5.31. For a gap of 10 nm, a strong near-field coupling would be expected, which is here however not the case, due to imperfections in the fabrication process leading to inaccurate gap spacings. Hence, at a gap spacing of 10 nm we are very likely still in the touching disks regime.

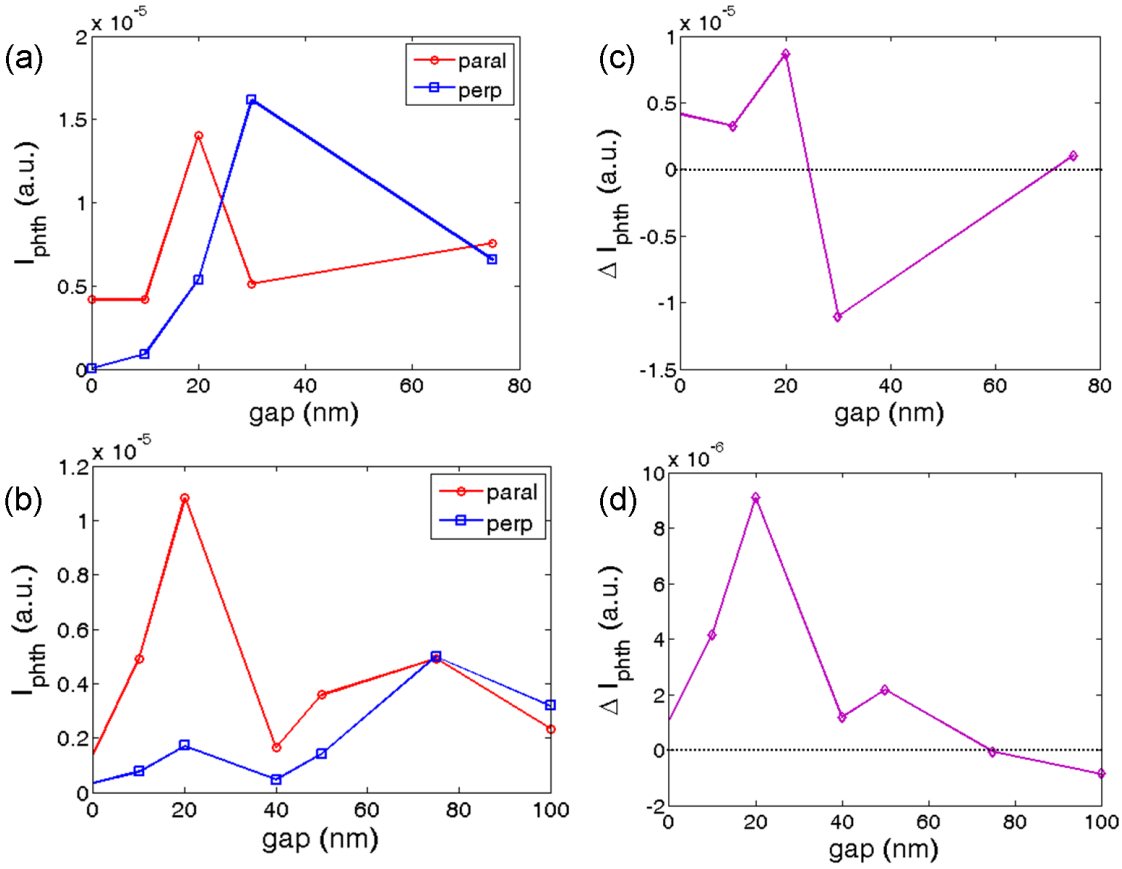

Figure 5.30 – Comparison of photothermal signals of $Heat \parallel$ and $Heat \perp$ for a chain of 17 (a,c) and 19 (b,d) disks (d=150nm): (a,b) Corrected photothermal signal I_{phth} as a function of the gap. (c,d) $\Delta I_{phth} = I_{Heat,\parallel} - I_{Heat,\perp}$ as a function of gap.

Increasing the gap to a width of 20 nm, ΔI_{phth} exhibits a maximum, indicating a strong coupling which is expected for a small disk spacing.

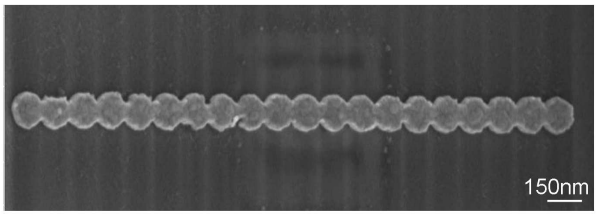

Figure 5.31 – SEM image with a tilted sample (37°) of a chain composed of 20 touching disks (150 nm diameter).

For the 17 disks chain with a gap of 30 nm, ΔI_{phth} drops to negative values, which means that $I_{Heat,\perp}$ is larger than $I_{Heat,\parallel}$. At a gap of 75 nm, ΔI_{phth} is almost zero, indicating that at this gap width the disks are already in an uncoupled regime. In fact, heated uncoupled disks in a chain are expected to behave like single disks, hence no difference between $I_{Heat,\parallel}$ and $I_{Heat,\perp}$ would be expected. In the case of the 19 disks chain (Fig. 5.30 (d)) ΔI_{phth} decreases relatively steadily from its maximum at a gap of 20 nm. It approaches zero at a disk distance of 75 nm and drops to a negative value for the largest gap. Previously, both spectroscopic measurements and holographic images have revealed that the disks in a chain are uncoupled for a large gap. Hence, the photothermal analysis is in agreement with our previous studies on coupling.

Overall, the photothermal analysis confirms qualitatively the results obtained in previous studies of the coupling regime in nanodisk chains. Furthermore, the measurements of the photothermal signals proved to give an additional quantitative insight.

5.3.5 Conclusion on Photothermal Imaging of Nanodisk Chains

In conclusion, we have shown that the technique of photothermal holography proves to be a novel imaging technique to probe the temperature increase in heated nanostructures. We have presented the fundamental difference between photothermal maps and scattering images. An analytical analysis has shown that the photothermal signal that is detected by our holographic setup is proportional to the temperature increase in the heated nanostructure.

The experimental validation for this proportionality was performed on chains with touching disks. However, a significant interpretation of the results was not possible due to the very limited number of the experimental data. A statistical analysis is planned.

Furthermore, we have shown that photothermal images differ strongly in amplitude and shape, depending on the coupling strength of the disks in a chain and on the polarization of the heating beam. A concrete analysis of the photothermal intensity allowed us to quantify

the coupling strength in two chains. The obtained results correspond qualitatively very well to spectroscopic and holographic results obtained previously.

5.4 Coupled Triangles

After extensively discussing the interaction of nanodisk chains with light, we will turn our attention to the coupled triangles structure, presented in Ch. 3, which consists of two 1 mm long right-angled tapered triangles closely spaced by a gap.

The origin of the idea to design this structure lies in the possibility to study the resonance modes of a coupled nanostructure as a function of the structure's size. In fact, when illuminating two coupled triangles with a beam polarized along the short leg axis, it is assumed that, due to the sharp angle, the triangle's width increases slowly with increasing length. Illuminating two closely spaced triangles with a beam polarized along the short leg axis, coupling effects alongside the gap are expected, resulting into near-field effects, modified plasmon resonance modes and modified far-field scattering. In fact, this design can be seen qualitatively as a system of coupled stripes with continuously changing length of the stripes. Under these considerations we are interested into studying the resonating modes of two coupled triangles as a function of its width and its gap size.

It has to be noted that the findings presented here are preliminary results and provide only a limited insight into the scattering characteristics of these novel structures. Another series of experiments and simulations are planned in the future. However, the study of the triangles resulted into interesting observations which we would like to present in the following.

Scattering and Photothermal Maps Revealing Resonances of Triangles For the study of the triangles we used direct and photothermal holography with the purpose of recording scattering and heating maps. To record the holographic images we use an illumination beam at a wavelength of 785 nm, polarized along the short axis of the triangles. For the study of the triangles we used direct and photothermal holography with the purpose of recording scattering and heating maps. To record the holographic images we use an illumination beam at a wavelength of 785 nm, polarized along the short axis of the triangles. The photothermal measurements were performed using a heating laser at 532 nm with an average heating power of 90 mW at a modulation frequency of $F_H = 511$ Hz. The heating beam is polarized parallel to the short axis of the triangles, i.e. along the same direction as the illumination beam, which is illustrated in the left-handed scheme in Fig. 5.32. The images of size 90×90 μm^2 were obtained with a microscope objective of $50\times$ magnification ($NA = 0.75$) and were in post-processing assembled to one global map of 1.25×1.35 mm^2 size. Note that the colorbars of all individual images (from direct and photothermal holography) which form the two global maps, are normalized to

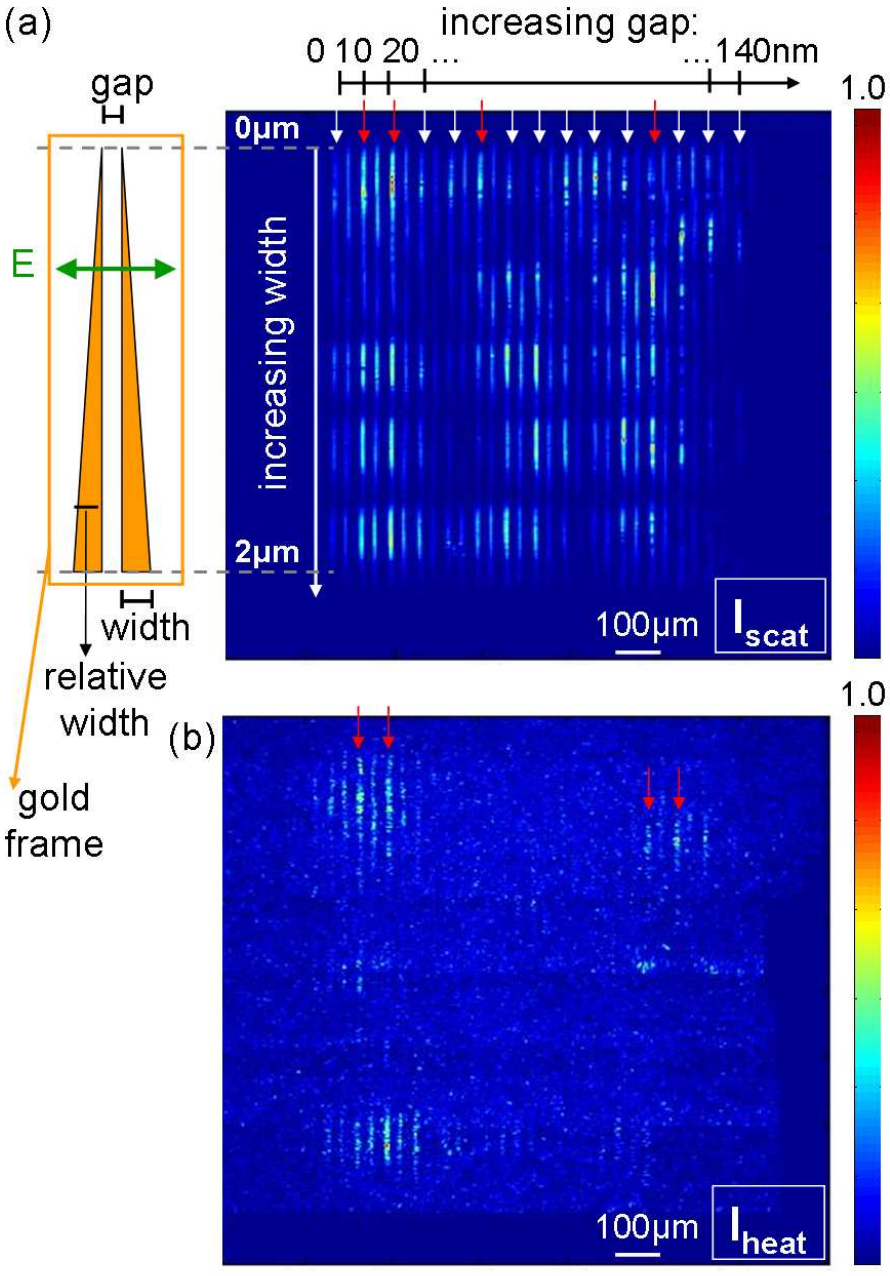

Figure 5.32 – The scheme on the left clarifies the geometry of the gold triangles and the gold frame. The green arrow denotes the polarization of the illumination and the heating beam. (a) Holographic (I_{scat}) and (b) photothermal intensity images (I_{heat}) of different triangle structures. The white and red arrows indicate the positions of the various coupled triangles. The intensities in both maps are normalized to 1.

1. The resulting scattering and photothermal maps are presented in Fig. 5.32 (a) and (b).

Regarding the geometry of the structure under study, the gap increases from left to right with a step of 10 nm (from 0 to 140 nm), resulting into 15 differently coupled triangles. The position of the triangles is highlighted by white and red arrows. Considering the coupled triangles approximately as coupled rods with continuously changing arm length, the relative width increases from top (0, triangle apex) to bottom (2 μm). The bright lines that are noticed at positions in between the signal from the triangles, result from the scattering of the gold frames which separate the coupled triangles from each other. The gold frame is also shown in the left-handed scheme in Fig. 5.32. [4] However, due to the polarization of the illumination laser which is perpendicular to the vertical lines of the gold frame, the influence of the scattering of the gold frame is relatively weak.

The scattering map reveals several zones of higher scattering intensities, denoted as I_{scat}, notably for the 10, 20, 50 and 110 nm sized gaps (see red arrows), indicating a stronger interaction with the illuminating light. Note that the gold frames next to a high scattering zone exhibit a more intense scattering which is attributed to the multiple scattering of the triangular structure. The appearance of zones of higher scattering is ascribed to the excitation of resonant modes in the triangles resulting into a strong interaction of light. Globally, these features appear for short triangle widths (for gaps of 10, 20, 50 and 90 nm), in the upper third part of the triangle (110 nm gap) and in the bottom half part (for gaps of 10, 20, 60, 70 and 110 nm). Notably, the scattering is distributed periodically over the triangle's length and relatively independent from the gap size.

The photothermal map differs strongly from the scattering map which confirms the profound difference between the origins of scattering and photothermal maps. The latter exhibits three zones of high photothermal intensities, denoted as I_{heat}: for small gaps (10, 20 and 30 nm) at small and large triangle widths, and for large gaps (110nm) at small widths (indicated by the red arrows in Fig. 5.32). Here, no periodicity of the intensity, although less intense, of the photothermal signal is immediately evident. Locally, near zones which exhibit a high photothermal intensity, we observe a higher photothermal signal of the frame compared to the frame signal near non-heated structures. Comparing these zones to the scattering maps, we notice that they are high scattering zones. Furthermore, it is seen that the gold frame and globally the triangles do not exhibit a notable heating. This may be due to the weak heating power which preferably heats small discontinuous structures.

In order to analyse quantitatively the zones of higher intensities, we plotted in Fig. 5.33 the cross sections of I_{scat} and I_{heat} along three different triangles for gap sizes of 20, 50 and 110 nm as a function of the triangle width. Because of the very small triangular angle, the width can be assumed to vary linearly. The values I_{phth} have been derived in

[4] It is remembered that each pair of triangles is separated by a gold frame as it was shown in Ch. 2 when presenting the nanostructuring of the samples.

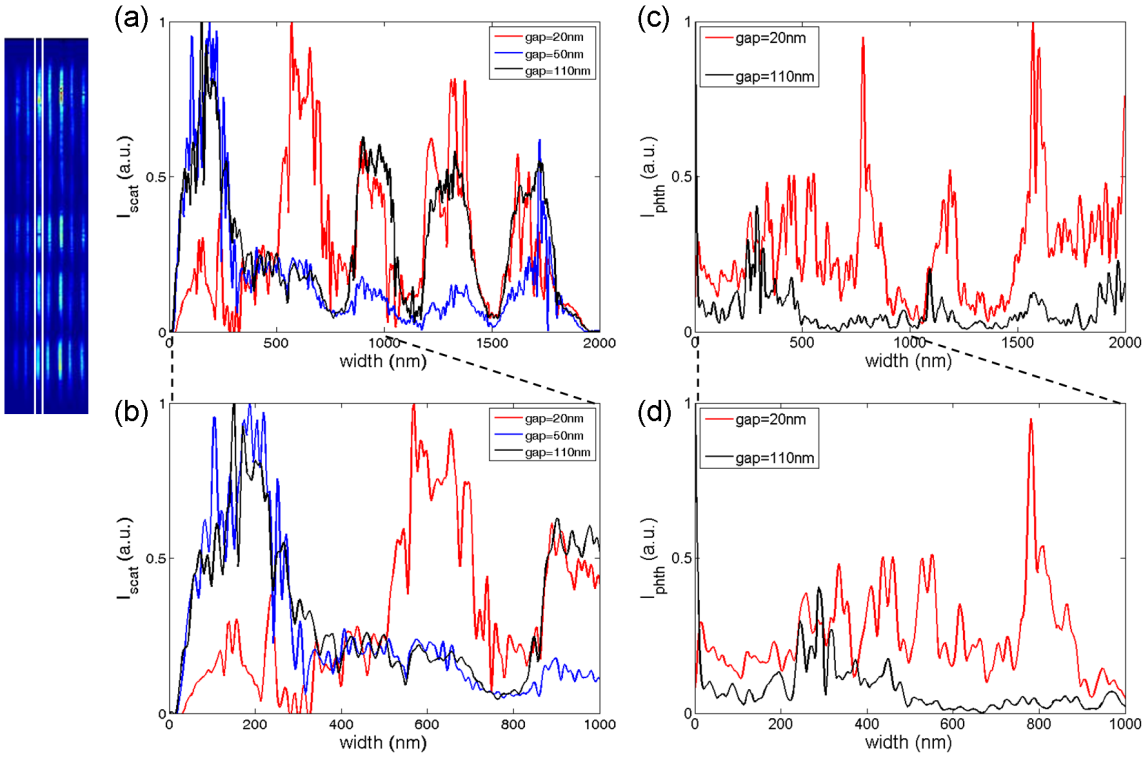

Figure 5.33 – Cross sections of holographic (a and b) images for coupled triangles with gaps of 20, 50 and 110 nm and photothermal (c and d) images for coupled triangles with gaps of 20 and 110 nm. The cross-sections are taken along the long side of the triangle pair (see left-handed scheme) for the triangles marked by the red-arrows in Fig. 5.32. The graphs (b) and (d) are zooms on the width range of 0-1000nm.

the same manner as for nanochains by background correcting I_{heat} and normalizing with I_{scat} using Eq. 5.8. The graph in Fig. 5.33 (a) confirms the observed periodicity of the scattered peak intensities I_{scat}, and we derive a period of about 400 nm. This periodicity becomes pronounced for widths larger than 900 nm and is almost the same for all three different gaps, only the magnitude of the scattered intensity differs which is weak in the case of the 50 nm gap and high in the other two cases. In order to examine more closely the scattering behaviour for smaller widths, Fig. 5.33 (b) plots only the width's range of interest between 0 and 1 μm. Apart from the intensity maximum at small widths, we notice for the smallest gap (20 nm) a second maximum at a width of around 600 nm which has been already observed in Fig. 5.33 (a).

The observed periodic distribution of maxima of scattered light with a periodicity of about 400 nm is attributed to the appearance of different resonance modes in the coupled triangles. The size of the period is about half of the illumination wavelength which is a further indication for resonant modes.

The photothermal intensities have been plotted only for the 20 and 110 nm sized gaps, since the 50 nm spaced triangles did not reveal any particular photothermal intensities. In Fig. 5.33 (c,d) we observe a periodicity which diminishes with increasing width from 500 nm to 320 nm. Examining the photothermal intensities in the reduced width range (see Fig. 5.33 (d)), a peak value at a width of 800 nm for a 20 nm gap is perceived in overall noisy signal. For a gap of 110 nm, the intensity I_{phth} peaks near a width value of 300 nm. We notice that the positions of highest scattering and heating intensities do not correspond to each other. Whereas the triangles, which are spaced by a 20 nm gap, scatter light strongly at a width of about 600 nm, the maximal heating is observed for a 200 nm larger width.

Comparison to Near-Field Simulations For the purpose of a more complete view of the scattering behaviour we performed near-field simulations. For these simulations we modelled two rectangular structures of size width×length, separated by a fixed gap where the length is two times the width in order to account for the impact of the continuous structure. The geometry is illustrated in the scheme in Fig. 5.34. A TIR illumination was used with an electric field vector parallel to the width. With changing width dimension (from 50 nm to 100 nm with a step of 10 nm), the scattered near-field intensity enhancement is calculated in the gap 10 nm above the structure and averaged over the gap surface in order to obtain I_{mean}. The graph shown in Fig. 5.34 compares I_{mean} to I_{scat}, denoting the experimentally obtained scattering intensities values.

The near-field intensity curve from simulations exhibits a very high intensity at a width of 60 nm which is not seen here. We recognize that both curves show a similar behaviour. Both quantities exhibit a (local) maximum at about 600 nm. I_{scat} displays another intensity increase around 900 nm. This local maximum may be confirmed by the simulation

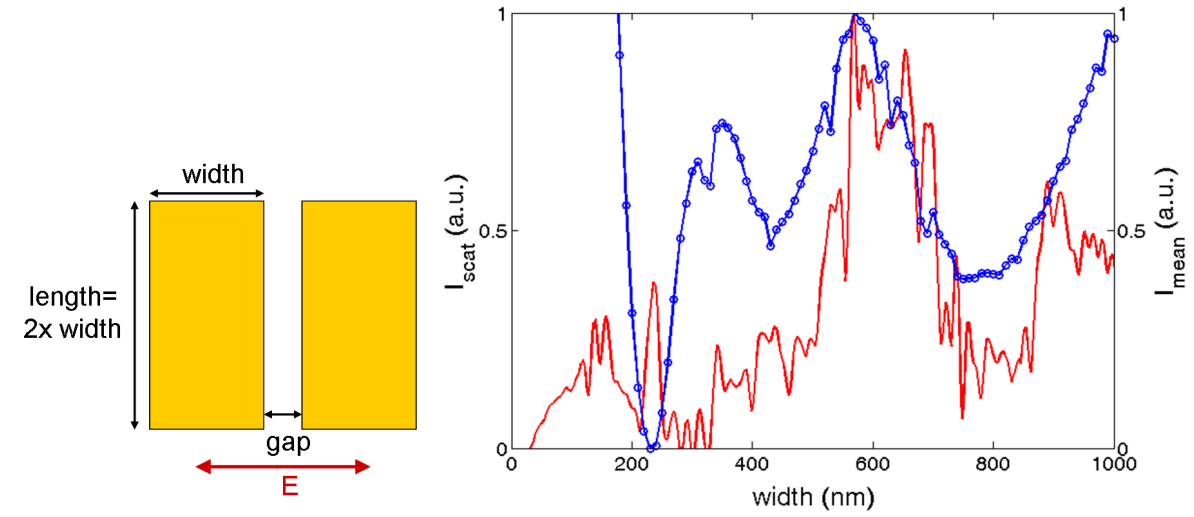

Figure 5.34 – The sketch illustrates the geometry used for the simulation. The graph compares measurement (I_{scat}, red) and simulation (I_{mean}, blue circles) for two triangles with a gap of 20 nm.

which exhibits an increase in I_{mean} from a 900 nm width towards larger widths. Overall, we conclude that the near-field simulations agree well with the far-field scattering intensities which leads to the assumption that strong near-field intensity enhancements result into a strong far-field scattering that can be detected by our holographic technique.

Conclusion on Triangles In conclusion, we have presented preliminary results of the scattering behaviour of two coupled triangles. We have studied direct holographic and photothermal images, resulting into scattering and heating maps of a series of differently coupled triangles. The scattering maps revealed a periodicity of scattering maxima, almost independently of the gap dimension, with a period of half the exciting wavelength, indicating the excitation of resonant modes in the structure.

The heating map proved that a strong scattering can result into a strong heating which affects neighbouring absorbing structures due to multiple scattering of the modulated field. We have shown that the position of the strongest scattering does not coincide with the strongest temperature increase. Overall, we confirmed the different natures of the origins of both map types.

Finally, a simulation study of the scattered near-field enhancement has revealed a strong agreement with the experimental scattered intensity as a function of the triangle's width.

5.5 Conclusion on the Application of Holography to Plasmonics

We have devoted this chapter almost entirely to the presentation and discussion of the results obtained on nanodisk chains. At first, we analysed in detail the far-field scattering spectra of numerous nanochains by measurements and simulations. We have shown that depending on the polarization of the exciting light, nanodisk chains exhibit longitudinal and transverse modes, which are characterized by an energy splitting. The resonance position of the transverse mode in a chain is constant, independently of the disk number and usually found at a higher energy than the longitudinal mode. By contrast, the resonance wavelength of the longitudinal mode fluctuates with increasing chain length. The resonance dependence on the gap width between the disks in a chain exhibits an exponential decay behaviour, regardless of disk size or disk number. This behaviour is similar to the exponential decay observed in the case of two coupled nanodisks which is explained in the frame of the dipolar-coupling model. We derived a decay constant which is the same for all chains, meaning that the decay trend is completely independent of the nanodisk size, but only dependent on the gap-diameter ratio. In both measurements and simulations the same characteristics of the scattering spectra are found which results in an excellent qualitative agreement between both.

We used digital heterodyne holography to study the spatial far-field scattering characteristics of nanodisk chains, a technique that is unknown in the domain of plasmonics for the three-dimensional imaging of nanoobjects. This study has been completed by simulating the near-field of chains. We investigated the impact of both intrinsic and extrinsic factors on the scattering pattern of nanodisk chains and showed that the scattering pattern is very sensitive to these factors. The polarization of the exciting light plays an important role for the characteristics of the scattering pattern. Depending on the polarization, longitudinal modes, transverse modes or a mixture of weakly coupled transverse and single disk modes are excited in the chain, which result in different shapes of the far- and near-field scattering maps. The scattering pattern of longitudinal modes is characterized by hot spots originating from the chain, whereas the far-field scattering of the transverse modes originate mainly from the scattering of the light at the chain ends. Near-field simulations confirmed a strong dependence of the near-field's amplitude and distribution above the chain on the excitation configuration. It was shown that the near-field enhancement is the highest for a longitudinal mode excitation. Not only the impact of the polarization of the incident beam but also the influence of the wavelength was investigated, and we have demonstrated that the smaller the difference is between resonance wavelength and illumination wavelength, the stronger becomes the near-field enhancement. Far-field scattering maps revealed a higher number of hot spots and strong directional scattering for an illumination close to the resonance of the chain which we

interpreted as a signature for a resonating chain. Furthermore, a strong directional scattering is one of the characteristics of a resonating antenna, therefore, we can speak of the nanodisk chain as a nanoantenna. In the course of the examination of the directional scattering behaviour, we have discussed Fourier space images and analysed three-dimensional surface plots in detail in order to reveal particular features for a directional scattering.

In the third part of this chapter we applied photothermal heterodyne holography to study the heating and coupling of nanochains. Using this technique we recorded photothermal maps of the plasmonic chains. An analytical analysis showed that the signal delivered by photothermal images is in good approximation directly proportional to the increase in temperature. A comparison between direct and photothermal holographic images demonstrated a significant discrepancy between scattering maps and heating maps which confirms the different origins of the two physical phenomena. Hence, we have presented a novel method to study the heating distribution in plasmonic nanostructures and applied this technique to nanodisk chains by recording heating maps with a heating beam polarized parallel or perpendicular to the chain axis as a function of the gap dimension. The obtained maps result into different amplitudes and distributions of the photothermal signal over the chain, meaning that a chain is heated differently depending on the polarization of the heating beam and on the chain geometry. It is expected that a chain heated with a beam polarized perpendicular to its axis, results into an ensemble of heated (uncoupled) single disks, whereas a parallel polarized heating beam induces a heating of the coupled chain. We chose to examine the difference between the two photothermal signals (resulting from the two different polarizations of the heating beam) for different gap dimensions in order to account for the coupling strength between the disks. For two different chain types, we obtained a maximum of the coupling strength at a gap width of 20 nm which is in good agreement with previous results.

Lastly, we presented preliminary results of the scattering and heating characteristics of coupled triangles. Depending on the triangle width, resonant scattering modes have been revealed and confirmed by near-field simulations. Furthermore, it has been shown that a strongly scattering zone does not coincide necessarily with the zone of the strongest temperature increase.

We have proved that both direct heterodyne holography and photothermal holography are powerful tools to study the properties of plasmonic nanostructures. Whereas direct holography records a three-dimensional picture of the scattered light by a nanoobject, allowing further insight into the angular distribution, photothermal holography directly probes the temperature increase in a heated nanostructure and furthermore, reveals different temperature distributions depending on the nanostructure and the heating beam polarization. Although the resolution of the holographic setup is near-diffraction limited, both techniques allow to gain insight into fundamental physical properties of the nanostructures.

To our knowledge it is the first time that plasmonic nanostructures have been investigated using holography. Overall, this study provides an overview of the scattering characteristics that can be observed by this three-dimensional far-field technique. Although the interpretation of the results is rather qualitative at this stage of early development of the technique, which is mainly due to the complexity of the studied systems, we are convinced that both direct holography and photothermal holography give new insight into the physics of plasmonics and are promising techniques in the future.

Conclusions and Prospects

Most of the work of this thesis was centred on an optimization and precise characterization of the possibilities of digital heterodyne holography in order to adept it to the demanding application of nanoantenna characterization. One of the main achievement of this thesis work has been the successful application of holography to map in three dimensions the field scattered by nanostructures. To our knowledge, this is the first time that the technique of holography was used in the domain of plasmonics for the characterization of gold nanostructures. Here, we proved that digital heterodyne holography is a tool which has the ability to fully map the electromagnetic field of complex nanostructures.

It has to be stressed out that the analysis of the scattering pattern of the nanostructures was not always straightforward, and that we encountered difficulties to properly interpret our measurements mostly due to the imperfections of the samples. In this context, this thesis work constitutes a first attempt to probe and reveal the limitations of the technique of digital heterodyne holography when applied to plasmonic nanostructures. Knowledge of its limitations will be precious for future studies that envisage to surmount them.

The following list summarizes the holographic technique's limitations that we encountered during our studies:

- One of the most pertinent limitations is the need of a full structural characterization of each nanoobject by scanning electron beam microscopy in order to know beforehand possible defaults of the nanostructures. Obviously, this observation would be really time-consuming since one sample contains much more than 6000 nanostructures, and one has to consider if a full characterization is realistic.

- The used numerical aperture (NA = 0.95) limits the angle range of the recorded scattering pattern to a half-cone of 72° in air and 39° in glass. Large NA immersion optics cannot be used, as they would forbid the use of total internal reflection (TIR), which was necessary for dark-field operation. In order to overcome this limit one could think of masking the illumination beam efficiently which can be quite challenging.

- This brings us to another limitation: the TIR configuration, which is quite complicated, being an asymmetric illumination incident from the glass substrate. A far

more simple technique would be a direct illumination. However, in this case again the strong illumination signal has to be filtered out in order to avoid blinding the CCD camera.

- One of the main advantages of holography is the recording of the phase of the scattered electromagnetic field which can provide information on local variations on the optical properties of the sample, e.g. the response of the nanostructure to an excitation with its resonance wavelength or the adsorption of molecules are characterized by a significant phase shift. However, the analysis of the optical phase obtained by a holographic setup is not straightforward, since holography is a diffraction limited technique, and therefore both the phase of the nanostructure and the phase of the substrate contribute to the recorded phase information. In order to be able to extract the phase contribution of the nanostructure, the knowledge of the phase of the substrate is essential. In this context, more work is necessary in order to determine the phase of a continuous metal surface.

- As stated during this study, a drawback of the presented holographic technique is that a direct comparison of the measured amplitudes of measurements under different conditions (e.g. varying polarization, illumination wavelength etc.) is not possible. This results into a lack of information when a comparison between different holograms is required. An absolute measurement would be desirable and useful (e.g. to estimate the ratio of light scattered by a nanostructure to the incident light), but very difficult to achieve due to the high sensitivity of the setup to the illumination beam.

Hence, the aim of future studies is to overcome these limitations in order to value the large potential of digital heterodyne holography and to make the technique more attractive for applications in plasmonics.

Beyond holography, which gives access to the spatial (3D) information of the light scattered in the far-field, we used two other techniques to obtain further information on the scattering behaviour of plasmonic nanostructures: spectroscopy of single nanoobjects and FEM simulations. Concerning the latter technique, in the course of this work we developed a simulation model, in order to calculate the far-field scattering and the near-field scattering by plasmonic nanostructures situated on a glass interface.

We have presented a detailed study on elementary nanoobjects in order to validate our experimental techniques and justify their application to plasmonic nanostructures. Our results proved to be in excellent agreement with theoretical predictions. Hence, we have shown that we are able to characterize the electromagnetic field of a nanostructure by combining digital heterodyne holography, sensitive spectrometry and numerical simulations.

As a more complex structure, the scattering characteristics of nanodisk chains, have been extensively studied. We demonstrated that the scattering pattern of nanodisk chains is very sensitive to both intrinsic and extrinsic factors, e.g. the polarization and wavelength of the incident light and the geometry of the nanostructure which was revealed both by measurements and simulations. We showed that, depending on the polarization, longitudinal modes, transverse modes or a mixture of weakly coupled transverse and single disk modes can be excited in the chain resulting into different shapes of the far- and near-field scattering maps.

In addition, we have applied the technique of photothermal holography to map the temperature increase of heated chains of nanodisks. We have demonstrated, that the photothermal signal gives us information on the temperature increase and on the heating distribution due to its proportionality to the temperature increase. Although this study was mostly preliminary, this technique has great potential to investigate the heating behaviour in continuous or more complex, discontinuous nanostructures.

Furthermore, we have developed the technique of frequency scanning heterodyne imaging, which is based on the heterodyne detection principle and scans the frequency domain of a system by systematically detuning the heterodyne beating frequency. This technique allows the detection of the frequency contents in a system and holds great promise for various applications. Here, we have shown that the frequency domain of a modulated temperature in an integrated circuit can be accessed. Another study we performed was aimed to analyse the rotational Brownian dynamics of heated gold nanorods in a liquid.

Prospects

As remarked before, this work is the first study that used holography to measure three-dimensional scattering maps of plasmonic nanostructures. This technique has proven its ability to map in one measurement the scattered electromagnetic field in three-dimensions. We are convinced that it will find many future applications in the field of plasmonics. In the following, we would like to give a short list of future projects and prospective applications:

Fano resonances We have shown that the characteristics of the scattering maps of nanostructures are extremely sensitive both to the illumination field (polarization of the beam, wavelength, orientation of k-vector, etc.) and to the plasmonic properties of the nanostructures under study (resonance wavelength, coupling strength, etc.). For example, by detuning the illumination wavelength, a change in the scattering has been observed. This sensitivity makes digital heterodyne holography one of the only techniques able to study structures that exhibit Fano resonances due to their asymmetric line-shape in the scattering spectra.

Rotation of Nanorods During this thesis work we have performed a preliminary study to investigate the Brownian dynamics of gold nanorods and its temperature dependence by applying an optical heating. The obtained results are promising but suffer a large uncertainty due to possible trapping effects. In this context further experiments are planned to investigate the temperature dependence of the rotational motion of nanorods by using a hot wire for heating the system instead of an optical heating in order to avoid rotational trapping.

"Nano-SNOM" Scanning near-field optical microscopy (SNOM) explores the near-field of a sample by measuring the scattered near-field with an optical probe. In this setup, the probe is usually fixed and in a controlled manner scanned over the sample's surface. We have seen, that holography allows the detection and localization of gold nanoparticles in a liquid. By combining the concept of SNOM and holography of freely moving nanoparticles, a novel method to detect the near-field of a sample is envisaged. We have initiated a project for the research on this new detection scheme in collaboration with F. Verpillat and M. Gross, from the Laboratoire Kastler Brossel (LKB) at the ENS in Paris, whose research studies are the 3D real-time localization and detection of nanobeads using holography.

The idea is the following: A micro-fluid chamber, filled with freely moving nanoparticles in a liquid, is coupled to the surface of the sample under investigation. When a nanoparticle gets in the vicinity of the sample's surface, it interacts with the near-field of the sample, and thus, an alteration of its light scattering will be created. By performing a statistical analysis of the light scattering by individual beads, one has access to the near-field structure of the sample.

Heating in Nanostructures We have shown that the signal of photothermal heterodyne holography is proportional to the temperature increase in plasmonic structures and applied it successfully to detect the photoinduced heating of nanodisk chains. Up to now the physics of heat generation and heat distribution in plasmonic nanostructures is poorly investigated. In this context, photothermal holography is a promising technique to fill the gap in experimental methods investigating the heating of nanostructures.

Appendix A

FEM Simulation Parameters - Fresnel Coefficients

The FEM model uses the three-dimensional scattered harmonic propagation mode. In this mode the scattered field is calculated which needs an accurate description of the total incident field in the whole simulation volume. Depending on the polarization of the incident light and the plane of incidence, different configurations have to be considered to describe fully the electric field in the whole simulation volume. Describing the experimental configuration for the measurement of scattering spectra, i.e. the case of reflection, the incident wave vector ${k_{inc}}^{Refl}$ propagates from +z to −z direction normal to the interface. The wave is polarized along the main axis of the nanostructure. Considering the experimental situation for holography, i.e. the case of transmission, the incident wave vector ${k_{inc}}^{Trans}$ propagates from −z to +z direction under an angle of α_i to the interface. In the latter case, several configurations of the electric field are possible, depending on the polarization of the wave (TE or TM wave) and on the choice of the plane of incidence (plane parallel or perpendicular to the long axis of the structure). All those configurations need individual descriptions of the electric field vector propagating in the simulation volume which are here considered and explained in detail.

A.1 Excitation Field in Reflection

In the case of reflection, the incident wave propagates from +z to −z direction and the electric field vector is oriented parallel to the x-axis, i.e. parallel to the long axis of the nanoobject. The corresponding electric field expressions that are used to describe the

field in the volume are quite simple:

$$\begin{aligned} n_1 &= n_{air} \\ n_2 &= n_{substrate} \\ r_{TM} &= \frac{n_2 - n_1}{n_2 + n_1} \\ t_{TM} &= \frac{2n_2}{n_2 + n_1} \\ E_x &= E_0\ exp(ik_0 n_1 z) + r_{TM}\ exp(-ik_0 n_1 z)(\forall z > 0) \\ &\quad + t_{TM}\ exp(ik_0 n_2 z)(\forall z < 0) \\ E_y &= 0 \\ E_z &= 0 \\ E_0 &= 1\ [V/m] \end{aligned}$$

n_1 denotes the refractive index of the medium of the incident wave and of the wave refracted on the interface, and n_2 denotes the refractive index of the medium of the transmitted wave. The wave is transverse magnetic (TM), i.e. the electric field is parallel to the plane of incidence, and r_{TM} and t_{TM} are the corresponding reflection and transmission coefficients. The incident wave vector is denoted as k_0. E_x, E_y and E_z are the components of the electric field, and E_0 is the incident field amplitude which amounts to 1 V/m for the sake of simplicity.

A.2 Excitation Field in Transmission

When describing the field in the transmission case under a non-zero incident angle of the incident wave, the electric field expressions become more complex. Furthermore, we have to differentiate between p- and s-polarized waves. Figure A.1 (a) depicts the p-polarized situation, when the electric field vector E_{i0} is parallel to the plane of incidence. The plane of incidence is defined by the propagation vectors of the incident and transmitted fields and represents the image plane. Figure A.1 (b) shows the s-polarization case.

p-polarization First, we consider the case of p-polarization. All vectors in Fig. A.1 (a) can be decomposed to the components in the (xyz) basis, if we use the standard plane wave notation $\vec{E} = \vec{E_0}\ exp(-j\vec{k_0}n\vec{r})$, with the components $\vec{E_0} = (\vec{E_{0x}}, \vec{E_{0y}}, \vec{E_{0z}})$ of the electric field amplitude vector, $\vec{k_0} = (\vec{k_{0x}}, \vec{k_{0y}}, \vec{k_{0z}})$ the free-space propagation vector, and $\vec{r} = (\vec{x}, \vec{y}, \vec{z})$ the radius vector in the Cartesian coordinate system. Thus we get according to Fig. A.1 (a):

$$\begin{aligned} \vec{E_i} &= (-\vec{E_{0i}}\cos\theta_1, 0, \vec{E_{0i}}\sin\theta_1)\ exp(-i(\vec{k_0}n_1\sin\theta_1\vec{x} + \vec{k_0}n_1\cos\theta_1\vec{z})) \\ \vec{E_r} &= (\vec{E_{0r}}\cos\theta_1, 0, \vec{E_{0r}}\sin\theta_1)\ exp(-i(\vec{k_0}n_1\sin\theta_1\vec{x} - \vec{k_0}n_1\cos\theta_1\vec{z})) \\ \vec{E_t} &= (-\vec{E_{0t}}\cos\theta_2, 0, \vec{E_{0t}}\sin\theta_2)\ exp(-i(\vec{k_0}n_2\sin\theta_2\vec{x} + \vec{k_0}n_2\cos\theta_2\vec{z})) \end{aligned}$$

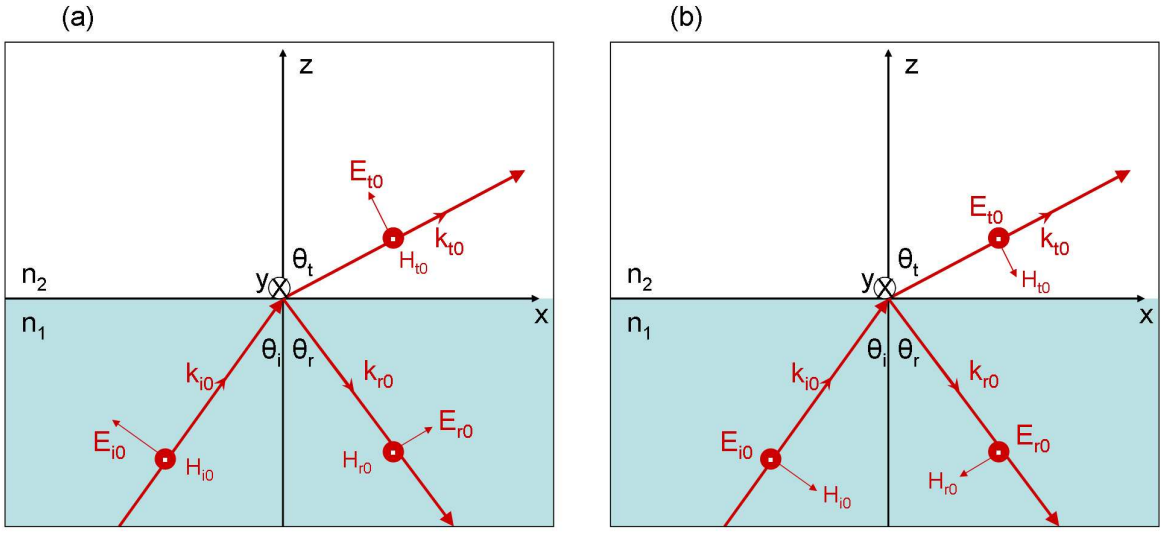

Figure A.1 – Scheme of the refraction and transmission of (a) a p- and (b) s-polarized incident wave.

In the present and in all following cases, we consider $|\vec{E_{0i}}| = 1$ V/m, for the sake of simplicity.

s-polarization Using Snell's law, i.e. $n_1 \sin\theta_1 = n_2 \sin\theta_2$, and the boundary condition for a dielectric interface, meaning that the tangential components of the $\vec{E}$ and $\vec{H}$ fields across the interface are continuous, we obtain the following Fresnel formulas with the Fresnel reflection r_{TM} and transmission coefficients t_{TM} for p-polarization:

$$\begin{aligned} E_{0r} &= r_{TM} E_{0i} \\ E_{0t} &= t_{TM} E_{0i} \\ t_{TM} &= \frac{2n_1 \cos\theta_1}{n_1 \cos\theta_2 + n_2 \cos\theta_1} \\ r_{TM} &= \frac{n_2 \cos\theta_1 - n_1 \cos\theta_2}{n_1 \cos\theta_2 + n_2 \cos\theta_1} \end{aligned}$$

Considering the case of total internal reflection, it is assumed that the light is fully refracted back into the medium, hence the transmitted wave goes to zero. This case has to be considered when writing down the expressions for the total internal reflection case.

Total Internal Reflection Case

Under total internal reflection (TIR) the incident light propagates from the substrate medium, with a refractive index of n_1, towards a less dense medium having n_2, i.e. $n_1 > n_2$, under an angle of incidence that is larger than the critical angle α_{crit} [1]. In this case the

[1] α_{crit} is defined as $(\sin(n_2/n_1))^{-1}$ and is 42° in the case of a glass-air interface.

light is fully reflected back into the medium. The penetration of a portion of incident light into the low refractive index medium, n_2, creates the evanescent field, which is represented by several small light waves propagating parallel to the interface and having decreased intensity with increasing distance from the interface. The TIR configuration is sketched for a s-polarized wave in Fig. A.2.

Here, we will give the analytical expressions for p- and s-polarized incident wave in the TIR case. These expressions were used for COMSOL modelling in the scattering formalism, when simulating the scattering of evanescent waves. For the simulations usually the

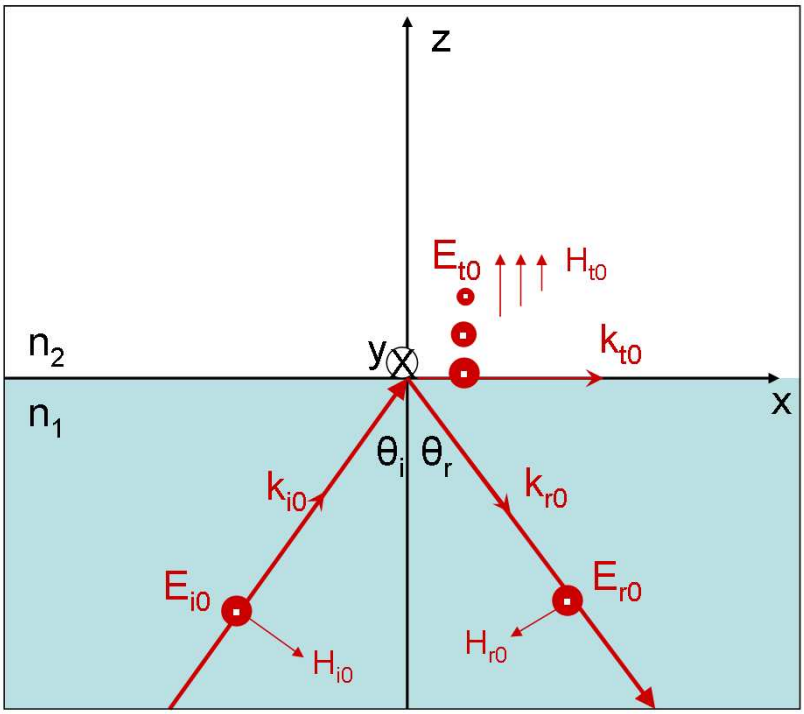

Figure A.2 – Scheme of an incident s-polarized wave in TIR configuration.

following notations for the angle of incidence, refraction and transmission and for the refractive indices were applied, and are the same in each considered illumination case:

$$\begin{aligned}
\alpha_i &= 45^\circ \\
\theta_1 &= \theta_i = \frac{2\pi}{360}\alpha_i[rad] \\
\theta_1 &= \theta_r \\
\sin\theta_2 &= \sin\theta_t = \frac{n_1}{n_2}\sin\theta_1 \\
\cos\theta_1 &= \sqrt{1-\sin\theta_1{}^2} \\
\cos\theta_2 &= \sqrt{1-\frac{n_1}{n_2}\sin\theta_1{}^2} \\
n_1 &= n_{substrate} \\
n_2 &= n_{air}
\end{aligned}$$

TIR: s-Polarization and y-z Plane as Plane of Incidence The configuration the most often considered during this work is the case of a s-polarized plane wave, propagating in the y-z plane, i.e. perpendicular to the axis of the nanoobject. In this case, the electric field has only a x-component.

We have stated that in the case of TIR no energy is transmitted across the interface. Therefore, we regard the expression for the transmitted wave:

$$\vec{E_t} = t_{TE,TIR}\ \vec{E_{0iy}}\ exp(-ik_t \sin\theta_2 x)\ exp(-ik_t \cos\theta_2 z) \tag{A.1}$$

$\vec{E_t}$ has to go to 0 when z goes to +infinity. In order to examine this condition in detail, we have a look at the $\cos\theta_2$ expression. As stated above we have $\frac{n_1}{n_2}\sin\theta_1 = \sin\theta_2 > 1$. Then, rewriting the angle $\cos\theta_2$ as $\cos\theta_2 = \pm i\ \sqrt{\frac{n_1}{n_2}\sin\theta_1{}^2 - 1}$, we state that Eq. A.1 goes to zero if we use

$$\cos\theta_2 = -i\ \sqrt{\frac{n_1}{n_2}\sin\theta_1{}^2 - 1} \tag{A.2}$$

Having these considerations in mind, we can write the following expressions describing a s-polarized wave in TIR configuration:

$$r_{TE,TIR} = \frac{n_1\sqrt{1-\sin\theta_1{}^2} - n_2(-i)\sqrt{\frac{n_1}{n_2}\sin\theta_1{}^2 - 1}}{n_1\sqrt{1-\sin\theta_1{}^2} + n_2(-i)\sqrt{\frac{n_1}{n_2}\sin\theta_1{}^2 - 1}} \tag{A.3}$$

$$t_{TE,TIR} = \frac{2n_1\sqrt{1-\sin\theta_1{}^2}}{n_1\sqrt{1-\sin\theta_1{}^2} + n_2(-i)\sqrt{\frac{n_1}{n_2}\sin\theta_1{}^2 - 1}} \tag{A.4}$$

$$\begin{aligned} E_{0x} &= exp(-ik_0 n_1 \sin\theta_1 y + \sqrt{1-\sin\theta_1{}^2}z) \\ &\quad + r_{TE,TIR}\ exp(-ik_0 n_1 \sin\theta_1 y - \sqrt{1-\sin\theta_1{}^2}z)\ (\forall z < 0) \\ &\quad + t_{TE,TIR}\ (exp(-ik_0 n_1 \sin\theta_1 y) exp(-k_0 n_2 \sqrt{1-\sin\theta_1{}^2}z))\ (\forall z > 0) \end{aligned} \tag{A.5}$$

$$E_{0y} = 0$$

$$E_{0z} = 0$$

$r_{TE,TIR}$ and $t_{TE,TIR}$ denote the reflection and transmission amplitude coefficients for TIR, and E_{0x}, E_{0y} and E_{0z} describe the electric field components for the x-, y- and z-axis.

TIR: s-Polarization and x-z Plane as Plane of Incidence In this illumination configuration, again the electric field vector has only one component, here the component along the y-axis. This case was used for example to simulate the excitation of transverse modes in a chain of nanodisks. The expressions for the reflection and transmission

coefficients are the same as in Eq. A.3.

$$\begin{aligned} E_{0x} &= 0 \\ E_{0y} &= exp(-ik_0 n_1 \sin\theta_1 x + \sqrt{1-\sin\theta_1{}^2}z) \\ &\quad + r_{TE,TIR}\, exp(-ik_0 n_1 \sin\theta_1 x - \sqrt{1-\sin\theta_1{}^2}z)\ (\forall z<0) \\ &\quad + t_{TE,TIR}\, (exp(-ik_0 n_1 \sin\theta_1 x) exp(-k_0 n_2 \sqrt{1-\sin\theta_1{}^2}z))\ (\forall z>0) \quad \text{(A.6)} \\ E_{0z} &= 0 \end{aligned}$$

TIR: p-Polarization and y-z Plane as Plane of Incidence If using p-polarized light, the electric field vector has two components. This is taken into account by the following formulas.

$$r_{TM,TIR} = \frac{n_2\sqrt{1-\sin\theta_1{}^2} - n_1(-i)\sqrt{\frac{n_1}{n_2}\sin\theta_1{}^2 - 1}}{n_2\sqrt{1-\sin\theta_1{}^2} + n_1(-i)\sqrt{\frac{n_1}{n_2}\sin\theta_1{}^2 - 1}} \quad \text{(A.7)}$$

$$t_{TM,TIR} = \frac{2n_1\sqrt{1-\sin\theta_1{}^2}}{n_2\sqrt{1-\sin\theta_1{}^2} + n_1(-i)\sqrt{\frac{n_1}{n_2}\sin\theta_1{}^2 - 1}} \quad \text{(A.8)}$$

$$\begin{aligned} E_{0x} &= 0 \\ E_{0y} &= (-\sqrt{1-\sin\theta_1{}^2})exp(-ik_0 n_1 \sin\theta_1 y + \sqrt{1-\sin\theta_1{}^2}z) \\ &\quad + r_{TM,TIR}\, \sqrt{1-\sin\theta_1{}^2} exp(-ik_0 n_1 \sin\theta_1 y - \sqrt{1-\sin\theta_1{}^2}z)(\forall z<0) \\ &\quad + t_{TM,TIR}\, (i\sqrt{1-\sin\theta_1{}^2})(exp(-ik_0 n_1 \sin\theta_1 y) \\ &\quad exp(-k_0 n_2 \sqrt{1-\sin\theta_1{}^2}z))(\forall z>0) \quad \text{(A.9)} \\ E_{0z} &= \sin\theta_1 exp(-ik_0 n_1 \sin\theta_1 y + \sqrt{1-\sin\theta_1{}^2}z) \\ &\quad + r_{TM,TIR}\ \sin\theta_1 exp(-ik_0 n_1 \sin\theta_1 y - \sqrt{1-\sin\theta_1{}^2}z)(\forall z<0) \\ &\quad + t_{TM,TIR}\ n_1/n_2 \sin\theta_1 (exp(-ik_0 n_1 \sin\theta_1 y) \\ &\quad exp(-k_0 n_2 \sqrt{1-\sin\theta_1{}^2}z))(\forall z>0) \quad \text{(A.10)} \end{aligned}$$

TIR: p-Polarization and x-z Plane as Plane of Incidence In the last case, the light is p-polarized and the x-z plane is used as the plane of incidence.

$$\begin{aligned}
E_{0x} &= (-\sqrt{1-\sin\theta_1{}^2})exp(-ik_0n_1\sin\theta_1 x+\sqrt{1-\sin\theta_1{}^2}z)\\
&\quad +r_{TM,TIR}\,\sqrt{1-\sin\theta_1{}^2}exp(-ik_0n_1\sin\theta_1 x-\sqrt{1-\sin\theta_1{}^2}z)(\forall z<0)\\
&\quad +t_{TM,TIR}\,(i\sqrt{1-\sin\theta_1{}^2})(exp(-ik_0n_1\sin\theta_1 x)\\
&\quad exp(-k_0n_2\sqrt{1-\sin\theta_1{}^2}z))(\forall z>0) \qquad \text{(A.11)}\\
E_{0y} &= 0\\
E_{0z} &= \sin\theta_1 exp(-ik_0n_1\sin\theta_1 x+\sqrt{1-\sin\theta_1{}^2}z)\\
&\quad +r_{TM,TIR}\,\sin\theta_1 exp(-ik_0n_1\sin\theta_1 x-\sqrt{1-\sin\theta_1{}^2}z)(\forall z<0)\\
&\quad +t_{TM,TIR}\,n_1/n_2\sin\theta_1(exp(-ik_0n_1\sin\theta_1 x)\\
&\quad exp(-k_0n_2\sqrt{1-\sin\theta_1{}^2}z))(\forall z>0) \qquad \text{(A.12)}
\end{aligned}$$

Appendix B

Square-Wave Function in Matlab

We describe shortly the program that we developed using **Matlab** in order to plot the square-wave function with a period of 2 kHz (used in Ch. 2.5.1) and its Fourier transform:

$$\begin{aligned} p &= 1/2000; \\ r &= 0.05; \\ dt &= 1/40960; \\ \text{[squar,t]} &= \text{gensig('square',p,r,dt);} \end{aligned}$$

where [squar,t] = gensig('square',p,r,dt) generates a signal of type "square", with period p (in seconds), time duration r of the signal and the spacing dt, i.e. sampling= 1/(80Hz·512). Then, the Fourier transform Y of the square-wave function is simply calculated with the following operation:

$$\begin{aligned} Y &= fft(squar, 1024); \\ Pyy &= abs(Y)/1024; \\ f &= 1/dt * (0:512)/1024; \end{aligned}$$

By plotting Pyy against the frequency range f we obtain the frequency domain of the square-wave function.

References

Absil, E., G. Tessier, M. Gross, M. Atlan, N. Warnasooriya, S. Y. Suck, M. Coppey-Moisan, and D. Fournier (2010). Photothermal heterodyne holography of gold nanoparticles. *Opt. Express 18*(2), 780–6.

Aizpurua, J., G. Bryant, L. Richter, F. García de Abajo, B. Kelley, and T. Mallouk (2005). Optical properties of coupled metallic nanorods for field-enhanced spectroscopy. *Phys. Rev. B 71*(23), 1–13.

Altet, J., E. Aldrete-Vidrio, D. Mateo, A. Salhi, S. Grauby, W. Claeys, S. Dilhaire, X. Perpiñà, and X. Jordà (2009). Heterodyne lock-in thermal coupling measurements in integrated circuits: Applications to test and characterization. *Rev. Sci. Instrum. 80*(2), 026101.

Alu, A. and N. Engheta (2008). Hertzian plasmonic nanodimer as an efficient optical nanoantenna. *Phys. Rev. B (Condensed Matter and Materials Physics) 78*(19), 195111.

Anger, P., P. Bharadwaj, and L. Novotny (2006). Enhancement and Quenching of Single-Molecule Fluorescence. *Phys. Rev. Lett. 96*(11), 3–6.

Aouani, H., O. Mahboub, E. Devaux, H. Rigneault, T. W. Ebbesen, and W. Jérôme (2011). Plasmonic Antennas for Directional Sorting of Fluorescence Emission. *Nano Lett.*, 2400–2406.

Atay, T., J.-H. Song, and A. V. Nurmikko (2004). Strongly Interacting Plasmon Nanoparticle Pairs: From Dipole-Dipole Interaction to Conductively Coupled Regime. *Nano Lett. 4*(9), 1627–1631.

Atlan, M., M. Gross, P. Desbiolles, E. Absil, G. Tessier, and M. Coppey-Moisan (2008). Heterodyne holographic microscopy of gold particles. *Opt. Lett. 33*, 500.

Baffou, G., C. Girard, and R. Quidant (2010). Mapping Heat Origin in Plasmonic Structures. *Phys. Rev. Lett. 104*(13), 1–4.

Baffou, G., M. P. Kreuzer, F. Kulzer, and R. Quidant (2009). Temperature mapping near plasmonic nanostructures using fluorescence polarization anisotropy. *Opt. Express 17*(5), 3291–8.

Bendix, P. M., S. Nader, S. Reihani, and L. B. Oddershede (2010). Direct Measurements of Heating by Electromagnetically Trapped Gold Nanoparticles on Supported Lipid Bilayers. *ACS NANO 4*(4), 2256–2262.

Berciaud, S., L. Cognet, P. Poulin, R. B. Weisman, and B. Lounis (2007). Absorption Spectroscopy of Individual Single-Walled Carbon Nanotubes. *Nano Lett. 7*(5), 1203–1207.

Berthelot, J., A. Bouhelier, C. Huang, J. Margueritat, G. Colas-des Francs, E. Finot, J.-C. Weeber, A. Dereux, S. Kostcheev, H. I. E. Ahrach, A.-L. Baudrion, J. Plain, R. Bachelot, P. Royer, and G. P. Wiederrecht (2009). Tuning of an optical dimer nanoantenna by electrically controlling its load impedance. *Nano Lett. 9*(11), 3914–21.

Bhaduri, B., A. Neild, and T. W. Ng (2008). Directional Brownian diffusion dynamics with variable magnitudes. *Appl. Phys. Lett. 92*(8), 084105.

Bharadwaj, P., B. Deutsch, and L. Novotny (2009). Optical Antennas. *Adv. Opt. Photon. 1*(3), 438–483.

Biagioni, P., J. Huang, L. Duò, M. Finazzi, and B. Hecht (2009). Cross Resonant Optical Antenna. *Phys. Rev. Lett. 102*(25), 1–4.

Biagioni, P., J.-S. Huang, and B. Hecht (2011). Nanoantennas for visible and infrared radiation. *arXiv:1103.1568*, 1–76.

Bidault, S., F. J. García de Abajo, and A. Polman (2008). Plasmon-Based Nanolenses Assembled on a Well-Defined DNA Template. *J. Am. Chem. Soc. 130*(9), 2750–2751.

Bohren, C. F. and D. R. Huffman (1983). *Absorption and scattering of light by small particles* (First ed.). New York: John Wiley and Sons.

Bonod, N., A. Devilez, B. Rolly, S. Bidault, and B. Stout (2010). Ultracompact and unidirectional metallic antennas. *Phys. Rev. B 82*(11), 1–6.

Boyer, D., P. Tamarat, A. Maali, B. Lounis, and M. Orrit (2002). Photothermal Imaging of Nanometer-Sized Metal Particles Among Scatterers. *Science 297*(5584), 1160–1163.

Brongersma, M. L., J. W. Hartman, and H. A. Atwater (2000). Electromagnetic energy transfer and switching in nanoparticle chain arrays below the diffraction limit. *Phys. Rev. B 62*(24), R16356—-R16359.

Brown, R. (1828). A brief account of microscopical observations made in the months of June, July and August, 1827, on the particles contained in the pollen of plants; and on the general existence of active molecules in organic and inorganic bodies. *Philosophical Magazine 4*, 161–173.

Cheong, F. C. and D. G. Grier (2010). Rotational and translational diffusion of copper oxide nanorods measured with holographic video microscopy. *Opt. Express 18*(7), 6555–62.

Cooley, J. W. and J. W. Tukey (1965). An Algorithm for the Machine Calculation of Complex Fourier Series. *Mathematics of Computation 19*, 297.

Crozier, K. B., A. Sundaramurthy, G. S. Kino, and C. F. Quate (2003). Optical antennas: Resonators for local field enhancement. *J. Appl. Phys. 94*(7), 4632.

Cuche, E., F. Bevilacqua, and C. Depeursinge (1999). Digital holography for quantitative phase-contrast imaging. *Opt. Lett. 24*(5), 291–3.

Cuche, E., P. Marquet, and C. Depeursinge (2000). Spatial filtering for zero-order and twin-image elimination in digital off-axis holography. *Appl. Opt. 39*(23), 4070–5.

Curto, A. G., G. Volpe, T. H. Taminiau, M. P. Kreuzer, R. Quidant, and N. F. van Hulst (2010). Unidirectional Emission of a Quantum Dot Coupled to a Nanoantenna. *Science 329*(5994), 930–933.

De Freitas, L. R., E. C. Da Silva, A. M. Mansanares, G. Tessier, and D. Fournier (2005). Sensitivity enhancement in thermoreflectance microscopy of semiconductor devices using suitable probe wavelengths. *J. Appl. Phys. 98*(6), 063508.

Demetrakopoulos, T. H. and R. Mittra (1974). Digital and Optical Reconstruction of Images from Suboptical Diffraction Patterns. *Appl. Opt. 13*(3), 665–670.

Devilez, A., B. Stout, and N. Bonod (2010a). Compact metallo-dielectric optical antenna for ultra directional and enhanced radiative emission. *ACS Nano 4*(6), 3390–6.

Devilez, A., B. Stout, and N. Bonod (2010b). Mode-balancing far-field control of light localization in nanoantennas. *Phys. Rev. B 81*(245128), 1–5.

Dilhaire, S., J.-M. Rampnoux, G. Pernot, G. Calbris, S. Grauby, C. Rossignol, S. Ermeneux, and E. Mottay (2008). Photothermal and photoacoustic imaging by ultrafast optical sampling. *J. Acoust. Soc. Am. 123*(5), 3705–3705.

Dorfmüller, J., D. Dregely, M. Esslinger, W. Khunsin, R. Vogelgesang, K. Kern, and H. Giessen (2011). Near-Field Dynamics of Optical Yagi-Uda Nanoantennas. *Nano Lett. 11*(7), 2819–2824.

Einstein, A. (1905). Über die von der molekularkinetischen Theorie der Wärme geforderte Bewegung. *Annalen der Physik 17*, 549.

Einstein, A. (1906a). Eine neue Bestimmung der Moleküldimensionen. *Annalen der Physik 19*, 289.

Einstein, A. (1906b). Zur Theorie der Brownschen Bewegung. *Annalen der Physik 19*, 371.

Esteban, R., R. Vogelgesang, J. Dorfmüller, A. Dmitriev, C. Rockstuhl, C. Etrich, and K. Kern (2008). Direct Near-Field Optical Imaging of Higher Order Plasmonic Resonances. *Nano Lett. 8*(10), 3155–3159. PMID: 18788785.

Ezzahri, Y., J. Christofferson, G. Zeng, and A. Shakouri (2009). Short time transient thermal behavior of solid-state microrefrigerators. *J. Appl. Phys. 106*(11), 114503.

Fano, U. (1941). The Theory of Anomalous Diffraction Gratings and of Quasi-Stationary Waves on Metallic Surfaces (Sommerfeld's Waves). *J. Opt. Soc. Am. 31*(3), 213–222.

Farahani, J. N., D. W. Pohl, H.-J. Eisler, and B. Hecht (2005). Single Quantum Dot Coupled to a Scanning Optical Antenna: A Tunable Superemitter. *Phys. Rev. Lett. 95*(1), 1–4.

Farzaneh, M., K. Maize, D. Lüerßen, J. A. Summers, P. M. Mayer, P. E. Raad, K. P. Pipe, A. Shakouri, R. J. Ram, and J. A. Hudgings (2009). CCD-based thermoreflectance microscopy: principles and applications. *J. Phys. D: Applied Physics 42*(14), 143001.

Fischer, H. and O. J. F. Martin (2008). Engineering the optical response of plasmonic nanoantennas. *Opt. Express 16*(12), 9144–54.

Fromm, D. P., A. Sundaramurthy, A. Kinkhabwala, P. J. Schuck, G. S. Kino, and W. E. Moerner (2006). Exploring the chemical enhancement for surface-enhanced Raman scattering with Au bowtie nanoantennas. *J. Chem. Phys. 124*(6), 061101.

Fromm, D. P., A. Sundaramurthy, P. J. Schuck, G. Kino, and W. E. Moerner (2004). Gap-Dependent Optical Coupling of Single Bowtie Nanoantennas Resonant in the Visible. *Nano Lett. 4*(5), 957–961.

Gabor, D. (1948). A New Microscopic Principle. *Nature 161*, 777–778.

Gabor, D. (1949). Microscopy by Reconstructed Wave-Fronts. *Proceedings of the Royal Society of London. Series A. Mathematical and Physical Sciences 197*(1051), 454–487.

Ghenuche, P. (2009). *Probing the Near-Field Optical Response of Plasmon Nanostructures with Two-Photon Luminescence Microscopy*. ICFO (Institut de Ciéncies Fotóniques) y Universitat Politécnica de Catalunya: PhD Thesis.

Ghenuche, P., S. Cherukulappurath, T. H. Taminiau, N. F. van Hulst, and R. Quidant (2008). Spectroscopic Mode Mapping of Resonant Plasmon Nanoantennas. *Phys. Rev. Lett. 101*(11), 116805.

Ghenuche, P., I. G. Cormack, G. Badenes, P. Loza-Alvarez, and R. Quidant (2007). Cavity resonances in finite plasmonic chains. *Appl. Phys. Lett. 90*(4), 041109.

Ghenuche, P., R. Quidant, and G. Badenes (2005). Cumulative plasmon field enhancement in finite metal particle chains. *Opt. Lett. 30*(14), 1882–4.

Girard, C. and R. Quidant (2004). Near-field optical transmittance of metal particle chain waveguides. *Opt. Express 12*(25), 6141–6.

Goodman, J. W. and L. W. Lawrence (1967). Digital Image Formation From Electronically Detected Holograms. *Appl. Phys. Lett. 11*(3), 77.

Greffet, J.-J. (2005). Nanoantennas for Light Emission. *Science 308*, 1561.

Greffet, J.-J., M. Laroche, and F. Marquier (2010, September). Impedance of a Nanoantenna and a Single Quantum Emitter. *Phys. Rev. Lett. 105*(11), 1–4.

Gross, M. and M. Atlan (2007). Digital holography with ultimate sensitivity. *Opt. Lett. 32*, 909.

Han, Y., A. M. Alsayed, M. Nobili, J. Zhang, T. C. Lubensky, and A. G. Yodh (2006). Brownian Motion of an Ellipsoid. *Science 314*(5799), 626–630.

Hao, F., Y. Sonnefraud, P. van Dorpe, S. A. Maier, N. J. Halas, and P. Nordlander (2008). Symmetry breaking in plasmonic nanocavities: subradiant LSPR sensing and a tunable Fano resonance. *Nano Lett. 8*, 3983–3988.

Hillenbrand, R. and F. Keilmann (2000, Oct). Complex Optical Constants on a Subwavelength Scale. *Phys. Rev. Lett. 85*, 3029–3032.

Hoffmann, J., C. Hafner, P. Leidenberger, J. Hesselbarth, and S. Burger (2009). Comparison of electromagnetic field solvers for the 3D analysis of plasmonic nanoantennas. *Proceedings of SPIE*, 73900J–73900J–11.

Hohenau, A., J. Krenn, J. Beermann, S. Bozhevolnyi, S. Rodrigo, L. Martin-Moreno, and F. Garcia-Vidal (2006). Spectroscopy and nonlinear microscopy of Au nanoparticle arrays: Experiment and theory. *Phys. Rev. B 73*(15), 1–7.

Huang, C., A. Bouhelier, J. Berthelot, G. C. Des-Francs, E. Finot, J.-C. Weeber, A. Dereux, S. Kostcheev, A.-L. Baudrion, J. Plain, R. Bachelot, P. Royer, and G. P. Wiederrecht (2010). External control of the scattering properties of a single optical nanoantenna. *Appl. Phys. Lett. 96*(14), 143116.

Huang, C., A. Bouhelier, G. C. des Francs, A. Bruyant, A. Guenot, E. Finot, J.-C. Weeber, and A. Dereux (2008). Gain, detuning, and radiation patterns of nanoparticle optical antennas. *Phys. Rev. B 78*(15), 155407.

Huang, J.-S., J. Kern, P. Geisler, P. Weinmann, M. Kamp, A. Forchel, P. Biagioni, and B. Hecht (2010). Mode Imaging and Selection in Strongly Coupled Nanoantennas. *Nano Lett. 10*(6), 2105–2110.

Huang, R., I. Chavez, K. M. Taute, B. Lukić, S. Jeney, M. G. Raizen, and E.-L. Florin (2011). Direct observation of the full transition from ballistic to diffusive Brownian motion in a liquid. *Nature Physics*, 1–5.

Huxtable, S., D. G. Cahill, V. Fauconnier, J. O. White, and J.-C. Zhao (2004). Thermal conductivity imaging at micrometre-scale resolution for combinatorial studies of materials. *Nature Materials 3*(5), 298–301.

Jain, P. K., W. Huang, and M. A. El-Sayed (2007). On the Universal Scaling Behavior of the Distance Decay of Plasmon Coupling in Metal Nanoparticle Pairs: A Plasmon Ruler Equation. *Nano Lett. 7*(7), 2080–2088.

Joud, F., F. Laloë, M. Atlan, J. Hare, and M. Gross (2009). Imaging a vibrating object by Sideband Digital Holography. *Opt. Express 17*(4), 2774–2779.

Joud, F., N. Warnasooriya, P. Bun, F. Verpillat, S. Y. Suck, G. Tessier, M. Atlan, P. Desbiolles, M. Coppey-Moisan, M. Abboud, and M. Gross (2011). 3D exploration of light scattering from live cells in the presence of gold nanomarkers using holographic microscopy. *3D Research 2*, 2:1–2:8.

Kelly, K. L., E. Coronado, L. L. Zhao, and G. C. Schatz (2003). The optical properties of metal nanoparticles: The influence of size, shape, and dielectric environment. *J. Phys. Chem. B 107*(3), 668–677.

Kinkhabwala, A., Z. Yu, S. Fan, Y. Avlasevich, K. Muellen, and W. E. Moerner (2009). Large single-molecule fluorescence enhancements produced by a bowtie nanoantenna. *Nature Photonics 3*(11), 654–657.

Knight, M. W., H. Sobhani, P. Nordlander, and N. J. Halas (2011). Photodetection with Active Optical Antennas. *Science 332*(6030), 702–704.

Koenderink, A. F. and A. Polman (2006). Complex response and polariton-like dispersion splitting in periodic metal nanoparticle chains. *Phys. Rev. B*, 1–4.

Kokkinakis, T. and K. Alexopoulos (1972). Observation of Radiative Decay of Surface Plasmons in Small Silver Particles. *Phys. Rev. Lett. 28*(25), 1632–1634.

Kosako, T., Y. Kadoya, and H. F. Hofmann (2010). Directional control of light by a nano-optical Yagi–Uda antenna. *Nature 4*(March).

Kottmann, J. P. and O. J. F. Martin (2001). Retardation-induced plasmon resonances in coupled nanoparticles. *Opt. Lett. 26*(14), 1096–1098.

Kreibig, U. and M. Vollmer (1995). *Optical Properties of Metal Clusters*. Berlin: Springer.

Kreis, T., M. Adams, and W. P. O. Jueptner (1997). Methods of digital holographic: a comparison (Proceedings Paper). *Proc. SPIE 3098*, 224–33.

Krenn, J., A. Dereux, J. Weeber, E. Bourillot, Y. Lacroute, J. Goudonnet, G. Schider, W. Gotschy, A. Leitner, F. Aussenegg, and C. Girard (1999). Squeezing the Optical Near-Field Zone by Plasmon Coupling of Metallic Nanoparticles. *Phys. Rev. Lett. 82*(12), 2590–2593.

Kretschmann, E. (1971). Die Bestimmung optischer Konstanten von Metallen durch Anregung von Oberflächenplasmaschwingungen. *Zeitschrift für Physik A: Hadrons and Nuclei 241*, 313–324. 10.1007/BF01395428.

Kretschmann, E. and H. Raether (1968). *Z. Naturf. A 23*, 2135.

Kronrod, M. A., N. S. Merzyakov, and L. P. Yaroslavskii (1972). Reconstruction of a hologram with a computer. *Soviet Physics Technical Physics 17*, 333–334.

Kühn, S., U. Håkanson, L. Rogobete, and V. Sandoghdar (2006). Enhancement of Single-Molecule Fluorescence Using a Gold Nanoparticle as an Optical Nanoantenna. *Phys. Rev. Lett. 97*(1), 017402.

Lal, S., S. Link, and N. J. Halas (2007). Nano-optics from sensing to waveguiding. *Nature Photonics 1*, 641–648.

Lasne, D., G. A. Blab, S. Berciaud, M. Heine, L. Groc, D. Choquet, L. Cognet, and B. Lounis (2006). Single nanoparticle photothermal tracking (SNaPT) of 5-nm gold beads in live cells. *Biophys. J. 91*(12), 4598–604.

Lassiter, J. B., M. W. Knight, N. A. Mirin, and N. J. Halas (2009). Reshaping the plasmonic properties of an individual nanoparticle. *Nano Lett. 9*(12), 4326–32.

Le Clerc, F., L. Collot, and M. Gross (2000). Numerical heterodyne holography with 2D photodetector arrays. *Opt. Lett. 25*, 716.

Leith, E. and J. Upatnieks (1962). Reconstructed wavefronts and communication theory. *J. Opt. Soc. Am 52*(10), 1123–1130.

Leith, E. N. and J. Upatnieks (1964). Wavefront Reconstruction with Diffused Illumination and 3-Dimensional Objects. *J. Opt. Soc. Am 54*, 1295–1300.

Lester, M. and D. C. Skigin (2011). An optical nanoantenna made of plasmonic chain resonators. *J. Opt. 13*(3), 035105.

Lévêque, G. and R. Quidant (2008). Channeling light along a chain of near-field coupled gold nanoparticles near a metallic film. *Opt. Express 16*(26), 22029–22038.

Lezec, H. J., A. Degiron, E. Devaux, R. A. Linke, L. Martin-Moreno, F. J. Garcia-Vidal, and T. W. Ebbesen (2002). Beaming Light from a Subwavelength Aperture. *Science 297*(5582), 820–822.

Li, J., A. Salandrino, and N. Engheta (2007). Shaping light beams in the nanometer scale: A Yagi-Uda nanoantenna in the optical domain. *Phys. Rev. B 76*(24), 245403.

Lieb, M. A., J. M. Zavislan, and L. Novotny (2004). Single-molecule orientations determined by direct emission pattern imaging. *J. Opt. Soc. Am. B 21*(6), 1210.

Liu, M., T.-W. Lee, S. Gray, P. Guyot-Sionnest, and M. Pelton (2009). Excitation of Dark Plasmons in Metal Nanoparticles by a Localized Emitter. *Phys. Rev. Lett. 102*(10), 1–4.

Liu, N., M. L. Tang, M. Hentschel, H. Giessen, and A. P. Alivisatos (2011). Nanoantenna-enhanced gas sensing in a single tailored focus. *Nature Materials 10*(May), 631–636.

Liu, Z., A. Boltasseva, R. Pedersen, R. Bakker, A. Kildishev, V. Drachev, and V. Shalaev (2008). Plasmonic nanoantenna arrays for the visible. *Metamaterials 2*(1), 45–51.

Liu, Z., M. D. Thoreson, A. V. Kildishev, and V. M. Shalaev (2009). Translation of nanoantenna hot spots by a metal-dielectric composite superlens. *Appl. Phys. Lett. 95*(3), 033114.

Maier, S., M. Brongersma, P. Kik, and H. Atwater (2002). Observation of near-field coupling in metal nanoparticle chains using far-field polarization spectroscopy. *Phys. Rev. B 65*(19), 1–4.

Maier, S. A. (2007). *Plasmonics: Fundamentals and Applications*. Berlin: Springer.

Maier, S. A., M. L. Brongersma, P. G. Kik, S. Meltzer, A. A. G. Requicha, and H. A. Atwater (2001). Plasmonics — A Route to Nanoscale Optical Devices. *Advanced Materials 13*(19), 1501–1505.

Maier, S. A., P. G. Kik, H. A. Atwater, S. Meltzer, E. Harel, B. E. Koel, and A. A. G. Requicha (2003). Local detection of electromagnetic energy transport below the diffraction limit in metal nanoparticle plasmon waveguides. *Nature Materials 2*, 229–232.

Mann, C., L. Yu, C.-M. Lo, and M. Kim (2005). High-resolution quantitative phase-contrast microscopy by digital holography. *Opt. Express 13*(22), 8693–8698.

Marquet, P., B. Rappaz, P. J. Magistretti, E. Cuche, Y. Emery, T. Colomb, and C. Depeursinge (2005). Digital holographic microscopy: a noninvasive contrastimaging technique allowing quantitative visualization ofliving cells with subwavelength axial accuracy. *Opt. Lett. 30*(5), 468–470.

Meier, M. and A. Wokaun (1983). Enhanced fields on large metal particles: dynamic depolarization. *Opt. Lett. 8*(11), 581–583.

Merlein, J., M. Kahl, A. Zuschlag, A. Sell, A. Halm, J. Boneberg, P. Leiderer, A. Leitenstorfer, and R. Bratschitsch (2008). Nanomechanical control of an optical antenna. *Nature Photonics 2*(4), 230–233.

Mie, G. (1908). Beiträge zur Optik trüber Medien, speziell kolloidaler Metallösungen. *Ann. Physik 25*, 377–445.

Mohammadi, A., V. Sandoghdar, and M. Agio (2008). Gold nanorods and nanospheroids for enhancing spontaneous emission. *New Journal of Physics 10*(10), 105015.

Mühlschlegel, P., H.-J. Eisler, O. J. F. Martin, B. Hecht, and D. W. Pohl (2005). Resonant Optical Antennas. *Science 308*(5728), 1607–1609.

Muskens, O. L., V. Giannini, J. A. Sánchez-Gil, and J. Gómez Rivas (2007). Optical scattering resonances of single and coupled dimer plasmonic nanoantennas. *Opt. Express 15*(26), 17736–46.

Nicola, S. D., P. Ferraro, A. Finizio, and G. Pierattini (2001). Correct-image reconstruction in the presence of severe anamorphism by means of digital holography. *Opt. Lett. 26*(13), 974–976.

Nicola, S. D., P. Ferraro, A. Finizio, and G. Pierattini (2002). Wave front reconstruction of Fresnel off-axis holograms with compensation of aberrations by means of phase-shifting digital holography. *Optics and Lasers in Engineering 37*(4), 331 – 340.

Nordlander, P., C. Oubre, E. Prodan, K. Li, and M. I. Stockman (2004). Plasmon Hybridization in Nanoparticle Dimers. *Nano Lett. 4*(5), 899–903.

Novotny, L. (2007a). Chapter 5: The history of near-field optics. *50*, 137 – 184.

Novotny, L. (2007b). Effective Wavelength Scaling for Optical Antennas. *Phys. Rev. Lett. 98*(26), 266802.

Novotny, L. and B. Hecht (2006). *Principles of Nano-Optics*. Cambridge: Cambridge University Press.

Olk, P., J. Renger, M. T. Wenzel, and L. M. Eng (2008). Distance Dependent Spectral Tuning of Two Coupled Metal Nanoparticles. *Nano Lett. 8*(4), 1174–1178. PMID: 18338870.

Palik, E. D. (1998). *Handbook of Optical Constants of Solids II* (Second ed.). San Diego, CA: Academic.

Pellegrini, G., G. Mattei, and P. Mazzoldi (2009). Tunable, directional and wavelength selective plasmonic nanoantenna arrays. *Nanotechnology 20*(6), 065201 (5pp).

Pelton, M., J. Aizpurua, and G. Bryant (2008). Metal-nanoparticle plasmonics. *Laser & Photonics Reviews 2*(3), 136–159.

Perrin, F. (1934). The Brownien movement of an ellipsoide. - The dielectric dispersion of ellipsoidal molecules. *J. Phys. Rad. 5*, 497–511.

Perrin, F. (1936). Brownian movement of an ellipsoid (II). - Free rotation and depolarisation of fluourescences. - Translation and diffusion of ellipsoidal molecules. *J. Phys. Rad. 7*, 1–11.

Pramod, P. and K. G. Thomas (2008). Plasmon Coupling in Dimers of Au Nanorods. *Adv. Mat. 20*(22), 4300–4305.

Prodan, E., C. Radloff, N. J. Halas, and P. Nordlander (2003). A Hybridization Model for the Plasmon Response of Complex Nanostructures. *Science 302*(5644), 419–422.

Quinten, M., A. Leitner, J. R. Krenn, and F. R. Aussenegg (1998). Electromagnetic energy transport via linear chains of silver nanoparticles. *Opt. Lett. 23*(17), 1331–3.

Rechberger, W., A. Hohenau, A. Leitner, J. R. Krenn, B. Lamprecht, and F. R. Aussenegg (2003). Optical properties of two interacting gold nanoparticles. *Opt. Comm. 220*(1-3), 137–141.

Righini, M., P. Ghenuche, S. Cherukulappurath, V. Myroshnychenko, F. J. Garcia de Abajo, and R. Quidant (2009). Nano-optical Trapping of Rayleigh Particles and Escherichia coli Bacteria with Resonant Optical Antennas. *Nano Lett. 9*(10), 3387–3391. PMID: 19159322.

Righini, M., G. Volpe, C. Girard, D. Petrov, and R. Quidant (2008). Surface Plasmon Optical Tweezers: Tunable Optical Manipulation in the Femtonewton Range. *Phys. Rev. Lett. 100*(18), 186804.

Rogobete, L., F. Kaminski, M. Agio, and V. Sandoghdar (2007). Design of plasmonic nanoantennae for enhancing spontaneous emission. *Opt. Lett. 32*(12), 1623–1625.

Romero, I., J. Aizpurua, G. W. Bryant, and F. J. García De Abajo (2006). Plasmons in nearly touching metallic nanoparticles: singular response in the limit of touching dimers. *Opt. Express 14*(21), 9988–99.

Rosencwaig, A., J. Opsal, W. L. Smith, and D. L. Willenborg (1985). Detection of thermal waves through optical reflectance. *Appl. Phys. Lett. 46*(11), 1013–1015.

Ruijgrok, P. V., N. R. Verhart, P. Zijlstra, A. L. Tchebotareva, and M. Orrit (2011). Brownian Fluctuations and Heating of an Optically Aligned Gold Nanorod. *Phys. Rev. Lett. 107*(3), 037401.

Schnars, U. and W. Jüptner (1994). Direct recording of holograms by a CCD target and numerical reconstruction. *Appl. Opt. 33*(2), 179.

Schnars, U. and W. Jüptner (2005). *Digital Holography*. Berlin Heidelberg: Springer-Verlag.

Schnars, U. and W. P. O. Jüptner (2002). Digital recording and numerical reconstruction of holograms. *Measurement Science and Technology 13*(9), R85–R100.

Schnell, M., A. Garcia-Etxarri, J. Alkorta, J. Aizpurua, and R. Hillenbrand (2010). Phase-resolved mapping of the near-field vector and polarization state in nanoscale antenna gaps. *Nano Lett. 10*(9), 3524–8.

Schuck, P. J., D. P. Fromm, A. Sundaramurthy, G. S. Kino, and W. E. Moerner (2005). Improving the Mismatch between Light and Nanoscale Objects with Gold Bowtie Nanoantennas. *Phys. Rev. Lett. 94*(1), 14–17.

Seol, Y., A. E. Carpenter, and T. T. Perkins (2006). Gold nanoparticles: enhanced optical trapping and sensitivity coupled with significant heating. *Opt. Lett. 31*(16), 2429–2431.

Shelton, W., K. Bonin, and T. Walker (2005). Nonlinear motion of optically torqued nanorods. *Phys. Rev. E 71*(3), 1–8.

Smythe, E. J., E. Cubukcu, and F. Capasso (2007). Optical properties of surface plasmon resonances of coupled metallic nanorods. *Opt. Express 15*(12), 7439–47.

Sommerfeld, A. (1899). Ueber die Fortpflanzung elektrodynamischer Wellen längs eines Drahtes. *Annalen der Physik 303*(2), 233–290.

Sommerfeld, A. (1909). Über die Ausbreitung der Wellen in der drahtlosen Telegraphie. *Annalen der Physik 333*(4), 665–736.

Sönnichsen, C. and A. P. Alivisatos (2005). Gold nanorods as novel nonbleaching plasmon-based orientation sensors for polarized single-particle microscopy. *Nano Lett. 5*(2), 301–4.

Sönnichsen, C., T. Franzl, T. Wilk, G. von Plessen, J. Feldmann, O. Wilson, and P. Mulvaney (2002). Drastic Reduction of Plasmon Damping in Gold Nanorods. *Phys. Rev. Lett. 88*(7), 77402.

Stadelmaier, A. and J. H. Massig (2000). Compensation of lens aberrations in digital holography. *Opt. Lett. 25*(22), 1630–1632.

Stockman, M. I. (2011). Nanoplasmonics : The physics behind the applications. *Physics Today* (February), 39–44.

Su, K.-H., Q.-H. Wei, X. Zhang, J. J. Mock, D. R. Smith, and S. Schultz (2003). Interparticle Coupling Effects on Plasmon Resonances of Nanogold Particles. *Nano Lett. 3*(8), 1087–1090.

Suck, S. Y., S. Collin, N. Bardou, Y. De Wilde, and G. Tessier (2011). Imaging the three-dimensional scattering pattern of plasmonic nanodisk chains by digital heterodyne holography. *Opt. Lett. 36*(6), 849–851.

Suck, S. Y., G. Tessier, N. Warnasooriya, A. Babuty, and Y. De Wilde (2010). Frequency-resolved temperature imaging of integrated circuits with full field heterodyne interferometry. *Appl. Phys. Lett. 96*(12), 121108.

Synge, E. H. (1928). A suggested model for extending microscopic resolution into the ultra-microscopic region. *Phil. Mag. 6*, 356—-362.

Sönnichsen, C. (2001). *Plasmons in metal nanostructures*. Ludwig-Maximilians-Universität München: PhD Thesis.

Taminiau, T. H., R. J. Moerland, F. B. Segerink, L. Kuipers, and N. F. van Hulst (2007). $\Lambda/4$ resonance of an optical monopole antenna probed by single molecule fluorescence. *Nano Lett. 7*(1), 28–33.

Taminiau, T. H., F. D. Stefani, and N. F. van Hulst (2008). Enhanced directional excitation and emission of single emitters by a nano-optical Yagi-Uda antenna. *Opt. Express 16*(14), 10858–10866.

Tang, L., S. E. Kocabas, S. Latif, A. K. Okyay, D.-S. Ly-Gagnon, K. C. Saraswat, and D. A. B. Miller (2008). Nanometre-scale germanium photodetector enhanced by a near-infrared dipole antenna. *Nature Photonics 2*(4), 226–229.

Tessier, G., S. Hole, and D. Fournier (2001). Quantitative thermal imaging by synchronous thermoreflectance with optimized illumination wavelengths. *Appl. Phys. Lett. 78*, 2267.

Tessier, G., G. Jerosolimski, S. Hole, D. Fournier, and C. Filloy (2003). Measuring and predicting the thermoreflectance sensitivity as a function of wavelength on encapsulated materials. *Rev. Sci. Instrum. 74*, 495.

Tirado, M. M. and J. Garcia de la Torre (1979). Translational friction coefficients of rigid, symmetric top macromolecules: Application to circular cylinders. *J. Chem. Phys. 71*(6), 2581–2587.

Tirado, M. M. and J. Garcia de la Torre (1980). Rotational dynamics of rigid, symmetric top macromolecules: Application to circular cylinders. *J. Chem. Phys. 73*(4), 1986–1993.

Vogelgesang, R., J. Dorfmüller, R. Esteban, R. T. Weitz, A. Dmitriev, and K. Kern (2008). Plasmonic nanostructures in aperture-less scanning near-field optical microscopy (aSNOM). *Physica Status Solidi 245*(10), 2255–2260.

Warnasooriya, N., F. Joud, P. Bun, G. Tessier, M. Coppey-Moisan, P. Desbiolles, M. Atlan, M. Abboud, and M. Gross (2010). Imaging gold nanoparticles in living cell environments using heterodyne digital holographic microscopy. *Opt. Express 18*(4), 3264.

Weber-Bargioni, A., A. Schwartzberg, M. Schmidt, B. Harteneck, D. F. Ogletree, P. J. Schuck, and S. Cabrini (2010). Functional plasmonic antenna scanning probes fabricated by induced-deposition mask lithography. *Nanotechnology 21*(6), 065306.

Willingham, B. and S. Link (2011). Energy transport in metal nanoparticle chains via sub-radiant plasmon modes. *Opt. Express 19*(7), 6450–61.

Wissert, M. D., C. Moosmann, K. S. Ilin, M. Siegel, U. Lemmer, H. Group, N. Science, and L. Technology (2011). Gold nanoantenna resonance diagnostics via transversal particle plasmon luminescence. *Opt. Express 19*(4), 3686 – 3693.

Wissert, M. D., A. W. Schell, K. S. Ilin, M. Siegel, and H.-J. Eisler (2009). Nanoengineering and characterization of gold dipole nanoantennas with enhanced integrated scattering properties. *Nanotechnology 20*(42), 425203.

Wokaun, A., J. P. Gordon, and P. F. Liao (1982). Radiation Damping in Surface-Enhanced Raman Scattering. *Phys. Rev. Lett. 48*(14), 957–960.

Wood, R. (1902). On a remarkable case of uneven distribution of light in a diffraction grating spectrum. *Philosophical Magazine Series 6 4*(21), 396–402.

Yamaguchi, I., J. Kato, S. Ohta, and J. Mizuno (2001). Image Formation in Phase-Shifting Digital Holography and Applications to Microscopy. *Appl. Opt. 40*(34), 6177–6186.

Yamaguchi, I. and T. Zhang (1997). Phase-shifting digital holography. *Opt. Lett. 22*(16), 1268–70.

Yang, S.-C., H. Kobori, C.-L. He, M.-H. Lin, H.-Y. Chen, C. Li, M. Kanehara, T. Teranishi, and S. Gwo (2010). Plasmon hybridization in individual gold nanocrystal dimers: direct observation of bright and dark modes. *Nano Lett. 10*(2), 632–7.

Yang, T. and K. B. Crozier (2008). Dispersion and extinction of surface plasmons in an array of gold nanoparticle chains : influence of the air / glass interface. *Opt. Express 16*(12), 8570–8580.

Yu, L. and M. K. Kim (2005). Wavelength-scanning digital interference holography for tomographic three-dimensional imaging by use of the angular spectrum method. *Opt. Lett. 30*(16), 2092–2094.

Yu, N., E. Cubukcu, L. Diehl, D. Bour, S. Corzine, J. Zhu, G. Höfler, K. B. Crozier, and F. Capasso (2007). Bowtie plasmonic quantum cascade laser antenna. *Opt. Express 15*(20), 13272–13281.

Zenneck, J. (1907). Über die Fortpflanzung ebener elektromagnetischer Wellen längs einer ebenen Leiterfläche und ihre Beziehung zur drahtlosen Telegraphie. *Annalen der Physik 328*(10), 846–866.

Zhang, T. and I. Yamaguchi (1998). Three-dimensional microscopy with phase-shifting digital holography. *Opt. Lett. 23*(15), 1221–1223.

Zhang, W., L. Huang, C. Santschi, and O. J. F. Martin (2010). Trapping and sensing 10

nm metal nanoparticles using plasmonic dipole antennas. *Nano Lett. 10*(3), 1006–11.